
Functional and structural organisation of the visual system in human albinism

Ivan Arturo Alvarez Ferreira, BSc MSc

A thesis submitted to University College London
in fulfilment of the requirements for the degree of

Doctor of Philosophy

Developmental Imaging and Biophysics Section

Institute of Child Health

University College London

2017

Thesis declaration form

I, Ivan Arturo Alvarez Ferreira, confirm that the work presented in this thesis is my own. Where information has been derived from other sources, I confirm that this has been indicated in the thesis.

Signature:

Date:

Acknowledgements

I would like to thank, first and foremost, my doctoral supervisors Chris Clark and Alki Liasis for their help and guidance, as well as their confidence in the relevance of this work. During my doctoral studies I have been immensely fortunate to receive the help of a further three excellent, if unofficial, advisors; Sam Schwarzkopf, Geraint Rees and Marty Sereno. Their kind help and unerring advice has meant this work was able to transform from conception to reality.

Amongst my colleagues, I would like to give special thanks to Benjamin de Haas, Merina Su and Rebecca Lyness, whose scientific contribution, knowingly or unwittingly, greatly improved the work presented in this thesis. I would also like to thank Jamie Kawadler, Clare Gibbard, Patrick Hales, Kiran Seunarine, Matthew Grech-Sollars, Hannah Cooper, Suejen Perani, Ellie Shamshiri, Sonja Soskic, Time Tierney, Ramneek Jouhal, David Carmichael, Jon Clayden, all the other members of the Developmental Imaging and Biophysics Unit, past and present, for their support and company while navigating the vicissitudes of a PhD.

The clinical work presented here would not have been possible without the kind support of Richard Bowman, Tina Banks and Siân Handley at Great Ormond Street Hospital and Tony Moore and Magella Neveu at Moorfields Eye Hospital. We are also deeply grateful to all the participants who took part in the studies for kindly providing their time.

And finally, a great thank you to my parents, who encouraged me on this journey from day one, and to my partner, Hannah Dade, whose unwavering patience, boundless kindness and steady supply of biscuits kept me going through the best and the worst of a PhD. This work is very much dedicated to her.

This work was possible thanks to generous support by a UCL SLMS Grand Challenge Studentship in Biomedicine, funded by the UCL School for Life and Medical Sciences, UCLH/UCL Comprehensive Biomedical Research Centre and the Specialist Biomedical Research Centres at Moorfields/UCL and Great Ormond Street/UCL.

Abstract

Albinism is a developmental disorder which involves the misrouting of optic nerve projections, leading to an abnormally organised visual system. Despite the aberrant input, people with albinism have relatively normal vision and experience the world in much the same way as their peers. This thesis explores the functional and structural organisation of visual cortex in human albinism using magnetic resonance imaging (MRI) techniques.

This thesis covers four main experiments. **Experiment 1** deals with stimulus optimisation for population receptive field (pRF) mapping in healthy adults. pRF mapping is a functional MRI technique for estimating cortical receptive field characteristics non-invasively. In this experiment, a stimulus configuration optimized for short acquisition time requirements is presented and implemented in subsequent experiments.

Experiment 2 combines the pRF approach for retinotopic localization with diffusion MRI tractography in healthy adults to show evidence for direct extrastriate connections of the human optic radiation. The optic radiation is the principal white matter pathway for relaying retinal input to visual cortex, and typically considered a projection to primary visual cortex. In this experiment, independent pathways of the optic radiation to visual areas V2 and V3 are identified, and functional-structural methodologies developed for Experiment 4.

Experiment 3 investigates the functional organisation of visual cortex in participants with albinism. A pRF mapping approach was implemented, identifying abnormal retinotopic organisation and altered receptive field properties in extrastriate visual cortex. In addition, we explore evidence for and against a dual receptive field model of visual field representation in albinism.

Experiment 4 examines the structural and functional connectivity of early visual system in human albinism. In particular, differences in white matter microstructure and inter-hemispheric visual map connectivity are found between participants with albinism and a cohort of healthy controls. This thesis highlights the capacity and limitations of developmental plasticity in human albinism.

Table of contents

Thesis declaration form.....	2
Acknowledgements.....	3
Abstract.....	4
Table of contents.....	5
List of figures.....	10
List of tables.....	13
Contributions.....	14
Publications arising from this work	15
Presentations arising from this work.....	15
Abbreviations	16
General introduction.....	19
Chapter 1 Neurodevelopment of the visual system.....	21
1.1 Introduction.....	22
1.2 Anatomy of the visual system	22
1.2.1 Peripheral visual system.....	22
1.2.2 Central visual system	25
1.3 Development of the visual system	27
1.3.1 Development of the retina.....	27
1.3.2 Development of the chiasm	27
1.4 Mechanisms of axonal guidance	28
1.4.1 Crossed versus uncrossed projections.....	28
1.4.2 Topographic mapping	31
1.4.3 Neurochemical signalling in albinism	33
1.5 Melanin biosynthesis.....	33
Chapter 2 Human albinism	36
2.1 Introduction.....	37
2.2 Classifications of albinism	37

2.2.1	Oculocutaneous albinism (OCA)	38
2.2.2	Ocular albinism (OA).....	40
2.2.3	Syndromes	41
2.3	Clinical features.....	41
2.3.1	Foveal hypoplasia.....	41
2.3.2	Iris transillumination.....	42
2.3.3	Abnormal optic disc morphology	42
2.3.4	Abnormal eye position and movements.....	42
2.3.5	Dermatological concerns	42
2.4	Misrouting of the optic nerves	43
2.4.1	Optic nerve misrouting in non-human species	43
2.4.2	Measuring optic nerve misrouting in humans	46
2.5	Albinism as a case of developmental plasticity	49
2.5.1	Neural plasticity vs. reorganisation	49
2.5.2	Functional organisation in albinism and achiasma	50
2.6	Outstanding questions.....	52
Chapter 3 Methodology		54
3.1	Introduction.....	55
3.2	Functional MRI.....	55
3.2.1	Physiological principles.....	55
3.2.2	MR imaging of the BOLD response	57
3.2.3	Mapping the visual system.....	59
3.3	Diffusion-weighted MRI	62
3.3.1	Diffusion-weighted imaging.....	62
3.3.2	Modelling diffusion	64
3.3.3	White matter tractography	68
Chapter 4 Optimisation of population receptive field mapping in fMRI.....		70
4.1	Abstract.....	71
4.2	Introduction.....	71
4.3	Materials and methods	74
4.3.1	Participants	74
4.3.2	Stimulus design.....	74

4.3.3	MRI acquisition and pre-processing	80
4.3.4	Phase-encoded analysis	81
4.3.5	Population receptive field (pRF) estimation.....	81
4.3.6	Model cross-validation	83
4.4	Results	86
4.4.1	Region delineation.....	86
4.4.2	Model validation	88
4.4.3	Goodness of fit.....	88
4.4.4	Effect of mean luminance periods on pRF estimates	90
4.4.5	Stimulus configuration and pRF size.....	92
4.4.6	Effects of display size on pRF estimates	97
4.4.7	pRF vs. phase-encoded estimation of stimulus eccentricity	97
4.5	Discussion.....	98
4.6	Conclusion	102
Chapter 5 Extrastriate projections in human optic radiation		103
5.1	Abstract.....	104
5.2	Introduction.....	104
5.3	Materials and methods	106
5.3.1	Participants	106
5.3.2	Behavioural measures.....	106
5.3.3	Visual stimulation	107
5.3.4	MRI acquisition.....	108
5.3.5	Functional imaging analysis	108
5.3.6	Diffusion imaging analysis.....	109
5.3.7	Tract segmentation	110
5.3.8	V3A control region.....	111
5.4	Anatomical results.....	112
5.4.1	Visual field-based segmentation	112
5.4.2	Hierarchy-based segmentation	112
5.4.3	False positive rate estimation.....	117
5.5	Microstructural results	117
5.5.1	Effect of covariates.....	118
5.5.2	Visual field-based segmentation	118
5.5.3	Hierarchy-based segmentation	118

5.6	Discussion.....	122
5.6.1	Relative projection size	122
5.6.2	Microstructural findings.....	123
5.6.3	Role of extrastriate projections	123
5.6.4	Pulvinar contributions.....	124
5.7	Conclusion	125
Chapter 6 Visual population receptive fields in human albinism		127
6.1	Abstract.....	128
6.2	Introduction.....	128
6.3	Materials and methods	130
6.3.1	Participants	130
6.3.2	Ophthalmological measures.....	132
6.3.3	Retinal imaging.....	132
6.3.4	Eye movement recordings	137
6.3.5	fMRI visual stimulation	140
6.3.6	MRI acquisition and pre-processing	141
6.3.7	Population receptive field (pRF) modelling.....	142
6.4	Results	143
6.4.1	Region delineation.....	143
6.4.2	Overlapping representations of ipsi- and contralateral visual fields	143
6.4.3	Variation in population receptive field size.....	144
6.4.4	Line of decussation	152
6.4.5	Receptive field position shift	157
6.4.6	Dual receptive field (DRF) modelling	157
6.5	Discussion.....	162
6.5.1	Phenotype analysis	163
6.5.2	Nature of the contralateral representation	166
6.5.3	Modelling responses to single and dual receptive fields	166
6.6	Conclusion	167
Chapter 7 Interhemispheric connectivity in human albinism		168
7.1	Abstract.....	169
7.2	Introduction.....	169

7.3	Materials and Methods	170
7.3.1	Participants	170
7.3.2	Retinotopic mapping.....	170
7.3.3	MRI acquisition.....	171
7.3.4	Tractography analysis	171
7.3.5	Functional connectivity analysis.....	172
7.4	Results	173
7.4.1	Structural connectivity.....	173
7.4.2	Hierarchical segmentation of the splenium.....	179
7.4.3	Functional connectivity	187
7.4.4	Lateralised functional connectivity.....	192
7.5	Discussion.....	193
7.5.1	Stable interhemispheric structural connectivity	193
7.5.2	Altered functional connectivity.....	194
7.5.3	Role of interhemispheric transfer in albinism	196
7.6	Conclusion	197
Chapter 8 General discussion.....		199
8.1	Introduction.....	200
8.2	Summary of findings	200
8.2.1	Optimisation of population receptive field mapping in fMRI.....	200
8.2.2	Extrastriate projections in human optic radiation.....	201
8.2.3	Visual population receptive fields in human albinism	201
8.2.4	Interhemispheric connectivity in human albinism	202
8.3	Discussion of findings.....	202
8.4	Future directions	205
8.5	Clinical relevance	207
8.5.1	Diagnosis and prognosis.....	207
8.5.2	Development of future treatments	207
References		208

List of figures

Figure 1.1 Transverse view of the mammalian retina.....	24
Figure 1.2 Retinogeniculostriate pathway in the human visual system.	26
Figure 1.3 Molecular mechanisms of optic chiasm midline crossing and avoidance.....	30
Figure 1.4 Molecular mechanisms of axonal guidance for topographic mapping.....	32
Figure 1.5 Biosynthetic pathways for melanogenesis	35
Figure 2.1 Diagram of optic nerve decussation in healthy and albino humans.	45
Figure 2.2 Degree of optic nerve fibre decussation in the pigeon, rat and human.....	45
Figure 2.3 <i>in vivo</i> retinotopic mapping of primary visual cortex in human albinism.	48
Figure 3.1 Haemodynamic response function.	57
Figure 3.2 Haemodynamic response function with variable temporal sampling.	58
Figure 3.3. GLM designs in task-based fMRI	59
Figure 3.4 Major retinotopic areas in human visual cortex.	61
Figure 3.5 Water diffusion in restricted and unrestricted mediums	63
Figure 3.6 The diffusion tensor	65
Figure 3.7 Spherical deconvolution model of fibre orientation	67
Figure 3.8 White matter tracrography	69
Figure 4.1 Chequerboard stimulus design and Fourier transform	76
Figure 4.2 Stimulus design for pRF mapping	78
Figure 4.3 Time series predictions for stimulation to a single pRF	84
Figure 4.4 Sample time-series and model prediction from pRF model.	85
Figure 4.5 Polar angle maps derived from pRF modelling.....	87

Figure 4.6 Model model cross-validation results	89
Figure 4.7 Model goodness of fit (R^2) for three stimulus configurations.....	91
Figure 4.8 pRF size across eccentricities for three stimulus configurations.....	94
Figure 4.9 Eccentricity estimates from pRF and phase-encoded methods	96
Figure 5.1 Striate and extrastriate segments of the human optic radiation.....	113
Figure 5.2 Segments of the optic radiation in 30 participants	114
Figure 5.3 Expanded view of optic radiation segments.....	115
Figure 5.4 Coronal section of streamline visitation maps in optic radiation	116
Figure 5.5 Streamline counts for V1, V2 and V3 projections in optic radiation	120
Figure 5.6 Microstructural values across V1, V2 and V3 projections in optic radiation.....	121
Figure 6.1 Visual field perimetries for participants with albinism.....	134
Figure 6.2 Retinal OCT for participants with albinism demonstrating foveal hypoplasia ..	135
Figure 6.3 Retinal layer thickness	136
Figure 6.4 Eye movement traces during fixation.....	139
Figure 6.5 Hemifield stimulus design	141
Figure 6.6 Eccentricity retinotopic maps in albino early visual cortex.....	146
Figure 6.7 pRF size across eccentricities following hemifield stimulation.....	150
Figure 6.8. Line of decussation estimates derived from pRF modelling.....	154
Figure 6.9. pRF backprojection for overlapping hemiretina representations.....	156
Figure 6.10 Single and dual pRF model fits.....	159
Figure 6.11 Cortical activity maps for single and dual pRF model fits	161
Figure 7.1 Probabilistic tractography of the splenium of the corpus callosum	176
Figure 7.2 Volumetric estimates of splenium and corticospinal tract in albinism.....	177

Figure 7.3 Microstructural markers in splenium and corticospinal tract.....	178
Figure 7.4 Hierarchical segmentation of the splenium.....	182
Figure 7.5 Streamline count and cortical target volume in splenium segmentation.....	183
Figure 7.6 Volumetric estimates in splenium segmentation	184
Figure 7.7 Microstructural markers in splenium segmentation.....	185
Figure 7.8 Interhemispheric functional connectivity in V1, V2 and V3	190
Figure 7.9 Differences in functional connectivity between albinos and controls.....	191

List of tables

Table 2.1 Genetic classification of human albinism	38
Table 4.1 Within-subject pairwise t-tests, assessing differences in pRF size as estimated from three stimulation conditions across nine regions of interest.....	95
Table 6.1 Albinism diagnosis and phenotype description for participants A1-A5	131
Table 7.1 Bayesian statistical hypothesis testing for structural interhemispheric connectivity analysis	186

Contributions

The experiment presented in **Chapter 4** was designed in collaboration with Sam Schwarzkopf, and MRI data were acquired with the assistance of Sam Schwarzkopf and Benjamin de Haas at the Wellcome Trust Centre for Neuroimaging, University College London. MRI data presented in **Chapter 5** were acquired with the assistance of Tina Banks at Great Ormond Street Hospital. Ophthalmological and eye movement data presented in **Chapter 6** were acquired and interpreted with the assistance of Alki Liasis and Siân Handley at Great Ormond Street Hospital. MRI data presented in **Chapter 6 and Chapter 7** were acquired with the assistance of Marty Sereno, Rebecca Lyness, Benjamin de Haas and Christina Moutsiana at the Birkbeck-UCL Centre for Neuroimaging, University of London. All other data acquisition, analysis and interpretation were carried out by the author, and all mistakes solely my own.

Publications arising from this work

Alvarez I, de Haas B, Clark CA, Rees G, & Schwarzkopf DS (2015). Comparing different stimulus configurations for population receptive field mapping in human fMRI. *Frontiers in Human Neuroscience*, 9, 96.

Alvarez I, Schwarzkopf DS & Clark CA (2014). Extrastriate projections in human optic radiation revealed by fMRI-informed tractography. *Brain Structure and Function*, 220, 2519-2532.

Presentations arising from this work

Alvarez I, Lyness CR, Handley SE, Liasis A, Schwarzkopf DS, Sereno MI & Clark CA. (2015, Poster). Chiasmal misrouting and visual space representations: Modelling population receptive fields in human albinism. Computational Vision Summer School 2015, Freudenstadt, Germany.

Alvarez I, Lyness CR, Handley SE, Liasis A, Schwarzkopf DS, Sereno MI & Clark CA. (2015, Poster). Characterising visual population receptive fields in human albinism. Organisation for Human Brain Mapping 2015, Honolulu (HI), USA.

Alvarez I, Schwarzkopf DS & Clark CA (2014, Talk). Extrastriate projections in human visual system: Evidence from fMRI-informed tractography. Applied Vision Association 2014, York, UK.

Alvarez I, Schwarzkopf DS & Clark CA (2013, Talk). Segmenting the optic radiation using fMRI-informed tractography: Extrastriate projections in human thalamocortical visual system. Society for Neuroscience 2013, San Diego (CA), USA.

Alvarez I, De Haas B, Clark CA, Rees G & Schwarzkopf DS (2013, Poster). Optimal stimulation for population receptive field mapping in human fMRI. Vision Sciences Society 2013, Naples (FL), USA.

Alvarez I & Clark CA (2012, Poster). Human optic radiation revealed through fMRI-informed white matter tractography. UCL Neuroscience Symposium 2013, London, UK.

Abbreviations

General

- **2D** – Two-Dimensional
- **3D** – Three-Dimensional
- **LCD** – Liquid Crystal Display
- **OCT** – Optical Coherence Tomography

Anatomy and Physiology

- **dHb** – Deoxy-Haemoglobin
- **DRF** – Dual Receptive Field cell
- **Hb-O₂** – Oxy-Haemoglobin
- **HRF** – Haemodynamic Response Function
- **LGN** – Lateral Geniculate Nucleus
- **LO** – Lateral Occipital
- **LOC** – Lateral Occipital Complex
- **MT+/V5** – Middle Temporal Human Visual Area V5
- **OR** – Optic Radiation
- **pRF** – Population Receptive Field
- **RF** – Receptive Field
- **RGC** – Retinal Ganglion Cell
- **RPC** – Retinal Progenitor Cell
- **SC** – Superior Colliculus
- **SRF** – Single Receptive Field cell
- **V1** – Primary Visual Cortex, Striate Cortex
- **V2, V3, V4, etc.** – Extrastriate Visual Areas
- **VO** – Ventral Occipital
- **VOC** – Ventral Occipital Complex

Chemistry

- **DHI** – 5,6-dihydroxyindole compound
- **DHICA** – 5,6-dihydroxyindole-2-carboxylic compound
- **Nogo** – Neurite outgrowth inhibitor
- **NrCAM** – Neuronal cell adhesion molecule
- **Shh** – Sonic Hedgehog morphogenic protein
- **TRP-1** – Tyrosinase-Related Protein 1

- **TRP-2** – Tyrosinase-Related Protein 2
- **VEGF-A** – Vascular endothelial growth factor A

Albinism

- **OA** – Ocular Albinism
- **OA1** – Ocular Albinism Type 1, Nettleship-Falls syndrome, X-linked OA
- **OA2** – Ocular Albinism Type 2, Forsius-Eriksson-Miyake or Åland eye disease
- **OCA** – Oculocutaneous Albinism
- **OCA1** – Oculocutaneous Albinism Type 1
- **OCA1A** – Oculocutaneous Albinism Type 1A
- **OCA1B** – Oculocutaneous Albinism Type 1B
- **OCA1MP** – Minimal Pigmentation OCA
- **OCA1TS** – Temperature-Sensitive OCA
- **OCA2** – Oculocutaneous Albinism Type 2
- **OCA3** – Oculocutaneous Albinism Type 3, Rufous OCA
- **OCA4** – Oculocutaneous Albinism Type 4

Neuroimaging

- **BOLD** – Blood Oxygenation Level Dependent response
- **CSD** – Constrained Spherical Deconvolution
- **dmRI** – Diffusion Magnetic Resonance Imaging
- **EPI** – Echo-Planar Imaging
- **FA** – Fractional Anisotropy
- **fMRI** – Functional Magnetic Resonance Imaging
- **FOD** – Fibre Orientation Distribution
- **HARDI** – High Angular Resolution Diffusion Imaging
- **MD** – Mean Diffusivity
- **MRI** – Magnetic Resonance Imaging
- **PD** – Proton Density
- **SD** – Spherical Deconvolution
- **SE** – Spin Echo
- **TE** – Echo Time
- **TR** – Repetition Time
- **VEP** – Visual Evoked Potentials

Mathematics and Statistics

- **ANOVA** – Analysis of Variance
- **DoG** – Difference of Gaussians
- **FT** – Fourier Transform
- **FWHM** – Full Width at Half Maximum
- **GLM** – General Linear Model
- **PCA** – Principal Component Analysis
- **SD** – Standard Deviation
- **SEM** – Standard Error of the Mean

General introduction

Over the past three decades, the understanding of the human brain has undergone a rapid transformation, with the advent of techniques that allow the non-invasive study of both structure and function in living, acting human beings. The prevalent approaches so far have seen great success in studying the anatomy and morphology of the brain in one hand, and its physiological correlates of behaviour and cognition on the other, as relatively independent lines of enquiry. In recent years, a drive has emerged to combine these approaches and provide a joint view, where brain function is intrinsically dependent on the anatomical substrate on which it takes place. Under this view, the capacity of any brain system to process information is directly subtended by the integrity and extent of the underlying anatomical organisation that permits the flow of information.

In this doctoral thesis, the functional-structural relationships of the human visual system will be explored on two complementary levels; first in healthy adults by combining functional localisation of visual regions and white matter tracking techniques to reveal the substrata of functionally relevant connections between visual regions in the brain. Secondly, we will explore the functional and structural organisation of such areas and pathways in human albinism, as an example case of developmental plasticity giving rise to altered anatomy and functional organisation of the visual system.

This thesis is divided into eight chapters, covering the following topics; **Chapter 1** presents an overview of the neurodevelopment of the visual system, and of the genetic, molecular and neuronal factors affected in albinism. **Chapter 2** presents a survey of human albinism in general, focusing on the neuroanatomical and functional imaging literature in particular. Issues of plasticity and reorganisation in the visual system are specifically addressed, proposing albinism as a case of developmental plasticity under abnormal visual input. **Chapter 3** discusses the foundations for the experimental methods used in this thesis, namely functional magnetic resonance imaging (fMRI) and diffusion magnetic resonance imaging (dMRI). **Chapter 4** describes an experiment titled “Optimisation of population receptive field mapping in fMRI”, which establishes an efficient stimulus protocol for conducting model-based visual field mapping in fMRI, and subsequently implemented in later chapters. **Chapter 5** describes an experiment titled “Extrastriate projections in human optic radiation”, exploring evidence for putative direct thalamo-cortical projections between the lateral geniculate nucleus and visual areas beyond primary visual cortex, as an example of method fusion in neuroimaging, by combining functional and structural imaging methods. Methodological improvements discussed in Chapters 4 and 5 are then implemented in subsequent chapters. **Chapter 6** describes an experiment titled “Visual population receptive fields in human albinism”, exploring the representation of visual space in striate

and extrastriate visual cortex under abnormal retinal input, its receptive field properties and possible explanations for the underlying organisation of abnormal retinal information. **Chapter 7** describes an experiment titled “Interhemispheric connectivity in human albinism”, which examines evidence for and against abnormal anatomical organisation and altered inter-hemispheric transfer of visual information as a consequence of a misrouted chiasm. Finally, **Chapter 8** presents a general discussion of the experimental chapters and conclusions to be drawn, highlighting the novel findings in understanding the normal and abnormal visual system, and the development of integrated functional-structural thinking in understanding complex brain systems.

Chapter 1

Neurodevelopment of the visual system

1.1 Introduction

The world that surrounds us is a bountiful source of sensory stimulation, with a constant stream of input bombarding our sensory organs. For humans, chief amongst them are the eyes – the visual system has the preeminent task of detecting, processing, selecting and interpreting that stream of visual input we receive. Not only is vision ecologically relevant, it also provides us with a window into the general organisation of the nervous system, by exploring the rules that govern sensory transformation and neuronal computation. In particular, by examining scenarios of altered functional or anatomical development, such as in albinism, we understand the limits of such rules, and achieve a clearer understanding of the underlying organising principles that dictate the structure and function of the visual system.

For the purposes of this chapter, discussion of the visual system is divided into three sections; first, a brief overview of visual system neuroanatomy highlighting areas of interest for the investigations presented in this thesis. Second, a description of the neurodevelopment of the visual system, with particular emphasis on the structures and mechanisms affected in albinism. Finally, a review of the melanin biosynthesis pathway, and components affected in albinism.

1.2 Anatomy of the visual system

1.2.1 Peripheral visual system

The visual system starts with its sensory organs, the eyes. The human eye is a complex set of tissues and fluids with the principal role of focusing light onto the retina, a tissue layer containing light-sensitive photoreceptor cells.

The retina is a complex structure, formed by six neuron cell types, ganglion cells, amacrine cells, bipolar cells, horizontal cells and the photoreceptor cells; rods and cones, as well as supportive glial cell types, including Müller glia, astrocytes, endothelial cell and microglia (Bassett & Wallace, 2012). In the mammalian arrangement, as light enters the retina, it first encounters a layer of ganglion cells, followed by the inner and outer synaptic layers, containing amacrine, bipolar and horizontal cells, and finally the photoreceptor cells (**Figure 1.1**). Due to this arrangement, the human retina is sometimes described as ‘inverted’, and a direct consequence of this arrangement is the existence of a blind spot. The blind spot is the area where the axonal bundle originating from the ganglion cells passes through the

retina and exits the orbit of the skull, forming the optic nerve. The lack of photoreceptor cells at this location means no visual input is captured, and that particular portion of the visual field is not detected.

Another important feature of the retina is the macula, a yellow-pigmented disc sitting at the centre of the retina. The macula differs histologically from the rest of the retina by its high concentration of photoreceptor cells. At its centre is the fovea, a depression on the retinal surface that contains the highest concentration of cone photoreceptors. The fovea represents the centre of vision and is responsible for high visual acuity, important for resolving fine detail, as well as colour discrimination (Kaiser & Boynton, 1996). Moving away from the fovea spatial resolution decreases; in the parafoveal region the concentration of cones sharply drops and rod photoreceptors become predominant. Beyond the macula, visual acuity drops further into the peripheral zones of the retina. The variability in photoreceptor density across the retina leads to important organisational features further upstream, as the fovea is over-represented in the proportion of outgoing fibres of the retina, in relation to its relatively small size (Curcio & Allen, 1990).

How is the visual world represented in the retina? To answer this question, we must first examine the optics of the eye. The refractive action of the lens on incoming light projects an inverted image on the retina, where the lower visual field is projected on the upper retina and vice-versa. Equally, the left side of the visual scene is projected onto the right side of the retina, leading to a fully left-right, up-down inverted version of the visual scene. As the fovea corresponds to the central point of vision, this is the only point that is not inverted in the retinal representation and serves as the guiding point when defining visual space in terms of the retinal image. From it, two arbitrary divisions of the monocular visual field can be made; first the horizontal axis delineates the upper and lower visual field as separated by a horizontal line crossing the fovea. Second, along the vertical axis, the left and right visual field are separated by a vertical line crossing the fovea. In terms of the retinal image, these horizontal divisions correspond to the upper and lower retina and the vertical sections as the nasal and temporal retina, based on which anatomical landmark, the nose or temporal bone, is most proximal. It should be noted that these divisions do not correspond to the intrinsic organisation of the retina, but is merely a geometrically convenient description for understanding the relationship between visual space, anatomy, and the retinal image.

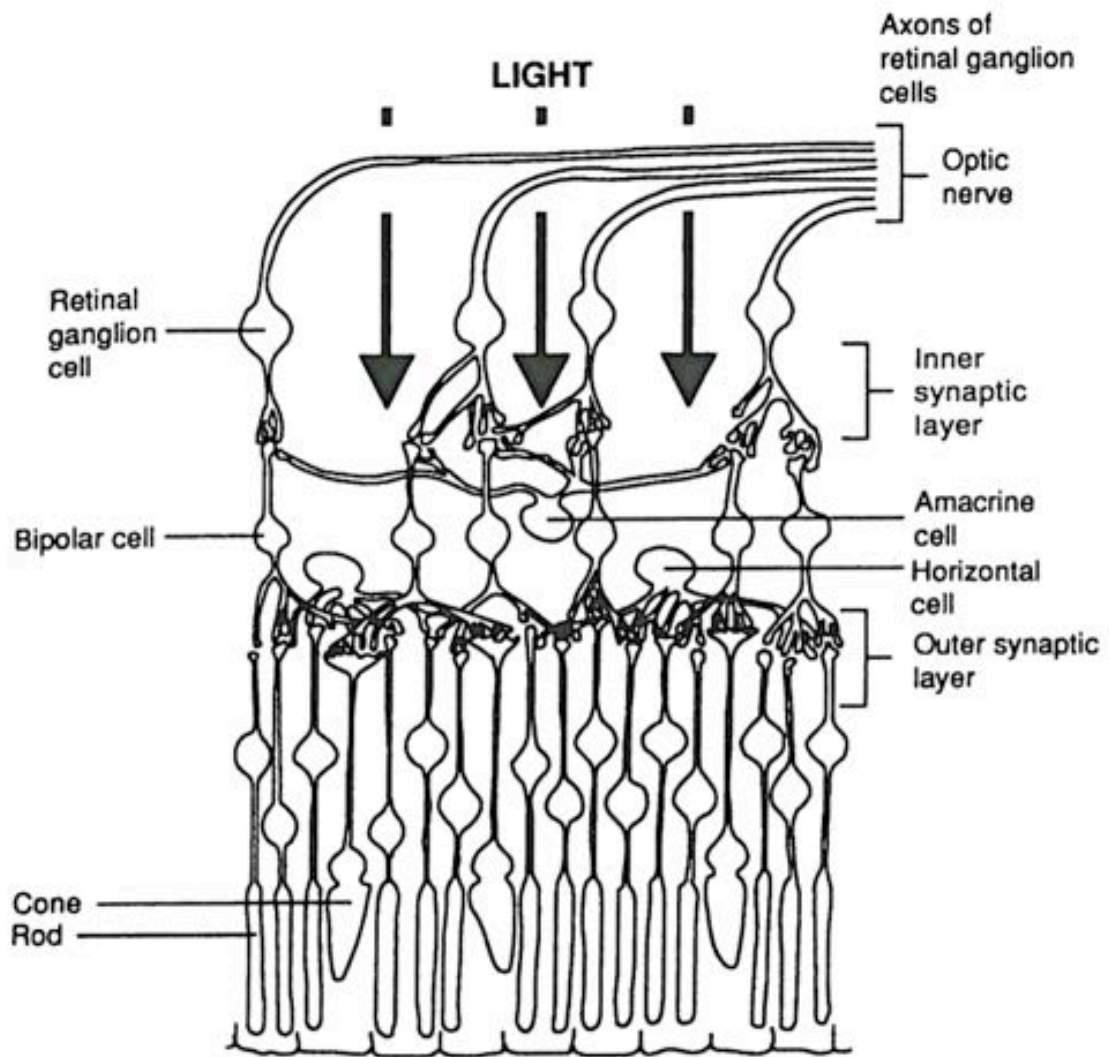


Figure 1.1 Transverse view of the mammalian retina. As light enters the retina, it passes multiple layers of neural tissue before reaching the photoreceptor cells, cones and rods, where phototransduction takes place, leading to neural signalling upwards towards ganglion cells and out of the retina, creating the 'inverted retina'. Adapted from Tovée (1996).

1.2.2 Central visual system

Beyond the retina, the larger human visual system is organised in a series of relays connecting the sensory organs with cortical and subcortical cerebral structures involved in processing visual information. Of these relays, the predominant one is the retinogeniculostriate pathway, both in terms of number of connections to visual cortex, and in severity of impairment when damaged (Edmond & Foroozan, 2006; Boot et al., 2010).

The retinogeniculostriate pathway consists of three main white matter relays (**Figure 1.2**). First, the optic nerve originating from retinal ganglion cells, leaves the eye through the blind spot and then partially crosses cerebral hemispheres at the optic chiasm. This crossover is limited to the nasal retinal fibres, with approximately 55% of fibres crossing over to the contralateral hemisphere, with 45% of fibres remaining in the ipsilateral hemisphere (Creel et al., 1974). As a result, visual information is lateralised, with left visual field projected to the right hemisphere and the right visual field projected to the left hemisphere; this anatomical arrangement is fundamental for the functional organisation observed in cortical regions. In each hemisphere, the combined uncrossed fibres of the ipsilateral eye and the crossed fibres of the contralateral eye form the optic tract, which projects from the optic chiasm to the lateral geniculate nucleus (LGN) in the thalamus and superior colliculus (SC) in the midbrain. The LGN forms an important processing stage and relay station that both projects to and receives input from cerebral cortex. Finally, the optic radiation projects from the LGN to the occipital cortex. From there, visual information is disseminated through a series of short and long-range connections between cortical areas in the occipital lobe and beyond.

As information arrives to primary visual cortex (also known as striate cortex, or V1), it follows a structured pattern conferred by the anatomical arrangement of white matter connections and representation in thalamic regions. In its functional organisation, V1 follows a topographic map of the projectional retina, known as retinotopy. In a retinotopic map, neighbouring cells in cortex represent neighbouring parts of the visual field. One conceptually useful way to describe this representation is through encoding of spatial information along two dimensions: eccentricity and polar angle. Eccentricity, the radial distance from the fovea, is encoded anterior-posteriorly in V1, with the centre of vision represented at the occipital pole and the more peripheral areas of visual space encoded away from it. Polar angle, a relative coordinate, is represented in the superior-inferior axis in V1.

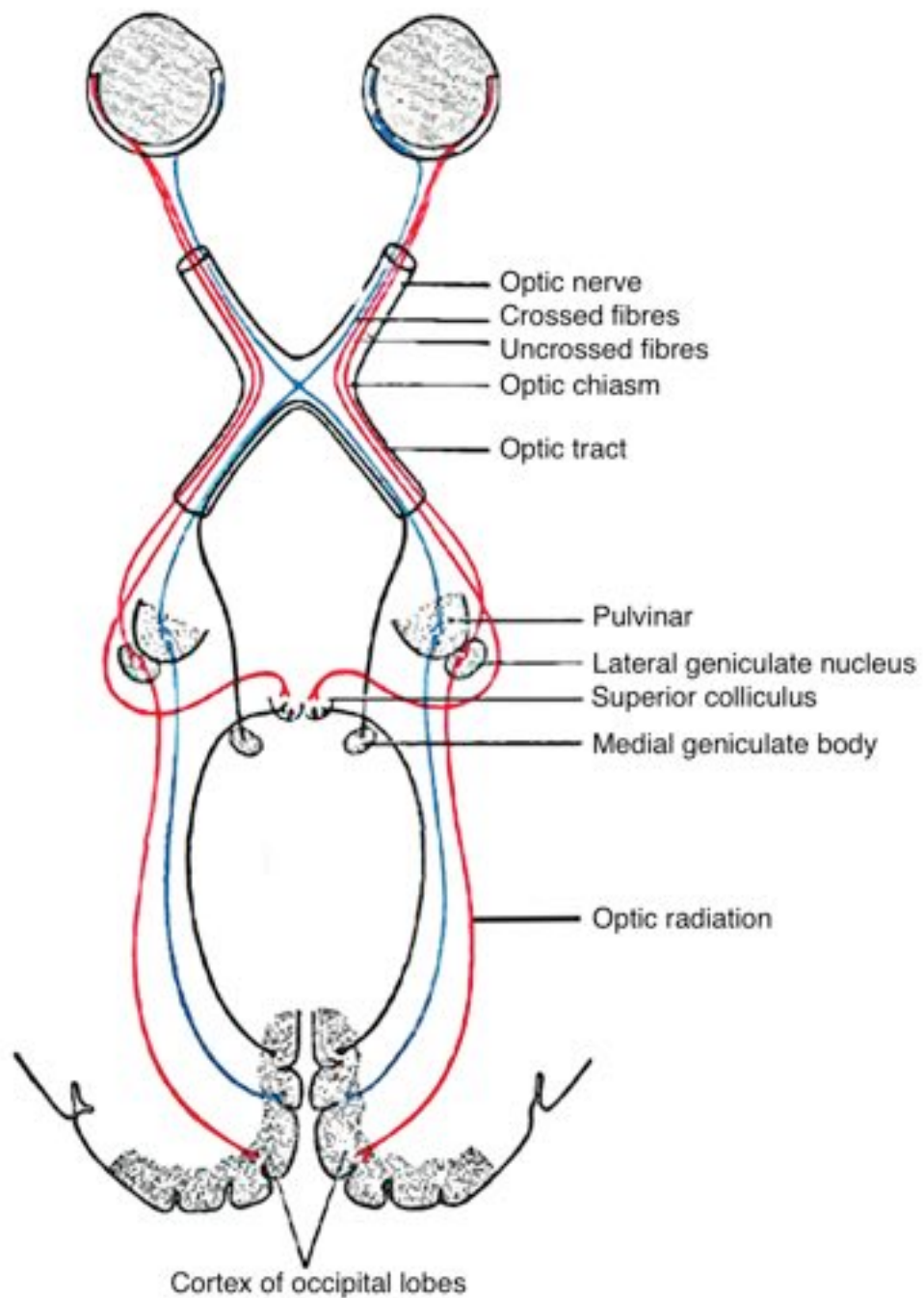


Figure 1.2 Retinogeniculostriate pathway in the human visual system. The main white matter relays are noted, including the optic nerve, chiasm, optic tract and optic radiation. Note the fibres originating at the nasal retina (blue) cross over at the optic chiasm, while the temporal retina (red) remains uncrossed. Adapted from Gray (1918; 2000).

1.3 Development of the visual system

1.3.1 Development of the retina

The mammalian retina can be conceptualised as developing in two stages. First, a stage comprising a homogeneous monolayer with proliferation of undifferentiated retinal progenitor cells (RPC), followed by a second stage of cell specialisation and layer differentiation. RPCs are multi-potent neurons which during development give rise to the six neuronal cell types found in the retina (retinal ganglion cells, horizontal cells, amacrine cells, bipolar cells, rod photoreceptors and cone photoreceptors), as well as Müller glial cells, RPC neurogenesis and differentiation begins in the centre of the retina, and spreads radially (Centanin & Wittbrodt, 2013). Under the competence model, RPCs pass through successive states in a fixed temporal order. At each stage, they can generate a differentiated cell type, or transit to the next stage with more restricted multi-potency potential (Bassett & Wallace, 2012). This model posits a stereotyped order for the generation of retinal cell types, with retinal ganglion cells (RGC) arising first, followed by horizontal cells, cone photoreceptors, amacrine cells, rod photoreceptors, and bipolar cells, in that order (Finlay, 2008). However, it should be noted that there is considerable overlap in the neurogenesis onset of these cell types (Reese, 2011).

The precise timing of retinal neuron genesis and differentiation is important in albinism, as work in rodents has demonstrated that the timing of RGC neurogenesis is altered in albinism, and has downstream effects at the level of the optic chiasm (Marcus et al., 1996; Rice et al., 1999). More specifically, RGCs originating in the nasal retina and destined to eventually cross the optic chiasm develop normally in albino mice, while RGCs in the temporal retina have delayed neurogenesis and delayed migration out of the retina (Rachel et al., 2002; Bhansali et al., 2014). However, the exact mechanism of how the genetic origins of albinism give rise to delayed RGC neurogenesis and eventually chiasmal misrouting, remains unclear (Jeffery & Erskine, 2005).

1.3.2 Development of the chiasm

How do newly developed RGCs know which way to go? This problem of axonal guidance has seen considerable interest over the past three decades, and is central to our understanding of the chiasmal malformations observed in albinism. Axonal guidance in the mammalian retina is actively regulated by a series of proteins specifically influencing the rate, direction and ordering of cell migration.

As RGCs develop in the retina, first in the central retina, and then progressively more peripheral, they migrate towards the optic disc, where axons leave the retina forming the optic nerve. As the optic nerve forms, RGCs axons are grouped into fascicles supported by a intra-fascicular mesh of glial cells, providing structural cohesion and support to the optic nerve, making it resistant to mechanical strain introduced by eye movements (Jeffery & Erskine, 2005). Fascicle-building in the optic nerve is mediated by the Semaphorin family of proteins, specifically Sema5A and Slit2 expressed in glia cells and providing inhibitory signals to RGC axons to induce tightly packed bundles of axons (Erskine & Herrera, 2014).

As RGC axons approach the site of the optic chiasm, their trajectory can be characterised in three phases. First, early RGCs form both crossed and uncrossed projections, although the fate of the uncrossed projections is unclear. These early axons demarcate the future site of the chiasm, providing a delineated pathway for future axons (Petros et al., 2008). Second, axons from the ventrotemporal retina approach the chiasm midline, and in turn remain along the ipsilateral course towards the optic tract. Axons from all other retinal regions traverse the chiasm and project to the contralateral optic tract (Guillery et al., 1995). Finally, as new axons from the peripheral retina arrive to the site of the chiasm, they cross over project contralaterally. This includes late-born RGCs from the ventrotemporal retina, which now project contralaterally, instead of ipsilaterally (Drager, 1985; Petros et al., 2008).

How is this complex selection process achieved? Sperry (1963) first proposed the chemoaffinity hypothesis, wherein if both the retina and chiasmal target zones contained matching chemical gradients, then RGCs can use this chemical signalling to guide axonal growth. This hypothesis has since been corroborated with modern methods, with a number of molecular mechanisms playing a role in RGC guidance (for a comprehensive review, see Cang & Feldheim, 2013; Erskine & Herrera, 2014). For the purposes of this overview, we will divide the mechanisms of interest into two parts; first, those involved in resolving crossed versus uncrossed projections in the chiasm. Second, those mechanisms involved in organising topographic mapping.

1.4 Mechanisms of axonal guidance

1.4.1 Crossed versus uncrossed projections

Axonal divergence at the chiasm is mediated by a set of genetic and molecular drivers that express at different stages and provide attractive or repulsive signals to axonal growth. These include the Slit-Robo cell signalling pathway, the Ephrin/Ephs family of molecules and receptors, and semaphorins amongst others (Williams et al., 2004; Erskine & Herrera,

2014). Different molecular mechanisms are implicated in the crossed and uncrossed retinal projections (**Figure 1.3**), and will be dealt with in turn.

The crossed retinal projection is principally mediated by three molecular regulators: Neuronal cell adhesion molecule (NrcAM), the Neuropilin-1 receptor and vascular endothelial growth factor A (VEGF-A). NrcAM is present in the developing retina at all sites except for the ventrotemporal retina. Later in development, NrcAM expression expands into the ventrotemporal retina, coinciding with the emergence of crossed fibres originating from this site (Williams et al., 2006). In parallel, Neuropilin-1 is expressed by RGC axons destined to cross to the contralateral optic tract. VEGF-A is found at the chiasmatal midline, and binds with Neuropilin-1 to induce axonal crossing. If either Neuropilin-1 or VEGF-A is suppressed, a reduction in the rate of axonal crossing is observed (Erskine et al., 2011). In summary, both retinal signalling by NrcAM and interactions at the chiasm by Neuropilin-1 and VEGF-A are necessary to ensure midline axonal crossing.

The uncrossed retinal projection is in turn mediated by a different set of molecular signalling molecules; here the principal molecules implicated are EphB1/ephrin-B2, Sonic Hedgehog (Shh) morphogenic protein and neurite outgrowth inhibitor (Nogo). RGCs are typically directed to the chiasmatal midline and must be repulsed in order to create ipsilateral projections. This midline avoidance is mediated by the expression of EphB1 receptors in ventrotemporal RGCs, but not in axons originating from the rest of the retina (Petros et al., 2008). Upon reaching the chiasmatal midline, RGCs extend a retinal growth cone which interacts differently with midline radial glia depending on their EphB1 content. Radial glia in the chiasm express ephrin-B2, which upon contact with retinal growth cones expressing EphB1 generate a repulsive action, inducing the axons to retract, and continue on course to the ipsilateral optic tract. On the other hand, if the approaching axon does not express EphB1, it experiences extension and growth, inducing crossing to the contralateral optic tract (Nakagawa et al., 2000; Williams et al., 2003). In conjunction with ephrin-B2, Shh and Nogo expressed in the chiasmatal midline also play roles in inhibiting midline crossing by ipsilateral axons, and guidance towards the ipsilateral optic tract (Erskine & Herrera, 2014). Thus, once more, signalling present in the retina (EphB1) and at the chiasm (ephrin-B2, Shh, Nogo) are responsible for determining the fate of crossed and uncrossed projections at the chiasm.

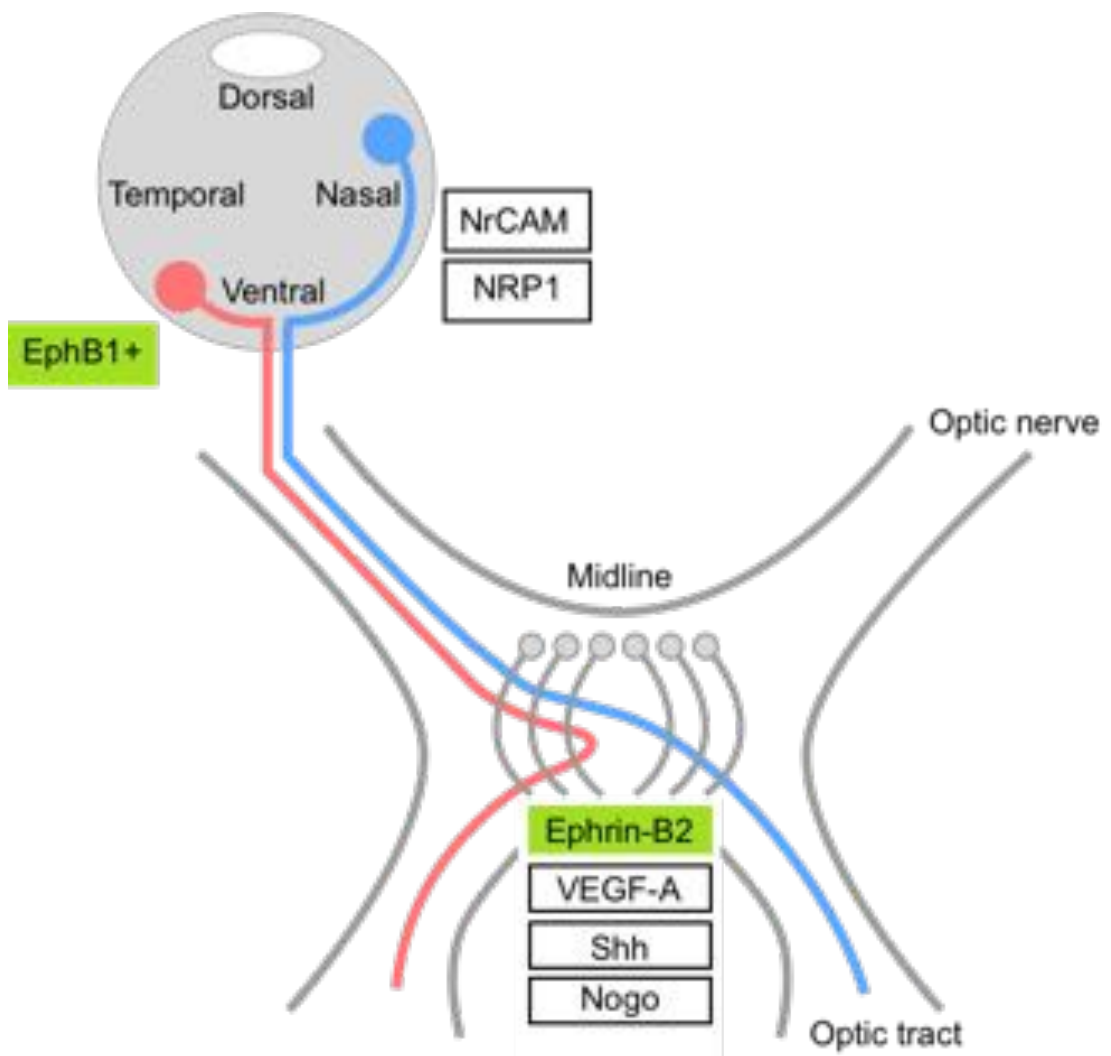


Figure 1.3 Molecular mechanisms of optic chiasm midline crossing and avoidance. Retinal ganglion cells (RGC) originating in the ventrotemporal retina express the receptor EphB1, leading to a repulsive interaction with ligand Ephrin-B2 when they come into contact in the midline of the chiasm. Proteins NrCAM and Neuropilin-1 (NRP-1) are expressed across other retinal regions and encourage axonal crossing at the chiasmal midline by interactions with radial glia and VEGF-A, respectively. Sonic Hedgehog (Shh) and neurite outgrowth inhibitor (Nogo) play modulatory roles in inhibiting midline crossing by ventrotemporal RGCs.

1.4.2 Topographic mapping

A consistent feature of the mammalian visual system, both in cortical and subcortical structures, is the retinotopic correspondence of visual space representations. In order to maintain this correspondence, retinal axonal guidance must obey a strict plan of termination sites, guided by genetic and molecular mechanisms (Cang & Feldheim, 2013). This is of particular interest in albinism, as the organisation of retinotopic correspondence in cortical visual areas under abnormal chiasmal input remains unclear (Hoffmann & Dumoulin, 2015).

Out of the mammalian retina, both genetic and activity-dependent mechanisms play a role in ensuring correct topographic mapping (Cang & Feldheim, 2013). The primary molecular signalling mechanism giving rise to topographic mapping between the retina and primary target zones at the LGN and SC are the Eph/ephrin signalling molecules. Ephrins are a family of membrane-bound ligand proteins that bind with Eph receptors, and allow bi-directional signalling. The interactions between Ephs and ephrins are best understood as a signal competition model, where the relative concentrations of Ephs or ephrins influence the targeting of axonal growth (Yu & Bargmann, 2001; Williams et al., 2004). EphA/ephrin-A are expressed along the nasal-temporal axis of both the retina, and the target regions LGN, SC and V1 (Cang & Feldheim, 2013). Opposite gradients of EphA and ephrin-A are found in the nasal-temporal axis in the retina, in the dorsal-ventral axis in LGN and anterior-posterior axis in the SC, respectively (see Figure 1.4). Critically, Ephrin-A bearing axons are repelled by EphA, explaining topographic axonal targeting. For example, temporal RGCs have high EphA on their membrane surface and are repelled by ventral LGN which has high EphrinA, directing axons towards the dorsal surface of LGN. Furthermore, disrupting EphA or ephrin-A levels during development disrupts organised topographic mapping (Rashid et al., 2005).

While EphA/ephrin-A are the primary signalling molecules topographic correspondence, they are not unique or sufficient for visual system development. Firstly, we have focused on the nasal-temporal retinal axis as it is the most relevant to albinism. However, a different set of proteins and ligands, EphB/ephrin-B and Wnt3 are important for topographic correspondence along the dorso-ventral retinal axis. Other factors influencing topographic axonal guidance include molecules such as GPI-linked repulsive guidance molecule (RGM), semaphorins and Shh, as well as activity-dependent factors (Cang & Feldheim, 2013).

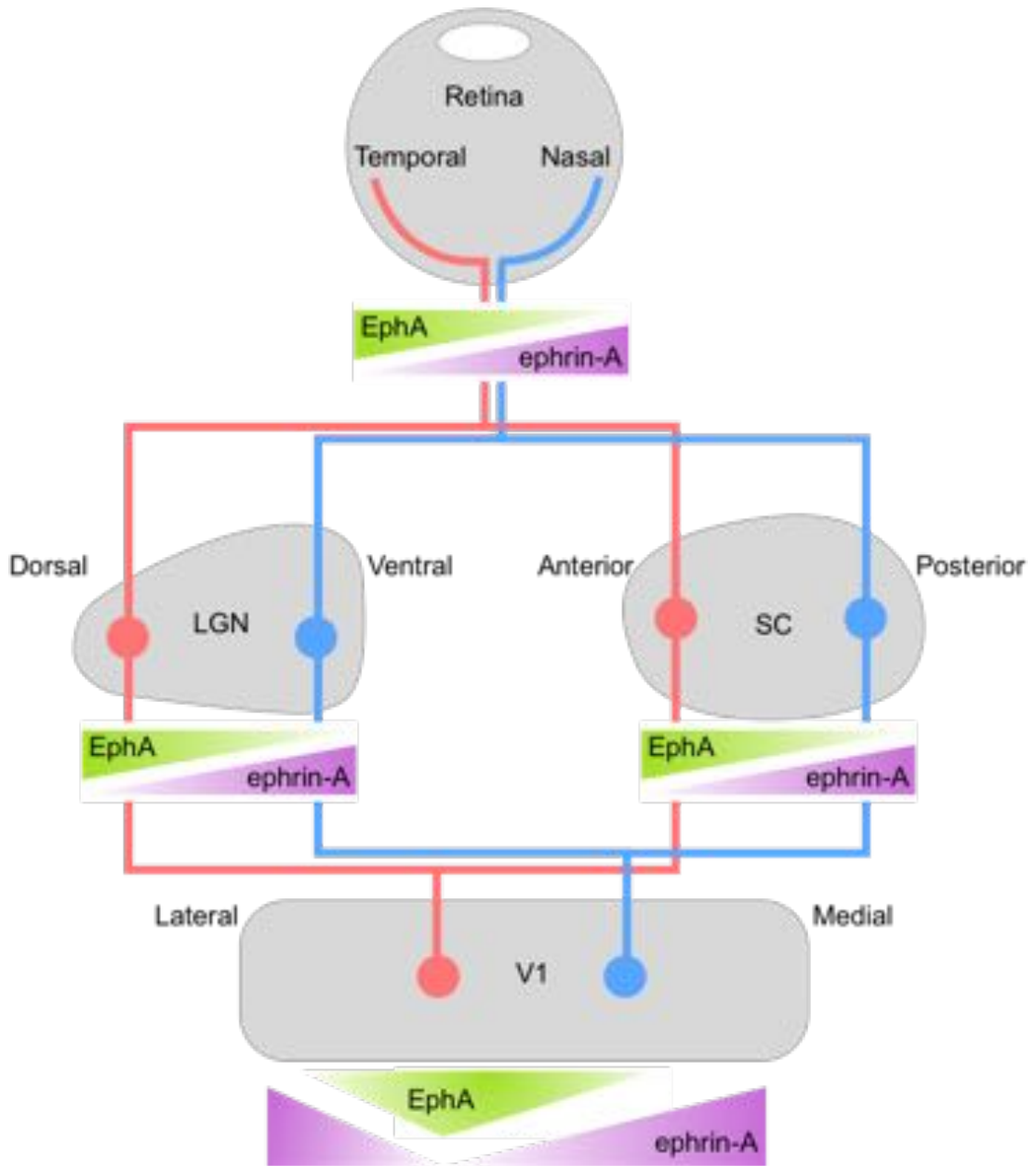


Figure 1.4 Molecular mechanisms of axonal guidance for topographic mapping of nasal-temporal retinal axis. Temporal retinal ganglion cells express Eph-A receptors, which encourage axonal migration towards matching target regions in dorsal lateral geniculate nucleus (LGN) and anterior superior colliculus (SC). Similarly, Nasal retinal ganglion cells express ephrin-A ligands, and match target regions in ventral LGN and posterior SC. Both subcortical structures project to primary visual cortex (V1) which contains opposing gradients of EphA and ephrin-A expression regulating axonal termination sites.

1.4.3 Neurochemical signalling in albinism

Albinism is typically characterised as an alteration in the melanin biosynthetic pathway leading to abnormal visual system development, including overcrossing of RGCs at the chiasm. It is therefore possible that a deficit in EphB1 expression in the ventrotemporal retina or ephrinB2 in the chiasm are responsible mechanisms for the abnormally crossed axons (Williams et al., 2003). Indeed, Rebsam et al. (2012) suggest incorrect axonal divergence in the albino mouse is attributable to reduced expression of EphB1 receptors in ventrotemporal RGCs, leading to a segregated representation in the LGN. This is consistent with the view that albinism is fundamentally a deficit of the retina, with consequences for the organisation of the optic chiasm, LGN and later visual system (Kaas, 2005).

In addition to retinal expression of EphB1, further studies in the albino mouse points to a contribution by alterations in the temporal aspects of retinal neurogenesis. First, more RGCs are born in early retinal neurogenesis in the albino, leading to an early overproduction of ipsilateral RGCs at this stage (Rachel et al., 2002). Second, a delay in the timing of RGC specification in the ventrotemporal retina is associated with abnormal axonal crossing at the chiasm, possibly missing the time window for the development of markers necessary for midline avoidance (Illia & Jeffery 1996; Bhansali et al., 2014).

In conjunction, these results point to albinism experiencing an alteration in the mechanisms of axonal crossing at the chiasm, and not strictly of topographic mapping. While abnormal LGN layer organisation is found in albinism, gross retinotopic correspondence is preserved, both in subcortical and cortical structures (Kaas, 2005; Hoffmann & Dumoulin, 2015). Therefore, we may propose that deficits in the specific mechanisms of chiasmal midline crossing and avoidance affects the naso-temporal retina representation in visual cortex.

1.5 Melanin biosynthesis

The production, transport and uptake of melanin in the mammalian body are referred to as the process of melanin biosynthesis. Melanin is a biopolymer, endogenously produced and responsible for the external pigmentation of the skin, hair and eyes. As a macromolecule, it contains indolic compounds derived from the oxidation of the amino acid tyrosine, which confers it light absorbing properties. In mammals, these properties have multiple functions, including shielding tissue from sunlight, heat dissipation and pigmentation for camouflage and display (Riley, 1997).

Humans display three forms of the melanin compound: eumelanin, pheomelanin and neuromelanin. Eumelanin confers a black or brown pigmentation and is primarily responsible for the colouration of skin and hair. Pheomelanin confers pink-red pigmentation, and is found prominently in red hair. Both eumelanin and pheomelanin contribute not only to external colouration, but also to the normal development and function of the eye and inner ear (Simeonov et al., 2013). Finally neuromelanin is exclusively found in specialised populations of cells in the brain, primarily in the substantia nigra. Neuromelanin is thought to regulate the neurotoxicity of transition metals and other substances found in subcortical structures, but its exact role remains unclear (Federow et al., 2005; Zucca et al., 2014).

The production of melanin, melanogenesis, begins with the oxidation of the amino acid tyrosine to dopaquinone by the rate-limiting enzyme tyrosinase (see **Figure 1.5**). This triggers a series of chemical reactions, mediated by the tyrosine-related proteins TRP-1 and TRP-2. Firstly, dopaquinone is oxidised to dopachrome, followed by tautomerisation, either to 5,6-dihydroxyindole (DHI) or catalysed by TRP-2 to 5,6-dihydroxyindole-2-carboxylic acid (DHICA). DHICA is further oxidised by TRP-1 mediation to indole-5,6-quinone carboxylic acid. Finally, DHI, mediated by tyrosinase, is converted into indole-5,6-quinone and merged with the DHICA synthesis route to produce eumelanin. In a separate, enzyme-independent pathway for the production of pheomelanin, dopaquinone is converted with the addition of glutathione to cysteinyl-dopa and subsequently into pheomelanin (Riley, 1997; Ando et al., 2007).

In humans, melanogenesis occurs in specialised organelles (melanosomes) of specialised cells, the melanocytes. Under normal circumstances, melanin is synthesised in the melanosome and then transported to other cells, most notably the skin cells of the epidermis (Riley, 1997). Melanocytes are found in a variety of tissues, including skin, hair and crucially, the uveal layer of the eye, including the iris, and in the retinal pigment epithelium, immediately posterior to the photoreceptors in the retina. The presence of melanin in these structures is critical for the normal development of the eye and its retinal projections to the rest of the visual system (Neveu & Jeffery, 2007; Summers, 2009).

As it becomes apparent, various steps in the process of melanin synthesis can be susceptible to breakdown. In the case of albinism, the melanosomes are present and structurally intact, but devoid of melanin. This can occur due to a failure in the production of tyrosinase or tyrosine-related proteins, a specific fault during the chain of reaction events in melanogenesis or a failure in the transport of intermediate or final compounds in and out of the melanosome (Simeonov et al., 2013). Absence of tyrosinase in particular, is considered a key feature in albinism and therefore a useful marker in clinical diagnosis. Levels of tyrosinase may be assessed by incubating hair bulbs from the individual's scalp in tyrosine.

Under the presence of endogenous tyrosinase from the hair bulb, the preparation will produce visible pigmentation (Kinnear et al., 1985). In addition to the hair bulb test, more recent genetic testing has allowed the identification of specific mutations leading to deficits in specific steps of melanin biosynthesis. The following section provides a classification of albinism based primarily on these genetic approaches.

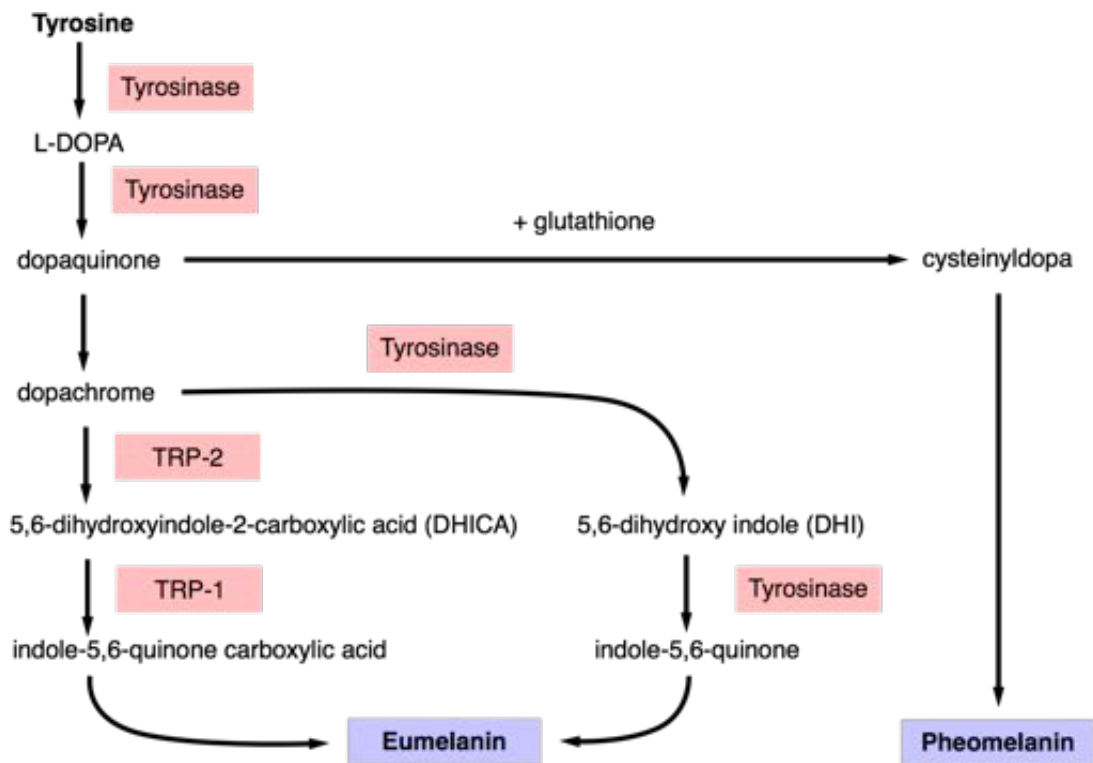


Figure 1.5 Biosynthetic pathway for the production of melanin (melanogenesis). Note the regulatory effects of the amino acid tyrosinase, as well as the tyrosinase-related proteins TRP-1 and TRP-2, affected in albinism. Catalysts denoted in red, resulting melanin compounds in blue.

Chapter 2

Human albinism

2.1 Introduction

Albinism, from the Latin *albus*, meaning white, is a congenital disorder associated with a deficit in the pigment melanin. In humans, albinism commonly manifests as reduced or absent pigmentation in the eyes, skin and hair. It is also typically associated with a number of ophthalmological complaints, including reduced visual acuity, high refractive errors, abnormal eye movements, impaired stereopsis and light sensitivity. As an inherited condition, it is relatively rare, affecting between 1:17,000 and 1:20,000 individuals world-wide (Grønskov et al., 2007; Martínez-García & Montoliu, 2013), but displaying a higher prevalence in sub-Saharan Africa, with between 1:2,000 and 1:5,000 individuals affected in that region (Cruz-Inigo et al., 2011; Kiprono et al., 2014). Albinism is of particular interest to the study of the visual system, as poor retinal pigmentation is associated with abnormal development of the visual system. This creates an anatomical and functional organisation unique to individuals with albinism, that informs our understanding of the biological heuristics involved in the development of the visual system and the plastic capacity of the brain for organisation under abnormal retinal input.

This chapter will first provide an overview of the types of albinism and their clinical features, followed by a discussion of the optic nerve misrouting characteristic of albinism, its measurement by invasive and non-invasive means, and outstanding questions to be addressed in following experimental chapters.

2.2 Classifications of albinism

In humans, albinism is a broad term encompassing a heterogeneous group of rare congenital disorders, all characterised by a reduction or absence of the pigment melanin in the fundus of the eye. Classifications of albinism differ, and types of albinism have previously been organised based on their clinical presentation, biochemical markers and genetic origin (Kinnear et al., 1985; Summers, 2009; Martínez-García & Montoliu, 2013), with exact categorisation being a topic of active debate (Montoliu et al., 2013; Simeonov et al., 2013). What follows is a classification based primarily on the genetic origin of the disorders. Under this scheme, albinism may be broadly classified into three major types: oculocutaneous albinism (OCA), ocular albinism (OA) and syndromic albinism (**Table 2.1**).

Table 2.1 A classification of human albinism based on genetic mutations and their disruption to the process of melanin biosynthesis. Albinism is broadly divided into oculocutaneous albinism (OCA), ocular albinism (OA) and complex multi-gene syndromic forms of albinism.

Condition		Gene	Mechanism affected	
OCA	OCA1	OCA1A	<i>TYR</i>	No tyrosinase production
		OCA1B	<i>TYR</i>	Partial tyrosinase production
		OCA1MP	<i>TYR</i>	Partial tyrosinase production
		OCAT1TS	<i>TYR</i>	Partial tyrosinase production
	OCA2	<i>OCA2</i>	Deficit in p -protein production	
	OCA3	<i>TYRP1</i>	Deficit in tyrosinase stabilisation	
	OCA4	<i>SLC45A2</i>	Deficit in tyrosinase transport	
OA	OA1	<i>GPR143</i>	Deregulated melanosome growth	
	OA2	<i>CACNA1F</i>	Unclear	
Syndromes	Hermansky-Pudlak	<i>HPS</i>	Multi-factorial syndrome	
	Chédiak-Higashi	multi-gene	Multi-factorial syndrome	
	Griscelli	multi-gene	Multi-factorial syndrome	
	Elejalde	multi-gene	Multi-factorial syndrome	
	Cross-McKusick-Breen	multi-gene	Multi-factorial syndrome	

2.2.1 Oculocutaneous albinism (OCA)

OCA is the most common type of albinism, and characterised by reduced or complete absence of the pigment melanin in the eyes, skin and hair. Individuals with OCA typically show blue or red eyes, very fair skin and white or lightly coloured hair. Common complaints include poor acuity, high refractive errors, abnormal eye movements, poor depth perception, strabismus, photosensitivity, as well as a higher incidence of skin cancer (Kinnear et al., 1985; Summers, 1996). OCA is caused by an autosomal genetic mutation, meaning both parents must carry a copy of the mutated gene in order for an albino offspring to be born. These mutations lead to specific disruptions in the synthesis of melanin, and may be subdivided into four subtypes (OCA1, OCA2, OCA3, OCA4) based on the exact locus of the mutation, although further sub-classifications has been proposed (Montoliu et al., 2013). The first type, OCA1, is the most common and involves a mutation in the tyrosinase gene, comprising a group of 'tyrosinase-related' forms of albinism. OCA2-4 are caused by mutations in other genes, all affecting the production, transport or uptake of melanin at various stages.

2.2.1.1 OCA1

Tyrosinase-related OCA1 is caused by a mutation of the tyrosinase gene *TYR* in chromosome 11q14-21 (Oetting & King, 1999). *TYR* is crucial in the production of tyrosinase, the very first step in the process of melanin synthesis (Simeonov et al., 2013). Different mutations to the *TYR* gene can produce variable levels of tyrosinase synthesis, therefore leading to either a complete deficiency in the production of melanin (OCA1A) or, in rare cases, some residual activity in the tyrosinase enzyme (OCA1B, OCA1MP, OCA1TS) depending on the nature of the mutation.

Individuals with OCA1A are prototypical of albinism, with no melanin present in eyes, skin or hair at birth, and pigmentation does not develop through life (Summers, 2009). The eyes appear translucent pink and hair and skin white, with no tanning when exposed to sunlight. Hair bulb tests show no presence of tyrosinase. Individuals with OCA1B, in contrast, develop a small amount of melanin later in life, despite none being present at birth. The residual tyrosinase activity leads to yellow pigmentation of the hair and skin, variable with ethnic background (Hu et al., 1980).

OCA1MP and OCA1TS are rare forms of oculocutaneous albinism with residually active tyrosinase. Individuals with OCA1MP, standing for 'minimal pigmentation', develop variable levels of heterogeneous pigmentation and are typically associated with low hair bulb tyrosinase in both child, and one parent but not the other (Summers, 2009). Temperature-sensitive OCA, or OCA1TS, is a rare mutation where production of tyrosinase becomes temperature-sensitive. Tyrosinase synthesis is greater at low temperatures, leading to pigmentation in the cooler zones of the body, arms and legs, but not so on the torso (Summers, 1996). In both cases, hair bulb tests show reduced, but present, tyrosinase activity.

2.2.1.2 OCA2

OCA2, also known as 'tyrosinase-positive OCA', is the second most common type of albinism after OCA1, and is caused by a mutation of the *OCA2* gene on chromosome 15q11-13 (Oetting & King, 1999). The mutation is associated with a deficiency in the production and upkeep of the *P* protein, which is involved in the transport of tyrosinase to the melanosome. Deficiency in the *P* protein leads to a build-up of tyrosinase outside the melanosome, impeding the normal synthesis of melanin (Simeonov et al., 2013). Individuals with OCA2 typically have some visible pigmentation and milder ophthalmological impairments compared to OCA1. OCA2 is more prevalent in populations of African descent (Mártinez-García & Montoliu, 2013).

2.2.1.3 OCA3

OCA3, also known as red or rufous OCA, is associated with a recessive mutation in the *TYRP1* gene in chromosome 9q23 (Oetting & King, 1999). *TYRP1* is structurally similar to the *TYR* gene and is involved in the stabilisation of tyrosinase during melanin biosynthesis, and without it, tyrosinase degrades rapidly (Simeonov et al., 2013). While necessary for the synthesis of the black-brown eumelanin, a *TYRP1* deficiency does not affect the production of red pheomelanin, leading to the particular pigmentation of reddish-brown skin and ginger-red hair seen in individuals with OCA3 (Summers, 1996).

2.2.1.4 OCA4

OCA4 is a rare tyrosinase-positive form of oculocutaneous albinism, caused by a mutation to the *SLC45A2* gene in chromosome 5p (Summers, 2009). This gene is functionally similar to *OCA2*, leading to a deficit in the transport of tyrosinase during melanin biosynthesis (Simeonov et al., 2013). Phenotypically, it closely resembles *OCA2*, with particular regional incidence in Japan, and to a lesser extent in European countries (Mártinez-García & Montoliu, 2013).

2.2.2 Ocular albinism (OA)

OA is considered a milder form of albinism, and is characterised by hypopigmentation of the eyes, with reduced or normally pigmented skin and hair. Both the iris and fundus of the eye have reduced, but seldom absent, pigmentation. Common complaints include poor visual acuity, nystagmus, strabismus and photophobia, as well as difficulties with stereoscopic vision (Charles et al., 1993; Grønskov et al., 2007).

OA is subdivided into two types: OA1 and OA2. The most common type is ocular albinism type 1 (OA1), also known as Nettleship-Falls syndrome or X-linked ocular albinism. As the name suggests, this form is caused by a mutation in the X chromosome, specifically in the *GPR143* gene (Oetting & King, 1999). The GPR143 protein synthesised by the *GPR143* gene is involved in regulation of melanosome growth. In OA1, melanosomes can grow abnormally large, disrupting the process of melanin synthesis. Since males only carry one copy of the X chromosome, the incidence of X-linked OA is higher in the male population, approximately 1 in 60,000 males (Rosenberg & Schwartz, 1998). Ocular albinism type 2 (OA2), also known as Forsius-Eriksson-Miyake syndrome or Åland eye disease, is also caused by an X-linked mutation, in this case, in the *CACNA1F* gene (Jalkanen et al., 2007). Its clinical presentation is very similar to OA1, with the addition of high comorbidity with protanopic dichromatic colour blindness (Rosenberg et al., 1990).

2.2.3 Syndromes

Finally, several rare pathological syndromes are associated with albinism. These are conditions where albinism is a secondary feature. Due to its resemblance to OCA, the primary syndrome in this category is Hermansky-Pudlak syndrome. Caused by a mutation of the *HPS* gene (Montoliu et al., 2013), Hermansky-Pudlak syndrome is associated with a lipid-storage defect leading to tendency to internal bleeding. Given the potential severity of the condition, clinicians seeking a diagnosis of OCA may also screen for the genetic markers of Hermansky-Pudlak syndrome, particularly early in life (Summers, 2009). Other rare disorders with features of albinism include Chédiak-Higashi syndrome, Griscelli syndrome, Elejalde syndrome and Cross-McKusick-Breen syndrome (Montoliu et al., 2013; Simeonov et al., 2013). While linked to OCA and OA in the characteristic reduction or absence of melanin, these conditions differ substantially from other forms of albinism, both in their genetic origin and their clinical presentation. Syndromic forms of albinism are commonly comorbid with neurological deficits including peripheral neuropathy, microphthalmia, fibromatosis and cognitive deficits (Kinnear et al., 1985; Summers, 1996). Syndromic forms of albinism fall outside the scope of this thesis, and therefore all following discussion will refer solely to OCA and OA in human albinism.

2.3 Clinical features

The clinical presentation of individuals with albinism is generally similar between OCA and OA, with varying degrees of severity, with OCA1 being the most severe, followed by OCA2, OCA3 and OCA4, and finally OA1 and OA2 being the least severely affected.

2.3.1 Foveal hypoplasia

Foveal hypoplasia refers to the underdevelopment of the fovea, and is a common feature of all types of albinism (Summers, 2009). It is defined clinically as the absence of a foveal reflex and reduced or absent pigmentation in the retinal pigment epithelium of the fovea. When investigated with optical coherence tomography (OCT), a retinal imaging technique, the foveal pit appears absent and significant thickening is observed in the outer retinal layers (Mohammad et al., 2011). The lack of a clearly defined fovea and increased tissue presence at the foveal site typically leads to reduced visual acuity, with close-distance vision being the most affected (Kinnear et al., 1985; Hoffmann et al., 2007; Summers, 2009). Depth discrimination is also reduced, in line with the degree of foveal hypoplasia (Summers, 1996).

2.3.2 Iris transillumination

Individuals with albinism often present reduced pigmentation in the iris, appearing red or pink to the naked eye. Complete or partial transillumination of the iris is uncommon, seen in approximately 40% of cases (Kinnear et al., 1985). Increased transillumination is associated with greater sensitivity to brightness, leading to photophobia in the more severe cases.

2.3.3 Abnormal optic disc morphology

Refractive errors are common in albinism, and more severe than in the general population (Summers, 1996). Close-distance vision is most affected, but refractive errors may include myopia (near-sightedness), hyperopia (farsightedness), presbyopia and astigmatism. Clinical management is often restricted to the use of corrective glasses.

2.3.4 Abnormal eye position and movements

Strabismus, also known as heterotropia, is a misalignment of the eye focus, and is relatively common in albinism (e.g. Charles et al., 1993). It hampers binocular vision and affects visual acuity. Nystagmus, or involuntary eye movements, are also highly prevalent in albinism (Summers, 2009). Nystagmus takes the form of a biphasic eye movement, firstly a slow smooth pursuit movement followed by a fast saccade to the original point of fixation. In albinism, these movements are typically periodic and impair the ability to fixate vision on an object of interest, limiting fine detail vision by displacing the projection of the object of interest away from the foveal region of the retina. Approximately half of people with albinism and manifest nystagmus adopt an abnormal head posture, which reduces or eliminates the nystagmus (Kinnear et al., 1985). Both strabismus and nystagmus can be managed with patching therapy, pharmacologically, or via surgical intervention to decrease their severity (Summers, 2009).

2.3.5 Dermatological concerns

Individuals severely deficient in skin pigmentation, most common in OCA1, show an increased risk of sunburn and skin cancer (Kiprono et al., 2014), making limited sun exposure and dermatological care part of the clinical management of the condition.

2.4 Misrouting of the optic nerves

A key feature of albinism is an abnormal visual system, not only in terms of hypopigmentation and underdevelopment of the retina, but also in the retinal projections to visual cortex, with the most salient feature being an abnormal decussation of the optic nerve at the level of the chiasm (see **Figure 2.1**). In healthy humans, this crossing is the source of visual field lateralisation in cortical and subcortical representations of the retina, with the nasal portion of the retina projecting to the contralateral hemisphere and the temporal portion of the retina projecting to the ipsilateral hemisphere. In albinism this crossing is abnormal, leading the majority of fibres to project to the contralateral hemisphere, leaving a weak temporal retinal projection to the ipsilateral hemisphere.

2.4.1 Optic nerve misrouting in non-human species

The exact mechanism by which this misrouting occurs is not yet clear, but it is a distinct morphological feature of albinism observed in a variety of mammalian species, including the rat (Lund, 1965), cat (Creel, 1971; Stone et al., 1978; Creel et al., 1982; Guillery, 1986), mink (Sanderson et al., 1974), white tiger (Guillery & Kaas, 1971), old world monkey (Guillery et al., 1984), wallaby (Guillery et al., 1999) and human (Creel et al., 1974; Guillery et al., 1975). The degree of chiasmal crossover in healthy animals is directly related with the placement of eyes on the head, with species that have laterally placed eyes, showing large or complete amounts of crossover of the optic nerve to the contralateral hemisphere, while species with front-facing eyes, including felines and primates, show various degrees of ipsilateral and contralateral input from the same eye (**Figure 2.2**). This feature is important for binocular stereoscopic vision, as information from both eyes corresponding to the same hemiretina are integrated at the cortical level (Hubel & Wiesel, 1962).

Throughout much of the 1970s and 1980s the most prominent model species for albinism was the Siamese cat, a breed where the production of melanin is modulated by environmental temperature, leading to the characteristic retinal hypopigmentation and optic nerve misrouting also seen in humans (Creel, 1971; Hubel & Wiesel, 1971). Work on the Siamese cat confirmed the direct link between the degree of retinal pigmentation and the severity of the chiasmal crossing abnormality (Creel et al., 1982). Electrophysiological studies investigating the neuronal responses to visual stimuli revealed that the Siamese cat displays two types of retinotopic organisation resulting from the abnormal projection from the nasal retina, named the Boston and Midwestern patterns (for a review, see Kaas, 2005). In the Boston pattern, primary visual cortex displays a continuous retinotopic map that extends from the contralateral into the ipsilateral visual field by up to 20° of visual angle. In contrast, the Midwestern pattern appears as two overlapping representations of the

ipsilateral and contralateral visual fields in the same cortical territory. Both of these arrangements have significant implications for the functional organisation of primary and extrastriate visual cortex. The Boston pattern provides a continuous representation of visual space by simply shifting the vertical meridian defining ipsilateral and contralateral visual fields. This configuration implies a conservation of the same developmental heuristics for organising retinotopic information as seen in healthy, non-albino individuals. The Midwestern pattern however, is a radically different way of organising information, with superimposed representations of distinct retinal inputs, forming a coherent picture of the visual world, as Midwestern-type cats display relatively normal visuomotor behaviour (Kaas, 2005). This configuration has two important organisational implications; a) cortical neurons must dissociate independent retinal inputs and b) suppression of the weak temporal input.

A Midwestern-type cortex contains an overlapping representation of nasal and temporal visual fields, requiring these inputs to be segregated and processed relatively independently, in order to avoid a confused representation of the visual world. This may be achieved by selective encoding of spatially neighbouring but input-specific cells. This type of input selectivity is well known in visual cortex, for example in ocular dominance columns (Hubel & Wiesel, 1969) and may account for the gross organisation of the Midwestern pattern. Indeed, an electrophysiological study of the Midwestern-type Siamese cat show representations of nasal and temporal retina in adjacent groups of cells in primary visual cortex (Kaas & Guillery, 1973).

A second implication of the Midwestern pattern is the suppression of the abnormal input. Siamese cats stimulated monocularly are severely impaired in the perception of stimuli in the ipsilateral hemifield, and few cells in the contralateral hemisphere are responsive to the abnormal retinal input (Hubel & Wiesel, 1971; Kaas & Guillery, 1973; Cooper & Blasdel, 1980). This suppression appears to be specific, as it cannot be induced by restricting retinal input through lid suture, but is instead attributed to the developmental factors in albinism (Kaas & Guillery, 1973). It may therefore be suggested that in the Midwestern pattern, information from the abnormal input is suppressed in order to allow for the processing of the normal, nasal input. This leads to the outstanding question of, what role does the abnormal projection play? Given that the retinotopic representation is consistently reported, it is possible that it plays a role not immediately apparent in investigations of early visual areas, as typically reported in electrophysiological studies. Instead, the abnormal input may contribute to the processing of visual information in higher visual areas, where large receptive fields and the integration of information across large zones of the visual field are the norm. Indeed, the exact role of abnormal retinal inputs as seen in albinism on the larger circuit of the visual system is poorly understood.

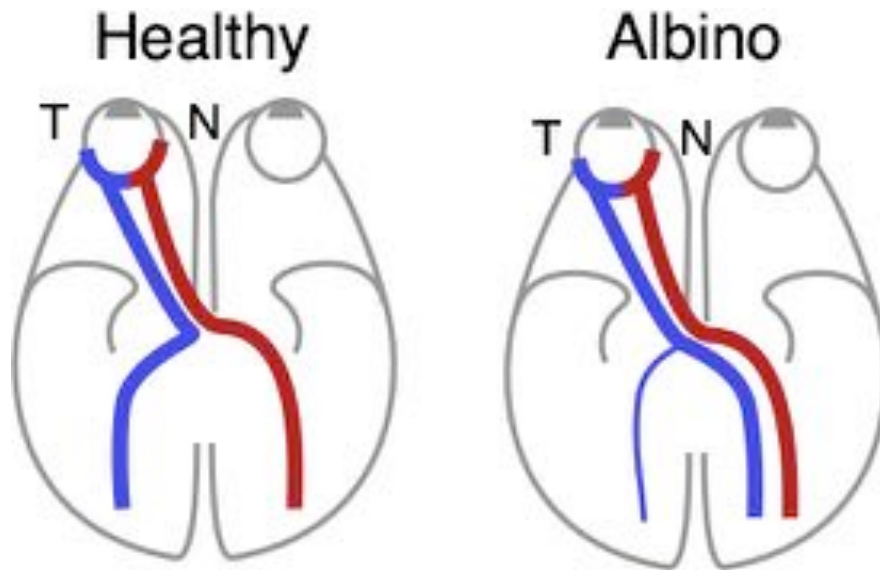


Figure 2.1 Schematic of optic nerve decussation in healthy and albino humans. The nasal retina (red) projects to the contralateral hemisphere in both cases, but the temporal retina (blue), which normally projects fully to the ipsilateral hemisphere, crosses over at the level of the optic chiasm to the contralateral side, leaving a weak temporal projection to the ipsilateral hemisphere in the albino. N = nasal, T = temporal.

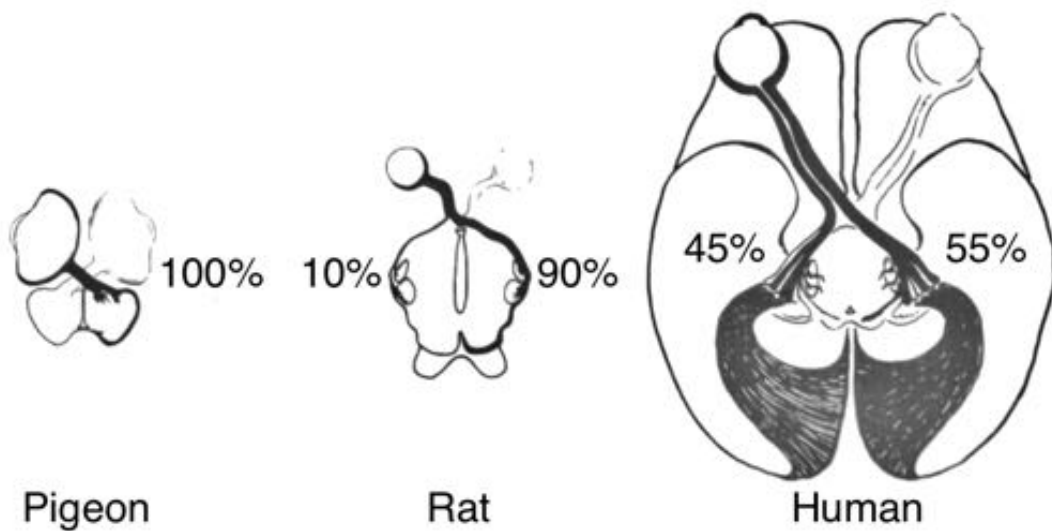


Figure 2.2 Degree of optic nerve fibre decussation in the pigeon, rat and human. A large projection of the temporal retina to the ipsilateral hemisphere is seen in species with forward-facing eyes, including humans. In species where the eyes are placed laterally, ipsilateral projections are small or non-existent. Adapted from Creel et al. (1974).

Given the evidence presented on cortical organisation under the abnormal retinal input in model species, it raises questions of retinotopic organisation in human albinism – foremost among them, whether either Boston or Midwestern patterns of retinotopic organisation can be observed in humans with albinism, and what consequences it has for the functioning of the visual system. The following section discusses the measurement of optic nerve misrouting in humans via invasive and non-invasive means, and the evidence for abnormal cortical organisation in occipital cortex in human albinism.

2.4.2 Measuring optic nerve misrouting in humans

While the optic nerve misrouting is an established feature of albinism, there is limited information of its morphological features when expressed in humans. One study by Guillery and colleagues (1975) inspected the structure of a human albino lateral geniculate nucleus (LGN) *ex vivo*, finding a similar pattern of altered layer structure as seen in the feline model of albinism (Guillery & Kaas, 1971; Cooper & Pettigrew, 1979).

Non-invasive anatomical MRI studies of human albinism have confirmed an abnormal retinogeniculate system, with reduced chiasmal width, smaller optic nerve and tract diameters and smaller LGN volumes when compared to healthy controls (Schmitz et al., 2003; von dem Hagen et al., 2005; Mcketton et al., 2014). Beyond the retinogeniculate projection, cortical abnormalities have also been reported in human albinism, with shorter calcarine sulci (Neveu et al., 2007), and increased grey matter and increased cortical thickness in the posterior calcarine region, corresponding to the foveal representation (Bridge et al., 2014). These findings are thought to reflect a reduction in neural pruning during development, as the degree of calcarine cortical thickness was negatively correlated with visual acuity. In addition, reduced grey matter and decreased gyrification have also been reported for ventral extrastriate areas, thought to reflect the reduced foveal input to the ventral system (von dem Hagen et al., 2005; Bridge et al., 2014). These findings reinforce the idea of an underdeveloped fovea linked to structural changes across the visual system, affecting its structural organisation.

In terms of functional organisation, the misrouting of the optic nerve may be detected via non-invasive procedures, such as recording visual evoked potentials (VEP) with electroencephalography (Creel et al., 1974; Carroll et al., 1980; Apkarian et al., 1983) or with functional MRI (Hedera et al., 1994; Morland et al., 2002; von dem Hagen et al., 2008). In VEP studies, the abnormal projection of visual information is identified by the asymmetric pattern of responses elicited in the occipital regions following monocular stimulation. In the healthy configuration, the temporal retina projects to the ipsilateral hemisphere while the nasal retina projects to the contralateral hemisphere, so that a full-field stimulus leads to symmetrical electrical responses in left and right hemispheres. In individuals with albinism,

however, the over-crossing of the temporal retina leads to a greater response in the contralateral hemisphere, creating a signal asymmetry between ipsi- and contralateral occipital electrode recordings. This approach allows the quantification of the misrouting based on evoked patterns and provides both a diagnostic and research tool (Dorey et al., 2003; Pott et al., 2003; Neveu et al., 2003; Hoffmann et al., 2005; Hoffmann et al., 2006). More recently, studies have investigated the pattern of neural activity elicited by visual stimulation with functional MRI (Brown et al., 2016). Early work by Hedera and colleagues (1994) showed it was possible to detect the asymmetric occipital response to monocular stimulation in albinism *in vivo* using BOLD. Implementing a wide field visual stimulus, Hedera et al. (1994) demonstrate responses both in the hemisphere contralateral to monocular stimulation and in the ipsilateral hemisphere, through the weak temporal projection. Indeed, Morland et al. (2002) confirmed these signals may be segregated by selectively stimulating either ipsi- or contralateral visual fields. More recently, Hoffmann et al. (2003) applied the phase-encoded retinotopic mapping technique to the study of albinism, revealing the functional organisation of primary visual cortex to be consistent with the Siamese cat model; monocular stimulation of both nasal and temporal retina led to enhanced activity in the contralateral hemisphere, while only temporal stimulation induced significant activity in the ipsilateral hemisphere (see **Figure 2.3**). Crucially, the contralateral representation of the visual field followed a Midwestern-type pattern, with overlapping representations of the temporal and nasal retina inputs, in agreement with electrophysiological studies in the albino green monkey (Guillery et al., 1984) and confirmed in later fMRI studies (Kaule et al., 2014).

The size of the abnormal contralateral projection varies across individuals with albinism, with the vertical line of decussation shifted between 2° and 15° of visual angle (Hoffmann et al., 2003; Hoffmann et al., 2005). By comparing fMRI responses and the phenotypes of participants, the degree of crossover was found to be predicted by the levels of pigmentation in hair and skin (von dem Hagen et al., 2007), in agreement with evidence in other mammalian species such as the cat and mink (Sanderson et al., 1974; Creel et al., 1982).

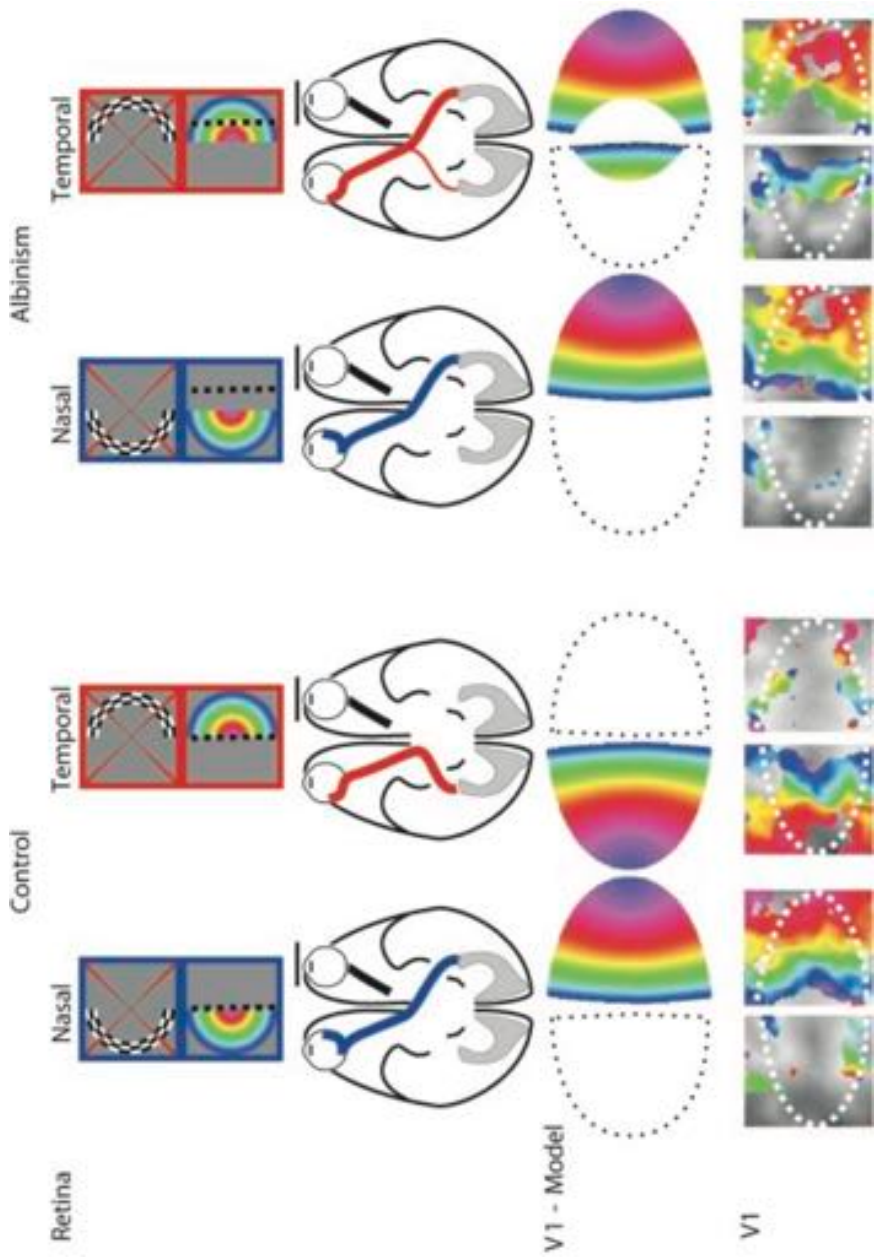


Figure 2.3 Schematic representation of the experimental results reported in Hoffmann et al. (2003). The nasal retina projection is similar in albinism as in control participants, showing a full hemifield representation in the contralateral hemisphere. The temporal retina, on the other hand, has a large abnormal projection to the contralateral hemisphere, where the most central portion of the visual field is represented in the same cortical territory as the nasal hemiretina. The more eccentric portions of the temporal retina project weakly to the ipsilateral hemisphere. Adapted from Hoffmann et al. (2003).

One currently outstanding point is whether the functional organisation of visual information is altered beyond early visual areas in albinism. A recent study by Kaule et al. (2014) investigated the cortical organisation of the ventral visual system in albinism, finding the retinotopic pattern observed in V1 was replicated in ventral occipital and parahippocampal visual areas. This finding highlights the robustness of coarse retinotopic organisation in the visual system, and the role V1 plays in propagating an organisational scheme through the ventral stream. While it remains to be seen whether the same organisation is observed in the dorsal stream of the visual system, these findings reinforce the idea that the visual system is resilient to broadly abnormal input, as is the case in albinism, and displays an adaptive capacity for organising such input. The following section discusses this plastic adaptation interpretation of the cortical organisation in albinism.

2.5 Albinism as a case of developmental plasticity

Albinism, in humans and other mammalian species with front-facing eyes, is characterised by a misrouting of the optic nerves at the level of the optic chiasm, leading to altered retinal projections and abnormal geniculate and cortical organisation. In face of such fundamentally altered input, it is therefore surprising that most individuals with albinism report near-normal visual perception and present relatively normal visuomotor behaviour. While albinism is linked with an increased incidence of visual deficits, including refractive errors, light sensitivity and eye movement disorders, such individuals with less severe forms of the condition retain good visual capabilities. The following section attempts to reconcile these two facts; altered visual input and relatively normal visual behaviour with an account of the cortical organisation of albinism as an example of developmental plasticity.

2.5.1 Neural plasticity vs. reorganisation

There is an important distinction between the concepts of neural plasticity and reorganisation. Reorganisation in the narrow sense, implies the loss of an already present function that is subsequently regained or altered by an adaptive process. It is defined by Wandell and Smirnakis (2009) as:

“[reorganisation] refers to a change in neural properties as the input statistics change (for example, after a retinal lesion) or the output demands change (for example, after muscle mass loss).” (p. 874)

Reorganisation typically refers to long-term changes that are distinct from adaptation, which are short-term changes, typically in response to dynamic changes in inputs, for example, contrast adaptation (Wandell & Smirnakis, 2009). In this strict sense, developmental conditions such as albinism are not examples of reorganisation, but of abnormal organisation arising from fundamentally altered inputs in the first place. In contrast, neural plasticity can refer to any alteration in organisation, arising from initial developmental constraints or later in life as a result of changes in input, output or structural constraints (Guzzetta et al., 2010). In this broader sense, neural plasticity encompasses both reorganisation, in the sense of adaptive change to a loss of function, and also the adaptive development of altered organisation in developmental conditions.

In the particular case of albinism, the chiasmatal misrouting occurs early in life (Neveu & Jeffery, 2007) and it is thought to drive the abnormal organisation in visual cortex (Guillery, 1986). Under the presence of abnormal retinal inputs, the albino visual system develops a unique pattern of organisation that is relatively stable through the lifespan of the individual (but see Neveu et al., 2003). Yet, the observed organisation of cortical circuitry under abnormal retinal input does not develop arbitrarily, but under the constraints of an existing programme of retinotopic organisation. Developmental plasticity is not an unconstrained process, with affordances made possible in some dimensions but not others. As previously discussed, in the Siamese cat two types of cortical organisation are found, the Boston and Midwestern types. Despite this apparent dichotomy, some commentators have observed a mixture of these patterns in a large number of Siamese cats, suggesting not two distinct populations, but rather a continuum of retinotopic patterns (Cooper & Blasdel, 1980), pointing to a common affordance or set of affordances, to alter functional organisation in visual cortex. In humans, albinism leads to a fundamentally altered retinotopic map in primary visual cortex (Hoffmann et al., 2003), but also to a consistent replication of this retinotopic pattern in ventral visual areas (Kaule et al., 2014), highlighting the stability of functional organisation across multiple visual areas, even in the face of altered retinotopy. These two forces, plasticity and stability, are central to understanding the affordances available to plastic reorganisation of the visual system, and its implications for both developmental conditions but also reorganisation following impairment.

2.5.2 Functional organisation in albinism and achiasma

How and where can the retinotopic programme be altered to accommodate the abnormal input in human albinism is an outstanding question, and one that the present work aims to illuminate. Our understanding of the anatomical and functional consequences of chiasmatal misrouting can be further expanded by the study of achiasma, a related developmental condition where retinal information from each eye is projected exclusively to the ipsilateral

hemisphere. Individuals with achiasma display a largely reorganised retinotopic map in V1, with overlapping, mirror-reversed representations of the nasal and temporal hemiretinas (Hoffmann et al., 2012). More strikingly, population receptive fields in achiasma are best explained by a model incorporating dual receptive fields, one for each mirror location in each hemiretina. Whether the dual receptive field model implies the encoding of information from both retinal locations at the level of individual cells is currently unclear. In the case of albinism, this does not appear to be the case, based on the electrophysiological evidence in Siamese cats (Hubel & Wiesel, 1971; Kaas & Guillery, 1973; Cooper & Blasdel, 1980) but also based on psychophysical evidence in humans (Klemen et al., 2012). Under a dual receptive field model, cells responsive to two mirrored retinal locations should experience adaptation to stimulation in either hemifield, and therefore display said adaptation when probed in the opposite hemifield. Using a tilt after-effect adaptation paradigm, Klemen and colleagues (2012) showed that individuals with albinism do not display the inter-hemifield adaptation expected from a dual receptive field encoding of visual information. Instead, they proposed visual field information is encoded in segregated hemifield dominance columns. Note that this dual receptive field organisation may hold for achiasma and not for albinism, considering retinal inputs from each eye remain segregated until high in the visual hierarchy in the case of achiasma (Davis-Thompson et al., 2013), an important constrain for the integration of visual information not necessarily present in albinism. Whether dual receptive fields are present or absent in human albinism, however, remains to be settled in the current absence of physiological evidence.

A further consideration in the organisation of visual information in albinism and achiasma, is whether the transfer of information across hemispheres is affected. In healthy individuals, interhemispheric transfer is necessary to create a complete representation of the visual world, as visual information is typically segregated into left and right visual fields at the level of the optic chiasm. In achiasma, area MT+/V5 was found to be the earliest visual area to be activated bilaterally following monocular stimulation (Davis-Thompson et al., 2013). This suggests area MT+/V5 may be the earliest point of entry for inter-hemispheric transfer, either via the corpus callosum or via subcortical pathways, and may be an important area for the integration of visual information across the visual field. While the interhemispheric transfer of information has not been explicitly tested in either human achiasma or albinism, structural MRI studies of either condition have not reported abnormalities in post-striate white matter (Hoffmann et al., 2012; Davis-Thompson et al., 2013; Bridge et al., 2014; Mcketton et al., 2014), potentially indicating stability in the interhemispheric pathways such as the corpus callosum.

2.6 Outstanding questions

The preceding discussion leaves a number of unanswered questions regarding the plastic reorganisation of the visual system, principally; (1) what are the consequences of abnormal retinotopic organisation beyond primary visual cortex and (2) how is retinotopic information integrated interhemispherically in albinism.

The visual system is a large, distributed network that processes sensory information at multiple levels. While most *in vivo* studies of albinism have focused on the cortical organisation in V1, the retinotopic organisation of extrastriate areas remains largely uncharted. In order to understand the underlying principles that drive the overlapping representations of nasal and temporal hemiretinas and its propagation to extrastriate visual areas, a detailed understanding of the properties of visual receptive fields encoding this information would be beneficial. As such, three questions remain to be answered about retinotopic organisation in human albinism:

- What are the retinotopic organisations of extrastriate visual areas?
- What are the receptive field properties of striate and extrastriate visual areas?
- Is there *in vivo* evidence for dual receptive fields in human albinism?

A clearer understanding of the functional organisation of the visual system in albinism would allow a link between *in vivo* findings in human with extensive knowledge of the condition in animal models, particularly in regards to the likely neuronal representation of the visual field. In addition, albinism is a heterogeneous condition with varying clinical outcomes. A closer understanding of how variability in visual system organisation is related to phenotype presentation is critical for establishing a mechanistic understanding of cortical abnormalities in albinism.

Furthermore, in order to form a complete representation of the visual scene and carry out visuomotor behaviour, it is necessary to integrate information from left and right visual fields to build a coherent picture of the visual world. Given the abnormal retinal inputs evidenced in albinism, this may result in abnormally organised interhemispheric connectivity of the visual system, both structural and functional. Two questions are therefore proposed:

- Do anatomical differences exist in the interhemispheric relay of visual information, particularly between the occipital lobes?
- Is the functional connectivity between left and right visual areas abnormal in human albinism?

Both the preceding questions regarding functional organisation and questions regarding the nature of structural and functional connectivity in human albinism are tackled in Chapter 6 and 7, respectively.

Chapter 3

Methodology

3.1 Introduction

In order to study the functional and structural organisation of the visual system in human albinism, magnetic resonance imaging (MRI) methods are predominantly used in this thesis. Functional MRI methods are well suited to explore the organisation of retinotopic representations in visual cortex due to its capacity to resolve cortical signals at high spatial resolution, while diffusion-weighted MRI is uniquely positioned to reconstruct brain white matter pathways, as the only method currently available for achieving this *in vivo*. This chapter provides a brief description of both functional and diffusion-weighted MRI methods.

3.2 Functional MRI

Among the tools that have emerged over the past quarter century to populate the repertoire of neuroscientific methodologies, functional magnetic resonance imaging (fMRI) is one of the most successful in informing our understanding of neural activity in the human brain *in vivo*. In this section, the physiological and imaging basis of fMRI will be explored, as well as its implications for examining the functional organisation of the human visual system.

3.2.1 Physiological principles

3.2.1.1 *The BOLD response*

When performing an MRI experiment, any paramagnetic material contained in the sample will cause an increase in local spin de-phasing, leading to lower signal in and around the material in question. One such paramagnetic substance found endogenously in the human brain is deoxygenated haemoglobin. Haemoglobin is a protein found in erythrocytes (red blood cells) which transports oxygen from the respiratory organs to body tissue, including the brain. Once the oxygen has been deposited in the local tissue, the proteins change from saturated (oxy-haemoglobin, Hb-O₂) to unsaturated form (deoxy-haemoglobin, dHb). These two forms differ in their magnetic properties; Hb-O₂ is diamagnetic, sharing magnetic properties with water and effectively inert for the purposes of MRI. On the other hand, dHb is paramagnetic: in the presence of an external magnetic field, it induces a local field distortion extending beyond the vasculature which contains the molecule in question.

Any sample subjected to MR imaging and containing a sufficient quantity of dHb will sustain a localised signal loss in the area where dHb is found, acting as an endogenous contrast agent. This signal loss is caused by an increase in local spin-state homogeneity and therefore increased T_2 relaxation. The key insight for functional imaging, is the physiological coupling between neural activity and levels of dHb. When a group of neurons experience increased neural activity, the area receives a relatively localised supply of Hb-O₂ leading to a change in the relative concentration of Hb-O₂ to dHb. Since the environment becomes less paramagnetic due to the influx of Hb-O₂, there is less spin de-phasing and therefore a larger signal detected from the area in question. This effect captured in MRI is the blood oxygenation level dependent (BOLD) response, first described by Ogawa et al. (1990). This principle relies on the interaction between neural activity and a compensatory vascular strategy; the larger the increase in neural activity, the more demand for resources a region exerts and the larger the vascular response exhibited to meet these demands.

3.2.1.2 Haemodynamic response function

The BOLD signal is characterised by a particular relationship between neural signalling and blood flow, also known as the haemodynamic response function (HRF). In brief, when a brain area is subject to increased activity, for example visual cortex during photic stimulation, there is an initial decrease in BOLD signal from baseline (initial dip), which is quickly matched by a sustained increase for the duration of the stimulus presentation, a post-stimulus drop of signal and finally a lower-than-baseline region (under-shoot) concluding in a gradual return to baseline (see **Figure 3.1**). Because the vascular compensatory strategies employed in the brain are not immediate in their actions, the BOLD response is often described as 'sluggish', meaning there is a certain time delay between the onset of the increased neural activity and BOLD signal peak, estimated to be in the region of 2-3 seconds (Nair, 2005). Once the 'sluggishness' of the BOLD response has been taken into account, the physiological origin of the particular shape of the HRF becomes evident; during initial stimulation oxygenated blood is lacking, leading to an increase in Hb-O₂ consumption and greater relative levels of dHb, causing the initial dip. Once the vascular response is elicited, the area is supplied with more Hb-O₂ than it can consume, leading to a sharp increase in BOLD signal; as the stimulation ends, Hb-O₂ supply decreases gradually, to the point of providing less Hb-O₂ than the baseline levels creating the undershoot, which is eventually rectified and the BOLD signal returns to baseline.

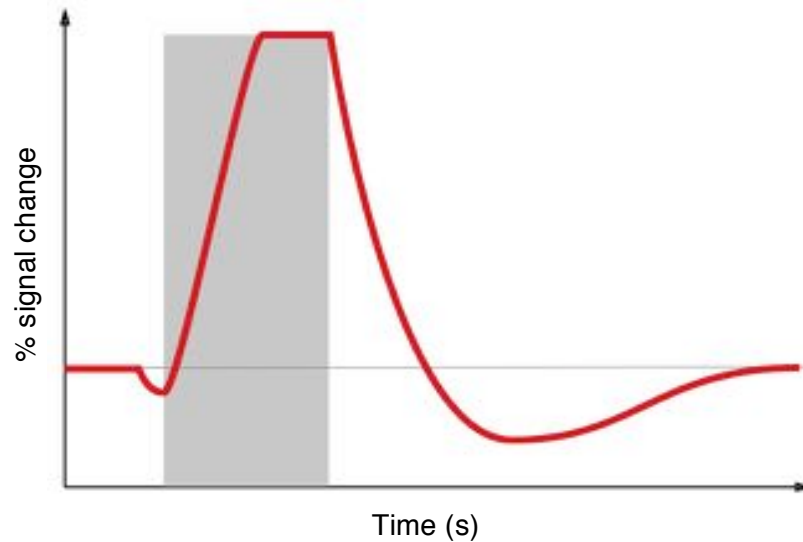


Figure 3.1 Temporal evolution of the haemodynamic response to a brief stimulus (grey bar).

3.2.2 MR imaging of the BOLD response

In order to capture the effects of BOLD signals with MR imaging, two components are required; a) an imaging sequence that maximises the contribution of local field inhomogeneities (T_2^*) to the overall image and b) a fast acquisition in order to capture the evolution of local signal distortions in order to estimate the HRF. Both of these requirements are fulfilled by echo-planar imaging (EPI), as discussed in the previous section. T_2^* -optimised EPI is the most commonly used pulse sequence for fMRI, since it permits sampling at a temporal rate that allows accurate estimation of the HRF. Since the BOLD response is 'sluggish', with a delay of approximately 2-3 seconds, reducing the sampling rate beyond that window of time would not yield further information, other than increasing the precision of peak estimation for the HRF (See **Figure 3.2**). In most applications of fMRI a temporal resolution of approximately 2-3 seconds is often sufficient to estimate the BOLD response.

Regarding spatial resolution, fMRI is constrained by the speed of acquisition (i.e. temporal resolution) and the physical limitations of the MRI system, such as the strength of the static field and the amplitude of the applied magnetic field gradients. An additional consideration is the speed of gradient switching, which is not only limited by the physical capabilities of the system, but also by the energy deposition caused by the fast switching on and off of gradients, which may cause peripheral nerve stimulation in human participants. For standard MRI systems, fMRI is typically conducted at resolutions of 3 – 5 mm in-plane voxels, while recent developments at high-field MRI have allowed fMRI acquisitions with 0.5 mm in-plane resolution or less (e.g. Zimmermann et al., 2011).

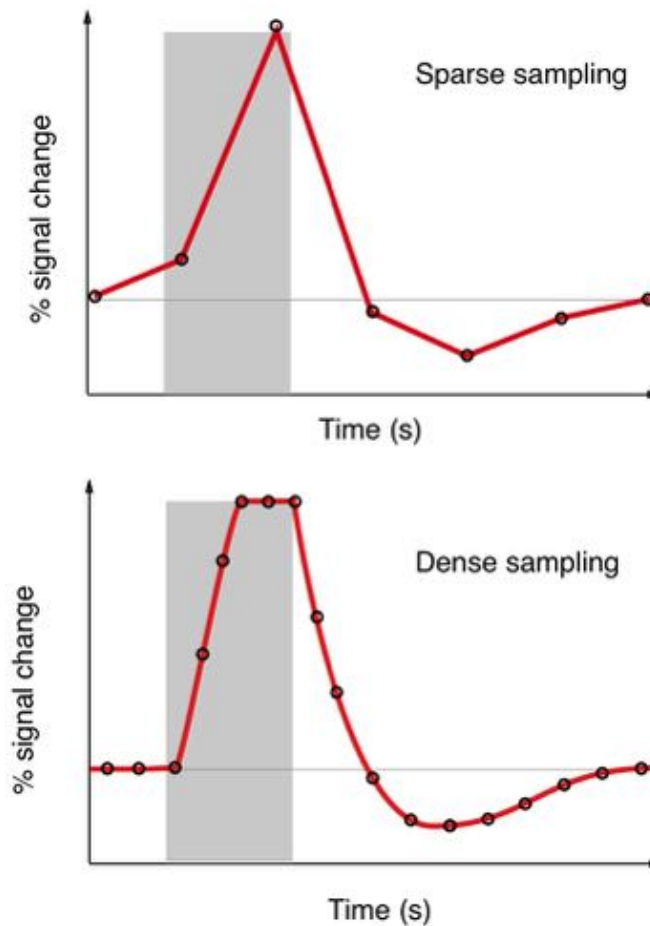


Figure 3.2 Haemodynamic response function with sparse and dense temporal sampling.

3.2.2.1 *Spatial specificity and neurovascular coupling*

A key question to determine the usefulness of fMRI as a research tool is to what degree does BOLD truly reflect neural activity. The spatial specificity of BOLD fMRI has been well characterised in both animal models and humans (see Logothetis, 2002) with good correspondence between the origin of the neural activity and the location of the observed BOLD signal, with a precision that allows functional characterisation of the main morphological features found in cerebral cortex, namely sulci and gyri. As for the neural origin of the BOLD signal, these seem to primarily depend on local field potential of neurons giving rise to the metabolic changes, this being the best predictor of BOLD signal (Logothetis, 2002). This neurovascular coupling allows us to remain confident on the use of BOLD as an accurate proxy measurement of underlying neural activity in healthy participants, although this relationship may be undermined in pathologies or special populations where the vascular system is abnormal.

3.2.3 Mapping the visual system

The study of conscious vision in live humans has been revolutionised by non-invasive techniques such as fMRI allowing the study of cortical responses *in vivo*, while a subject receives visual stimulation. In the following section two major groups of fMRI methodologies are discussed: general linear model experimental designs and retinotopic mapping methods.

3.2.3.1 General linear model (GLM) designs

Most fMRI experimental designs can be classified as either block or event-related designs based on the arrangement of stimulation. In block-design experiments a set of stimuli expected to produce very similar responses is presented serially for a sustained amount of time and then followed by a different set of stimuli or conditions (see **Figure 3.3**).

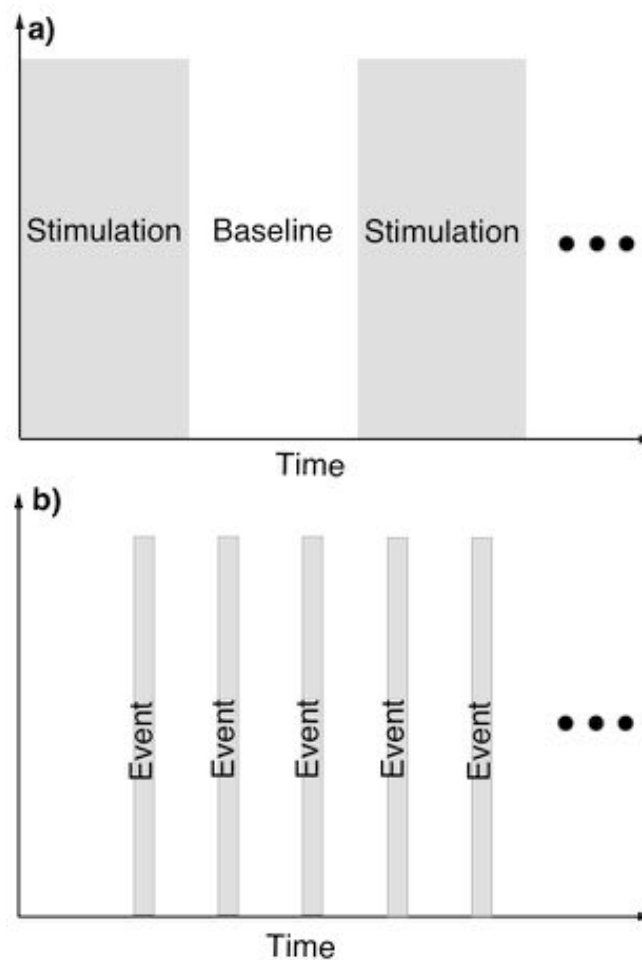


Figure 3.3. GLM designs in task-based fMRI. (a) Block designs depend on a sustained or repeated stimulus for a length of time while (b) event-related designs treat each occurrence of a stimulus as a separate instance.

Block designs aim to maximise the peak BOLD responses during each stimulus set by creating a sustained response throughout the block. Event-related designs on the other hand, rely on a single presentation of a stimulus to elicit a matched response, with different stimulus types presented at various intervals. Event-related designs allow conditions where sequential repetition of a stimulus is not desirable or where the nature of the order of stimulation is crucial to the research question.

Both block and event-related designs rely on the common principles of the general linear model (GLM). In both cases, the GLM is used as a statistical framework for comparing two or more conditions and determining whether these differ in their distributions or not (Friston, 1995b). While GLM methods are rigorous in their assumptions (e.g. statistical independence of observations, normal distribution of observations), it allows for powerful statistical inference and generalisability of the results to the population. These methods are contrasted to those described in the next section, of methods making no assumptions regarding the distribution of the data or group-generalisability of its results.

3.2.3.2 Retinotopic mapping

A commonly used fMRI procedure for vision research is phase-encoded retinotopic mapping, where sequential visual stimulation allows the topographical delineation of visual space representations in brain areas. Large parts of the occipital cortex, as well other visually responsive cortical and sub-cortical structures, are organised retinotopically – adjacent groups of neurons represent adjacent parts of visual space. In order to achieve this, visual space is encoded along two dimensions: polar angle, the angular position of a stimulus around the centre of fixation and eccentricity, the linear distance between the stimulus and the centre of fixation. The aim of retinotopic mapping is to sequentially stimulate along each of these dimensions to create an organised 'travelling wave' of activity along the polar or eccentricity representations (Engel et al., 1994). To elicit phase representations, a 'wedge' section of a contrast-reversing disc is rotated around the fixation point, covering the whole visual field in a single revolution. To elicit eccentricity representations, an expanding ring section of the same disc is used, moving sequentially from the centre of fixation to the visual periphery.

Both of these procedures produce similar responses through the retinotopically-organised regions that only differ in the phase of onset. As such, the resulting time-series can be interpreted as a series of phase-displaced sine waves, where the phase of a given voxel represents the position of the stimulus in visual space along the probed dimension (Serenó et al., 1995; DeYoe et al., 1996; Engel et al., 1997). This approach, allows the estimation of retinotopic organisation on the cortical surface of visually responsive regions and subsequently the delineation of visual regions based on their retinotopic properties (see

Figure 3.4). A recent development in retinotopic mapping has been the advent of population receptive field (pRF) mapping. pRF mapping relies on a model-based approach to estimate not only the polar and eccentricity representations but also the receptive field size for neurons contained in each sampled voxel (Smith et al., 2001; Dumoulin & Wandell, 2008). In brief, the pRF approach relies on creating a model of the stimulus aperture at every point in time during fMRI acquisition, which is then used to create a 'search space'; a set of possible pRF sizes for every point of space stimulated. The resulting combinations are then convolved with an estimate of the haemodynamic response function to create a predicted BOLD signal and compared to the actual data. By a process of parameter modelling, the best-fitted prediction is calculated for every voxel sampled. Such a method may be used to estimate retinotopic maps, as well as pRF size and cortical magnification factors, among others. This pRF mapping approach has been applied to study receptive field characteristics in both neurotypical and clinical populations (Wandell & Winawer, 2015).

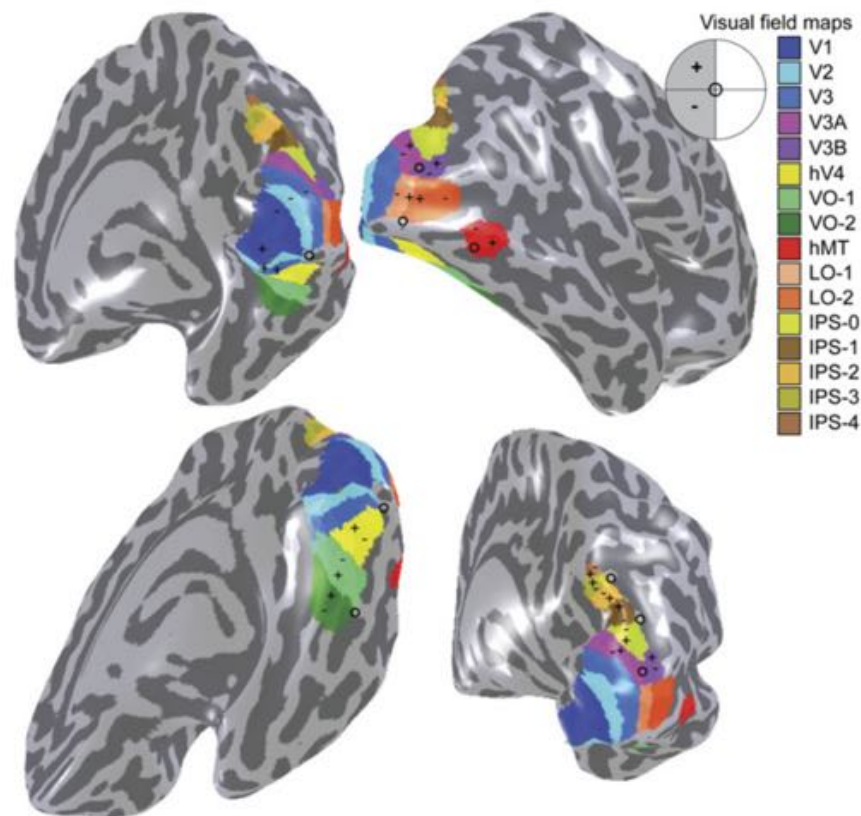


Figure 3.4 Major visual regions of the human occipital cortex as identified by retinotopic mapping, displayed on an inflated cortical surface render. Fovea indicated by “o” and upper and lower visual field representations indicated by “+” and “-”, respectively. Adapted from Wandell et al. (2007).

3.3 Diffusion-weighted MRI

A recent development in magnetic resonance techniques, diffusion-weighted MRI (dMRI) provides a window into the white matter structures that sustain the network of cortical and sub-cortical regions. At present, dMRI is the only technique available for mapping the white matter architecture *in vivo* (Jones et al., 2012) and is therefore of interest here to explore the anatomy and microstructure of connections between visual regions. This section discusses the physical and imaging principles on which dMRI operates, current models of neuroanatomical diffusion and their use in examining the structural organisation of the visual system.

3.3.1 Diffusion-weighted imaging

Diffusion MRI relies on its sensitivity to molecule displacement, specifically to the displacement of water in biological tissues (Le Bihan et al., 2001). Due to the influence of thermal energy, water suspended in a given medium diffuses randomly, an effect known as Brownian motion (Beaulieu, 2002). This displacement is described by Einstein's equation:

$$\langle r^2 \rangle = 6Dt \tag{Eq. 3.1}$$

Where the mean squared displacement of molecules is proportional to the time since onset (t) and a constant, the diffusion coefficient of free water (D). In an unrestricted medium, we expect water to displace equally in all directions. In contrast, when water molecules find themselves in a restricted environment, such as intra- and extra-cellular space in tissue, they are not able to move freely (**Figure 3.5**). In isotropic tissues, where the physical impedance is equal in all directions, water molecules will displace equally in all directions, in a reduced manner. If the tissue has an ordered structure, such as cerebral white matter, where fibres have a parallel, directional arrangement, it is deemed an anisotropic medium, and molecules will diffuse preferentially along the axis of the fibre directions, where the physical impedance is lowest.

This differential displacement, isotropic and anisotropic diffusion of water molecules in tissue, is the main signal captured by dMRI methods. In order to be sensitive to displacement of water molecules, an MRI sequence incorporates a magnetic gradient creating a phase-shift in the precession of water protons. Following a time interval to allow water molecules to diffuse, an equal but opposite refocusing gradient is applied, restoring

the phase-shift to its original position. If molecules within a voxel are stationary, or only diffuse within the voxel, the signal will be identical between a diffusion-weighted acquisition and the same sequence without a diffusion gradient applied. However, if water molecules have diffused along the direction of the gradient between the original and the re-focusing gradients, their de-phasing is not countered and therefore a loss of signal is observed. By comparing the magnitude of the signal with and without the gradient pulses, the portion of de-phasing caused by the diffusion of water molecules can be measured (Jones et al., 2012). This procedure is then repeated by applying the diffusion gradients along multiple directions, to estimate the directionality of diffusion in the sampled volume and thus inference of the likely orientation of the underlying tissue structure.

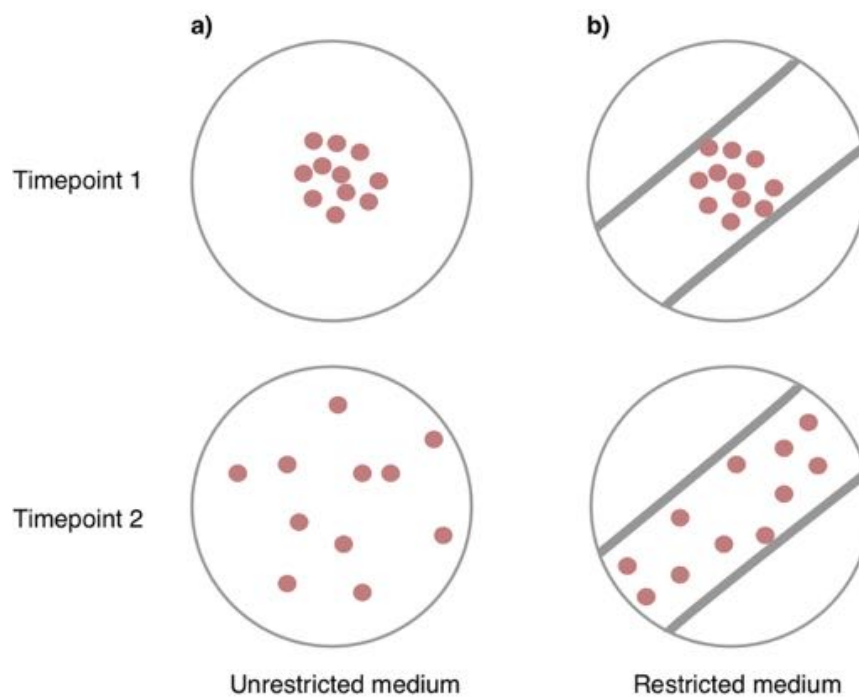


Figure 3.5 (a) In an unrestrictive medium, thermal noise will induce water molecules to diffuse equally in all directions. (b) In the presence of a restrictive medium, such as axonal tissue, water diffusion is restricted orthogonal to the fibre orientation but not parallel to the axonal fibres.

The relationship between the diffusion-sensitising magnetic gradient and the signal observed during a dMRI acquisition is described by the Stejskal-Tanner equation (Stejskal & Tanner, 1965);

$$\frac{S}{S_0} = e^{-bD} \tag{Eq. 3.2}$$

Where the difference in signal strength between a diffusion-sensitised acquisition (S) and the equivalent acquisition without a diffusion-sensitising magnetic gradient applied (S_0) is given by the diffusion coefficient (D) and a b-factor which incorporates the dMRI magnetic gradient terms, where;

$$b = \gamma^2 G^2 \delta^2 \left(\tau - \frac{\delta}{3} \right) \quad (\text{Eq. 3.3})$$

The b-factor is composed of the gyromagnetic ratio (γ) and the three main parameters that may be manipulated in a dMRI acquisition; the amplitude of the diffusion gradient (G), the duration of the gradient (δ) and the time interval between the initial labelling gradient and the re-focusing gradient (τ). By altering these three factors; gradient amplitude, duration and interval, a dMRI acquisition may be optimised to maximise the signal intensity difference generated by the application of the diffusion gradient.

The maximum recoverable signal from a dMRI acquisition is limited by similar considerations as in fMRI, namely the strength of the static field, amplitude and speed of magnetic field gradients and the induction of peripheral nerve stimulation. One additional consideration in dMRI is the inverse relationship between signal intensity and signal to noise ratio. As the b-factor increases, a larger proportion of water molecules are labelled by the diffusion-sensitising magnetic gradient, leading to a greater signal difference between the diffusion-sensitised and reference images. While this translates to effectively greater diffusion signal intensity, it is also concomitant with a reduction in signal to noise ratio. Most current dMRI sequences aim to enhance signal intensity while maintaining an acceptable level of signal to noise ratio (Jones et al., 2012).

3.3.2 Modelling diffusion

In recent years, various mathematical models have been proposed to describe the diffusion of water molecules in dMRI data. In this section, we will review two such models; first, the most common model of water diffusion, the diffusion tensor and second, constrained spherical deconvolution, a more advanced model implemented in subsequent chapters for the purposes of white matter tractography.

3.3.2.1 The diffusion tensor

The diffusion tensor is a mathematical description of water diffusion in three dimensions (**Figure 3.6**). It describes diffusion as occurring along three orthogonal directions, or eigenvectors ($\lambda_1, \lambda_2, \lambda_3$), with independent diffusion coefficients for each component (v_1, v_2, v_3). An isotropic voxel would therefore have equal magnitude along the three

eigenvectors, while an anisotropic voxel would have larger magnitude along at least one direction (Le Bihan et al., 2001).

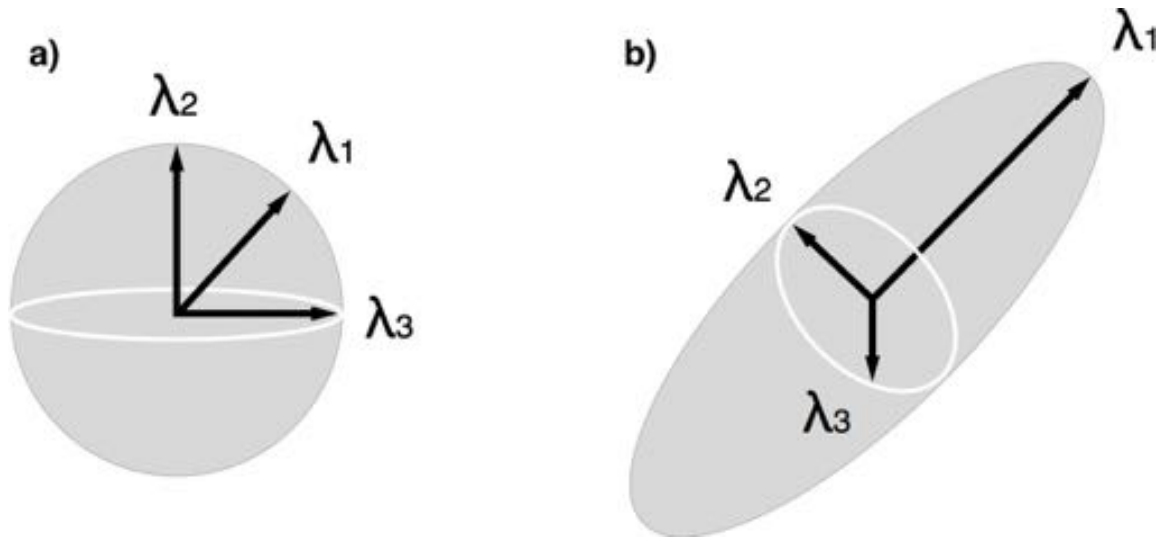


Figure 3.6 Two diffusion tensors describing (a) isotropic and (b) anisotropic diffusion. Note the length of principal eigenvectors are equal when diffusion is isotropic, whereas in anisotropic diffusion, the first eigenvector describes the principal direction of diffusion.

From the diffusion tensor description of any given voxel, we can derive a measure of the average level of diffusion, or mean diffusivity (MD):

$$MD = \frac{\lambda_1 + \lambda_2 + \lambda_3}{3} \quad (\text{Eq. 3.4})$$

Mean diffusivity is a rotationally invariant measure, representing the overall magnitude of diffusion. In order to quantify directional diffusivity, two further measures are used; axial diffusivity:

$$ADC_{||} = \lambda_1 \quad (\text{Eq. 3.5})$$

Which is the diffusivity along the principal direction of the diffusion tensor and radial diffusivity:

$$ADC_{\perp} = \frac{\lambda_2 + \lambda_3}{2} \quad (\text{Eq. 3.6})$$

Derived from the average diffusivity of the two directions orthogonal to the principal direction of diffusion. Finally, a measure of the degree of anisotropy in the diffusion tensor is derived as follows:

$$FA = \frac{\sqrt{3((\lambda_1 - \bar{\lambda})^2(\lambda_2 - \bar{\lambda})^2(\lambda_3 - \bar{\lambda})^2)}}{\sqrt{2(\lambda_1^2 + \lambda_2^2 + \lambda_3^2)}} \quad (\text{Eq. 3.6})$$

Where fractional anisotropy (FA) is a value ranging from 0 to 1, where 0 is perfect isotropy and 1 is perfect anisotropy. Both FA and MD are established biomarkers for tissue microstructure, used to characterise parameters of interest such as tissue integrity, myelination, and oedema (Ciccarelli et al., 2008).

The diffusion tensor model has been widely used in dMRI in the past decade (for a review, see Dell'Acqua & Catani, 2012) and is the most common method of modelling diffusion in the brain. Despite this, the tensor model is relatively simple and does not account for the complexity of the signal observed in dMRI; in particular the 'crossing fibres' scenario, where one voxel contains two or more fibre bundles oriented along different directions. Since the diffusion tensor model only accounts for one principal direction, it cannot incorporate multiple fibre information (Basser et al., 2000; Behrens et al., 2003). In order to circumvent this problem, various models have been proposed, incorporating multiple principal directions in the description of diffusion patterns (e.g. Parker et al., 2003, Tuch 2004; Behrens et al., 2007). In the following section, we describe one such model; constrained spherical deconvolution.

3.3.2.2 *Constrained spherical deconvolution*

First proposed by Tournier et al. (2007), constrained spherical deconvolution (CSD) is a mathematical approach to modelling the dMRI signal observed at each voxel, that goes beyond the simple diffusion tensor. More specifically, CSD aims to estimate the underlying fibre population within the voxel without making prior assumptions about the number or nature of fibre populations present in the voxel, unlike other multi-fibre methods (for examples, see Tuch, 2004; Behrens et al., 2007).

The foundation of CSD centres on the concept of a fibre orientation distribution (FOD). Mathematically, the FOD is a continuous distribution over a sphere, where each point represents a possible fibre orientation. By estimating multiple fibre orientations, the FOD

provides a measure of relative weighting of fibre populations on a spherical representation at each voxel. Thus, the FOD can be used to estimate the likely path of a fibre population across multiple voxels, enabling tractography algorithms to be applied, while also incorporating multiple fibre orientations at each voxel (Tournier et al., 2004).

In spherical deconvolution (SD), the FOD is estimated by first describing the response function of a single fibre population in white matter. The response function is equivalent to the dMRI signal measured in voxels containing a single fibre orientation. Practically, this is achieved by sampling the data from voxels in deep white matter with large FA values (e.g. $FA > 0.7$ in healthy adults). Next, the FOD is estimated by performing spherical deconvolution, a mathematical decomposition procedure, of the response function from the observed dMRI data at each voxel (see **Figure 3.7**). The aim of this procedure is to recover the underlying fibre populations without *a priori* assumptions regarding the number or orientations of fibres.

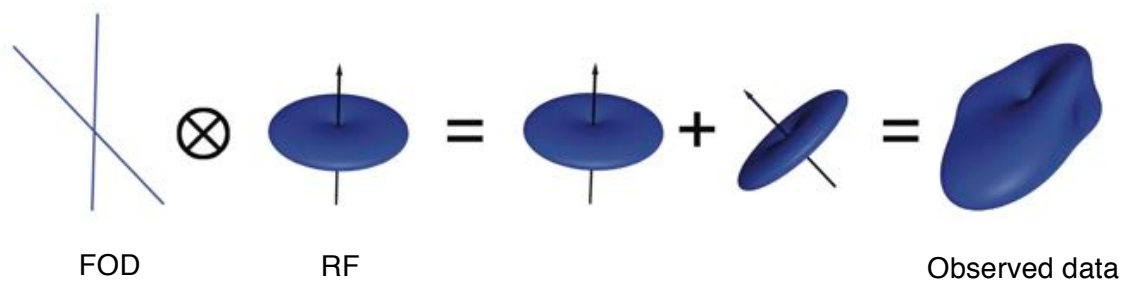


Figure 3.7 Graphical representation of spherical deconvolution. The fibre orientation distribution (FOD) is the product of a convolution of response functions along one or more fibre orientations, which can be extracted from the observed dMRI data. Adapted from Seunarine & Alexander (2009).

It should be noted that the FOD is limited by the noise present in the dMRI data itself, with two major issues arising; FOD negative lobes and angular resolution constraints. The presence of noise in the data can lead to negative values in the reconstructed FOD, which are physically impossible. In order to eliminate these spurious FOD elements, a non-negative constraint is added to the SD model, leading to *constrained* spherical deconvolution (CSD). Therefore, CSD is more robust to noise when compared to SD (Tournier et al., 2007). Secondly, the angular resolution of the FOD, that is, the minimum angle between two fibre orientations that can be resolved, is limited by the smoothness of the dMRI data (Tournier et al., 2012). In order to limit the angular resolution of the FOD to a value that can be estimated given the data constraints, a maximum angular frequency harmonic order term (l_{max}) is incorporated into the model. The maximum harmonic order is

determined by the degrees of freedom afforded by the data, equivalent the number of independent time points acquired:

$$l_{\max} = \frac{1}{2}(n+1)(n-1) \quad (\text{Eq. 3.7})$$

In the case of most HARDI (high angular resolution diffusion imaging) acquisitions, with approximately 50-60 diffusion-weighted volumes acquired, this value approximates $l_{\max} = 8$.

3.3.3 White matter tractography

Tractography is a 3D modelling technique, which reconstructs continuous, long-range white matter pathways from the local estimates of fibre orientations obtained from a diffusion model (Jones et al., 2012). The aim of tractography is to provide a virtual representation of the pathways and fascicles present in the neuroanatomy, *in vivo* and non-invasively. Indeed, this technique has seen prolific use for understanding anatomy, development and in numerous clinical applications (Ciccarelli et al., 2008).

As a modelling technique, tractography relies on a computer algorithm to trace paths across many voxels that follow the orientations at each voxel, called streamlines. As tractography exploits directional information, a model of the diffusion orientation at each voxel must first be obtained, be it the diffusion tensor or a more complex model. Secondly, the directional information is then interpolated into sub-voxel space, allowing the tractography algorithm to sample incremental steps, typically in the 0.1 – 1mm range (Hagmann et al., 2006). This step typically involves some degree of Gaussian smoothing to ensure contiguous orientation profiles in the sub-voxel space. Finally, the directional information across voxels is joined to create streamlines. Algorithms differ in the exact way this is achieved, but as general rule, they perform a step-wise progression where the continuous direction of a streamline is informed by the directional information in the present voxel; as the streamline moves into a new voxel, the directional information re-directs the streamline path (see **Figure 3.8**). Tractography algorithms in dMRI can be broadly classified under two groups; deterministic and probabilistic tractography. Deterministic tractography performs a streamline tracing procedure once for each voxel in the volume of interest. This is a typical approach to tractography with a diffusion tensor model, as a single orientation is provided at each voxel and therefore streamline tracing from a given voxel will have a unique solution. In probabilistic tractography, a multi-fibre model is used to provide more than one possible solution to streamline tracing in a single voxel. The orientation information at each voxel is a probability function, where streamline tracing is applied multiple times in to create a set of possible streamlines. This approach exploits the multiple

orientation information of more complex models, such as CSD, to reconstruct the presence of crossing fibres.

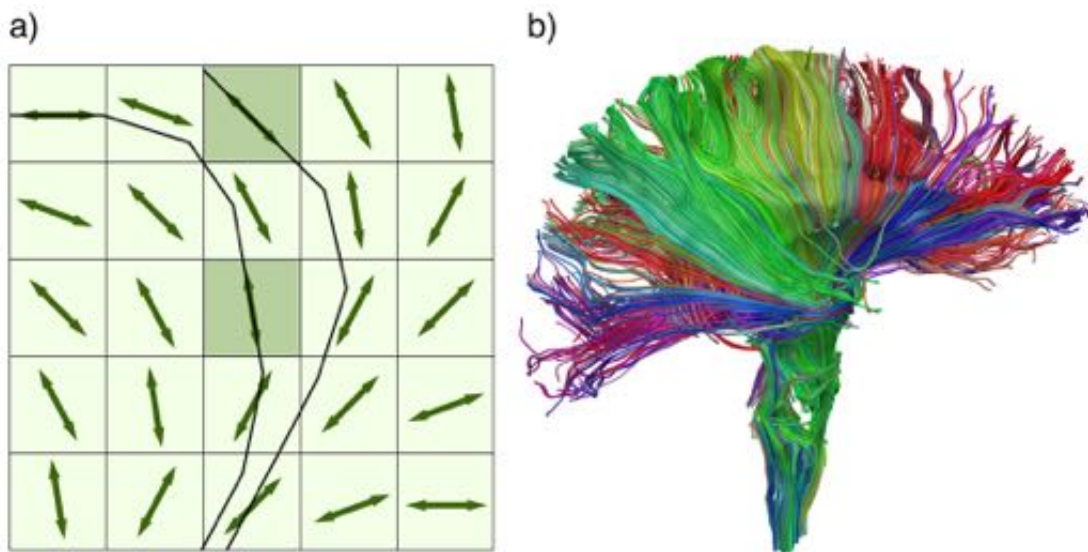


Figure 3.8 (a) Diffusion tensors at each pixel represent the principal direction of diffusion, which can be used to reconstruct the most likely path of white matter fibres with continuous streamlines. This example of deterministic tractography shows two streamlines generated from the dark pixels, with paths informed by the oriented tensor in each successive pixel. (b) This approach is used to generate reconstructions of white matter fascicles, such as the corpus callosum and corticospinal tract shown here.

Tractography methods also differ in their application, particularly how white matter pathways and fasciculi are reconstructed; two common applications are seed-based and whole-brain tractography. Seed-based approaches refer to an implementation of tractography where the streamline generation procedure is started from a sub-set of voxels within the dataset, a 'seed' region. The streamlines then propagate throughout the volume, typically reconstructing one or more specific white matter structures of interest. A whole-brain approach, in contrast, uses every voxel in the dataset as its seed region, tracing every white matter pathway and therefore creating a reconstruction of the whole brain, which can then be digitally dissected to select the structures of interest. The choice of tractography algorithm is typically informed by both the experimental question at hand and data acquisition limitations. In subsequent chapters probabilistic, seed-based tractography is applied to explore the anatomical organisation and microstructure of the visual system.

Chapter 4

Optimisation of population receptive field mapping in fMRI

4.1 Abstract

Population receptive field (pRF) mapping is a novel approach for measuring aggregate human visual receptive field properties from non-invasive signals detected using functional MRI. Direct estimation of receptive field properties in humans, both healthy and in conditions affecting the visual system such as albinism, were previously limited to invasive electrophysiological methods. With the introduction of pRF mapping, it is now possible to obtain *in vivo* estimates of receptive field properties in human visual cortex and localise such signals to functionally distinct visual areas. While recent studies have focused on the development and application of pRF methods in healthy individuals, little attention has been paid to the possible application pRF mapping in disorders of the visual system. This chapter focuses on the development of optimal stimuli configurations for pRF mapping that maximise signal-to-noise while reducing MRI acquisition time, making them suitable for use in a clinical population, such as albinism.

4.2 Introduction

The visual receptive field (RF) of a neuron is the area of the visual field upon which stimulation causes a response. Due to the retinotopic organisation of cortical visual field maps, selective responses to visual stimulation can be studied non-invasively in humans at a coarser resolution using functional magnetic resonance imaging (fMRI) (for a review, see Wandell & Winawer, 2011). In visual field mapping studies carried out in the 1990s, responses to systematic stimulation of the visual field were used to define the organisation of retinotopic maps in human cerebral cortex (Engel et al., 1994; Sereno et al., 1995; DeYoe et al., 1996; Engel et al., 1997). By calculating the phase-difference between a periodic visual stimulus presentation and fMRI signals recorded from occipital cortex, it was possible to estimate the position in visual space eliciting maximal responses at each cortical location (voxel). This in turn allowed the localization and delineation of different retinotopic visual field maps according to their polar angle and eccentricity representations (Wandell et al., 2007; Bridge, 2011).

While these methods are effective in localizing and delineating different retinotopic areas, they do not allow us to probe the underlying characteristics of the RFs of individual neurons, such as the tuning curve, size, or shape. To date, such characteristics can only be directly measured by invasive electrophysiological recordings. However, the signal captured by fMRI methods pools together the haemodynamic responses associated with activation of hundreds of thousands of neurons in a single voxel, so in visually responsive cortex the

signal from specific locations will reflect a complex aggregate of the properties of individual RFs. As visual cortex is organised retinotopically, at the spatial scale of fMRI methods these responses will reflect characteristics of many neurons encoding a common area of visual space, hence the concept has arisen of a population receptive field (pRF). Originally coined in electrophysiology (Victor et al., 1994), a pRF refers to the aggregate properties of a large number of neighbouring neurons, that by their topographic organisation share common features, such as responsiveness to stimulation to a given visual field location. Early work studied cortical pRFs indirectly; either by varying stimulus size to infer the cortical image point spread (Tootell et al., 1997), or by accounting for the responses of sampled voxels beyond the stimulus cycling frequency using a data-fitting approach to estimate the relative proportion of time a given voxel was active during stimulation, or duty cycle (Smith et al., 2001). Later work developed an explicit model-based approach, where the area of visual space that elicits responses in a single voxel is modelled as a Gaussian function (Larsson & Heeger, 2006). To do this, a simulated time series of the hypothetical fMRI signals given a certain receptive field profile is compared against the experimentally observed time series. By comparing multiple combinations of receptive field properties (e.g. location, spread) with the observed data, a best-fitting pRF model is obtained for each cortical location. Model frameworks for estimation of pRFs now integrate an array of visual stimulation scenarios and model components, allowing not only visual map localization but also the estimation of other parameters such as pRF size and cortical magnification factors (Dumoulin & Wandell, 2008; Harvey & Dumoulin, 2011).

Model-based approaches to estimating pRF characteristics allow the study of pRF dynamics (Haak et al., 2012; Zuiderbaan et al., 2012), the properties of striate (Verghese et al., 2014; Kok & de Lange, 2014), and extra-striate visual areas (Amano et al., 2009; Winawer et al., 2010; Harvey & Dumoulin, 2011; de Haas et al., 2014; Dumoulin et al., 2014; Kay et al., 2015; Puckett & DeYoe, 2015) as well as abnormal visual field representations in developmental disorders (Schwarzkopf et al., 2014) and disease (Baseler et al., 2011; Hoffmann et al., 2012; Brewer & Barton, 2014; Papanikolaou et al., 2014). Despite the growing popularity of this approach, it is currently unclear whether there is an optimal stimulus design for pRF estimation, and whether there are inherent biases in certain stimulus configurations.

In the seminal paper by Dumoulin and Wandell (2008) a combination of stimuli are used, including a polar angle wedge and eccentricity ring stimuli, as traditionally used in phase-encoded retinotopic mapping (Serenio et al., 1995; DeYoe et al., 1996; Engel et al., 1997), with the addition of a size-invariant bar traversing the visual field linearly along multiple orientations. The use of a moving bar aperture has been widely adopted, with many studies implementing it alone (Harvey & Dumoulin, 2011; Zuiderbaan et al., 2012; Brewer & Barton, 2014; de Haas et al., 2014; Dumoulin et al., 2014; Papanikolaou et al., 2014; Schwarzkopf

et al., 2014; Verghese et al., 2014). Despite this ready adoption, it remains unclear whether the use of a size-invariant bar aperture is optimal for pRF mapping. Binda et al. (2013) examined whether stimulus design created inherent biases in receptive field estimation in the neighbourhood of scotomas. When examining both bar and multifocal stimuli, that is, a stimulus where checkerboards segments are presented in pseudo-randomised groups in order to reduce the correlation between any given pair of segments, they concluded that both bar and multifocal designs biased pRF estimates when a virtual scotoma was introduced. Notably, these biases were reduced by actively modelling the scotoma in a multifocal design, but not in a bar stimulus design, pointing to biases in model estimation interacting with stimulus choice.

The choice of stimulus design is not only important to the accurate estimation of pRF properties, but also for the application of the method beyond healthy adults with normal vision. Visuotopic mapping experiments typically require participants to both maintain fixation on a central target and minimise movement for the duration of the MRI scan. Both of these aspects may be difficult for patients groups, particularly as both fixation stability and the ability to keep still decay with the duration of the MRI scan. Therefore, a stimulus optimised to elicit adequate signal-to-noise while maintaining a short scan duration is highly desirable for implementing pRF mapping in a clinical population such as albinism.

Stimulus optimization has previously been reported in phase-encoded retinotopic mapping methods, with various configurations proposed depending on the experimental question at hand (e.g. Tootell et al., 1997; Slotnick & Yantis, 2002). More recently, multifocal stimuli have been used as a way of boosting precision in retinotopic localization (Buracas & Boynton, 2002; Hansen et al., 2004; Vanni et al., 2005; Henriksson et al., 2012), but with significantly reduced explanatory power (Ma et al., 2013). In pRF modelling, Binda et al. (2013) report a similar reduction in power of a multifocal stimulus compared to sweeping bars, albeit with the additional finding that bars returned larger pRF sizes compared to the multifocal stimulus, highlighting a trade-off in pRF stimulus design that has yet to be studied systematically. In the present study, we investigated the effects of two design variables; eccentricity scaling and the use of stimuli defined in polar (simultaneous wedge and ring) vs. Cartesian (bars) coordinates on pRF model estimates. Multi-aperture stimulus designs, which include multifocal stimuli and the novel simultaneous wedge and ring stimulus used here, have not been previously explored in terms of pRF mapping efficiency, despite a theoretical advantage for them in terms of efficiency with which the pRF is measured. By definition, single aperture stimuli, such as sweeping bars, can only measure one stimulus dimension at a time. During the same time it takes the bar to sweep along a full set of directions, a traditional wedge or ring stimulus can collect several cycles thus potentially increasing the reliability with which that dimension is mapped. By further combining wedge and ring stimuli and presenting them simultaneously, both polar angle

and eccentricity coordinates can theoretically be estimated multiple times. The added value of a multi-aperture display can therefore improve the sampling rate of polar coordinate-defined stimuli towards increased stimulus efficiency. Here we compared three stimulus configurations to assess their relative efficiency for pRF mapping; a size-invariant sweeping bar as implemented in Dumoulin and Wandell (2008), a similar version of the stimulus that scaled logarithmically with eccentricity and a new polar coordinate-based simultaneous wedge and ring stimulus. This work presents an optimised stimulus configuration for accurate parameter estimation and reduced scan time, enabling pRF mapping in clinical and special populations.

4.3 Materials and methods

4.3.1 Participants

Eight healthy adults (6 males and 2 females, age range: 23-36) took part in the study. All participants were healthy, had normal or corrected-to-normal visual acuity, and provided written informed consent. The study was approved by the local ethics committee.

4.3.2 Stimulus design

Stimuli were generated in MATLAB (v8.0, Mathworks Inc., Natick, MA, USA) using Psychtoolbox (v3.0, Brainard, 1997; Pelli, 1997) and displayed on a back-projection screen in the bore of the magnet via an LCD projector. Participants viewed the back-projection via a mirror mounted on the head coil. The visual display subtended a maximum visual angle of 16° eccentricity from fixation for two participants and 9° eccentricity for a further six participants, in order to test the effects of viewing distance on estimates of stimulus eccentricity. All further stimuli measures are given for the large display area; the measures for the smaller display area were simply scaled down.

All three stimulus configurations shared the same underlying high-contrast carrier pattern but differed only in the arrangement of apertures revealing portions of the pattern. The pattern was defined by the following function;

$$I(x, y) = \sqrt{x^2 + y^2} \cos \left\{ \frac{2\pi(\sin\frac{\delta\pi x}{180} + \cos\frac{\delta\pi y}{180})}{4} + \theta \right\} \quad (\text{Eq. 4.1})$$

Here I is the pixel intensity at coordinates x and y relative to the centre of the screen, and the other parameters, θ and δ , configure the phase and spatial frequency of the pattern. The θ parameter varied across time from 0 to 4π in 72 equal steps of 32 ms duration and thus completed one cycle approximately every 1.15 s. The final parameter, δ , was a function of θ , given by;

$$\delta = \frac{\sin \theta}{4} + \frac{1}{2} \quad (\text{Eq. 4.2})$$

Pixel intensities, I , were then rectified such that all positive values were set to maximum luminance and all negative and zero values were set to minimum luminance. We then bounded each resulting frame within a circular region with radius 16° by setting all pixels outside that radius to mean luminance. Within a short band (12 pixels in width) at the fringes of the patterned region we scaled the contrast of each pixel linearly with distance from the centre to produce a blurred contrast edge.

The carrier therefore consisted of a dynamic, high-contrast pattern within a disc with radius 16° comprising square tessellated blocks 2.67° in diameter. Each block contained a drifting 'ripple-like' pattern of concentric shapes that varied across time in spatial frequency and phase. The motion in adjacent blocks thus varied in a checkerboard-like fashion between expansion and contraction. Finally, the overall orientation of the pattern was varied across trials in the experiment (see details below). Because of the motion energy, the square-wave luminance modulation, and the varying spatial frequencies, this pattern was very broadband to ensure maximal stimulation of visually responsive neurons (see **Figure 4.1**). The mean luminance of the stimulus was 775.05 cd/m^2 .

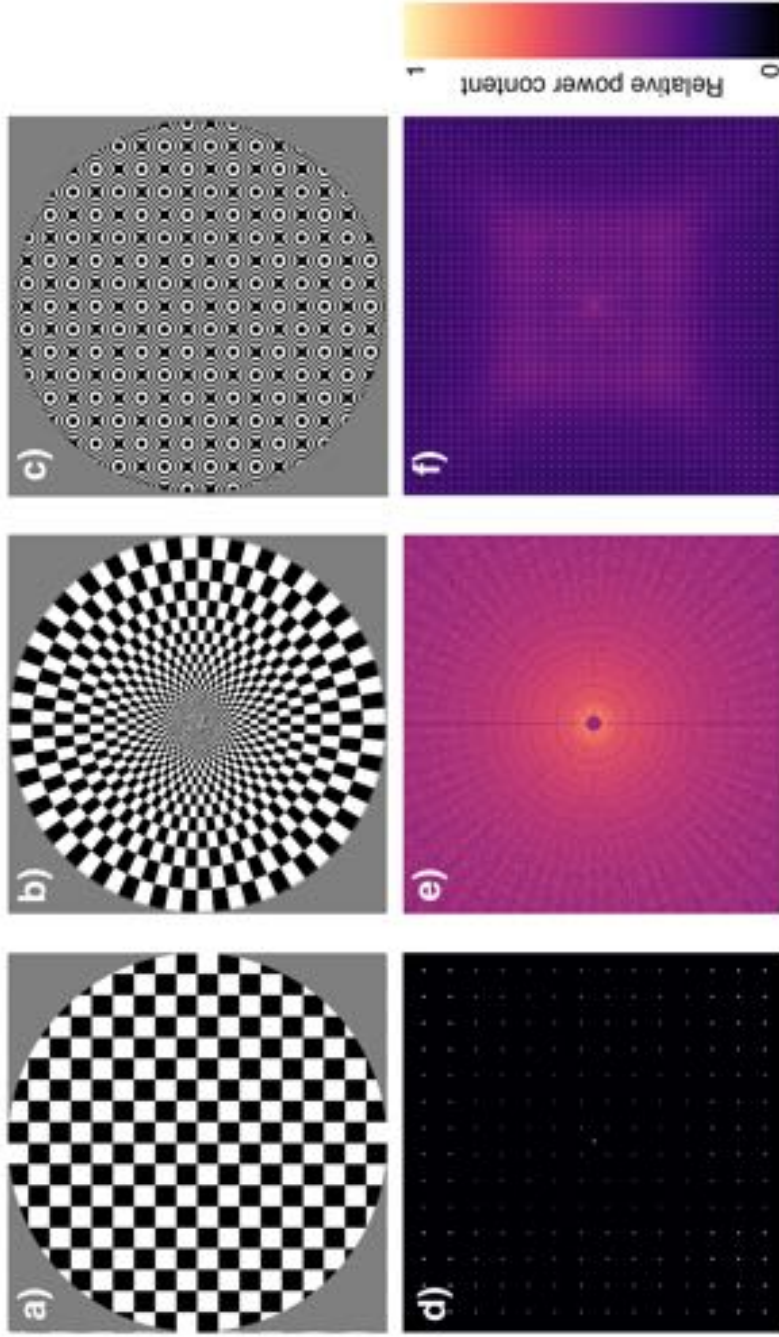


Figure 4.1 Three high-contrast checkerboard and pseudo-checkerboard stimuli, and their 2-dimensional Fourier transforms. (a) linear checkerboard, (b) radial checkerboard and (c) pseudo-checkerboard described in section 4.3.2, with their respective (d-f) 2D Fourier transforms, showing power content across spatial frequencies (arbitrary units). In image space (a-c) axes correspond to X and Y coordinates, while in Fourier space (d-f), the eccentric dimension corresponds to spatial frequency and the radial dimension to orientation. Note a linear checkerboard selectively samples resonant spatial frequencies, while the radial checkerboard is biased towards high power for low spatial frequencies and low power for high spatial frequencies. The pseudo-checkerboard is a broadband stimulus with homogenous power sampling across the Fourier space, conferred by varying spatial frequency in time, as displayed in **Figure 4.2**

While the conventional checkerboard design is used commonly in the literature, its implementation here would result in unwanted differences with regard to spatial frequency information between conditions, different low-level stimulus attributes, edge artefacts and energy confounds. For example, a standard ‘dartboard’-type polar checkerboard provides higher spatial frequency stimulation in the central visual field compared to the periphery. In addition, using such a carrier stimulus with bar apertures results in an apparent ‘swaying’ motion percept. Similarly, a Cartesian checkerboard displayed under bar apertures results in edge artefacts and different energy contents at various aperture positions. In order to compare bar stimuli with the simultaneous wedge and ring stimuli in a more balanced way, we implemented the broadband stimulus described above, affording greater homogeneity in spatial frequency. Virtually any stimulus content that drives visual responses may be used to sample retinotopic properties, with more complex stimuli such as natural scenes may be more effective in localizing higher visual areas (Saygin & Sereno, 2008; Huang & Sereno, 2013). Here, we have favoured a checkerboard-like pattern with homogenous spatial frequency distribution across eccentricity to remain as close as possible to the standard checkerboard pattern as possible while being matched as closely as possible between the three experimental conditions.

All three stimulus configurations contained the carrier pattern described above, but presented through different aperture configurations that clipped the stimulus pattern accordingly (see **Figure 4.2**). The first stimulus configuration comprised a single, bar aperture of constant size drifting along four possible directions. Each trial consisted of a bar sweep along a given direction, a second sweep along its orthogonal direction and a blank period of mean luminance grey background. This was followed by a second trial for which the direction of motion was reversed. We conducted a total of two trials per run. Each sweep of the bar aperture encompassed 24 volumes and each blank period 24 volumes, totalling 144 volumes per run. Two types of runs were conducted, one with stimulus sweeps along cardinal axes (0° , 90°) and one along oblique axes (45° , 135°). We collected two runs with opposite sweep directions for each type.

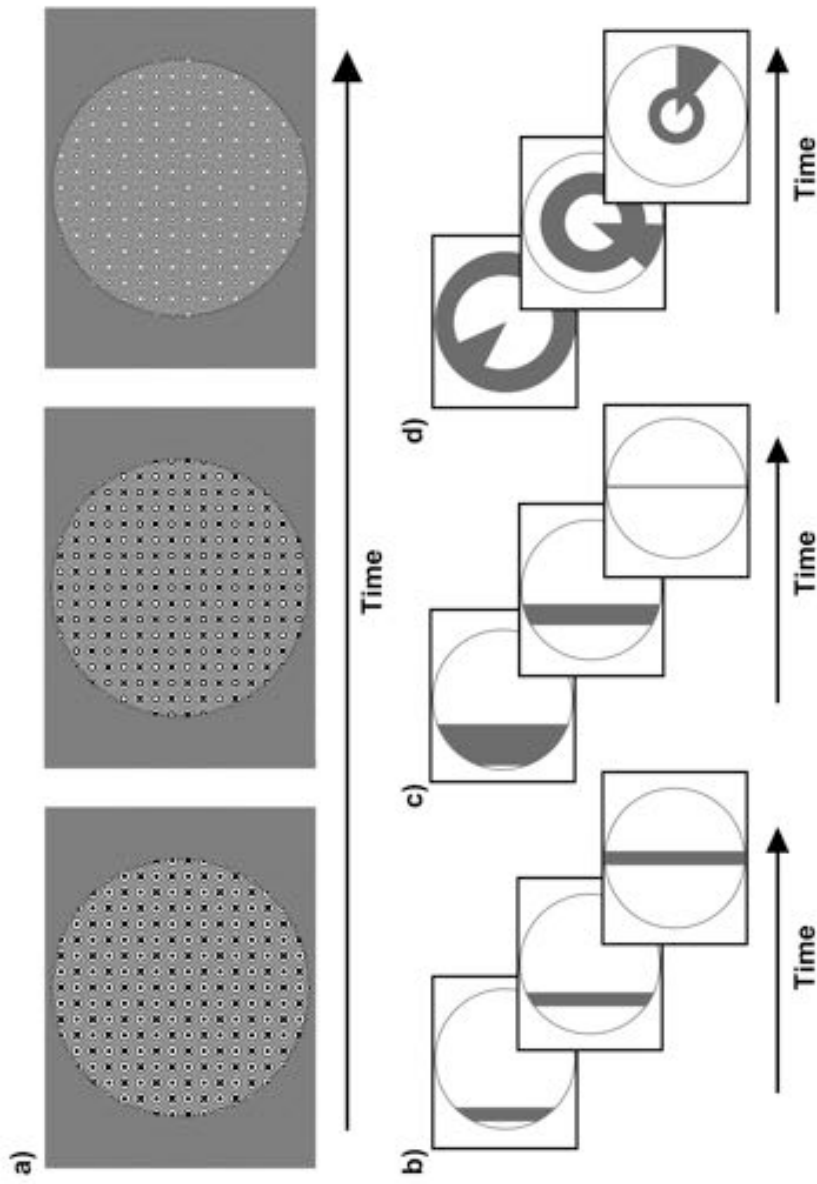


Figure 4.2 (a) Example frames from the stimulus carrier, a checkerboard-like, luminance-modulated pattern varying in spatial frequency, described in full in the methods section. Stimuli were presented with either (b) size-invariant bar apertures, (c) bars logarithmically-scaled with eccentricity or (d) a simultaneous 'wedge and ring' aperture, cycling at different frequencies and scaled logarithmically with eccentricity. Again, example frames are shown for each stimulus type.

In addition to the bar stimulus, we further explored the effects of bar aperture scaling in a sub-set of participants. Four of eight participants viewed an additional stimulus configuration consisting of bar apertures varying in width logarithmically according to their eccentricity to account for cortical magnification in visual cortex (Cowey & Rolls, 1974; Rovamo & Virso, 1979). Bar width varied from 0.06° at fixation to 9.01° at maximal periphery. Again, there were runs with stimulus sweeps along cardinal directions and along oblique directions. We collected two runs with opposite sweep directions for each type. Each run again totalled 144 volumes.

Finally, a stimulus configuration defined in polar coordinates comprising a 'wedge and ring' stimulus was presented. This consisted of two simultaneously presented apertures; one triangular ('wedge'), comprising 18° of the disc circumference, rotating clockwise or counter-clockwise around fixation plus an expanding or contracting annulus ('ring') aperture. The apertures changed position every 2.55s on the onset of each acquired volume. The ring component varied with eccentricity, increasing or decreasing in radius following a logarithmic function, with 50% of overlap between adjacent aperture steps. The wedge component did not vary in size, with 50% overlap between adjacent aperture steps. Both apertures cycled at different frequencies: 20 and 15 volumes were acquired for a single revolution of wedge (6 cycles) and rings (8 cycles), respectively. Two runs of the composite stimulus configuration were presented once in each direction of motion (clockwise/expanding and counter-clockwise/contracting) for 144 volumes each, including 24 mean luminance blank volumes in the final segment of each run. Therefore, a total of 288 volumes were collected, with a mean luminance blank period placed between the runs and a second blank period at the end of the second run.

The overall orientation of the stimulus pattern was determined by the trial condition. During presentation of bars with cardinal orientations (vertical, horizontal), the pattern was not rotated. During presentation of oblique bars, the pattern was rotated 45° . During presentation of the simultaneous wedge and ring stimulus, the pattern was rotated by the same angle as that of the wedge.

Finally, we estimated the individual haemodynamic response function (HRF) of visual cortex for each participant. In an additional run we presented short photic bursts consisting of a full-field (radius 16° visual angle) aperture of the pattern described above. A burst was presented for 1 volume and followed by 11 volumes of mean luminance blank screen. This was repeated 10 times, with a run totalling 120 volumes. In all runs we acquired 4 initial volumes while participants viewed a blank screen with only the fixation dot to allow the fMRI response to equilibrate.

The fixation dot was a blue disc of 0.42° diameter. It was surrounded by a 1° gap of mean luminance grey. Within the inner 0.5° of the mapping stimulus nearest to fixation the stimulus contrast was ramped up linearly. Each imaging run was subdivided into short time bins 200ms in duration. During each of these bins there was a 0.05 probability that the fixation dot would change colour to purple only constrained by the condition that the previous bin did not already contain a colour change. Participants were instructed to maintain fixation at all times and to monitor the fixation dot for colour changes upon which they were to press a button on an MRI-compatible response box.

4.3.3 MRI acquisition and pre-processing

Functional MR images were acquired on a Siemens 3T Magnetom Trio using a 32-channel head coil (Siemens, Erlangen, Germany). To avoid visual field restrictions we only used the bottom element of the head coil, totalling 20 channels. A gradient-echo echo-planar imaging (EPI) sequence was used (TR = 2550ms, TE = 37ms, 30 interleaved slices), with off-axial acquisition and effective resolution of $2.3 \times 2.3 \times 2.3\text{mm}^3$. A T1-weighted anatomical image (TR = 7.92ms, TE = 2.48ms, resolution = $1 \times 1 \times 1\text{mm}^3$) was acquired in-plane with the functional protocol to aid registration. B_0 maps (TR = 1020ms, TE = 12.46ms, resolution = $3 \times 3 \times 3\text{mm}^3$) were measured to estimate local field distortions. Finally, a high-resolution T1-weighted volume (TR = 1900ms, TE = 2.97ms, resolution = $0.5 \times 0.5 \times 1\text{mm}^3$) was acquired with the full head coil arrangement and used to reconstruct the cortical surface.

Each participant underwent one MRI scanning session, beginning with a T1-weighted anatomical image and followed by 10 runs of fMRI acquisitions; 2 runs of cardinal size-invariant bar stimulus, 2 runs of oblique size-invariant bar stimulus, 2 runs of cardinal logarithmically-scaled bar stimulus, 2 runs of oblique logarithmically-scaled bar stimulus and 2 runs of simultaneous wedge and ring stimulus. Each run lasted approximately 6 minutes, with the wedge and ring condition requiring half the acquisition time (12 min) compared with the Cartesian designs (24 min). A total of 1440 volumes were acquired per participant, and the order of presentation was counterbalanced between participants. Next, photic stimulation was presented for HRF estimation for 120 volumes (5.1 min), followed by the B_0 map. Finally, a high-resolution T1-weighted volume was acquired. Total imaging time for each participant was approximately 80 min.

High-resolution anatomical images were processed with FreeSurfer (Dale et al., 1999; Fischl et al., 1999) for white and grey matter segmentation and cortical surface reconstruction. A manual definition of the occipital lobe surface was created for each hemisphere in order to restrict data analysis to the posterior regions of cortex. Pre-processing of functional images was carried out in SPM8 (Wellcome Trust Centre for Neuroimaging, <http://www.fil.ion.ucl.ac.uk/spm>). The first 4 volumes of each functional run were removed

to allow for T1 equilibration effects. All images were then bias-corrected, realigned to the first image of the run and unwarped to correct for movement artefacts and field distortions (Friston et al., 1995a; Ashburner & Friston, 1997; Andersson et al., 2001; Hutton et al., 2002; Ashburner & Friston, 2005). We performed slice-timing correction to avoid variations in the time series due to the timing of slice acquisition. The images were subjected to a two-step registration; first to the anatomical scan acquired in-plane with the functional images and then to the high-resolution anatomical image that was acquired using the full 32-channel head-coil. Finally, the data were projected onto the reconstructed surface for each participant by interpolating volumetric data at each vertex location using a nearest-neighbour algorithm, and selecting the vertices falling at the median distance between the pial and white matter surfaces.

4.3.4 Phase-encoded analysis

All subsequent data analyses were conducted using custom MATLAB (v.8.0) software. Data from the simultaneous wedge and ring stimulus configuration were analysed with a traditional phase-encoded retinotopic mapping approach (Sereno et al., 1995; DeYoe et al., 1996; Engel et al., 1997). In brief, the mean luminance blank periods at the end of each run were removed. Smoothing was applied using a Gaussian full width at half maximum (FWHM) kernel of 5 mm on the inflated spherical surface, and data converted to relative signal change (% BOLD change) by de-trending and de-meaning individual time series. Each run was analysed independently via a fast Fourier transform procedure at each vertex to determine the power and phase at the two fundamental frequencies (6 cycles per run for polar angle, 8 cycles for eccentricity). As a result, the signal phase at the stimulation frequency of wedges reflected the polar angle position, and the signal phase at the stimulation frequency of rings reflected the eccentricity position at each vertex. Finally, HRF lag effects were discounted by averaging phase maps across runs of the stimuli cycling in opposite directions.

4.3.5 Population receptive field (pRF) estimation

We took a forward-modelling approach to the functional data to estimate the receptive field properties of the underlying neural populations based on Dumoulin and Wandell (2008) and as used by us in previous studies (Schwarzkopf et al., 2014; de Haas et al., 2014). The pRF model we employed is a two-dimensional Gaussian described by four parameters: two encoding the visual field position in Cartesian coordinates (X_0 , Y_0), the spatial spread of the receptive field (σ), and the amplitude of the signal (β). We estimated these parameters for the time series at each vertex of the sampled cortical surface, restricted to an occipital region of interest delineated manually on the inflated cortical surface, in five main steps:

1) *Model creation.* The model rests on the prior knowledge of the stimulus aperture presented for each stimulus configuration, and the assumption of a simple Gaussian receptive field. A three-dimensional search space of possible combinations of location and receptive field size was created within bounds of the maximum eccentricity stimulated (see above for details of the visual display). This search space was then sampled for candidate locations in X_0 and Y_0 in steps of 2.4° and σ values in 34 exponentially incremental steps from 0.32° to 32° . We created a predicted neural time series for each combination of these parameters by calculating, the sum of Gaussian receptive field weights that fall within a binary stimulus aperture for each time point of the stimulus.

2) *HRF estimation.* The haemodynamic response function was estimated on a per-participant basis by taking the photic stimulation data, identifying and removing outlier values which departed more than 1.5 standard deviations from the mean for each trial, averaging the signal across trials and then fitting a double gamma function (Friston et al., 1995b). The free parameters modelled were the delay of the response, the delay of the undershoot and the ratio between these two parameters, all relative to the onset of the stimulus.

3) *Surface smoothing.* Spatial smoothing (FWHM kernel = 8.3mm) was applied to functional data on the inflated spherical surface to reduce local minima for the model fitting and produce a local-scale conjugate, which reflected the broad response at the supra-voxel level.

4) *Coarse fit.* Time series predictions generated using the search space parameters were convolved with the HRF estimation to produce a predicted time series (**Figure 4.3**). Each resulting time series was then compared to the smoothed data at a given vertex, calculating the Pearson correlation between smooth data and prediction. The parameter values of the prediction that yielded the highest correlation were used as starting parameters for the fine fit. Only positively correlated vertices with a high enough coefficient of determination, $R^2 > 0.05$, were included in fine fitting.

5) *Fine fit.* The un-smoothed data were compared to the prediction and the parameters of the model were fitted, aiming to minimize the squared residuals between data and prediction. The Nelder-Mead algorithm for unconstrained nonlinear minimization (Lagarias et al., 1998) was used (implemented as the function *fminsearch* in MATLAB v8.0) for parameter optimization, using the results of the coarse fit as starting point. In addition to pRF position and size, this step also explicitly modelled the signal amplitude (β). The resulting parameter maps were then projected onto an inflated cortical surface for rendering.

The pRF model estimation was performed independently for each of the three stimulus configurations (size-invariant bars, logarithmically-scaled bars, and the simultaneous wedge and ring stimulus) for each participant. Sample time-series and best-fitting model predictions under each condition are presented in **Figure 4.4**. As a further level of analysis, the size-invariant and logarithmically-scaled bar conditions were each split by run into cardinal and oblique directions and again fitted by pRF model estimation independently.

4.3.6 Model cross-validation

In order to assess the performance of pRF models derived from different stimulation conditions, we performed a series of cross-validation procedures on data acquired under size-invariant and simultaneous wedge and ring stimulation. In each test, the time series observed in one stimulus condition (validation dataset) was predicted by a pRF model generated from an independent stimulus condition (training dataset) and the known stimulus aperture of the predicted condition. Independent model predictions and observed time series were then correlated to assess the performance of each model and more broadly, the generalisability of pRF models to different conditions of stimulation.

Two target datasets were selected to be predicted: cardinal and oblique directions of size-invariant bar stimulation. In turn, each target dataset was predicted by a pRF model based on a) opposite-direction bars stimulation or b) simultaneous wedge and ring stimulation. Correlation coefficients between model predictions and observed target time series were calculated and transformed into Fisher's z values. Resulting z values were averaged across vertices of each region of interest and compared between conditions by aggregating predictions from opposite bar orientations and predictions from wedge and ring stimulation.

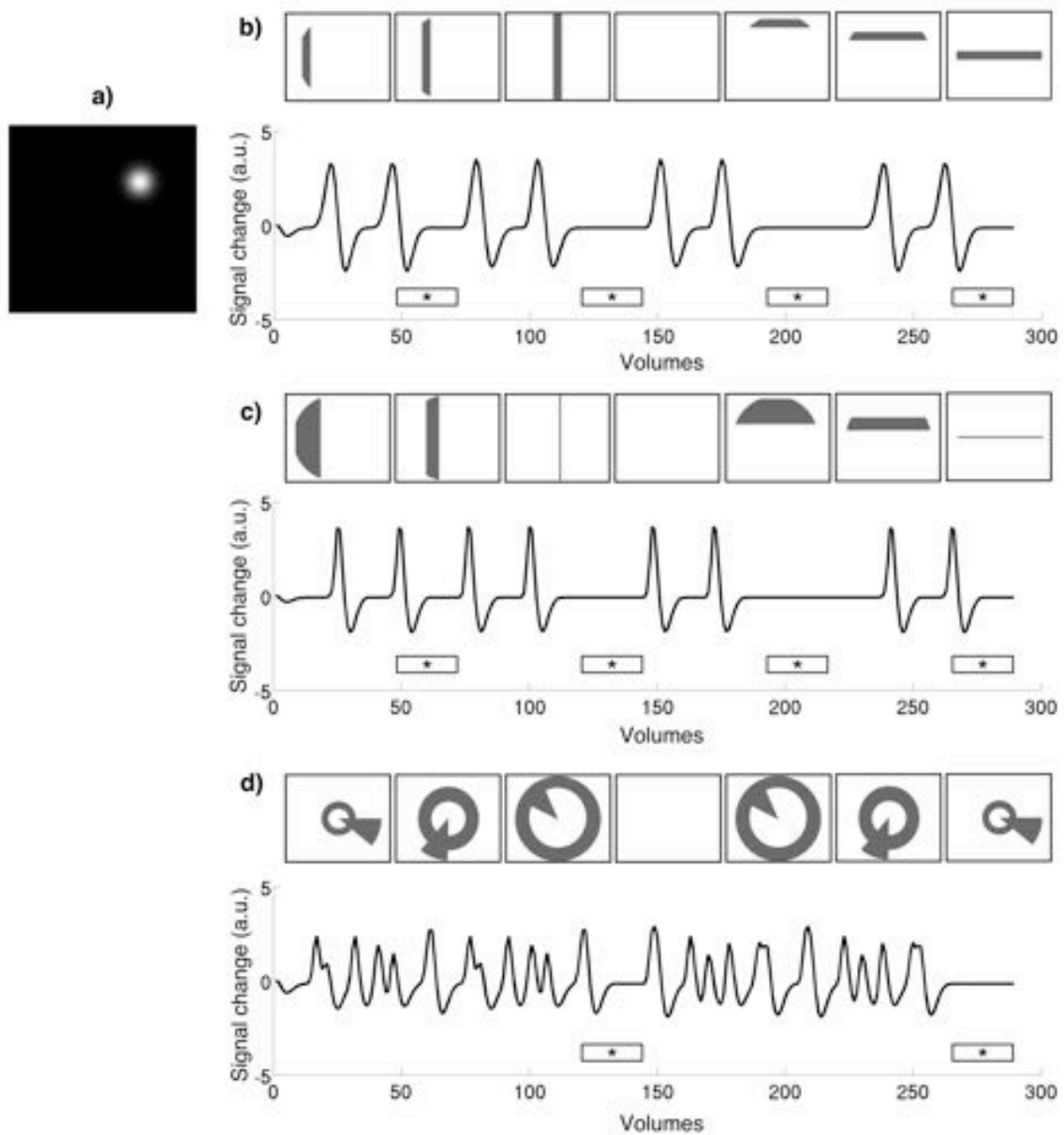


Figure 4.3 Time series predictions for stimulation to a single pRF (a) under size-invariant bars (b), logarithmically-scaled bars (c) and simultaneous wedge and ring (d) stimulus configurations. Use of a standard bar design produces large baseline zones that are uninformative to the model as to pRF location and spread. In contrast, the simultaneous wedge and ring stimulus based on polar angle coordinates stimulates the pRF more frequently, providing more elicited events fitted by the model. Stimulus frames are illustrative and do not correspond to specific time points along the time-series. Mean luminance periods indicated by asterisk bars.

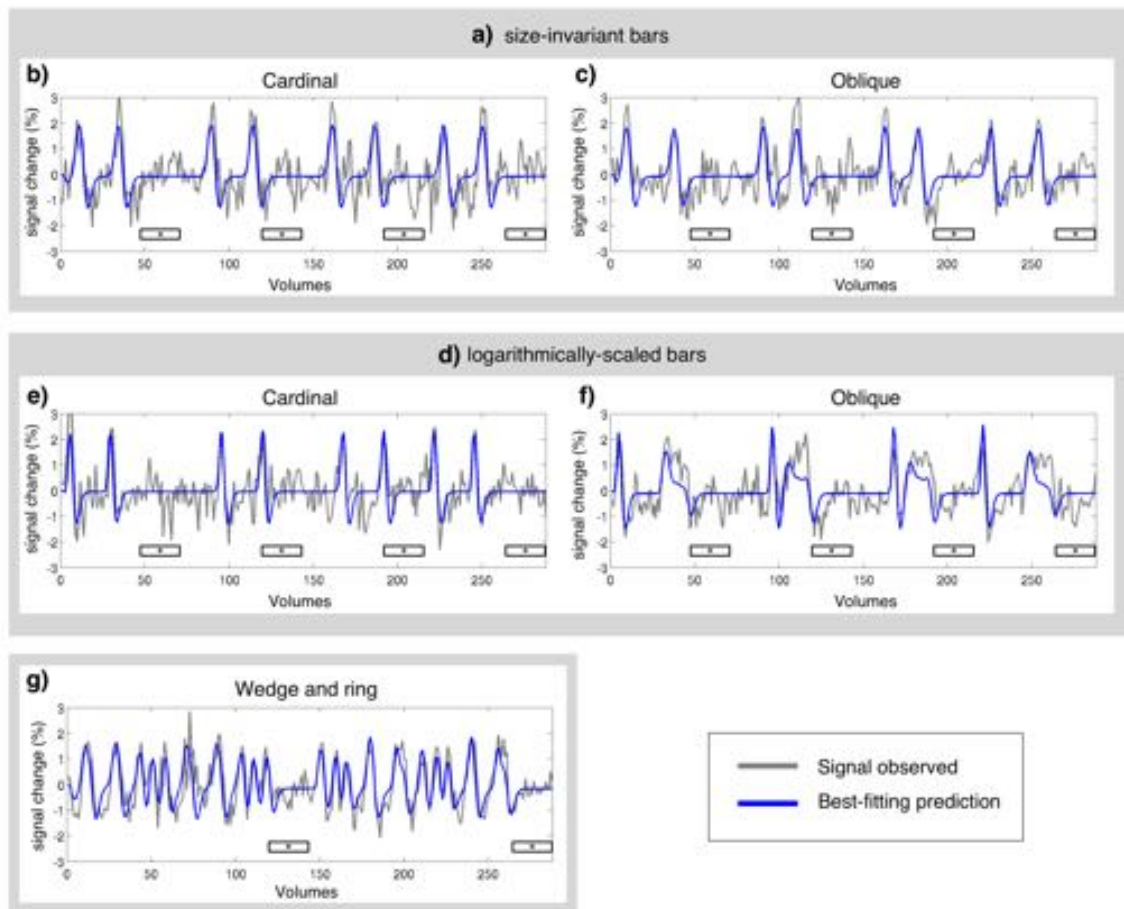


Figure 4.4 Sample time-series and best-fitting model prediction for one vertex (cortical surface element) in area V2 from a representative participant. Time-series are presented for three main conditions and four sub-conditions; (a) size-invariant bars, including its (b) cardinal and (c) oblique sweep directions; (d) logarithmically-scaled bars, including its (e) cardinal and (f) oblique sweep directions; and finally (g) simultaneous wedge and ring stimulation. Mean luminance periods indicated by asterisk bars. All conditions were fitted independently.

4.4 Results

4.4.1 Region delineation

We manually delineated retinotopic maps in FreeSurfer using the polar angle and eccentricity representations derived from the pRF model. Early visual areas including primary visual cortex (V1), areas V2, V3, V3A, V3B, V4, V5/MT+ and V7 were reliably identified under all conditions of stimulation (see **Figure 4.5** for a representative participant). Region delineations were performed under the size-invariant bar condition for all participants. We did not find the defining boundary between lateral occipital areas LO-1 and LO-2 in all participants, and therefore favoured a joint definition of the lateral occipital complex (LOC). Similarly, we identified a ventral occipital complex (VOC) in all participants. For the human homologue of macaque area V5/MT+, also called temporal occipital to more accurately reflect anatomical location in the human (Wandell & Winawer, 2015) we identified at least one vertical meridian reversal in all participants, but were unable to reliably assign the map to either TO-1 or TO-2, each containing a phase-reversal, and therefore chose to label this region as V5/MT+ across all participants.

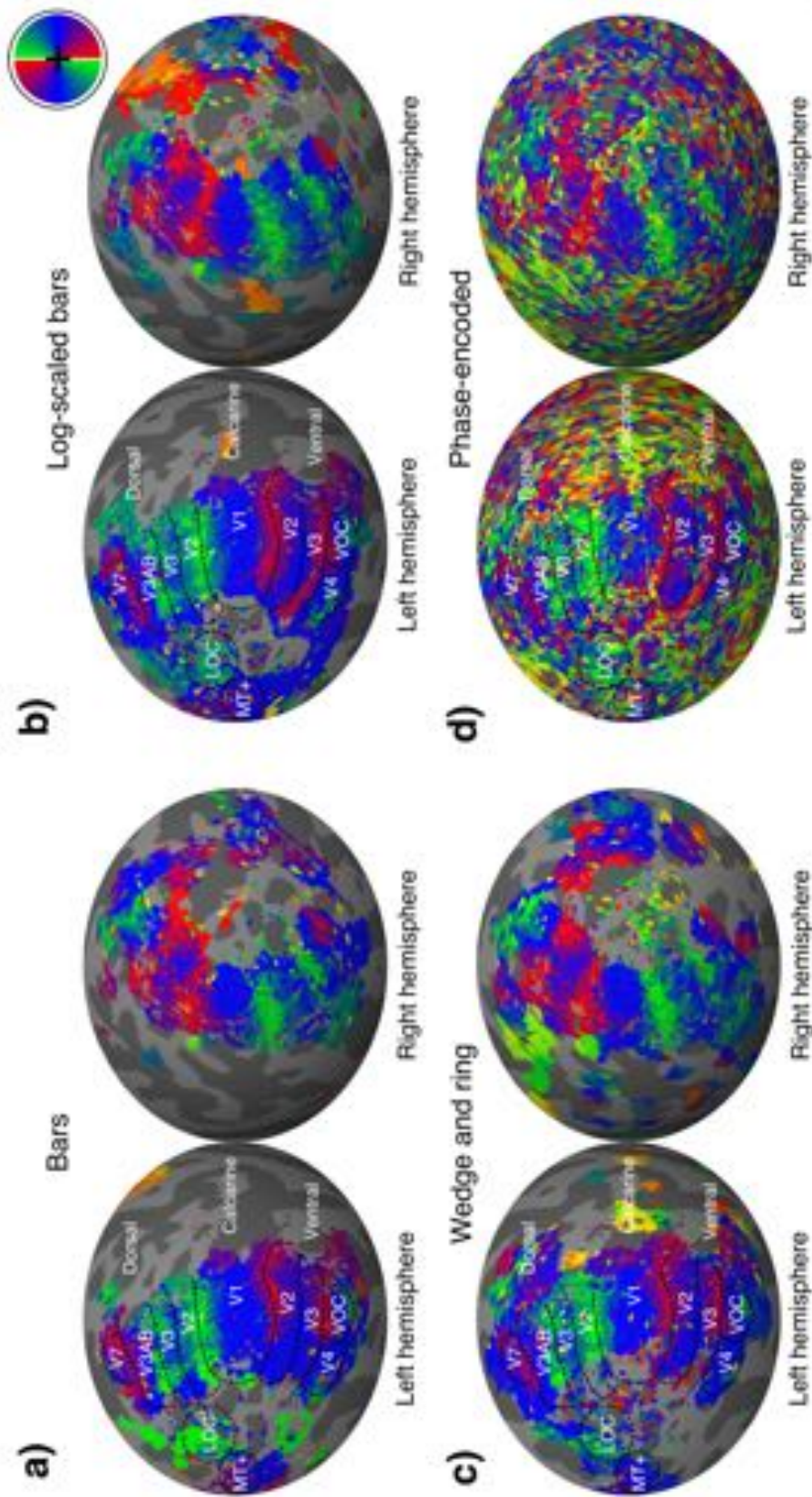


Figure 4.5 Polar angle maps overlaid on inflated left hemisphere for a representative participant. Polar angle estimates were derived independently from population receptive field modelling under stimulation by (a) size-invariant bars, (b) logarithmically-scaled bars and (c-d) simultaneous wedge and ring stimuli. Regions of interest are labelled and boundaries highlighted for the size invariant bars condition, which was used to identify those regions. Colour corresponds to visual field position, as indicated by the colour wheel in the upper right corner.

4.4.2 Model validation

To assess the performance of pRF models derived from different stimuli, we performed a series of cross-validation tests. First, pRF models were estimated from data obtained under cardinal and oblique bar stimulation independently, as well as from simultaneous wedge and ring stimulation. Second, predictions were generated from two conditions; either cardinal or oblique bar pRF models and simultaneous wedge and ring pRF models. Finally, the model predictions were compared against an independent *observed* time series, obtained under the remainder condition. The bar pRF model outperformed the wedge and ring pRF model in prediction accuracy, as assessed by independent samples t-test, in areas V1 ($t=5.55$, $df=15$, $p<.001$), V2 ($t=3.47$, $df=15$, $p<.01$) and V3 ($t=2.64$, $df=15$, $p<.05$), but not in any other region of interest (see **Figure 4.6**, $N = 8$ for all tests, Bonferroni correction for multiple comparisons applied). This reliability advantage is not surprising, considering the geometric similarity between cardinal and oblique sweeping bars designs. Nevertheless, the difference in reliability was extremely small, with a maximum predictive difference of $z = 0.03$ ($R^2 < .001$) between bar and wedge and ring predictor models.

4.4.3 Goodness of fit

Having demonstrated comparable reliability across the different experimental conditions tested, we compared goodness of fit as quantified by the coefficient of determination (R^2) of our experimental conditions. Strictly, a direct comparison of the conditions based solely on the goodness of fit would be misleading because they are not only based on different models but also on different data. As such it would be incorrect to interpret differences in goodness of fit as differences in efficiency or reliability of the procedure. However, in practical terms, the goodness of fit achieved by each procedure is important because, provided precision of each method is similar, the goodness of fit determines how many voxels survive statistical thresholding, i.e. the statistical power of the method. Furthermore, the models compared differed only in visual stimulation and not in the number of free parameters or the nature of the model fitted.

We compared three stimulus configurations: size-invariant bars, bars varying logarithmically in size with eccentricity, and a simultaneous wedge and ring aperture, also scaled logarithmically for eccentricity. In addition, we also included independent pRF fits for the cardinal and oblique directions of both size-invariant and logarithmic bars, as sub-conditions. To ensure parameter estimates were comparable, we thresholded each vertex within a region of interest at goodness of fit values $R^2 > 0.1$. The number of vertices surviving thresholding did not differ significantly across conditions (ANOVA, $F=.48$, $df=3$, $p=.726$).

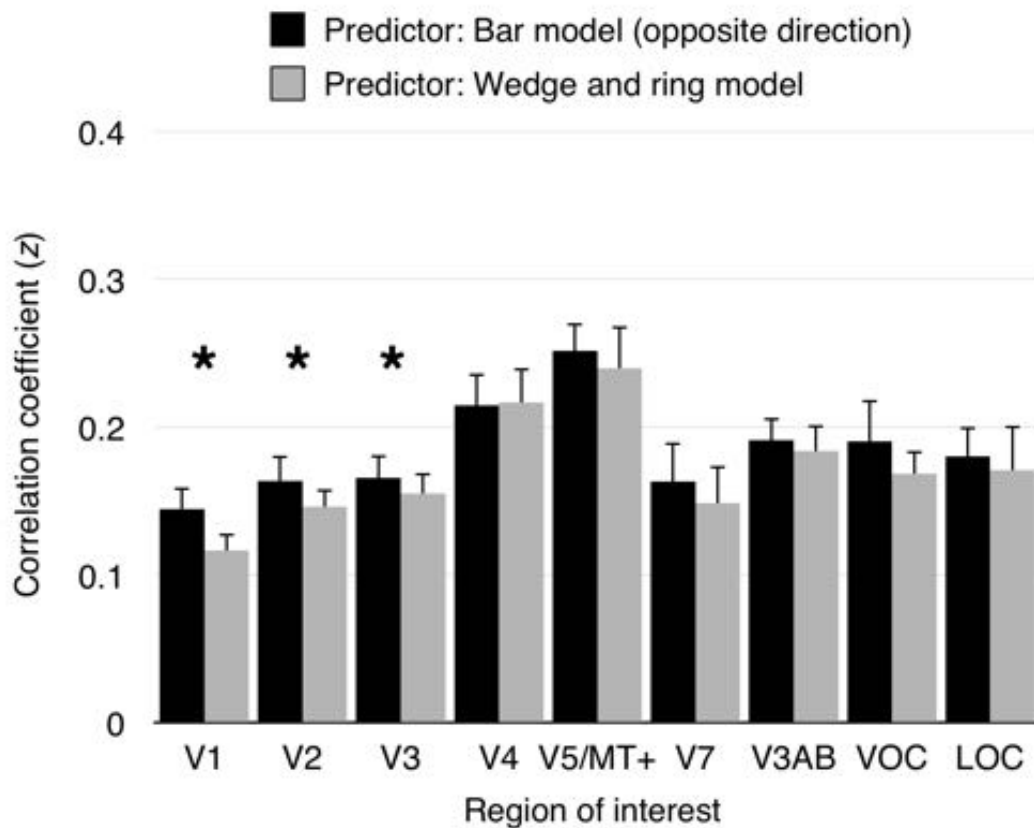


Figure 4.6 Model cross-validation. Cardinal and oblique orientations of size-invariant bars were predicted by a pRF model derived from either opposite bar direction or simultaneous wedge and ring stimulation. Model prediction were correlated with the signal observed in the predicted condition. Data from cardinal bars predicted from the oblique bars pRF model and oblique bars predicted from the cardinal bars pRF model were collapsed into ‘opposite bar direction’ predictions. Similarly, predictions of either cardinal or oblique bars signal predicted from the simultaneous wedge and ring pRF model were collapsed into simultaneous wedge and ring predictions. Correlation coefficients were transformed to z-values (Fisher’s z-transformation). A significant difference in prediction was observed in areas V1 (z difference = 0.03), V2 (z difference = 0.02) and V3 (z difference = 0.01), but not in higher visual areas. $N = 8$ for all tests.

We tested goodness of fit (R^2) values across stimulus conditions with a repeated-measures design ANOVA (see **Figure 4.7**). We found a main effect of condition ($F=29.37$, $df=6$, $p<.001$), with no significant contribution of inter-subject variability ($F=1.48$, $df=18$, $p=.101$). The simultaneous wedge and ring stimulus configuration afforded marginally better fits ($mean R^2=0.26 \pm 0.01 SEM$) than either the size-invariant ($mean R^2=0.17 \pm 0.01 SEM$) or logarithmically-scaled ($mean R^2=0.14 \pm 0.01 SEM$) bar stimuli. Crucially, these results rested on only half the amount of data and scanning time compared to size-invariant or logarithmically-scaled bars, indicating a time-to-acquire advantage.

4.4.4 Effect of mean luminance periods on pRF estimates

To accurately estimate pRF parameters, a baseline measure is introduced by acquiring data during a mean luminance period while no modulation of contrast or spatial frequency is taking place (Dumoulin & Wandell, 2008). The bar stimuli and the simultaneous wedge and ring stimulus conditions in our design were matched for the number of data points, that is, each scanning run comprised 144 volumes regardless of condition. This means that both runs of the bar stimulus with opposite directions and the two directions of the simultaneous wedge and ring stimulus each totalled 288 volumes. Therefore, the benefit in goodness of fit for the wedge and ring stimulus could not trivially be explained by the amount of data collected in each condition – in fact, it remained even when twice the amount of data was used for the bar stimuli by collating runs with cardinal and oblique sweep directions.

However, it could be argued that the length of mean luminance periods affects the goodness of fit. Compared to the simultaneous wedge and ring design, in the bar design there were twice as many volumes during which mean luminance frames were presented. As **Figure 4.3** shows, the reduced goodness of fit for the bar stimuli could therefore be due to the fact that there was more unexplained variance caused by the longer periods during which the model predicted a zero response. In order to test this possibility, we performed a control analysis where the number of mean luminance volumes acquired during size-invariant bar stimulation was truncated from 48 to 24 volumes per run to match the number of mean luminance volumes in a single run of the simultaneous wedge and ring stimulus. The resulting truncated data were then fitted with the pRF model described above, revealing a significant difference between the original ($mean R^2 = 0.14 \pm 0.01 SEM$) and truncated ($mean R^2 = 0.17 \pm 0.01 SEM$) models ($t = 3.85$, $df = 7$, $p < .01$). However, this difference was markedly smaller than the advantage afforded by the ridge configuration, and within the variability range of the stimuli probed here, indicating the number of mean luminance volumes did not fully account for goodness of fit differences observed between bar-type and wedge and ring stimuli. Moreover, this modest increase in the goodness of fit after truncation was accompanied by a decrease in the degrees of freedom.

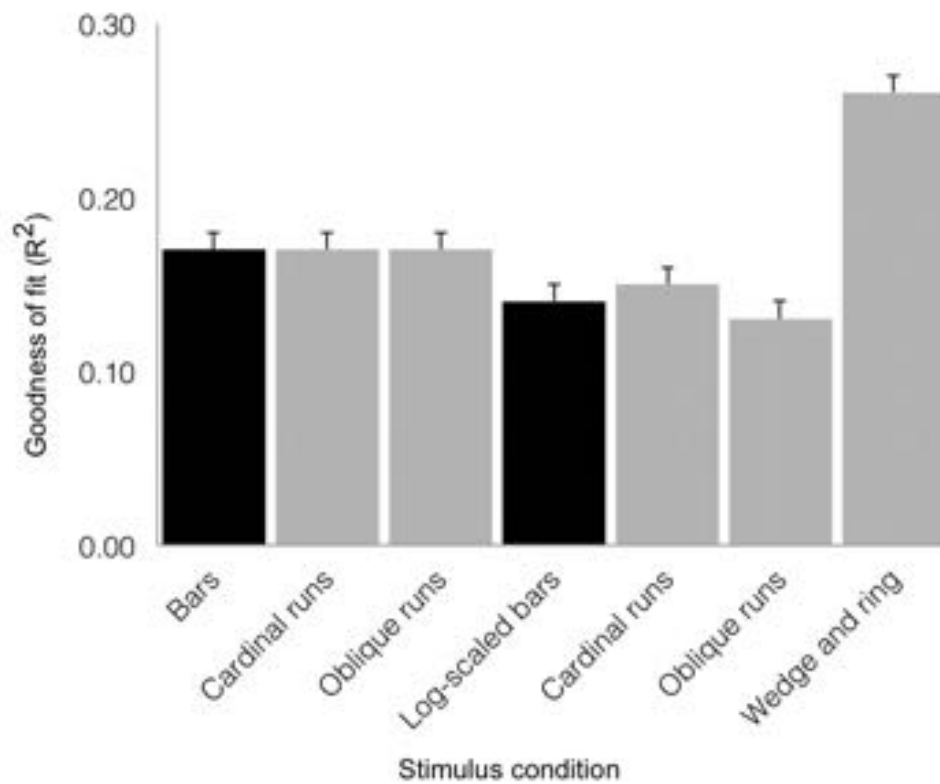


Figure 4.7 Group average goodness of fit (R^2) for the three stimulus configurations as derived from sum of squared residuals between the observed time series and model predictions for regions V1, V2 and V3 combined (error bars correspond to SEM). Black shading denotes estimates from 576 volumes acquired and grey shading denotes estimates derived from 288 volumes acquired. Simultaneous wedge and ring stimulation produced better data fits, while requiring half the data compared to size-invariant or logarithmically-scaled bars collapsed across bar directions.

4.4.5 Stimulus configuration and pRF size

The size of the pRF denotes the two-dimensional spread of the visual field locations from which responses in the sampled vertex can be elicited and is quantified by the standard deviation (σ) of the two-dimensional Gaussian in degrees of visual angle. Typically, the size of single neuron receptive fields increases with eccentricity (Hubel & Wiesel, 1977; Van Essen et al., 1984) and along the visual map hierarchy in primates (Zeki 1978; Maunsell & Newsome, 1987; Felleman & Van Essen, 1991). Similarly, pRF sizes also scale with eccentricity and position in the visual hierarchy (e.g. Dumoulin & Wandell 2008). Here, we tested the effects of our three different stimulus configurations on pRF size estimates.

4.4.5.1 pRF size: size-invariant vs. logarithmically-scaled bar apertures

Estimates for V1, V2 and V3 followed the expected pattern of monotonic increase with eccentricity (**Figure 4.8a-c**). pRF sizes estimated from the size-invariant bar conditions covered approximately 0.7-2.8° in V1, 0.8-4.0° in V2 and 1.1-5.8° in V3, in broad agreement with values reported in the literature (Smith et al., 2001; Dumoulin & Wandell, 2008; Amano et al., 2009; de Haas et al., 2014; Schwarzkopf et al., 2014). These results were in contrast with bar apertures accounting for the effects of cortical magnification, i.e. expanding logarithmically with eccentricity, as tested in a subset of 4 participants. The latter provided significantly lower pRF size estimates for V1 (0.4-2.3°), V2 (0.7-2.7°) and V3 (0.8-4.4°) (all participants $p < .001$, see Table 5.1 for pairwise t-tests).

We also examined the effect of stimulus configuration on pRF size in higher visual regions (**Figure 4.8d-i**). As expected from the organisation of cortical visual regions, there was a monotonic relationship between hierarchical position and pRF size. Note the differentiation in pRF size estimates in ventral region V4 (**Figure 4.8e**), where the size-invariant bar conditions produced larger pRFs at highly eccentric representations. This was statistically significant when compared to the logarithmically-scaled condition (see **Table 4.1** for pairwise t-tests, Bonferroni correction for multiple comparisons applied). Results presented here for size-invariant bars are consistent with reports in the literature of pRF sizes in the range of 2-6° for area V4 (Winawer et al., 2010). Similar effects of stimulus configuration were observed in the ventral occipital complex (VOC), encompassing map VO-1 and VO-2 and the lateral occipital complex (LOC), encompassing LO-1 and LO-2 (**Figure 4.8h-i**). Estimates of pRF size were consistent with expectations of linear increase with cortical hierarchy, with estimates for LO regions in the range of 2-9°. These data are consistent with previous estimates of pRF size for human LO regions (Larsson & Heeger, 2006; Amano et al., 2009). As a general trend, larger pRF size estimates were observed in the size-invariant bars condition compared to the cortical magnification-scaled conditions, with significant divergence between logarithmic and size-invariant bars in VOC and LOC.

4.4.5.2 pRF size: size-invariant vs. simultaneous wedge and ring apertures

The hierarchical increase in pRF size with cortical area across V1, V2, V3 and V4 was replicated, with smaller pRF size estimates in the simultaneous wedge and ring stimulus condition (V1 = 0.7-2.4°; V2 = 0.9-3.2°; V3 = 1.0-4.9°; V4 = 1.4-5.9°) when compared to the size-invariant condition (all comparisons $p < .05$, see **Table 4.1** for individual pairwise t-tests). In early visual areas V1, V2 and V3 (**Figure 4.8a-c**) pRF sizes differences between conditions are non-distinguishable in central visual field representations, below 2° eccentricity. More eccentric representations, and those of higher visual areas diverge, with smaller pRF size estimates for the simultaneous wedge and ring stimulus.

Of particular interest was area V5/MT+ (**Figure 4.8f**), where the simultaneous wedge and ring condition produced significantly smaller pRFs ($\sigma = 1.0-8.0^\circ$) than the size-invariant condition ($\sigma = 2.7-12.3^\circ$). This is at odds with previous human fMRI data, which estimated the pRF size of V5/MT+ to be between 5° and 11° (Amano et al., 2009). The present data suggest that pRF size estimates in the region V5/MT+ may be more susceptible to stimulus configuration, compared with early visual areas.

In addition to the linear effects on pRF size, we also observed an interaction of eccentricity with pRF size differentiation across conditions. In areas V7, VOC and LOC (**Figure 4.8g-i**), but also earlier areas in the visual hierarchy such as V4 and V5/MT+, the difference in pRF size across conditions scaled with eccentricity, with larger differences at the more eccentric positions. In order to test this, we performed a linear regression on the pRF size increment with eccentricity and compared the slope of the fits between size-invariant bars and simultaneous wedge and ring presentations across participants. For region V1, we found no difference in the linear fit slopes between conditions (*mean slope difference* = 0.01 ± 0.02 SEM $t = 0.29$, $df = 7$, $p = .780$), while regions V2 (*mean slope difference* = 0.04 ± 0.02 SEM), V3 (*mean slope difference* = 0.09 ± 0.02 SEM), V4 (*mean slope difference* = 0.16 ± 0.05 SEM), V5/MT+ (*mean slope difference* = 0.34 ± 0.08 SEM), V3AB (*mean slope difference* = 0.10 ± 0.02 SEM) and VOC (*mean slope difference* = 0.40 ± 0.13 SEM) showed a significant slope difference between conditions (all comparisons $p < .05$, $N = 8$). This indicated the wedge and ring condition consistently returned smaller pRF sizes relative to the size-invariant condition at highly eccentric representations. No significant slope differences were observed in regions V7 (*mean slope difference* = 0.23 ± 0.09 SEM $t = 2.31$, $df = 7$, $p = .054$) or LOC (*mean slope difference* = 0.15 ± 0.10 SEM $t = 1.56$, $df = 7$, $p = .163$).

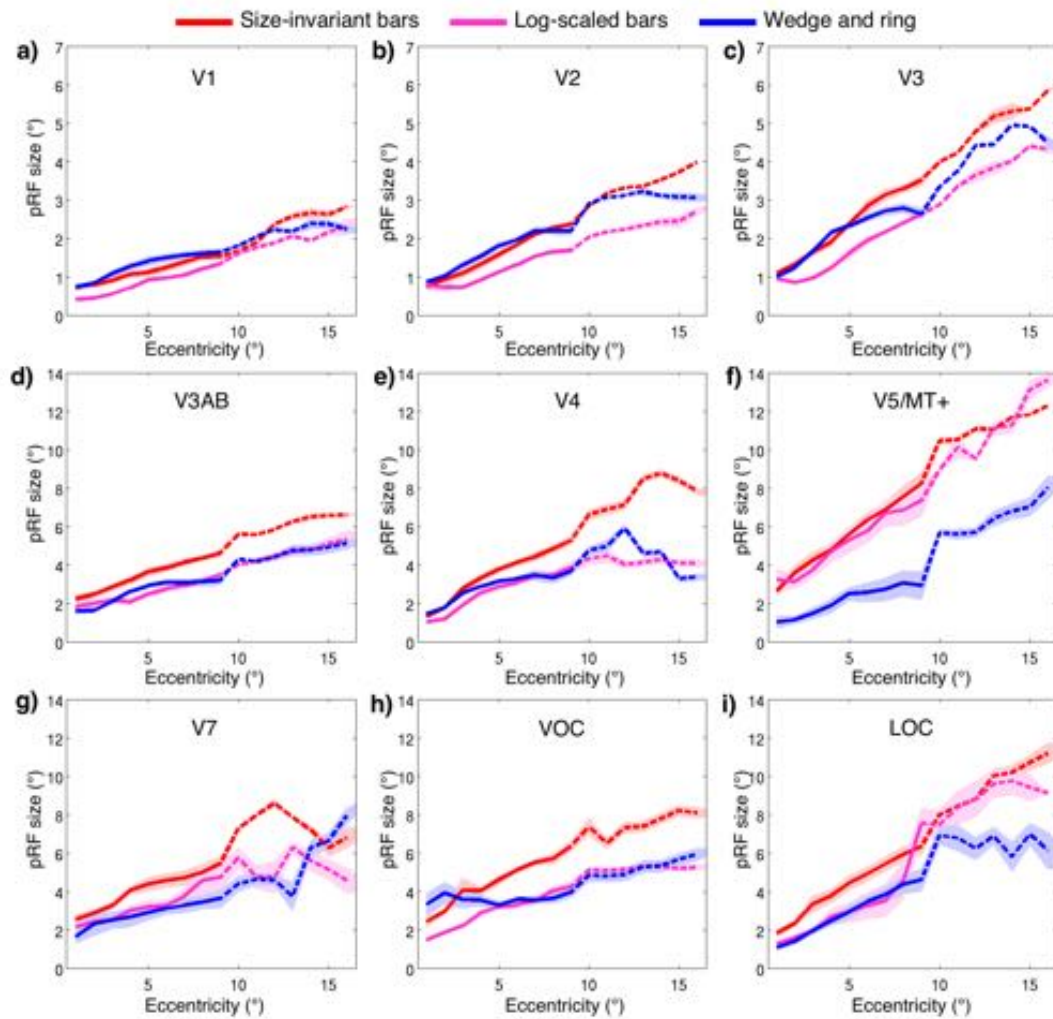


Figure 4.8 Population receptive field size (σ , in degrees of visual angle) across two ranges of visual field eccentricities; 9° (solid line, six participants) and 16° (dashed line, two participants). Vertices were binned and averaged across participants in steps of 1° of eccentricity and plotted for three stimulus configurations; size-invariant bars (red), logarithmically-scaled bars (magenta) and simultaneous wedge and ring stimulus (blue) across nine regions of interest. Shaded area corresponds to SEM. Note the wedge and ring stimulus configuration produced smaller pRF size estimates across the cortical hierarchy, both in striate (a) and early extra-striate (b, c, d) regions. Most markedly, the wedge and ring stimulus produced significantly smaller pRF size estimates in area V5/MT+, a difference of 1-4° when compared to the bar stimuli.

Table 4.1 Within-subject pairwise t-tests assessing differences in pRF size (in degrees of visual angle) between size-invariant, logarithmically-scaled bars and size-invariant bars and simultaneous wedge and ring stimulus design across nine regions of interest; V1, V2, V3, V4, V5/MT+, V7, V3AB, VOC and LOC. Positive t-values indicate larger pRFs in the first condition, degrees of freedom in parenthesis. $N = df - 1$ in all cases. Bonferroni-corrected p -values indicated by asterisks.

	Size invariant bar vs. logarithmically-scaled bar stimulation									
	V1	V2	V3	V4	V5	V7	V3AB	VO	LO	
Subject 1	3.67 (3682)***	41.25 (2483)***	32.76 (1921)***	48.59 (1157)***	39.07 (508)***	17.56 (649)***	34.94 (652)***	45.62 (673)***	28.85 (1351)***	
Subject 2	65.35 (2238)***	52.72 (1416)***	53.16 (1256)***	70.59 (954)***	21.92 (327)***	42.91 (593)***	63.16 (776)***	45.60 (136)***	69.21 (1683)***	
Subject 3	19.08 (3697)***	7.90 (2872)***	30.88 (2655)***	49.66 (1616)***	31.77 (537)***	25.88 (664)***	39.68 (1721)***	31.96 (374)***	15.66 (1314)***	
Subject 4	23.49 (2918)***	30.63 (2302)***	36.33 (1961)***	30.77 (1201)***	22.87 (471)***	5.84 (223)***	53.41 (1150)***	10.86 (212)***	10.73 (633)***	
Subject 5										
Subject 6										
Subject 7										
Subject 8										
	no logarithmically-scaled bar stimulation									
	Size invariant bar vs. wedge and ring stimulation									
	V1	V2	V3	V4	V5	V7	V3AB	VO	LO	
Subject 1	0.73 (3634)**	0.51 (2501)**	25.29 (1922)***	72.09 (1203)***	28.34 (384)***	0.35 (525)*	34.18 (1147)***	30.65 (464)***	19.98 (1609)***	
Subject 2	3.00 (2378)***	8.67 (1646)***	36.07 (1339)***	50.34 (1173)***	32.29 (546)***	25.53 (730)***	36.20 (1037)***	13.86 (70)***	36.34 (2257)***	
Subject 3	15.72 (4061)***	17.07 (2668)***	5.87 (2501)**	30.42 (1506)***	46.66 (399)***	36.46 (593)***	38.27 (1831)***	31.20 (439)***	24.41 (1226)***	
Subject 4	50.58 (3253)***	15.47 (2288)***	0.98 (1842)**	9.80 (1129)**	6.82 (201)**	15.15 (266)***	20.85 (1342)***	6.10 (248)***	1.53 (361)**	
Subject 5	13.45 (2564)***	7.22 (1951)***	18.90 (1462)***	12.09 (434)***	18.72 (2)***	3.37 (31)**	12.32 (393)***	0.62 (90)**	9.03 (77)***	
Subject 6	13.84 (2862)***	4.40 (2646)***	18.40 (2206)***	45.62 (1327)***	32.01 (704)***	15.62 (447)***	19.37 (1371)***	8.71 (472)***	23.93 (771)***	
Subject 7	27.17 (3018)***	11.42 (2363)***	7.55 (1938)***	56.72 (1219)***	17.42 (66)***	8.75 (473)***	73.92 (2634)***	18.18 (307)***	24.77 (515)***	
Subject 8	13.86 (2070)***	28.48 (1861)***	48.93 (1571)***	45.19 (720)***	.	14.56 (48)***	39.73 (963)***	26.68 (161)***	14.67 (72)***	

* $p < .05$, ** $p < .01$, *** $p < .001$

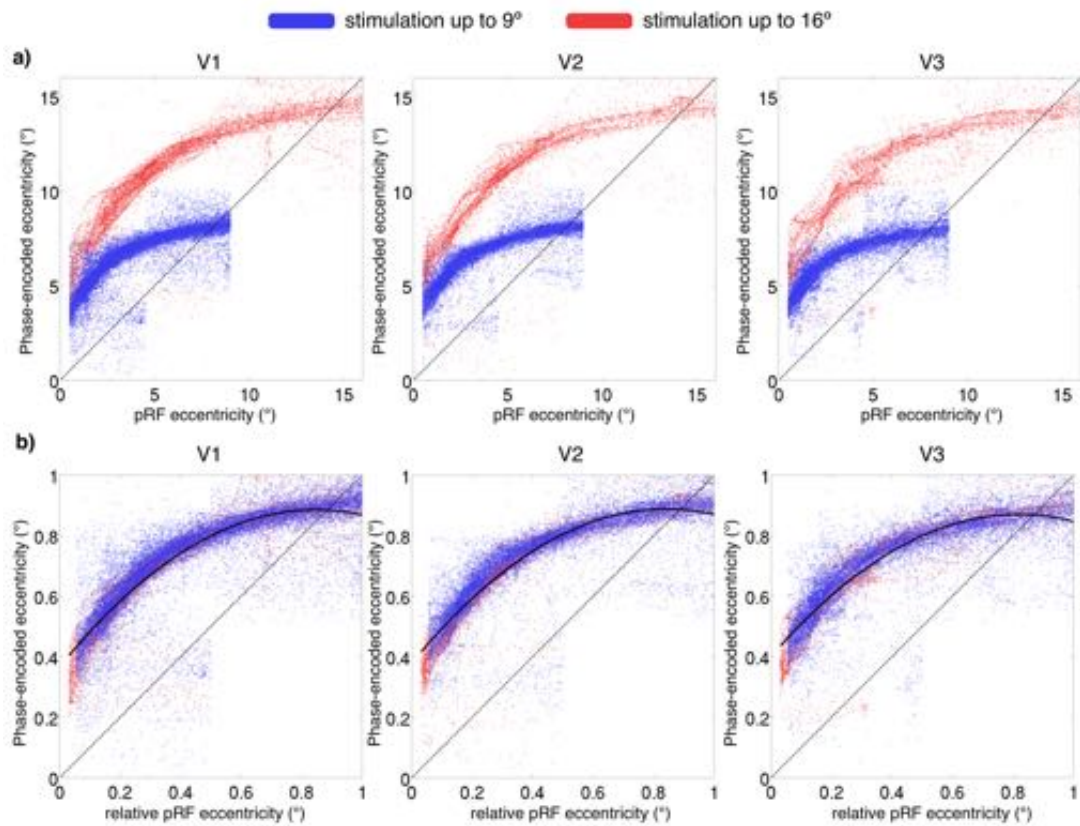


Figure 4.9 Comparison of eccentricity estimates by pRF and phase-encoded methods for regions V1, V2 and V3. Each point represents a single surface vertex in a single participant, only vertices with goodness of fit $R^2 > 0.05$ displayed. (a) The maximum eccentricity of the stimulus differed between participants (16° display in red and 9° display in blue), reproduced in the eccentricity estimates where two distinct populations are seen. (b) Values normalized by maximum eccentricity show a similar discrepancy for phase-encoded estimates relative to the pRF estimates, independent of maximum stimulus size. Dashed line denotes identity; i.e. a perfect correspondence between the pRF and phase-encoded estimates of eccentricity. Solid line in (b) denotes best-fitting second-level polynomial over all participants.

4.4.6 Effects of display size on pRF estimates

An effective stimulus design for pRF mapping is one that produces accurate estimates of the property sampled independently of extraneous factors such as viewing distance; therefore a design that introduces biases at different viewing distances is likely to be suboptimal. In order to test this, two participants viewed the stimuli described here with an eccentric coverage of 16° from fixation, while a further six participants viewed them with 9° coverage from fixation. We compared the goodness of fit (R^2) of the pRF model in three stimulus designs (size-invariant bars, logarithmically-scaled bars and simultaneous wedge and ring stimulus) across the two viewing distances with a between-subjects univariate ANOVA model across all regions of interest. R^2 values were significantly larger at 16° eccentricity compared to 9° eccentricity under the size-invariant ($F=8.31$, $df=34$, $p<.01$) and logarithmically-scaled bar stimuli ($F=11.14$, $df=34$, $p<.01$). This is unsurprising, given the larger display elicited activations in the more peripheral representations of visual space, therefore providing stimulus-related signals in a larger expanse of cortical territory, compared to the smaller display. Crucially, when comparing the goodness of fit in the wedge and ring condition, there was no significant difference between participants who viewed the small and large screen display ($F=2.07$, $df=34$, $p=.159$), pointing to a robust fit of the pRF model in the simultaneous wedge and ring condition independent of viewing distance. We also tested whether the model was biased in its estimates of pRF size by an interaction between display size and stimulus configuration. To assess this, we calculated the mean difference in pRF size between participants who experienced the 9° display vs. the 16° display in 20 equally-spaced eccentricity bins, spanning the range of 0.5° to 9° of eccentricity for all regions of interest. We found the 16° display produced marginally larger pRFs under the size-invariant bar stimulus (*mean difference*=0.72°), compared to the simultaneous wedge and ring stimulus (*mean difference*=0.60°, $t=2.34$, $df=8$, $p<.05$), with both results being within the levels of observed inter-individual variability

4.4.7 pRF vs. phase-encoded estimation of stimulus eccentricity

A currently unsolved issue in modelling cortical pRF characteristics is the possible introduction of model-dependent biases. Dumoulin and Wandell (2008) argue for a bias in eccentricity estimation using phase-encoded methods, with an over-estimation of eccentricity at the lower boundaries, which is enhanced for areas with large pRF sizes.

We compared phase-encoded estimates of eccentricity, extracted from data acquired during simultaneous wedge and ring aperture stimulation, with eccentricity estimates obtained from the pRF model fitting of the same data in regions V1, V2 and V3. If there were an exact correspondence between the two eccentricity estimates, data would lie on a straight line across the eccentricity space. Instead, we found an over-estimation of the

stimulus eccentricity from the phase-encoded method relative to the pRF estimates in a non-linear, eccentricity-dependent fashion (see Figure 4.9a). These results replicate previous findings of an overestimation of eccentricity by the phase-encoded method (Dumoulin and Wandell, 2008). Discrepancies in phase-encoded eccentricity estimates were also independent of the range of values sampled, as normalization of eccentricity values revealed similar profiles for participants presented with maximum eccentricities of 16° and 9° (Figure 4.9b).

4.5 Discussion

Optimal stimulus design is an important consideration in fMRI experimental planning, both in providing targeted elicitation of the desired signals and reducing potential confounds such as physiological noise and participant motion. Here, we considered three stimulus configurations and their effects on model estimates of pRFs. We identified two factors that significantly influenced model estimates: eccentricity scaling and Cartesian vs. polar coordinate based apertures.

Three experimental conditions were compared; size-invariant bars, logarithmically-scaled bars and a simultaneous wedge and ring stimulus, with all producing comparable retinotopic maps (see **Figure 4.5**). Goodness of fit metrics revealed that conditions performed similarly, with a marginal advantage for the wedge and ring condition, even when compared to twice as much data fitted in the bar conditions. This advantage is important in terms of acquisition time, as prolonged scan sessions typically lead to increased subject motion, and a stimulus configuration that affords efficient estimation in a short period of time is desirable for studies where scan time is limited or the population of interest does not tolerate extended scan sessions. The advantage may be accounted for by the use of stimuli defined in polar rather than Cartesian coordinates, as within the same time period any given pRF can be stimulated more often under the simultaneous wedge and ring configuration, with more signal fluctuations recorded and accounted for by the pRF model, compared to the standard bar configurations. This effect is illustrated in **Figure 4.3**, where the pRF prediction under bar-type stimulation contains a larger proportion of uninformative periods compared to the simultaneous wedge and ring stimulus. Indeed, this advantage in more frequent elicitation of desired signals may be achieved with any stimulus configuration incorporating multiple apertures of any geometry, as long as the fundamental frequencies of apertures are de-correlated. Pragmatically, a multifocal approach with maximum length sequence (M-sequence) maximizes the efficient elicitation of signals in the shortest possible time (Buracas & Boynton, 2002; Vanni et al., 2005; Henriksson et al., 2012). While it may appear as if multifocal M-sequence approaches are therefore optimal for retinotopic

stimulation, they suffer from reduced explanatory power (Ma et al., 2013). In addition, multifocal stimuli produce poorer retinotopic maps and reduced goodness of fit in pRF modelling (Binda et al., 2013), revealing a trade-off between model accuracy and predictive power. This difference with slow travelling wave designs, such as both our bar and simultaneous wedge and ring designs, might be due to the fact that these slower designs maximize the difference between high temporal frequency noise and the mapping signal. To achieve comparable signal-to-noise ratios, a multifocal design presumably would require long epochs for each multifocal stimulus frame, which would greatly inflate data acquisition times. We therefore propose the travelling wave simultaneous wedge and ring stimulus as a potential compromise between these two competing interests in pRF mapping.

A further consideration for visual field sampling efficiency, is the heterogeneous sampling afforded by eccentricity-scaled stimuli defined in a Cartesian coordinate system, in this case, logarithmically-scaled bars. For pRFs lying outside diagonal lines in visual space, these will be sampled at different fineness, that is, the thickness of the sweeping bar, in each orientation of the sweep. As such, a pRF may be under- or over-estimated by unequal levels of fineness in each sampling orientations. This heterogeneity is not present in polar coordinate defined stimulus, such as the simultaneous wedge and ring stimulus, therefore increasing confidence in the robustness of visual space sampling.

An efficient stimulus configuration for pRF mapping not only elicits the desired signals, but also results in reliable model estimates of the underlying neuronal properties of interest. In order to assess reliability, we conducted a series of cross-validation tests. While the conventionally used size-invariant bar stimulus showed a subtle benefit in terms of reliability in early visual areas, cross-model reliability was largely similar across the conditions tested, indicating models derived from different stimulus configuration were comparable.

Nevertheless, differences in model predictions were observed, particularly in estimates of pRF size. The manipulation of eccentricity scaling played an important role in pRF size estimation; size-invariant bars returned in pRF sizes in multiple cortical locations comparable to previous studies (Larsson & Heeger, 2006; Dumoulin & Wandell, 2008; Amano et al., 2009; Winawer et al., 2010), while eccentricity-scaled stimuli resulted in smaller pRF size predictions (c.f. Binda et al., 2013). In particular, the difference in pRF size was more marked for highly eccentric representations when compared to logarithmically-scaled bars and simultaneous wedge and ring stimuli. When examining extrastriate regions higher in the visual system hierarchy than early retinotopic cortices a similar pattern was found; here the effects were more marked, as these regions tend to contain voxels with larger pRFs. This was particularly true for areas such as V5/MT+ that may be more susceptible to biases by stimulus configuration compared to striate cortex. Differences in pRF size estimation may be due to the relatively large portion of the visual field covered by

the logarithmically-scaled apertures, where larger field coverage at the periphery stimulates the larger receptive fields more effectively. The large field coverage design is intended to more closely reflect the known distribution of receptive field sizes in cortex; by matching net stimulus coverage with the total cortical extent, it could be argued such a design provides a more accurate estimation of receptive field properties, by incorporating the known constraints of cortical magnification. A further consideration is the possible mediation of pRF size estimates by non-classical receptive fields exerting suppressive effects. In the case of the size-invariant stimulus the suppressive effect will be minimized, as the transient bar is likely to cover a limited fraction of the non-classical receptive fields in more eccentric locations and therefore return a larger pRF size estimate. In contrast, stimuli scaled for cortical magnification have increased coverage of the non-classical receptive fields, therefore potentially increasing the contribution of surround suppression and effectively reducing the pRF size estimate. Such effects only become apparent at highly eccentric representations, where suppressive contributions are spatially differentiated by the two stimuli configurations. Previous work extended the pRF model to incorporate inhibitory surround interactions rather than merely describing it by a two-dimensional Gaussian as in the present experiments (Zuiderbaan et al., 2012; Schwarzkopf et al., 2014). By accounting for the extent and strength of inhibitory interactions, the differences in pRF sizes we observed in the different stimulus conditions could be reduced. However, in practise the centre-surround pRF model does not typically differ substantially from the standard two-dimensional Gaussian model (e.g. Schwarzkopf et al. 2014).

An additional consideration regarding the influence of stimulus design on pRF size estimates, is the presence of mean luminance blank periods during stimulation. These periods allow the estimation of baseline activity at a given pRF under visual stimulation, without modulation by contrast and spatial frequency. This is particularly relevant for regions with large receptive field sizes, where baseline activity may not be easily estimated unless the stimulus aperture is removed (Dumoulin & Wandell, 2008). Arguably, modulation of the duration and temporal position of mean luminance periods may affect the pRF model estimates, including receptive field position and size. Inadequate sampling of mean luminance periods in a given stimulus design would lead to overestimation of the baseline response of large pRFs and consequently, under-estimation of pRF size. To test this, we performed a control analysis where the number of mean luminance volumes was modulated, and compared model estimates derived. This analysis revealed only very small differences in goodness of fit, emphasising the differences in pRF estimates observed between experimental conditions were not trivially explained by the length or temporal positioning of mean luminance periods.

pRF modelling as implemented here and in previous literature relies on the assumption that a linear spatial summation of discrete components of a receptive field form an accurate

picture of the whole receptive field. Recent work has shown non-linear spatial summation effects in striate and extrastriate cortex (Kay et al., 2013). The violation of such assumptions likely plays a role in the estimation of pRF size, as the spatial pattern of different stimuli conditions present different spatial integration problems, which may interact with non-linear summation effects, particularly over large receptive field locations in extrastriate regions. In addition, long-range suppression effects from distant spatial representation may play a further role in modulating estimated pRF sizes (Nurminen et al., 2010). Again, the significantly larger coverage of logarithmically-scaled or simultaneous wedge and ring stimulation is likely to lead to increased long-range suppression, and therefore reduced pRF size estimates. Whether the estimates derived from size-invariant or cortical magnification-scaled stimuli are a more veridical reflection of the underlying neuronal receptive field, remains unclear.

Finally, we found a discrepancy between eccentricity estimates from phase-encoded models compared to those based on pRF modelling of the same data, especially in more central locations. While it is possible that the particular pRF model used here introduces other biases, these results are in agreement with the previous literature (Dumoulin & Wandell, 2008) suggesting that phase-encoded methods consistently misestimate pRF eccentricity representation. Phase-encoded methods infer the pRF centre location from the peak of the signal; however, particularly for ring stimuli, the maximal response may not occur when the stimulus passes the pRF centre, thus resulting in poor estimation of positions in near-foveal representations. While the ground truth of eccentricity must be determined empirically, one indication that this discrepancy indeed reflects a bias in phase-encoded methods is that it is a function of relative, not absolute eccentricity (i.e. it depends on where a given pRF falls relative to the maximum eccentricity of the mapping stimulus, regardless of its absolute eccentricity). Therefore, model-based approaches are likely to be superior to phase-encoded analysis for the estimation of visual field position.

In summary, we have demonstrated the effects of stimulus configuration on model-based pRF estimates and identified two stimulus design factors influencing model estimates. Accounting for cortical magnification played a significant role in the estimation of pRF size, with eccentricity-scaled stimuli returning smaller pRF sizes, particularly in eccentric locations and regions with known large receptive fields (e.g. V5/MT+). Choice of Cartesian or polar coordinate-based stimuli influenced both model accuracy and predictive power, with the bar stimulus providing higher accuracy and lower predictive power, while the simultaneous wedge and ring stimulus afforded higher power, with a reduction in accuracy. Here, we demonstrate that a novel simultaneous wedge and ring stimulus provides robust model fits in a significantly reduced acquisition time, while providing comparable parameter estimates in early visual cortex, and smaller pRF size estimates in higher visual areas when compared to previously reported stimulus configurations. The multi-aperture wedge and

ring stimulus is therefore recommended for applications involving populations where scan time is restricted or where prolonged scan sessions are not desirable, but where accurate estimation of pRF parameters is required.

4.6 Conclusion

In summary, we have demonstrated the effects of stimulus configuration on model-based pRF estimates and identified two stimulus design factors influencing the quality of results derived. The assessed stimulus configurations revealed inefficiency in using the standard single and size-invariant bar aperture. Instead, we recommend an eccentricity-scaled, multi-dimensional stimulus configuration for accurate parameter estimation when limited acquisition time is a practical limitation, such as in clinical populations. In the following chapters eccentricity-scaled, 'wedge and ring' stimuli are used for retinotopic mapping and pRF parameter estimation in both healthy and albino populations.

Chapter 5

Extrastriate projections in human optic radiation

5.1 Abstract

The human optic radiation is the main pathway for conveying visual input to occipital cortex, but it is unclear whether it projects beyond primary visual cortex (V1). In this study, we used functional MRI mapping to delineate early visual areas in 30 healthy volunteers and virtually trace the course of the optic radiation between the lateral geniculate nucleus and these areas with diffusion tractography. The objectives for this study are two-fold; first, to determine the termination area of the optic radiation as reconstructed with diffusion tractography and second, to establish the normative anatomical description and methodological framework for investigating subcortical and cortical white matter pathways in albinism.

Direct thalamo-cortical projections to areas V2 and V3 were found in all hemispheres tested, with a distinct anatomical arrangement of superior-inferior fibre placement for dorsal and ventral projections, respectively, and a medio-lateral nesting arrangement for projections to V1, V2 and V3. Finally, segment-specific microstructure was examined, revealing sub-fascicular information. This is to date, the first in vivo demonstration of direct extrastriate projections of the optic radiation in humans. In addition, this work demonstrates method fusion in MRI as an approach to resolve function-structural relationships in the visual system which can be applied to clinical population such as albinism.

5.2 Introduction

The optic radiation (OR) is the most prominent white matter relay in the visual system, conveying information from the lateral geniculate nucleus (LGN) to the occipital cortex. There has been considerable interest in the neuroanatomy and organisation of the OR, as it remains an area of specific risk in resection of the anterior temporal lobe (Sincoff et al., 2004). Such resections can lead to unintended damage to the OR, leading to visual field defects in 48-100% of patients undergoing anterior temporal lobe resections (Winston et al., 2011).

The human OR has been classically described in post-mortem dissections (e.g. Ebeling & Reulen, 1988) and histological slices (Wahler-Lück et al., 1991; Bürgel et al., 1999) and its anatomical course is well documented. Originating at the LGN, the OR is divided into three distinct fibre bundles; anterior, central and posterior. The anterior bundle, runs anteriorly above the temporal horn of the lateral ventricle, forming Meyer's loop over the temporal lobe before turning posteriorly. The central bundle projects laterally from thalamus across

the roof of the temporal horn. The posterior bundle runs directly posterior from LGN and joins the other bundles, with all three blending at the level of the sagittal stratum (Peuskens et al., 2004). The merged fibres then run posteriorly and terminate in the vicinity of the calcarine sulcus (Rubino et al., 2005). These three anatomical bundles convey information of different portions of the visual field, with the anterior, central and posterior bundle representing the upper, central and lower visual field, respectively (Peltier et al., 2006; Pujari et al., 2008; Párraga et al., 2012).

More recently, the OR has also been visualized in vivo using diffusion MRI tractography (Basser et al., 2000). Early reports implementing diffusion tensor methods reconstructed the bundle division of the OR (Catani et al., 2003), while more recent work using probabilistic approaches showed reliable estimation of the course of the OR in agreement with post-mortem descriptions (Sherbondy et al., 2008; Clatworthy et al., 2010; Hofer et al., 2010). Tractography reconstructions of the OR have proven useful beyond providing an anatomical description, particularly in presurgical planning (Powell et al., 2005; Yogarajah et al., 2009) but also in intra-operative image guidance (Daga et al., 2012; Winston et al., 2012), and for studying microstructural changes in disease (Bridge et al., 2009; El-Rafei et al., 2011; Kolbe et al., 2011; Groppo et al., 2012).

Despite the growing interest, little work has been conducted exploring the functional significance of white matter fibres – i.e. what representations do distinct fibre populations carry from one region to another (but see Dougherty et al., 2005; Kim et al., 2006; Saenz & Fine, 2010). In the case of the OR, spatial visual information is highly segregated; both the LGN (Chen et al., 1999; Schneider et al., 2004) and occipital cortex (Tootell et al., 1998; Wandell et al., 2011) follow a retinotopic organisation with direct connections between homologous representations of visual space (Reid & Alonso, 1995). As a consequence, damage to specific portions of the OR leads to blindness in a specific segment of the visual field, such as hemianopsia or quadrantanopsia (e.g. Barton et al., 2005).

While the functional segregation of visual field quadrants in OR bundles is well established, it remains unclear whether these projections reach beyond primary visual cortex (V1). In animal models such as the cat (Garey & Powell, 1971; Maciewicz, 1975) and flying fox (Manger & Rosa, 2005) LGN projections to areas V2, V3 are well established in tracer studies. In the macaque, anterograde and retrograde tracer evidence suggest a direct projection to extrastriate areas (Yukie & Iwai, 1981), specifically areas 18 and 19 (Benevento & Yoshida, 1981; Fries, 1981). While this hypothesis has been contested by negative findings (Yoshida & Benevento, 1981; Benevento & Standage, 1982), later experiments using fluorescent dyes support the presence of a direct LGN to V2 projection (Bullier & Kennedy, 1983; Kennedy & Bullier, 1985). The intriguing possibility of a direct extrastriate projection in the macaque, the predominant model species used to inform our

understanding of visual system architecture, begets the question of whether this organisation also exists in the human. This study presents the first in vivo evidence for direct OR projections to regions V2 and V3 in human occipital cortex using diffusion MRI tractography.

5.3 Materials and methods

5.3.1 Participants

30 healthy adults (12 males, age range 21-35) took part in the study. All participants had normal or corrected-to-normal visual acuity and provided written informed consent. This study was approved by the UCL Research Ethics Committee (University College London, London, United Kingdom).

5.3.2 Behavioural measures

Variability in anatomical macro- and micro-structure is known to correlate with both demographic factors (e.g. sex, age) and with behavioural markers (Le Bihan, 2003). In order to determine if inter-subject variability in visually guided behaviour was predictive of anatomical markers, we collected behavioural measures for hand and ocular dominance. Specifically, we hypothesised that interhemispheric differences may be correlated with a statistical preference for use of the left or right visual field in everyday behaviour, which in turn is likely reflected in hand dominance preference. We also collected ocular dominance as a control metric, as no relationship between eye dominance and anatomical variability was expected.

In order to assess hand dominance, we used the Edinburgh Handedness Inventory, a 10-item self-report questionnaire probing the lateralization of hand use in everyday tasks (Oldfield, 1971). Hand dominance scores were rated on a scale between -100 to 100, with negative numbers indicating a tendency towards left-handedness and positive numbers a tendency towards right-handedness. Participants scored an average of 84.76 ± 6.54 SEM, with 27 participants identified as right-handers (scoring over 50) and 1 participant identified as left-handed (scoring under -50).

Ocular dominance was assessed using the hole-in-card test, also known as the Dolman method (Seijas et al., 2007). The participants held a 300 x 220 mm card at arms length and view a 130x130 mm object, in this case a painting, at approximately 3 m distance through the 25 mm hole on the centre of the card. The participant alternatively occluded one eye to

establish which eye is aligned with the distant object. The eye that upon occlusion causes the image of the target to disappear is considered the dominant eye. While the hole-in-card shows only moderate agreement with alternative tests of ocular dominance (Kommerell et al., 2003), it has high test-retest reliability (Rice et al., 2008) and was preferred due to its widespread use in the literature. Eye dominance as assessed with the hole-in-card test was a nominal measurement, with 14 left eye dominant and 16 right eye dominant participants. No significant correlation between demographic factors (age, gender) and behavioural measures (hand and eye dominance) were observed (Pearson's r , all pairwise comparisons $p > 0.05$).

5.3.3 Visual stimulation

Stimuli were generated in MATLAB (v8.0, Mathworks Inc., Natick, MA, USA) using Psychtoolbox (v3.0, Brainard, 1997; Pelli, 1997) and displayed on an MRI-compatible LCD monitor. The participant viewed the monitor through a mirror while laying supine in the bore of the scanner. The visual display subtended 10.40° of visual angle from fixation.

The stimulus was previously described in Chapter 5 and identical to the 'wedge and ring' configuration therein, which was found to be highly efficient for population receptive field (pRF) modelling. Briefly, it consisted of a 10.40° radius disc of a dynamic, high-contrast tessellated pseudo-checkerboard with a drifting 'ripple-like' pattern that varied across time in spatial frequency and phase. Mean luminance of the stimulus was 132.29 cd/m^2 .

The stimulus was presented through two simultaneous apertures: a wedge section of 17.14° angle rotated clockwise or counter-clockwise along the polar dimension and a ring section expanded or contracted eccentrically, scaling logarithmically between 0.11° and 4.62° width. Apertures changed position every 2.376 s, on the onset of each EPI volume acquired. Both apertures cycled at independent frequencies: 21 and 15 volumes per revolution respectively. A single run consisted of 10 wedge and 14 ring revolutions, followed by 24 volumes of mean luminance, totalling 238 volumes per run. Two runs were conducted, the first with clockwise wedge and expanding ring motion and the second with counter-clockwise wedge and contracting ring motion.

In addition to the 'wedge and ring' mapping stimulus, a second condition was presented, consisting of a short photic burst of a circular 10.40° radius aperture of the same pattern, presented for 1 volume and followed by 14 volumes of equiluminant grey background. Ten runs were conducted, totalling 150 volumes acquired.

Throughout both conditions, a 0.30° black centre-point cross was presented to aid fixation. Participants were instructed to attend and respond when the cross flashed in red, which

occurred in a semi-randomized fashion, with 100-150 events per run, each lasting 200 ms. Participant responses were recorded via an electronic response button and monitored to ensure engagement with the task, and therefore consistent eye fixation.

5.3.4 MRI acquisition

MR images were acquired on a 1.5T Avanto MRI system using a 32-channel head coil (Siemens Healthcare, Erlangen, Germany). The experimental session was divided into two consecutive sections taking place on the same day. For the first section only the bottom elements of the head coil were used, to avoid visual field restrictions. A gradient-echo EPI sequence was used (TR = 2376 ms, TE = 30 ms, 33 ascending slices, 18% inter-slice gap), with off-axial acquisitions maximizing occipital lobe coverage and effective resolution of 3 mm³ isotropic voxels for 4 participants and 3.3 mm³ isotropic voxels for 26 participants. A T1-weighted anatomical image (TR = 11 ms, TE = 4.94 ms, resolution = 1 mm isotropic) was acquired in-plane with the functional images to aid registration and B0 field maps (TR = 487 ms, TE₁ = 5.28 ms, TE₂ = 10.04 ms) were acquired to estimate local field inhomogeneities. For the second section, the full head coil arrangement was used and a further anatomical T1-weighted volume (TR = 11 ms, TE = 4.94 ms, resolution = 1 mm isotropic) was acquired to reconstruct the cortical surface, as well as a diffusion-weighted EPI protocol with 60 non-collinear gradient directions at b = 1000 s/mm² and 3 b = 0 s/mm² reference images (TR = 7300 ms, TE = 81 ms, maximum gradient amplitude = 40 mT/m⁻¹, 60 slices, resolution = 2.5 mm isotropic).

5.3.5 Functional imaging analysis

T1-weighted anatomical images were processed with FreeSurfer (Dale et al., 1999; Fischl et al., 1999). Volumes underwent automated segmentation to generate grey and white matter boundaries, and the grey matter surface reconstructed to create a smooth two-dimensional representation of cortex.

Functional EPI images were pre-processed in SPM8 (Wellcome Trust Centre for Neuroimaging, <http://www.fil.ion.ucl.ac.uk/spm>). All images were bias-corrected, realigned to the first image of each run to reduce movement artefacts, unwarped to correct for field inhomogeneities and slice timing-corrected to reduce variation in the time-series introduced by the timing of the slice acquisition. Finally, a two-step co-registration was performed on all functional images, by first registering to the in-plane anatomical T1-weighted image and then registered to the anatomical image acquired with the full 32-channel head coil array, in order to maximize registration precision.

fMRI data from the mapping condition were modelled using a pRF model using in-house software in MATLAB. Briefly, model predictions were based on the a priori knowledge of stimulus position during stimulation and the assumption of single Gaussian receptive field (Dumoulin & Wandell, 2008). This model prediction was then convolved with the haemodynamic response functions (HRF), individually estimated for each participant by fitting the time-series acquired during photic burst stimulation with a double gamma function (Friston et al., 1995b). Mapping data were sampled from volume-space to the cortical surface reconstructions, spatially smoothed (FWHM = 8.3 mm) and compared to the model predictions via Pearson's correlation coefficient. Parameter values of the predictive model that yielded the highest correlation were then used as the starting point for fitting the un-smoothed mapping data, using the Nelder-Mead algorithm for unconstrained nonlinear minimization (Lagarias et al., 1998). The winning model outputs were then smoothed across the cortical surface (FWHM = 5 mm) and projected onto the inflated cortical surface.

Polar angle estimates derived from the pRF model were displayed on the reconstructed cortical surface to delineate region boundaries between areas V1, V2 and V3 according to their retinotopic organisation (Serenó et al., 1995; DeYoe et al., 1996; Engel et al., 1997). Dorsal and ventral components of these areas were identified, creating six regions per hemisphere sampled: V1d, V1v, V2d, V2v, V3d and V3v. One additional region, V3A on the anterolateral boundary of dorsal V2, was delineated as a control area. Region definitions were then transformed into volume space to inform tractography.

5.3.6 Diffusion imaging analysis

Diffusion-weighted images were registered to the first, non-diffusion-weighted volume ($b = 0$) to correct for head motion and eddy-current artefacts using FSL-FDT (Behrens et al., 2003). Data were then analysed with MRtrix (Tournier et al., 2012) by fitting a diffusion tensor model and calculating fractional anisotropy (FA) and mean diffusivity (MD) maps. FA maps were subsequently thresholded to retain values at or above 0.7 and spatially eroded to create a white-matter skeleton mask. Voxels retained in the white matter skeleton were used to estimate the diffusion response function. The full diffusion data were then fitted with a constrained spherical deconvolution model (maximum harmonic order = 8) to produce a multi-fibre model of white matter diffusion at each voxel.

In order to reconstruct the path of the OR, a seed-to-target tractography approach was used. The LGN was manually defined on T1-weighted images for each participant, based on anatomical markers (Fujita et al., 2001) and used as 'seed' regions. While Fujita et al. recommend the use of proton density images for LGN delineation, advances in MRI sequence development since publication have allowed identification of the structure on T1-

weighted images based on the anatomical landmarks described therein. We therefore implemented the same landmark approach described in Fujita et al. (2001) on T1-weighted images.

Manual delineations aimed at minimizing contributions from neighbouring subcortical structures, including the pulvinar and superior colliculus, therefore a conservative definition of the LGN was preferred. Functionally defined visual maps were registered to diffusion space, and a single ROI consisting of voxels belonging to either area V1, V2 or V3 was used as a single target region in probabilistic tractography (step size = 0.2 mm, angular threshold = 1 mm, FA threshold = 0.1, streamlines = 10,000). This procedure was performed independently for each hemisphere, for each participant. A single target ROI approach was adopted in order to ensure unbiased sampling of the cortical targets, allowing the estimation of the number of streamlines terminating in each target area, rather than defining said number a priori by tracking each target region individually. The direction of tracking, thalamus to occipital, ensured an accurate reconstruction of the highly angular path of the OR at the level of Meyer's loop.

Resulting OR streamlines were displayed in TrackVis (<http://www.trackvis.org>) and manually constrained to reject anatomically incorrect streamlines. The following heuristic rules were applied; streamlines were rejected if they were a) crossing to the contralateral hemisphere, b) projecting superiorly from the LGN, c) projecting antero-inferiorly, into the temporal pole and d) projecting parallel to the medial wall of the posterior horn of the lateral ventricle. An average of 67% of streamlines were rejected (mean number of streamlines rejected = 6738 (67%) \pm 1341 (13%) *SEM*). This heuristic approach constrained the tractography to the known anatomical course of the OR (Ebeling & Reulen, 1998; Párraga et al., 2012), with the aim of increasing the confidence on the virtual reconstruction of the white matter tract and ensuring accurate sampling of microstructural parameters. The procedure was carried out independently for each hemisphere analysed.

5.3.7 Tract segmentation

OR tractography results were segmented using two different schemes; one constrained by the representations of upper and lower visual field (visual field-based) and one based on visual map hierarchy (hierarchy-based). These approaches were taken in order to segregate functionally-distinct segments of the optic radiation that are relevant to cortical sensory processing. The division of the visual field into upper and lower hemifields is a feature of retinotopic organisation that is preserved from retina, to the LGN and through the fibre arrangement of the optic radiation into cortical termination sites. Selective damage to the optic radiation causes specific visual loss in the upper or lower visual fields (Winston et al., 2012), indicating a functional division present along the course of white matter fibres within

the optic radiation. We therefore expect to segment the optic radiation into upper and visual field bundles based on their respective dorsal and ventral termination zones.

In early cortical processing, area V1 is typically considered the termination site for the optic radiation, but as we have seen contradictory evidence exists in the cat (Garey & Powell, 1971; Maciewicz, 1975) and macaque (Bullier & Kennedy, 1983; Kennedy & Bullier, 1985). We therefore hypothesise that the optic radiation can be further sub-divided into distinct projections to cortical areas V1, V2 and V3 in the human. In both visual field-based and hierarchy-based segmentations, a Boolean approach was implemented, using the inclusion (AND) and exclusion (NOT) criteria defined below.

For visual field-based segmentations, streamlines in the OR terminating in dorsal visual areas, representing the lower visual field (V1d, V2d, V3d) were classified as belonging to the 'dorsal' segment, while streamlines terminating in ventral areas, representing the upper visual field (V1v, V2v, V3v) were classified as part of the 'ventral' segment. In both cases, streamlines common to both upper and lower visual field representations were excluded.

For hierarchy-based segmentations, streamlines were divided into those projecting exclusively to each of the following cortical areas: V1, V2 and V3. For example, the V1 projection segment consisted of streamlines projecting to either V1d or V1v, but not V2 or V3 maps. In all cases, dorsal and ventral components were combined.

In summary, two segmentation schemes were applied to the OR in each hemisphere, resulting in five segments: dorsal, ventral, V1, V2 and V3 projections of the OR.

5.3.8 V3A control region

An additional condition with a control ROI was carried out in order to estimate the rate of acceptance of invalid streamlines, as an approximation of the false positive rate in the probabilistic tractography method implemented. Area V3A was chosen as the control ROI as no direct thalamic projections were expected based on the human and macaque literature. This region was selected for three principal reasons; (1) it is anatomically adjacent to area V3, and therefore similarly likely to be targeted by errant streamlines caused by errors in the tractography algorithm, (2) it is of a similar volume to areas V2 and V3, providing an equivalent target mass to the tractography algorithm and (3) no known reports in the human or macaque post-mortem tracer literature report a white matter bundle connecting LGN and V3A. While absence of evidence is not evidence of absence, area V3A has been widely studied in the macaque and more recently in the human (for a review, see Orban et al., 2004) with no report of direct anatomical connectivity to subcortical LGN.

Tractography was performed between the LGN and a single target region comprising areas V1, V2, V3 and V3A. The ratio of streamlines terminating in the control region against those terminating in areas V1, V2 or V3 was calculated and used as an estimate of the false positive rate of the method.

5.4 Anatomical results

Both striate and extrastriate projections of the OR were identified in all 60 hemispheres tested. Key structural characteristics were observed for both segmentation schemes, which are described in turn.

5.4.1 Visual field-based segmentation

Dorsal and ventral segments of the OR follow parallel, but distinct anatomical courses (see **Figure 5.1**). The dorsal segment projects laterally from the LGN and maintains a superior profile for the rest of its posterior course towards the occipital lobe. The ventral segment traces a similar anterior path, covering both the anterior and central bundles including Meyer's loop, but then follows an inferior profile spanning the whole anterior-posterior route. From an axial vantage point, the ventral segment fans out more laterally as it approaches occipital territories, while the dorsal segment retains a medial profile. This anatomical arrangement was observed across participants, with the superior-inferior division of the long segment of the OR being a marked feature visible in all hemispheres tested (see **Figure 5.2**).

5.4.2 Hierarchy-based segmentation

The arrangement of V1, V2 and V3 segments follows a media-lateral nesting pattern, with the V1 segment at its centre, surrounded by the V2 segment, which in turn is surrounded by V3 (**Figure 5.3**). All three segments follow a similar curved course, with the V1 segment being the most medial part of the tract, and V2 and V3 segments subsequently more lateral (see **Figure 5.4**). It is immediately apparent that the V1 segment is substantially larger than the V2 or V3 segments, which is in agreement with the existing idea of the OR as a primarily striate projection and also the larger cortical area span of V1 compared to V2 or V3 (Yan et al., 2009). The overall nesting arrangement was again observed in all tested hemispheres.

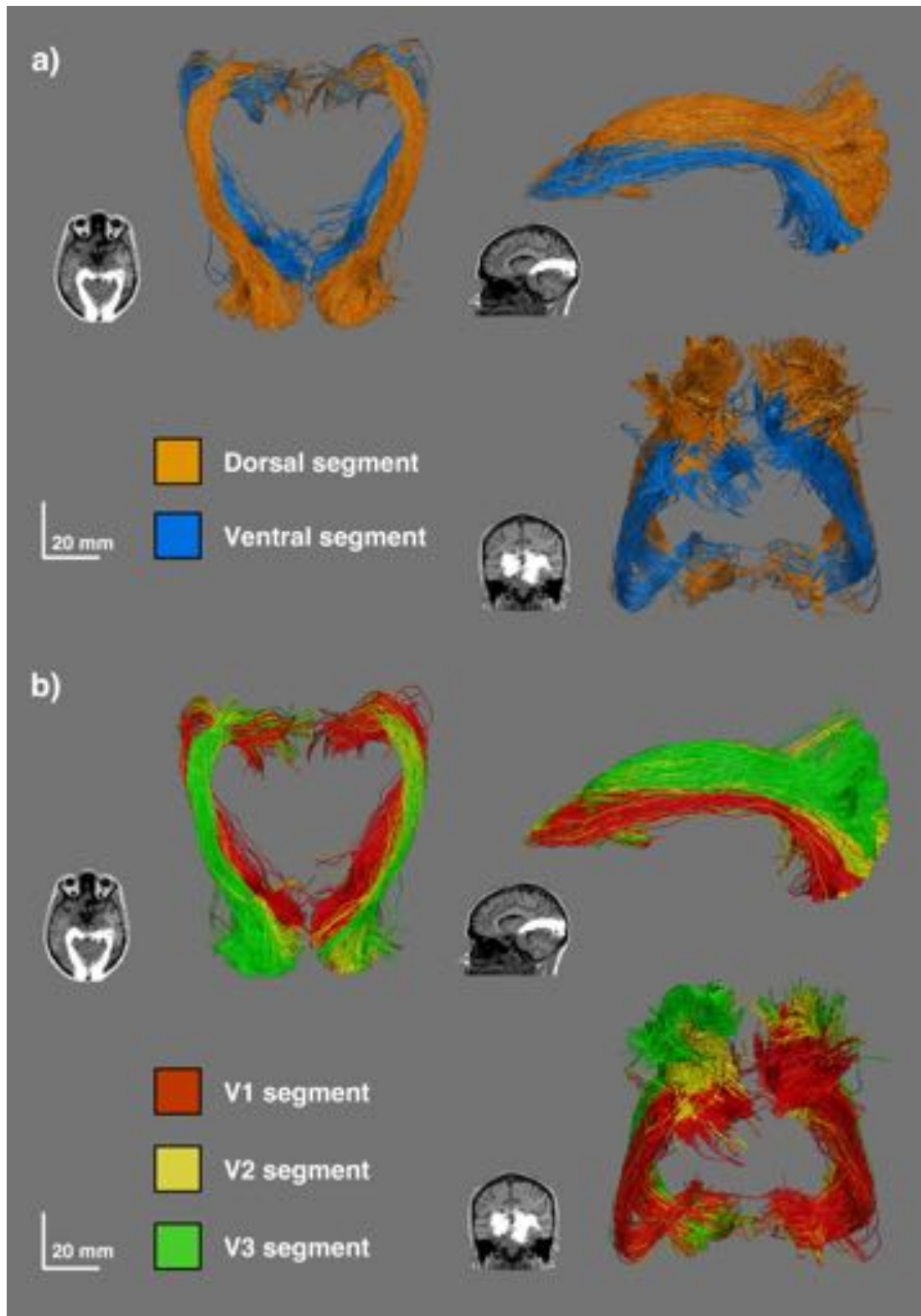


Figure 5.1 Segments of the optic radiation in a representative participant. (a) Visual field-based segmentation, with dorsal segments following a superior profile, and ventral streamlines populating the more inferior and lateral parts of the tracts. (b) Hierarchy-based segmentation, with V1, V2 and V3 projections displayed. V1 streamlines form the most medial segment, while V2 and V3 form a nesting pattern dorso-laterally.

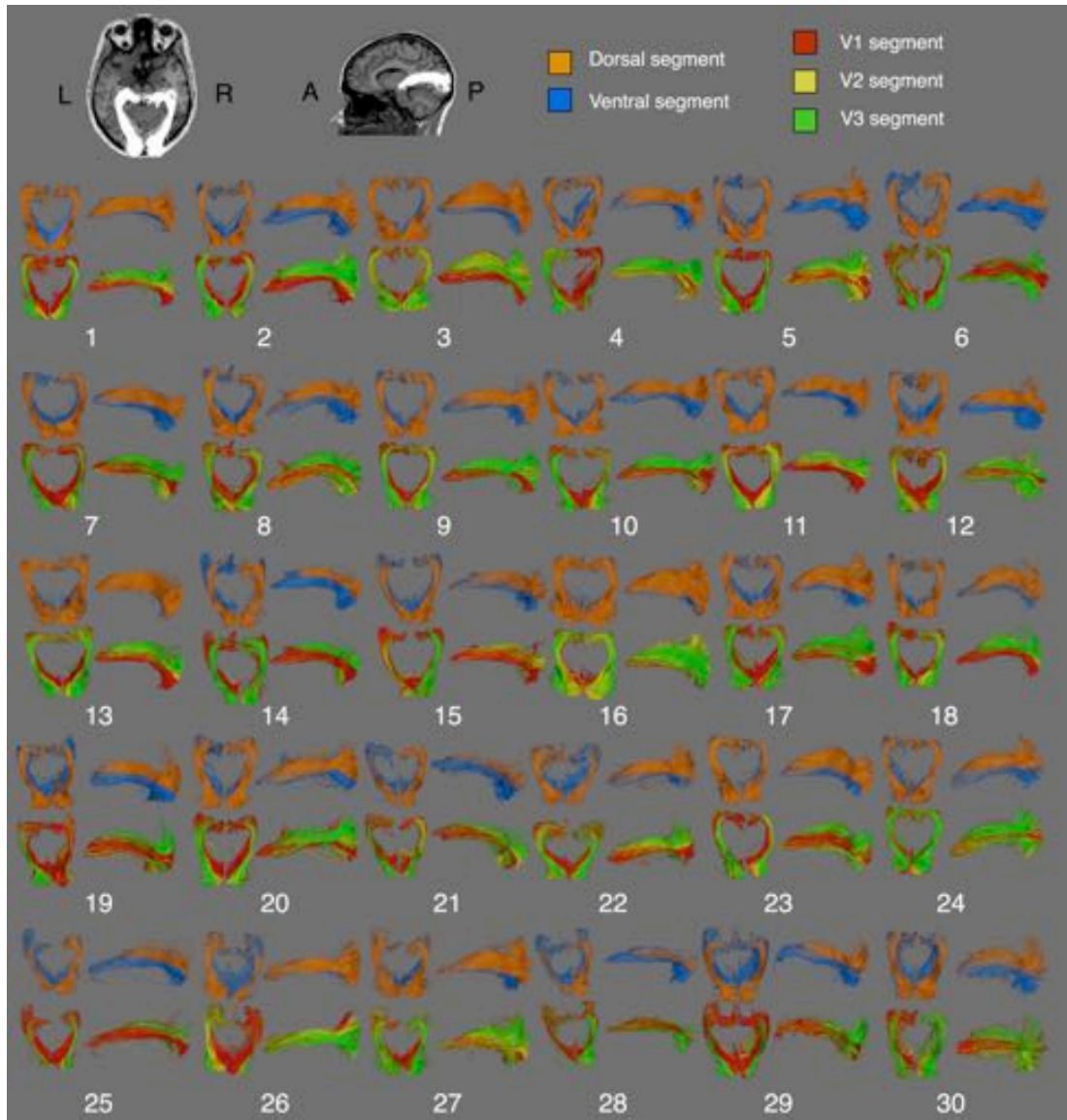


Figure 5.2 Segments of the optic radiation in all participants tested. Two views are presented, an axial view from a superior vantage point, and a left-sided sagittal view from a lateral vantage point. Visual field-based segmentations are presented in the top row, and hierarchy-based segmentations in the bottom row. Consistent anatomical courses are seen for all optic radiation segments, and the relative positioning of both dorso-ventral and V1-V2-V3 segments is conserved across all participants.

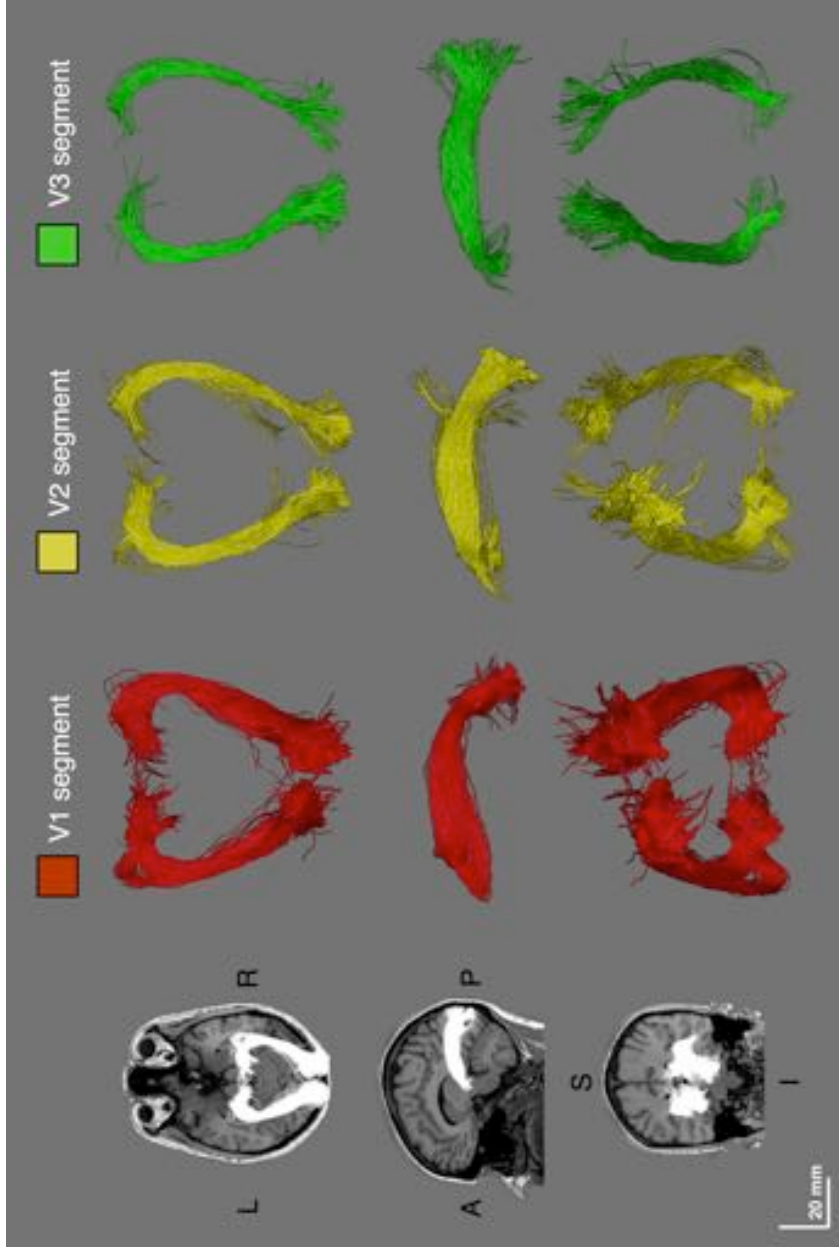


Figure 5.3 Hierarchy-based segmentation of the optic radiation in a representative participant. Segments terminating in regions V1, V2 and V3 are displayed, demonstrating the anatomical course of each segment. The V2 and V3 segments display similar course to V1, with a clearly defined lateral exit from the LGN, a highly angular turn at Meyer's loop and a prolonged posterior-medial course towards the occipital lobe. Note the termination zones for the V2 and V3 segments correspond to the more lateral positions of visual areas V2 and V3, in their dorsal and ventral segments abutting the occipital pole.

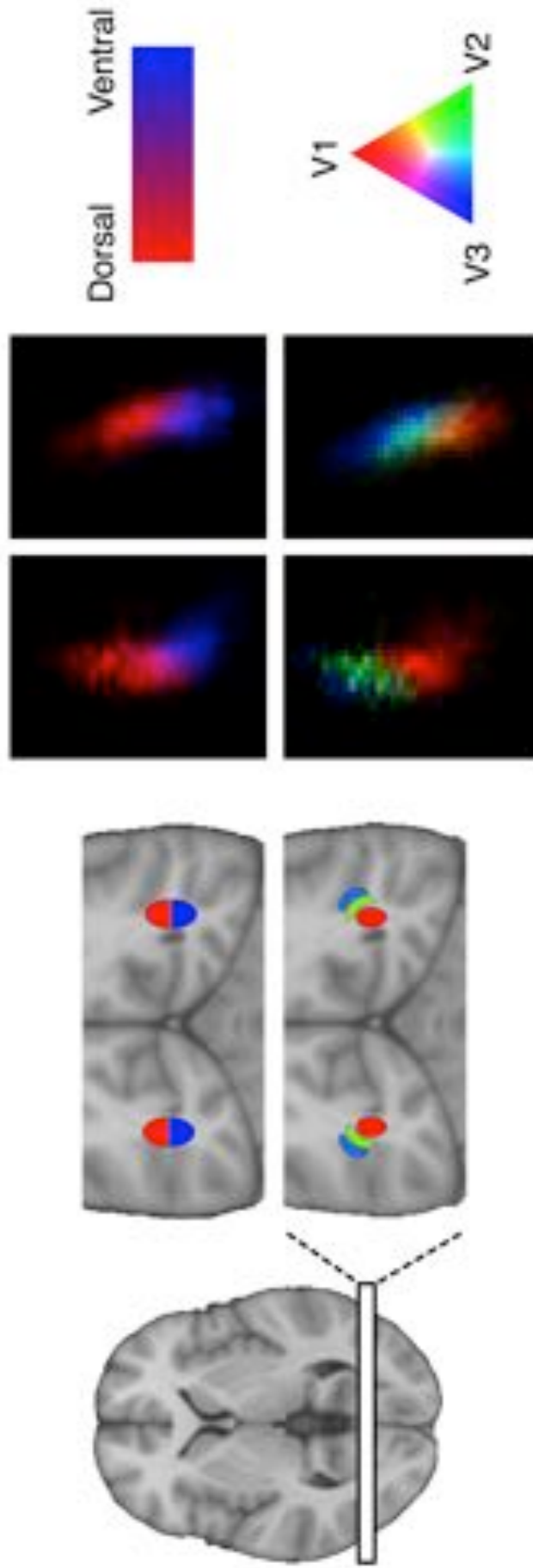


Figure 5.4 Visitation maps for optic radiation tractography in a representative participant, visualized on a single coronal slice immediately posterior to the lateral ventricle. Visual field-based segmentation shows the superior-inferior division of streamlines, in red and blue. Hierarchy-based segmentation discriminates streamlines into dorso-lateral nesting compartments, in red, green and blue. The dorsal portion of V2 and V3 segments of the optic radiation are over-represented, leading to a characteristic nesting pattern in the hierarchy-based segmentation.

5.4.3 False positive rate estimation

In order to assess the validity of streamline count estimations, a control condition was introduced where the ratio of streamlines terminating in area V3A against those terminating in regions V1, V2 or V3 was used as an estimate of the false-positive rate of the tractography method. Under this condition, a significantly smaller proportion of streamlines terminated in the control site (*Mean* = 85 (4%) \pm 24 (1%) *SEM*) compared to either area V2 (*Mean* = 427 (20%) \pm 76 (28%) *SEM*; pairwise t-test, $t = 6.33$, $df = 59$, $p < .001$) or V3 (*Mean* = 423 (20%) \pm 62 (23%) *SEM*; pairwise t-test, $t = 8.86$, $df = 59$, $p < .001$). Furthermore, when the same data were normalized based on the surface area (mm^2) of the corresponding target area, the hypothesized extrastriate projections to V2 ($t = 7.18$, $df = 59$, $p < .001$) and V3 ($t = 9.80$, $df = 59$, $p < .001$) retained a significantly greater proportion of streamlines when compared to the control area. This indicates that projections to areas V2 and V3 were not only larger than to the control site in real terms, as estimated by streamline count, but also in relative terms, while accounting for the cortical extent of the target region (see **Figure 5.5**).

5.5 Microstructural results

Microstructural measures in diffusion MRI are well established biomarkers tissue integrity and myelination (Ciccarelli et al., 2008). Specifically, fractional anisotropy (FA) in healthy tissue reflects coherent axonal bundle arrangement, while mean diffusivity (MD) can be linked to the presence of crossing fibres or less tightly packed axonal bundles (Catani et al., 2002). Due to the uncharacterised structure of the extrastriate projections reported in the study, we assessed the relative microstructural integrity of the different optic radiation segments in an exploratory analysis.

Microstructural markers were sampled by identifying the voxels traversed by all streamlines belonging to each tract segment, and computing the mean value for FA and MD in those voxels for each hemisphere. The number of streamlines retained in each tract segment was also extracted as a relative measure of segment size.

In order to test whether microstructural markers varied between visual field-based (dorsal, ventral) and hierarchical-based (V1, V2, V3) segments of the OR, we employed a series of mixed factorial ANOVA tests. Univariate models were preferred due to the exploratory nature of the study. All statistical analyses were carried out in SPSS (v21, IBM SPSS Statistics, IBM Corp., Armonk, New York, USA).

5.5.1 Effect of covariates

In order to test the effects of hierarchical segmentation scheme on outcome measures, we performed three independent mixed factorial ANOVAs, one for each outcome measure (FA, MD, streamline count). The ANOVA model incorporated hierarchical segmentation scheme and hemisphere as within-subject variables and age, gender, hand dominance and eye dominance as between-subject variables. These tests revealed no significant main effects or interactions (all effects $p > .05$) of any between-subject variables, namely age, gender, hand dominance or eye dominance. Therefore, in order to increase statistical power, the between-subject variables were dropped and a restricted model, only incorporating the within-subject variables (segmentation scheme and hemisphere) is presented here.

5.5.2 Visual field-based segmentation

Three mixed factorial ANOVA models were tested, examining the effect of visual field-based segmentation on the outcome measures described above. A significant effect of segmentation was found on MD ($F = 29.96$, $df = 1, 29$, $p < .001$) but not FA ($F = 1.80$, $df = 1, 29$, $p = .191$), with MD being higher in the ventral compared to the dorsal segment. For both MD and FA, a significant effect of hemisphere was observed (MD: $F = 102.84$, $df = 1, 29$, $p < .001$; FA: $F = 40.96$, $df = 1, 29$, $p < .001$), with a general tendency towards lower microstructural content in the right hemisphere (reduced FA, increased MD; see **Figure 5.6**).

The increase in mean diffusivity in the ventral segment can be partially attributed to the anatomical course of the two segments described above; with the ventral segment being more proximal to the posterior horn of the lateral ventricle compared to the dorsal segment. It is possible that a partial volume effect with adjacent cerebral spinal fluid influenced the increased diffusivity in the ventral segment. Nevertheless, the lack of concomitant differences in FA between segments suggest other factors, as cerebral spinal fluid contamination typically leads to decreased FA, so microstructural differences between these two segments must be interpreted with caution.

In addition to microstructural markers, a significant effect of segmentation on streamline count was found ($F = 25.04$, $df = 1, 29$, $p < .001$), with a larger streamline count in dorsal segments compared to ventral segments, independent of hemisphere ($F = 4.09$, $df = 1, 29$, $p = .052$).

5.5.3 Hierarchy-based segmentation

Three mixed factorial ANOVA models were tested, examining the effect of hierarchy-based segmentation and hemisphere on FA, MD and streamline count. A significant effect of

segmentation was found on both MD ($F = 92.74$, $df = 2$, 58 , $p < .001$) and FA ($F = 4.52$, $df = 2$, 58 , $p < .05$), with significant interactions of segmentation with hemisphere for both microstructural measures (MD: $F = 34.78$, $df = 2$, 58 , $p < .001$; FA: $F = 48.01$, $df = 2$, 58 , $p < .001$). To further investigate the interaction terms, post-hoc paired t-tests were performed, revealing differential effects of hemisphere on segment microstructure. Bonferroni correction for multiple comparisons was applied across all subsequent post-hoc tests.

For FA, values decreased with cortical hierarchy in the left hemisphere, with significant step-effects between V1 and V2 segments ($t = 5.96$, $df = 29$, $p_{\text{corr}} < .001$) and between V2 and V3 ($t = 8.78$, $df = 29$, $p_{\text{corr}} < .001$). In comparison, the right hemisphere exhibited the opposite effect, with an increase in FA between V1 and V2 segments ($t = 4.88$, $df = 29$, $p_{\text{corr}} < .001$) but no significant difference between V2 and V3 segments ($t = 0.36$, $df = 29$, $p_{\text{corr}} = .999$).

In the case of MD, a reduction of MD was observed with increasing cortical hierarchy, both in left (V1-V2: $t = 6.46$, $df = 29$, $p_{\text{corr}} < .001$; V2-V3: $t = 3.23$, $df = 29$, $p_{\text{corr}} < .05$) and right ORs (V1-V2: $t = 8.64$, $df = 29$, $p_{\text{corr}} < .001$; V2-V3: $t = 3.53$, $df = 29$, $p_{\text{corr}} < .05$).

Finally, the effect of hierarchy-based segmentation on streamline count was assessed, with a significant effect of segmentation ($F = 42.88$, $df = 2$, 58 , $p < .001$) and no interaction with hemisphere ($F = 0.22$, $df = 2$, 58 , $p = .800$). Within each hemisphere, a larger number of streamlines were found in the V1 segment compared to the V2 ($t = 8.04$, $df = 59$, $p_{\text{corr}} < .001$) or V3 segments ($t = 8.15$, $df = 59$, $p_{\text{corr}} < .001$). No significant difference between V2 and V3 segments was found ($t = 0.09$, $df = 59$, $p_{\text{corr}} = .930$).

In order to assess whether the effect of hierarchy-based segmentation on streamline count was driven by the difference in size between target regions, we normalized the streamline counts by dividing each seed-target pair (V1, V2 and V3) by the surface area (mm^2) of its corresponding target region, independently for each hemisphere. A main effect of segmentation was again observed ($F = 10.91$, $df = 2$, 58 , $p < .001$), with no interaction with hemisphere ($F = 0.28$, $df = 2$, 58 , $p = .868$). While the streamline count difference was originally driven by a greater proportion terminating in area V1, following normalization, the streamline count for area V1 was significantly lower when compared to the V2 ($t = 4.51$, $df = 59$, $p_{\text{corr}} < .001$) and V3 projections ($t = 5.64$, $df = 59$, $p_{\text{corr}} < .001$). No significant difference was observed between the V2 and V3 segments ($t = 1.07$, $df = 59$, $p_{\text{corr}} = .864$).

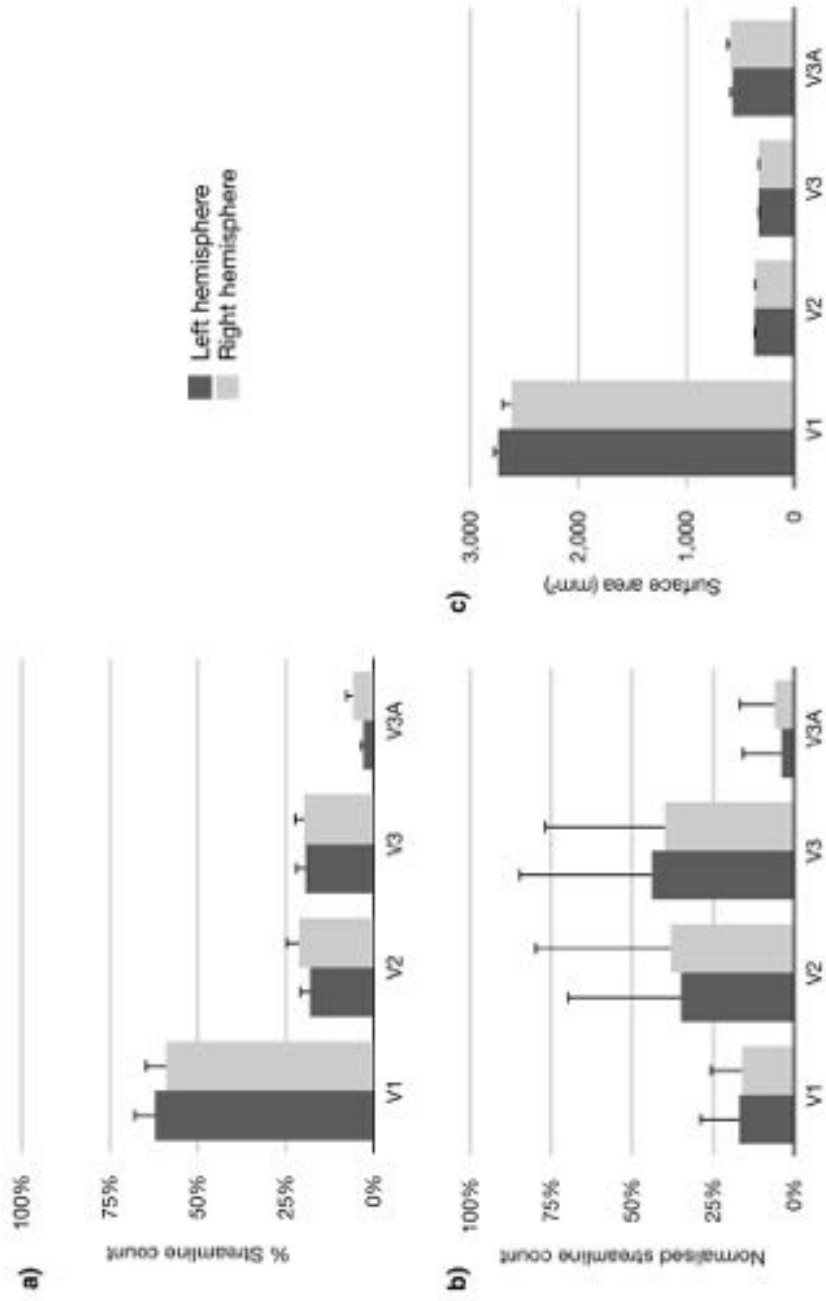


Figure 5.5 Streamline counts for three hierarchy-based segmentations of the optic radiation (V1, V2, V3) and one control region, V3A. Values displayed are (a) number of streamlines as a percentage of all streamlines in the optic radiation, (b) number of streamlines normalized by the surface area of the target region and (c) the surface area of the target region, in mm². Percentage streamlines for each hemisphere total 100%. Error bars indicate SEM.

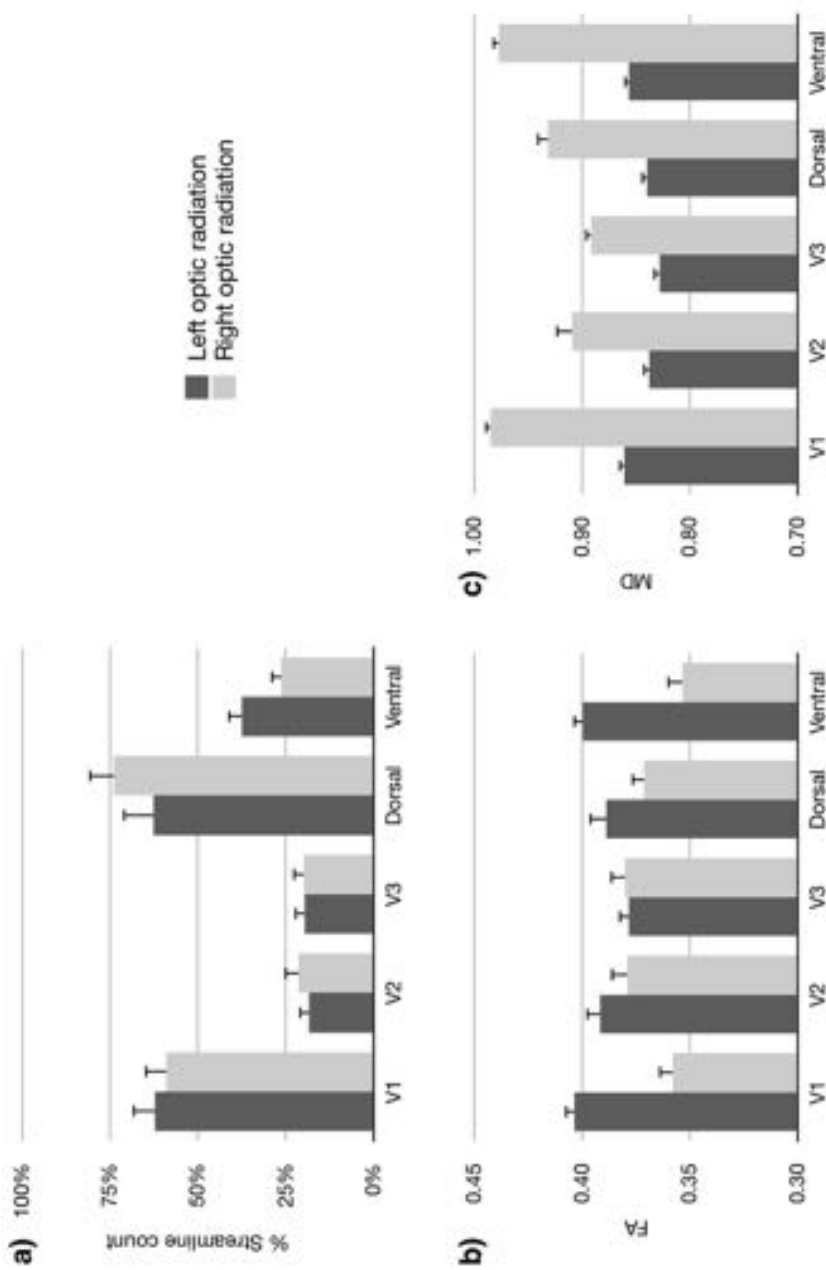


Figure 5.6 Microstructural values across thirty participants for hierarchy-based (V1, V2, V3) and visual field-based segmentation (dorsal, ventral) of the optic radiation. Values displayed are (a) number of streamlines as a percentage of all streamlines in the optic radiation, (b) mean fractional anisotropy (FA) and (c) mean diffusivity (MD). Percentage streamlines for each hemisphere total 100%. Error bars indicate SEM.

5.6 Discussion

In this work, we identified extrastriate projections of the OR to areas V2 and V3 of occipital cortex in humans, in agreement with the macaque literature (Yukie & Iwai, 1981; Benevento & Yoshida, 1981; Fries, 1981; Bullier & Kennedy, 1983; Kennedy & Bullier, 1985) and highlighting the anatomical homology of the retino-geniculate-striate pathway across primate species.

The OR projections to dorsal and ventral representation in occipital cortex follow anatomically distinct courses, with a predominance of upper visual field representation in the anterior bundle of the OR, in agreement with human dissection data (Ebeling & Reulen, 1988; Wahler-Lück et al., 1991; Peuskens et al., 2004; Peltier et al., 2006) and a superior-inferior divide along the anterior-posterior segment. Similarly, the hierarchical projection segments of the OR follow anatomically segregated courses, with a medio-lateral nesting pattern. Both of these findings are consistent with the proposed hypothesis of distinct bundles connecting retinotopic LGN locations with a matching retinotopic representation in occipital cortex.

5.6.1 Relative projection size

A larger V1 projection was observed bilaterally, when compared to connections with V2 and V3, as estimated by the relative number of streamlines terminating in each visual area. This finding is consistent with the idea of the OR as a primarily striate projection, but also with the overall larger cortical area representing V1, when compared to its neighbouring maps V2 and V3 (Yan et al., 2009). We confirmed that cortical area size played an important role in this regard by examining the effects of normalization by target surface area on the observed streamline counts. The direction of the effect was in fact reversed, with areas V2 and V3 displaying proportionally larger number of streamlines terminating at those sites, when compared to the V1 projection. As evidenced here, projections to extrastriate areas V2 and V3 in fact account for a greater proportion of all OR streamlines per mm² of cortical target zones.

Additionally, in order to provide an estimate of false-positive rate of the method implemented, we included a control site, V3A, to analyse the likelihood of generating streamlines to a cortical site where no direct thalamic projections were expected. In comparison to the control condition, projections to areas V2 and V3 were shown to be significantly larger, both in terms of number of streamlines reaching the target, and also when accounting for the surface area of the target zone. These results increase confidence

on the V2 and V3 projections having a true anatomical basis and are unlikely to be false-positive connections arising as an artefact of the probabilistic nature of the tractography algorithm as indicated by the control region V3A that was examined.

5.6.2 Microstructural findings

A hemispheric lateralization effect of OR microstructure was observed in all participants tested, with lower FA and higher MD in the right, compared to the left OR (illustrated in **Figure 5.6**). This result is consistent with the histological literature, where both the cortical (Bürgel et al., 1999) and the white matter area (Weinberger et al., 1982) of the left occipital region are found to be larger in the left than the right hemisphere. This hemispheric asymmetry would cause a detectable difference in microstructural measures, as larger, and more densely packed axonal bundles in the left hemisphere lead to increased FA and reduced MD, as reproduced in this study.

Perhaps more intriguing is the pattern of FA measured in hierarchy-based segmentations, where the left hemisphere displayed increased FA from V1 to V2 and V3, while the right hemisphere displayed an inverse pattern. An overall large tract volume in the left hemisphere, as previously noted, does not fully account for this observation and instead, it points towards a larger affordance of volume in the left OR sustaining a microstructurally robust V1 projection, while this affordance may be diminished in the smaller right OR. In real terms, the differential pattern of FA values across hierarchy-based segments of the OR is a small effect, as the variability between tract segments does not exceed $FA < 0.05$ in any single hemisphere. Nevertheless, such a pattern hints towards potential structural differences in white matter organisation beyond binary hemispheric effects and these findings suggest such variability may apply to specific segments of white matter pathways in isolation.

5.6.3 Role of extrastriate projections

The existence of direct thalamo-cortical projections to extrastriate regions is perhaps not surprising; the visual system can be conceptualized as a hierarchical structure with a high degree of modularity, with distinct feature processing occurring in parallel and integrated to form a representation of visual information. As such, this system requires the provision of input; principally, but not exclusively, via the retino-geniculate pathway to multiple early regions for parallel processing and feed-forward to higher areas in occipital cortex and beyond. In addition, a large amount of connections along the OR are feedback connections, providing a bidirectional bridge between sub-cortical and cortical processing of visual information (Van Essen & Maunsell, 1983; Felleman & Van Essen, 1991). While it is not possible to distinguish feed-forward from feed-back projections with tractography

techniques, direct extrastriate projections in human OR are likely to support both types of connection in V1 and at least feed-forward connectivity to extrastriate projections, in agreement with the structural arrangement seen in the macaque (Bullier & Kennedy, 1983; Kennedy & Bullier, 1985). In its entirety, the OR forms a substantial component in wider visual system, affording parallel and bidirectional connections to multiple levels of cortical and sub-cortical areas involved in the processing of visual input. What role this parallel connectivity plays in disorders of the visual system where the arrangement of retinal input is disrupted, as in albinism, remain to be determined. In subsequent chapters the methodological framework developed here will be implemented to explore the role of white matter pathways in albinism.

5.6.4 Pulvinar contributions

While typically described as a linear pathway, the visual system contains multiple parallel sources of retinal input to cortical visual areas. The principal one in both anatomical prominence and severity of impairment when damaged is the retinogeniculostrate pathway, to which the optic radiation belongs. But other important sub-cortical structures providing input to occipital cortex include the superior colliculus and pulvinar (Schneider & Kastner, 2005; Purushothaman et al., 2012). In particular the pulvinar presents a critical challenge to evidence of extra-striate connectivity from the LGN; it is both anatomically neighbouring to the LGN and is known to contain bi-directional axonal connections to areas V1, V2 and V4 in the macaque (Pessoa & Aldophs, 2010). The pulvinar is composed of three distinct nuclei, medial, inferior and lateral, of which the latter two contain at least two retinotopically-organised maps of visual space and receive input from striate and extrastriate visual cortex (Grieve et al., 2000; Shipp, 2000). While generally conceived as being involved in attention and emotional processing, recent evidence suggests a regulatory role for the pulvinar in multisensory integration and modulating extrastriate cortical activity (Zhou et al., 2016). In its anatomical connectivity, retrograde tracer studies in the macaque reveal monosynaptic connections between ventral pulvinar and areas V1, V2 and V4 (for a review, see Shipp, 2000), potentially confounding tractography evidence of direct LGN-extrastriate connectivity. We propose two lines of argument suggesting our results are not invalidated by the existence of pulvinar-extrastriate connectivity.

Firstly, while the pulvinar and LGN are neighbouring structures, they are anatomically distinct. We delineated the LGN bilaterally based on T1-weighted images and specifically aimed to reduce contributions from adjacent subcortical structures, including the pulvinar. Specifically, we identified as a region of low T1 signal relative to the surrounding tissue in the inferior thalamus, with a thin region of high T1 signal separating the LGN and pulvinar. It should be noted that identification and segregation of these structures based on *in vivo*

human MRI is challenging, therefore no complete certainty of anatomical localisation can be assumed. In particular, we observed significant ambiguity in our data regarding the dorsomedial termination of the pulvinar. However, for all subjects tested, the LGN definition was found antero-inferiorly to the pulvinar, as expected from human neuroanatomy.

Second, at present there is no evidence of direct pulvinar to V3 connectivity, as reported here for the LGN. Non-human primate tracer studies have so far reliably identified pulvinar connectivity to areas V2 and V4 (Shipp, 2000), but not area V3. It should be noted the homology between macaque and human V3 remains controversial (Serenó & Tootell, 2005), and the lack of evidence pulvinar-V3 connectivity in the monkey is not necessarily indicative of a lack of similar connectivity in the human. Nevertheless, a recent human diffusion tractography study identified strong anatomical connectivity between pulvinar and areas V1, V4, IPS and TO, and weaker connectivity to area V2 (Arcaro et al., 2015). In agreement with previous tractography studies in humans (Leh et al., 2008), patterns of anatomical connectivity of the ventral pulvinar are remarkably similar to the anatomical course of the optic radiation, suggesting projections from these structures may share white matter territories, making it difficult for tractography approaches to disambiguate contributions from LGN and pulvinar.

We should emphasise that at present we cannot discard the possibility of pulvinar contribution to the extrastriate projections, due to localisation ambiguity and shared white matter territories. Nevertheless, this study constitutes the first demonstration of optic radiation projections to extrastriate cortex, which may be improved on in the future with accurate high-resolution anatomical and fMRI localisation of the LGN and other contributing subcortical structures.

5.7 Conclusion

While typically described as a striate projection, the OR is hypothesized to connect the thalamus with extrastriate visual areas and in this study, we have identified and described direct OR projections to areas V2 and V3, in addition to striate cortex V1, in humans *in vivo*. The arrangement of tract segments reveals anatomical segregation of upper and lower visual field representations into dorsal and ventral segments, as well as distinct white matter segments connecting to areas V1, V2 and V3 following a medio-lateral nesting pattern identifiable in individual participants. Finally, microstructural differences between segments of the OR point to finer lateralization effects than previously considered, with significant differences in FA for V1 segments but not for extrastriate projections. While contributions from other subcortical structures such as the pulvinar cannot be discounted,

taken together, these findings point to a more nuanced functional arrangement of the human optic radiation than previously considered, with the combination of functional and diffusion MRI allowing the tracing of specific eloquent segments of the white matter pathway into extrastriate regions.

This study illustrates the advantages gained by a combined structural-functional approach to the understanding of the visual system and presents an example of method fusion in MRI where this may be achieved. In following chapters, a similar structural-functional approach is taken to study the wider organisation of the visual system in albinism, following on the methodological gains highlighted in the previous two chapters.

Chapter 6

Visual population receptive fields in human albinism

6.1 Abstract

Albinism is a congenital disorder associated with misrouting of the optic nerves, giving rise to abnormal visual field representations in occipital cortex. While each cortical hemisphere typically receives input from one hemifield, in albinism an overcrossing of temporal optic nerve fibres leads to partial representation of the temporal hemiretina in the hemisphere contralateral to the eye. Previous fMRI studies have characterised the broad topology of these representations in human visual cortex, but so far have not characterised the visual field properties of the abnormal representation. In this study, we present detailed fMRI population receptive field (pRF) mapping in a rare subset of participants with albinism who present minimal ocular nystagmus.

6.2 Introduction

Albinism is a congenital disorder associated with misrouting of the optic nerves, which leads to abnormal retinotopic organisation in sub-cortical and cortical visual areas (Creel et al., 1974; Carroll et al., 1980; Hedera et al., 1994; Morland et al., 2002). In humans, retinal projections are typically divided at the optic chiasm, with temporal hemiretina fibres projecting to the hemisphere ipsilateral to the eye, and nasal hemiretina fibres crossing the midline and projecting to the contralateral hemisphere. In albinism, however, the line of decussation is shifted, leading to an over-crossing of temporal hemiretina projections to the contralateral hemisphere and leaving a weak ipsilateral projection (Guillery et al., 1975; Neveu & Jeffery, 2007). Despite this gross anatomical and functional abnormality, individuals with albinism have relatively normal visual spatial perception and behaviour, retaining stereo vision (Kinnear et al., 1985; Summers, 1996).

The functional consequences of this misrouting are not fully understood; it is clear from studies in the cat that a distinct temporal visual field representation forms in the contralateral lateral geniculate body (Hubel & Wiesel, 1971) and visual cortex (Kaas & Guillery, 1973). Despite the commonality in developmental origin, the exact topology of visual field representations in albino cortex is variable (Cooper & Blasdel, 1980). In the Siamese cat, a model of albinism, two main types of organisation are observed; a reorganised cortex where representations span the ipsilateral and contralateral visual field continuously in one hemisphere, the ‘Boston’ pattern, and a non-reorganised cortex where representations of ipsilateral and contralateral visual fields overlap on the same cortical territory, the ‘Midwestern’ pattern (Guillery et al., 1974; Shatz & LeVay, 1979; Guillery, 1986). This latter case, however, is qualified by a reduced sensitivity to the abnormally-

routed visual field, which has been interpreted as evidence for suppression of the abnormal input (Guillery et al., 1974; Kaas 2005). More rarely, observed mostly in 'true' albino cats, as opposed to the partial albinism of the Siamese, a Midwestern-like pattern of overlapping representations with significant responses in the abnormal representation is seen. Indeed, this true albino pattern may be a more accurate model of albinism for primates. The, albeit limited, evidence from monkey electrophysiology (Guillery et al., 1984) and human fMRI (Morland et al., 2002; Hoffmann et al., 2003; Kaule et al., 2014) suggests overlapping representations of ipsilateral and partial contralateral visual fields on the same cortical territory. While these recent advances elucidate the topographic organisation of the visual field in human albinism, relatively little is known of the nature of the abnormal representations. This study seeks to clarify the nature of such representations in human albinos along three lines of enquiry.

First, it is unclear if the abnormal contralateral visual field representation is responsive to a broad range of visual locations, suggesting a role in spatial integration, or respond with the same degree of spatial sensitivity as their ipsilateral counterparts, suggesting a double coding of fine spatial detail within the same hemisphere (Kaas, 2005). We compare and contrast receptive field properties in ipsilateral and contralateral representations.

Second, albinism is a heterogeneous condition with variability in genetic origin, phenotype and associated comorbidities (Montoliu et al., 2013). Notably, the vertical line of decussation separating ipsilateral and contralateral representations is predicted by clinical markers such as levels of retinal pigment (Jeffery & Erskine, 2005; von dem Hagen et al., 2007). Here we ask, what is the relationship between clinical markers in albinism and receptive field properties in visual cortex?

Finally, the neural encoding of overlapping receptive fields remains poorly understood. One interpretation of the true albino pattern seen in primates is that organisation in visual cortex is conservative, retaining the original retinotopic plan despite the abnormal input and therefore giving rise to both ipsilateral and contralateral representations within the same cortical territory, organised in hemifield columns (Guillery et al., 1984; Guillery, 1986). However, in the albino, integration of information from ocular dominance columns would be confounded by the dual visual field representations, introducing sensory ambiguity into inter-ocular integration for stereoscopic vision (Klemen et al., 2012). As such, we may expect these integrating neurons to display sensitivity to both ipsilateral and contralateral receptive fields, or dual receptive field (DRF) cell. As such, DRF cells would not disambiguate hemifield information at the cortical level. An alternative interpretation is that integration cells may be selectively modulated by a single hemifield or classical single receptive field (SRF) cells. Such cells would require substantial intracortical plasticity in order to suppress hemifield crosstalk and give rise to stereoscopic vision (Klemen et al.,

2012). The presence or absence of evidence for DRFs may therefore inform how abnormal retinal input is integrated to produce stereoscopic vision and to what degree are retinotopic representations plastic in the abnormally developed visual cortex.

In order to carefully characterise receptive field properties in human albinism, we implemented the population receptive field (pRF) method described in Chapter 4 in a rare sub-population of participants with albinism and minimal nystagmus. Consistent fixation is critical for delivering retinotopically-localised visual stimulation, as the position of the stimulus aperture on the retina must be known in order to correctly reconstruct activity patterns in cortex (Dumoulin & Wandell, 2008; Wandell & Winawer, 2015). In the presence of involuntary eye movements the correspondence between the stimulus displayed and the retinal image cannot be ensured. Thus, fixation stability is a particular concern for visuotopic mapping in general (Binda et al., 2013) and pRF mapping in particular (Levin et al., 2010; Hummer et al., 2016). As nystagmus is a primary clinical feature of albinism, present in up to 88% of ocular albinism cases (Charles et al., 1993), it presents a significant challenge for delivering retinotopic stimulation in the presence of involuntary eye movements. In light of these considerations, we have opted to study a small group of individuals with albino phenotypes but presenting minimal nystagmus and consistent fixation. This approach allows us to conduct detailed investigations of retinotopic organisation and pRF properties, while linking imaging-derived metrics with phenotype markers on an individual-by-individual basis.

6.3 Materials and methods

6.3.1 Participants

Five participants with albinism (A1-A5) took part in the study (2 females, mean age = 23.80, $SD = 15.90$, age range = 9-50). A1 was diagnosed with oculocutaneous albinism type OCA1A, A2 and A3 were diagnosed with ocular albinism type OA1 and A4 and A5 were diagnosed with oculocutaneous albinism type OCA1B (for a full phenotype description, see **Table 6.1**). A4 and A5 are full siblings. Participants with albinism were selected for inclusion in the study due to their reported minimal nystagmus in the primary position. In addition to participants with albinism, 10 healthy adult controls (4 males, mean age = 26.30, $SD = 4.95$, age range: 21-36) took part in the study. All control participants had normal or corrected-to-normal visual acuity and provided written informed consent. This study was approved by the London - City and East Research Ethics Committee of the UK Health Research Authority.

Table 6.1 Albinism diagnosis and phenotype description for participants A1–A5 with albinism. A1, A4 and A5 were diagnosed with oculocutaneous albinism (OCA1A, OCA1B), and presented typical bilateral iris transillumination and a blonde fundus. A2 and A3, in contrast were diagnosed with ocular albinism (OA1) and presented regular fundus pigmentation and minimal iris transillumination. All participants tested negative for binocular stereopsis.

Participant	Sex	Age	Albinism	Best monocular visual acuity	Stereopsis (Frisby)	Hair colour	Iris transillumination	Macular appearance	Fundus photography
A1	F	21	OCA1A	0.140 LogMAR	no stereo	White blonde	Bilateral	Granular	Blonde fundus
A2	M	25	OA1	0.240 LogMAR	no stereo	Dark blonde	None	Granular	Regular pigmentation
A3	F	50	OA1	0.240 LogMAR	no stereo	Dark blonde	None	Granular	Regular pigmentation
A4	M	9	OCA1B	0.260 LogMAR	no stereo	Blonde	Bilateral	Granular	Blonde fundus
A5	M	14	OCA1B	0.200 LogMAR	no stereo	Blonde	Bilateral	Granular	Blonde fundus

6.3.2 Ophthalmological measures

All participants underwent ophthalmological screening prior to taking part in the study. Monocular visual acuity was assessed with an ETDRS chart (Ferris et al., 1982) at 4 m distance to threshold. Best monocular acuity for A1-A5 was at least 0.3 LogMAR (individual results in **Table 6.1**). The control group performed within expected boundaries for a healthy population (best monocular acuity; $M = 0.03$, $SD = 0.21$ LogMAR). All fMRI stimulation was delivered monocularly to the best-performing eye. In addition, participants with albinism were assessed for stereoscopic vision using the Frisby stereotest (Frisby Near Stereotest, Sheffield, UK). All five participants with albinism failed to demonstrate stereopsis at screening.

Visual field perimetry was assessed with automated perimetry equipment (Octopus 900, Haag-Streit Diagnostics, Koeniz, Switzerland) to two standard isopters (outer target size = 14e, inner target size = 12e, target speed = 5°/s). Resulting visual fields for participants with albinism and mean control isopters are shown in **Figure 6.1**. Detection boundary for the outer target at the horizontal meridian was taken as the maximum perceived eccentricity for each participant in subsequent analyses.

6.3.3 Retinal imaging

Optical coherence tomography (OCT) of the retina was performed with a spectral domain OCT device (SPECTRALIS, Heidelberg Engineering, Heidelberg, Germany) with active eye tracking (axial resolution = 7 μ m, lateral resolution = 14 μ m, scan rate = 40 kHz, scan depth = 1.8 mm). Retinal images were centred on the macula and acquired cross-sectionally. Each B-scan was 9 mm wide and consisted of 1,536 A-scans, with 36 averages acquired for each participant. Acquisition time was 38 ms per B-scan, ensuring minimal motion artefacts.

Figure 6.2 shows a sample cross-sectional scan for participants A1-A5 and a representative healthy control, confirming foveal hypoplasia in all participants with albinism. In order to assess variability in retinal layer thickness, automated segmentation of retinal OCTs was performed using the Heidelberg Explorer segmentation algorithm (Heidelberg Engineering, Heidelberg, Germany). Resulting retinal thickness estimates for a 5mm slice centred on the macula are presented in **Figure 6.3**, and mean layer thickness were taken forward as variables of interest for participants A1-A5.

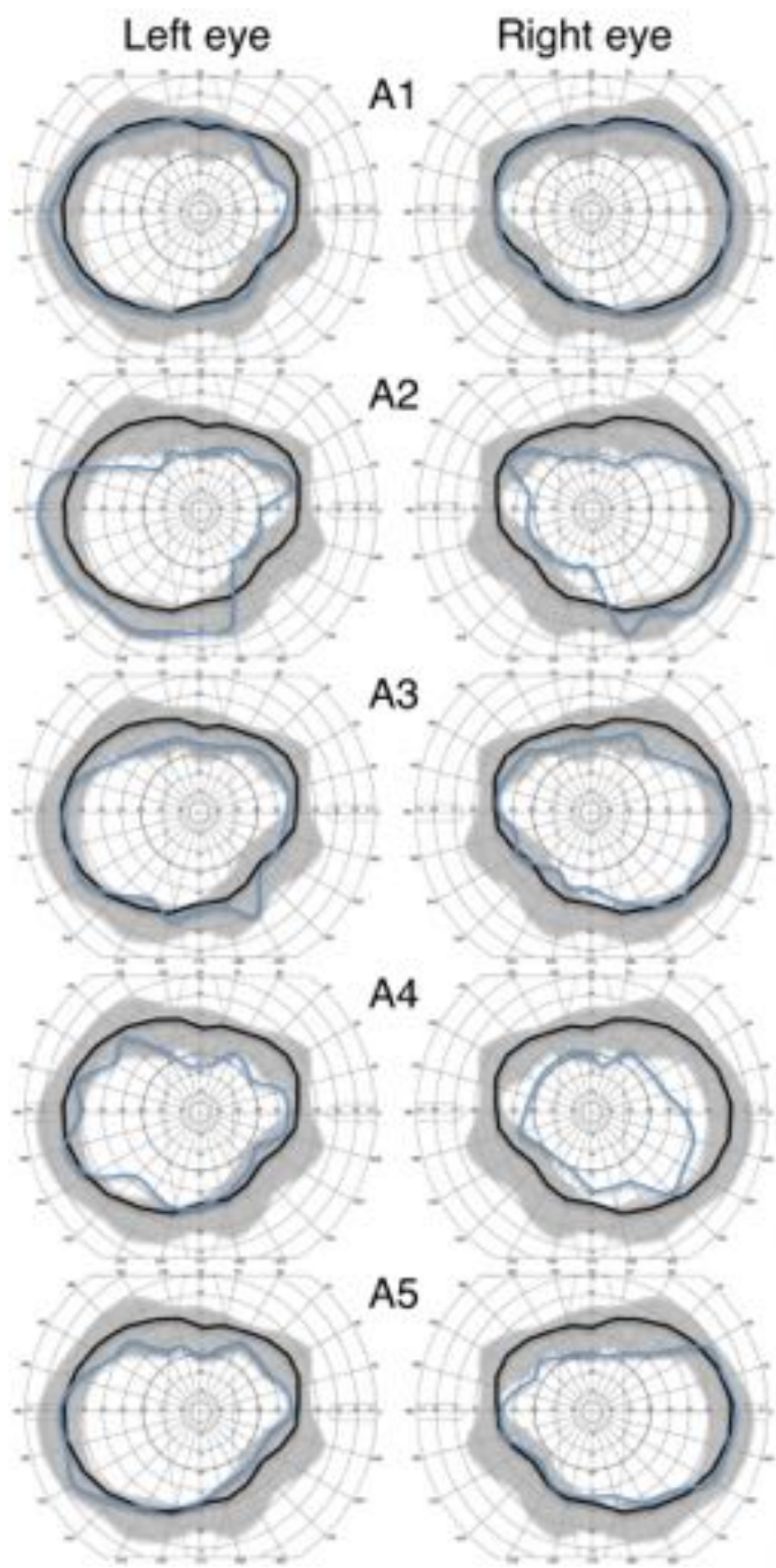


Figure 6.1 (previous page). Monocular visual field perimetry for five participants with albinism (A1-A5). Individual results for outer target perimetry (I4e) are displayed in blue, overlaid on the mean perimeter of 10 control participants in black. Target speed 5°/s. Outer perimeter for A1-A5 fall largely within the normal control perimeter, excepting a reduction in the nasal visual field in A2 and dorsal visual field for A4. During fMRI, monocular stimulation was delivered to the right eye for A2 and left for A1, A3, A4 and A5.

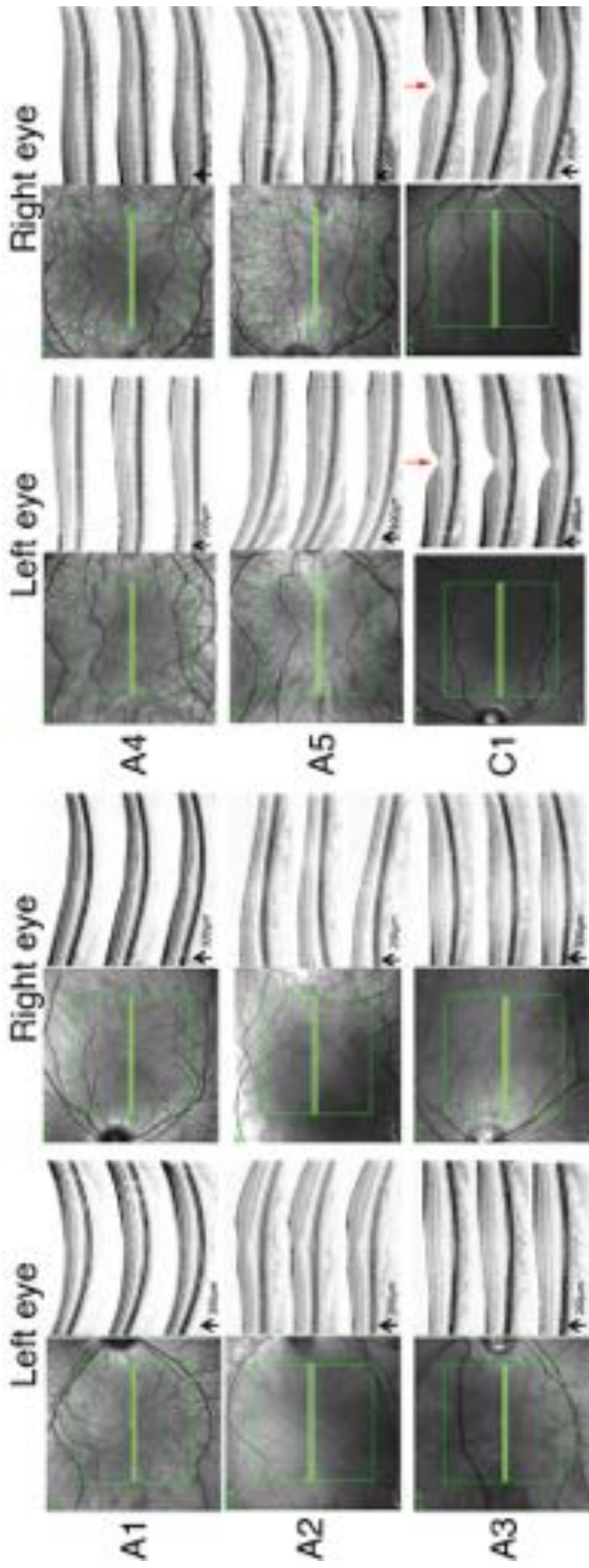


Figure 6.2 Optical coherence tomography (OCT) of the retina in five participants with albinism (A1-A5) and one representative control (C1). Transverse location and three axial slices are shown for the left (a-b) and right (c-d) eyes. Retinal scans were centred on the macula and show foveal hypoplasia, characteristic of albinism. The foveal pit, absent in A1-A5, is clearly visible in C1 (red arrow).

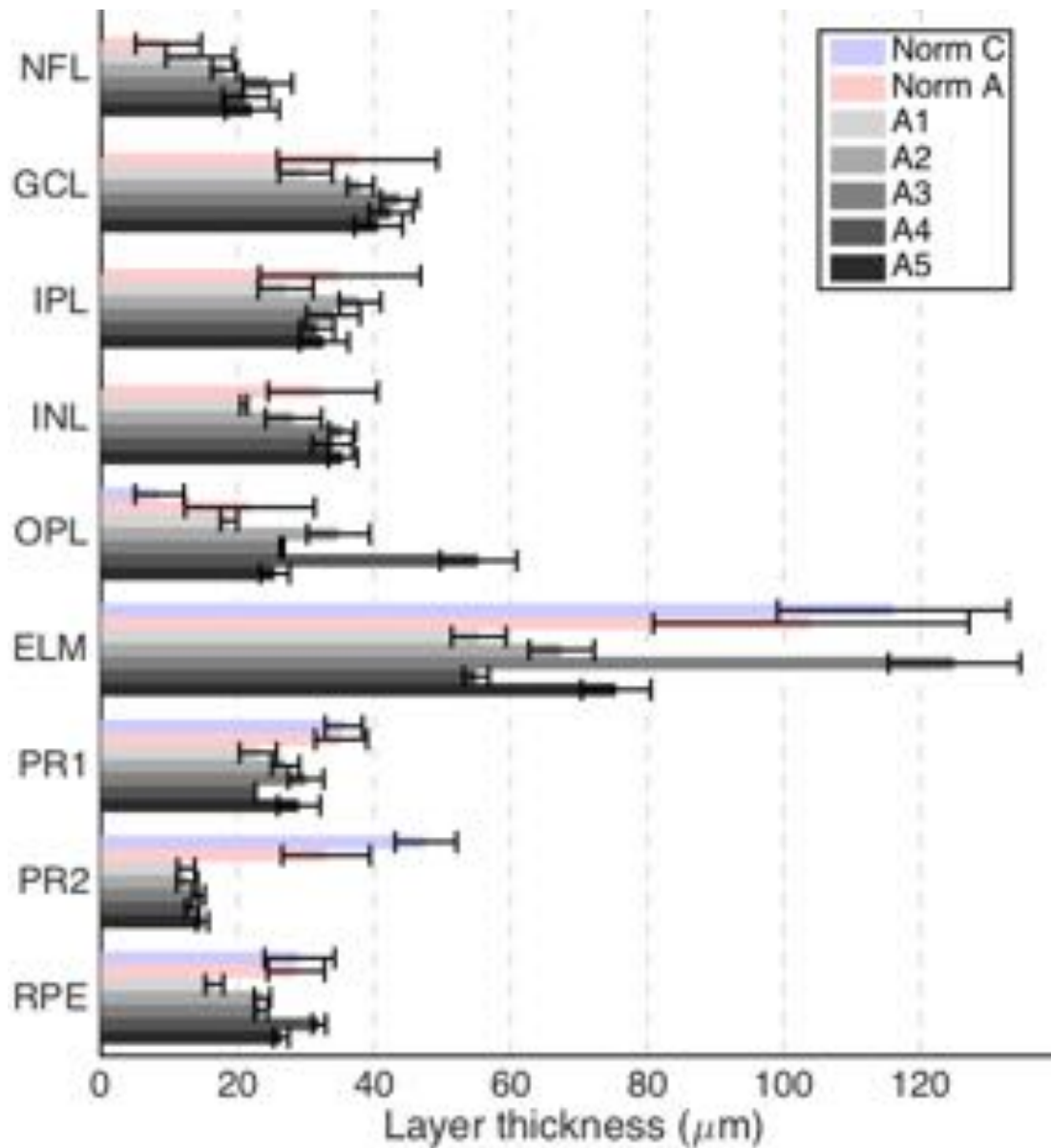


Figure 6.3 Retinal layer thickness in five participants with albinism (A1-A5) as estimated from OCT retinal segmentation, and normative values for healthy controls (Norm C) and albinos (Norm A), reproduced from Mohammad et al. (2011). NFL = nerve fibre layer, GCL = ganglion cell layer, IPL = inner plexiform layer, OPL = outer plexiform layer, ELM = external limiting membrane, PR1 = photoreceptor layer 1, PR2 = photoreceptor layer 2, RPE = Retinal pigment epithelium. Note the variability in GCL and RPE thickness, indicative of heterogeneity in developmental origin of albinism. These values are in line with normative retinal layer thickness values. A1-A5 values averaged between eyes. Error bars represent standard deviation.

6.3.4 Eye movement recordings

Consistent eye fixation is a requirement for pRF mapping and visuotopic mapping in general, particularly if fixation behaviour differs between two groups being investigated (Crossland et al., 2008; Bressler & Silver, 2010). We assessed the stability of eye movement at fixation outside the scanner for both participants with and without albinism to establish whether a group difference was expected during visual stimulation in the scanner.

Eye movement recordings were carried out with a head-mounted infrared eye tracker (JAZZ-novo, Ober Consulting, Poznan, Poland) sampling relative eye position during visual stimulation on an LCD screen (horizontal range = 35°, temporal resolution = 1000 Hz). First, a 1.15° fixation target was presented for 10 s in two locations, 20° to left or to the right from central fixation. A total of 5 events were presented in each position. Next, a central fixation target was presented for 300 s, with the participant instructed to maintain a constant head position and fixate to the targets as they appeared. Horizontal axis displacements during saccades between 20° targets were averaged and used as calibration baseline for the central fixation task. In order to quantify stability at central fixation, horizontal axis traces were visually inspected and blink artefacts identified and removed at their amplitude peak. Time points 200 ms immediately before and after blink peaks were also removed from the analysis. Resulting traces were then de-trended to remove linear drifts introduced by the apparatus. Standard deviations of horizontal axis displacement during central fixation were 0.57° for A1, 0.86° for A2, 0.84° for A3, 0.59° for A4, and 0.81° for A5. Fixation stability in the control group averaged 0.64° (95% CI = 0.15° - 1.13°). Therefore, we concluded that participants with albinism showed comparable horizontal stability to the control group, with no systematic deviation of gaze at central fixation.

To further characterise the time course of gaze fixation, we analysed horizontal displacement during fixation periods to assess any potential nystagmus-like waveform patterns (**Figure 6.4**). Note all participants with albinism displayed stable gaze fixation in the primary position, and no participant showed systematic deviation at the typical amplitudes of infantile nystagmus, of 5° or above (Abadi & Bjerre, 2002). When examined at finer scale, all participants showed unstructured micro-saccadic movements at amplitudes <0.5°. In addition, participant A3 revealed a nystagmus-like pattern of eye positions, with a decelerating exponential pattern with a period of approximately 1 second. A small latent nystagmus, not detected under routine clinical examination, is likely indicative of a more pronounced expression of ocular albinism. Nevertheless, the pattern is small in amplitude and unlikely to contribute to differences in fixation stability during fMRI stimulation. Together, these results confirmed in-scanner pRF mapping results are unlikely to be biased by differences in fixation stability between the groups.

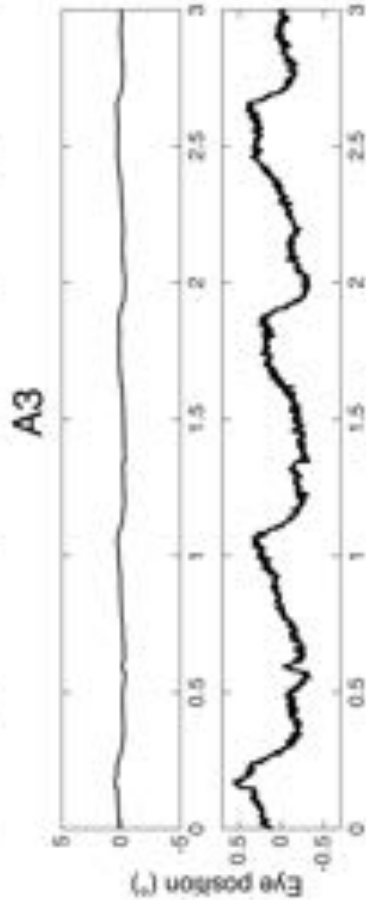
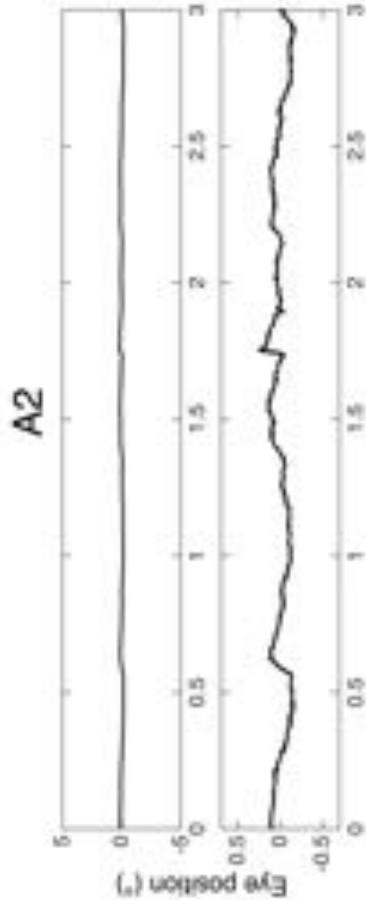
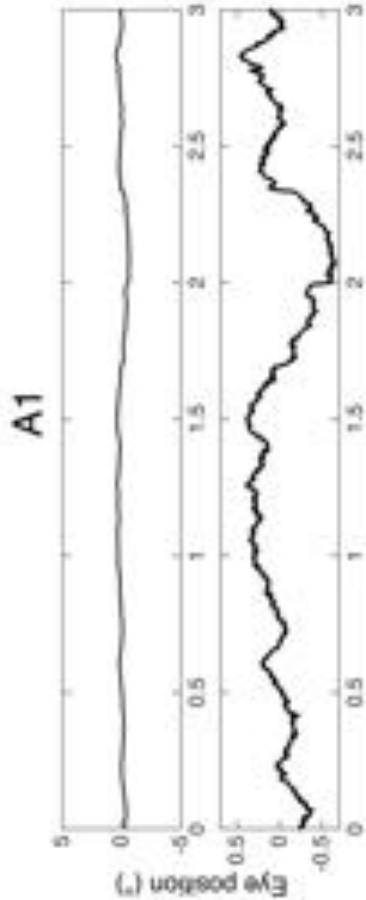
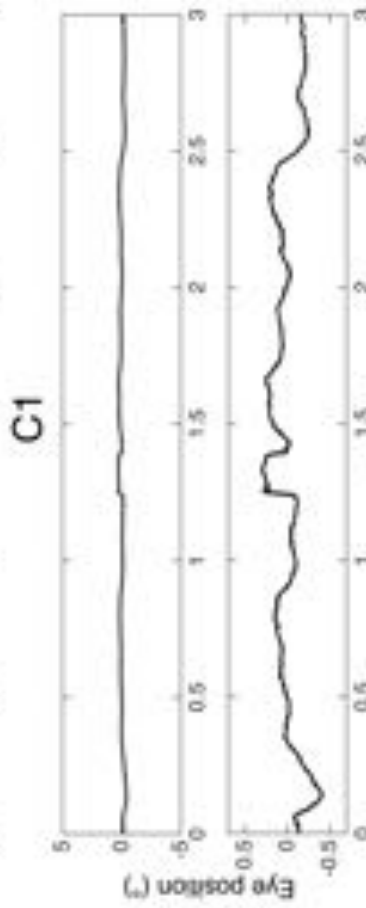
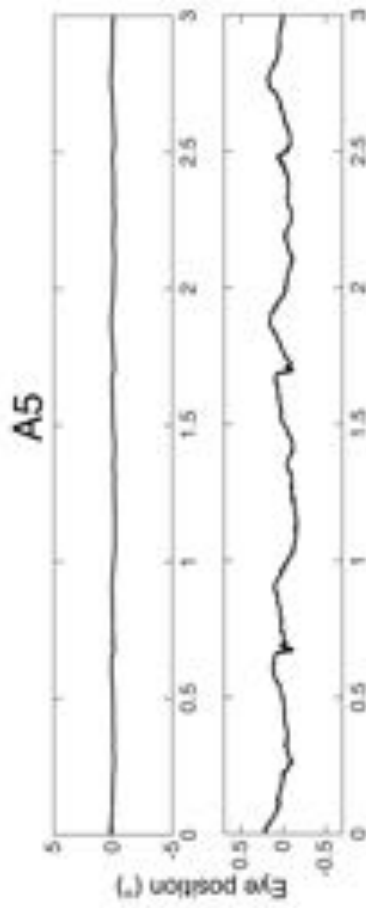
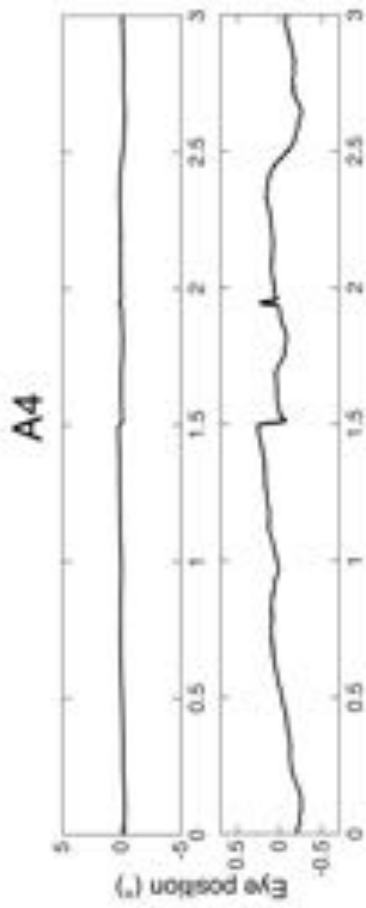


Figure 6.4 (previous page) Sample horizontal eye position traces during a 3 s fixation period in five participants with albinism (A1-A5) and a healthy control (C1). Deviation from baseline is shown at two scales, $\pm 5^\circ$ and $\pm 0.5^\circ$. At the larger scale, no significant deviation from baseline is apparent. At the smaller scale, unstructured micro-saccadic eye moments are apparent in A1, A2, A4, A5 and C1. A3 shows a nystagmus-like decelerating exponential pattern, albeit at amplitudes unlikely to significantly affect fixation stability during fMRI stimulation. Traces correspond to eye with best monocular acuity, stimulated in the fMRI experiment. Eye tracker sampling rate = 1000 Hz.

6.3.5 fMRI visual stimulation

Stimuli were generated in MATLAB (v8.0, Mathworks Inc., Natick, MA, USA) using Psychtoolbox (v3.0, Brainard, 1997; Pelli, 1997) and displayed on a back-projection screen in the bore of the magnet via an LCD projector. This arrangement allowed for wide field visual stimulation, ensuring the peripheral visual field was stimulated (Wu et al., 2012; Sereno et al., 2013), and potential ipsilateral representations in the peripheral zone of albino participants were stimulated.

The stimulus pattern consisted of a 62° radius disc of a dynamic, high-contrast tessellated pseudo-checkerboard with a drifting ‘ripple-like’ pattern that varied across time in spatial frequency and phase previously described in Chapter 4. This broadband pattern ensured effective stimulation of visually responsive neurons in visual cortex. The pattern was presented in two configurations; a hemifield mapping stimulus for pRF mapping and full-field configuration for estimation of the subject-specific haemodynamic response function. Stimuli were delivered monocularly, to the eye with best uncorrected visual acuity.

The hemifield mapping stimulus consisted of the pattern described, displayed on a single hemifield as divided by the vertical meridian, either ipsilateral or contralateral to the occluded eye, and presented through two simultaneous ‘wedge’ and ‘ring’ apertures on an equiluminant grey background. A wedge section of 18° of the stimulus circumference rotated either clockwise or counter-clockwise along the polar dimension while a truncated ring section expanded or contracted eccentrically, scaling between 0.66° and 27.54° span. Crucially, neither aperture extended beyond the vertical meridian (**Figure 6.5**). The maximum stimulated position for all participants was 62° from fixation.

Apertures presented cycled at different frequencies, with the wedge and ring apertures completing a full revolution every 56 s and 40 s, respectively. Apertures changed position every 1 s on the onset of each EPI volume acquired. A single run of the stimulus consisted of 5 wedge and 7 ring revolutions, followed by 30 volumes of equiluminant grey background, totalling 310 volumes acquired per run. A total of 4 runs were conducted, two presented ipsilateral and two contralateral to the occluded eye. Each pair contained one run with clockwise wedge rotation and expanding rings, and one run with counter-clockwise wedge rotation and contracting rings. The order of presentation was randomised across participants, with a total of 1240 volumes acquired per participant.

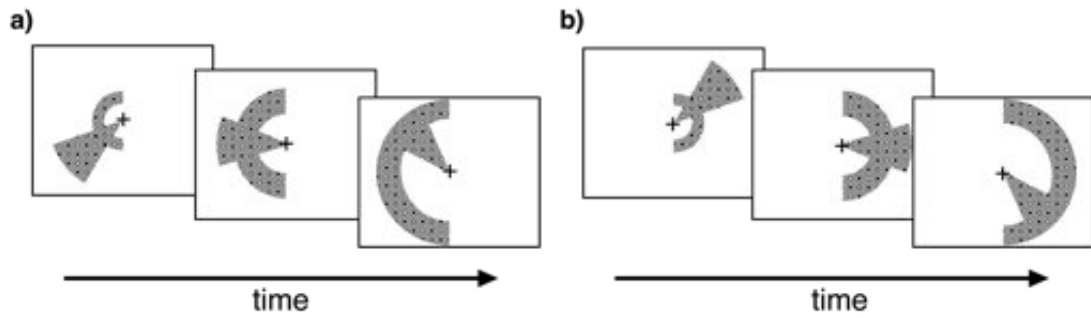


Figure 6.5 Visual stimulation was delivered monocularly and presented with two simultaneous apertures sampling the polar angle and eccentricity dimensions, respectively. Stimuli were shown either on the (a) left or (b) right hemifield, divided by the vertical meridian. Two runs were acquired for each hemifield, cycling in opposite directions and each followed by a mean luminance period. A fixation task was present throughout, where participants responded via a button press when the fixation cross changed colour. Fixation events lasted 200ms and appeared pseudo-randomly.

The full field configuration consisted of the stimulus pattern presented through a 62° radius circular aperture for 3 volumes, followed by 32 volumes of equiluminant grey background. This was repeated 10 times, totalling 350 volumes acquired.

Throughout both conditions, a fixation cross spanning 1.80° was presented to aid fixation. Participants engaged in an attentional task, consisting of a brief (200 ms) change in colour of the fixation cross, occurring semi-randomly with a probability of 5% for any given volume, with no consecutive events. Participants were instructed to attend to the cross and provide a response via an MRI-compatible response button every time they witnessed an event. Participant responses were monitored to ensure engagement with the task.

6.3.6 MRI acquisition and pre-processing

MR images were acquired on a 1.5T Avanto MRI system using a 32-channel head coil (Siemens Healthcare, Erlangen, Germany). During visual stimulation, the top elements of the head coil were removed (remaining coils = 20) to avoid visual field restrictions. A gradient echo EPI sequence (TR = 1 s, TE = 55 ms, 36 interleaved slices, resolution = $2.3 \times 2.3 \times 2.3$ mm) with parallel multiband acquisition of 4 simultaneous slices (Breuer et al., 2005) was aligned with the calcarine sulcus and used during hemifield mapping and full field stimulation. All EPI acquisitions included 10 dummy volumes at the beginning of each run that were automatically discarded to allow for stabilization of the longitudinal magnetization. An in-plane T1-weighted MPRAGE volume (TR = 1.15 ms, TE = 3.6 ms, resolution = $2 \times 2 \times$

2 mm) was acquired to aid registration, as well as a B0 field map (TR = 1.17 s, TE₁ = 10 ms, TE₂ = 14.76 ms) to estimate and correct for local field inhomogeneities. Finally, with the full 32-channel head coil arrangement, a high resolution T1-weighted MPRAGE volume was acquired (TR = 2.73 s, TE = 3.57 s, resolution = 1 x 1 x 1 mm).

High-resolution anatomical images were processed with FreeSurfer (Dale et al., 1999; Fischl et al., 1999), creating a cortical surface render for each participant. A manual definition of the occipital lobe surface was created for each hemisphere in order to restrict data analysis to the occipital cortex. Functional data were pre-processed in SPM8 (Wellcome Trust Centre for Neuroimaging, <http://www.fil.ion.ucl.ac.uk/spm>). All images were bias-corrected, realigned to the first image of the run and unwarped to correct for movement artefacts and field distortions. Resulting volumes were registered to the in-plane T1-weighted image and subsequently to the high-resolution T1-weighted image acquired with the full head coil arrangement. Finally, resulting volumes for each participant were projected onto the individual reconstructed surface by sampling voxels lying between cortex and the pial and white matter interface.

Haemodynamic response functions (HRF) were estimated for each individual participant by sampling data under full field stimulation and averaging the observed time series in the occipital region across trials. This signal was then fitted with a double gamma function (Friston et al., 1995b), resulting in an individual HRF for each participant's hemisphere.

6.3.7 Population receptive field (pRF) modelling

Hemifield mapping runs were analysed with a forward model pRF approach based on Dumoulin & Wandell (2008) and described in detail in Chapter 4. In brief, model predictions were generated from the *a priori* knowledge of stimulus position at each volume acquired, and under the assumption of an isotropic two-dimensional Gaussian pRF. Predictions were convolved with the individual HRF and compared to the observed signal in a two-stage procedure. First, a coarse fit was conducted by sampling predictions generated from an exhaustive grid of combinations of three pRF parameters (X and Y coordinates, and spatial spread, σ) and correlating them with a smooth version (FWHM = 8 mm) of the observed BOLD time courses. The parameters resulting in the highest correlation at each vertex then formed the starting point for a subsequent fit to the unsmooth data, using a constrained non-linear minimization procedure (Lagarias et al., 1998). Best-fitting model predictions therefore provided estimates of retinotopic location (X and Y coordinates) and pRF size (σ) for each vertex, as well as a scaling factor (β). The coefficient of determination (R^2) was taken as the model metric for goodness-of-fit.

Data resulting from stimulation to each hemifield were analysed independently, incorporating BOLD time series from clockwise and counter-clockwise runs in each hemisphere. While the stimulated eye differed between participants, all subsequent analyses and discussion refers to hemispheres ipsilateral and contralateral to the stimulated eye, and all further illustrations are presented as if stimulation was through the left eye, in the interest of clarity.

A further level of analysis was conducted to assess the validity of the dual pRF model of retinotopic encoding in human albinism. Data recorded during stimulation to left and right hemifields were joined and fitted with a) a single 2D Gaussian pRF model, as described above and b) a dual horizontally-mirrored 2D Gaussian pRF model, which incorporates a second receptive zone of the same size (σ) in the equivalent mirror location across the vertical meridian. Both models were fitted independently for each hemisphere.

6.4 Results

6.4.1 Region delineation

We manually delineated retinotopic maps on the inflated cortical surface based on polar angle and eccentricity representations derived from the pRF model. Maps were drawn in each hemisphere from data obtained under stimulation to the contralateral eye. Early visual areas V1, V2 and V3 were reliably identified in all participants, while defining boundaries for further areas was variable across participants. Therefore, in order to ensure consistent and sufficient sampling across groups, we restricted our analysis to visual areas V1, V2 and V3.

6.4.2 Overlapping representations of ipsi- and contralateral visual fields

All participants received monocular stimulation to either the nasal or temporal hemiretina, responses to which were modelled independently. In control participants, we observe clear lateralisation of visual field representations, with the nasal hemiretina represented in the contralateral hemisphere and the temporal hemiretina represented in the ipsilateral hemisphere, as expected (**Figure 6.6**). In participants with albinism, however, a contralateral representation of the temporal hemiretina was found overlapping the cortical territory of nasal hemiretina representations in areas V1, V2 and V3. This confirms the abnormal response lateralisation typically seen in albinism and in agreement with electrophysiological and MRI studies (Apkarian et al., 1983; Dorey et al., 2003; von dem Hagen et al., 2008).

Abnormal temporal hemiretina responses in the contralateral hemisphere were largely foveal or near-foveal, with the more eccentric representations reverting to the uncrossed pattern and appearing in the ipsilateral hemisphere. Considerable overlap was observed in the contralateral hemisphere, in agreement with the animal model of albinism (Guillery et al., 1974; Shatz & LeVay, 1979; Guillery, 1986) and previous fMRI studies (Hoffmann et al., 2003; Kaule et al., 2014).

An analysis of the number of voxels with significant responses ($R^2 > 0.01$) revealed all participants with albinism showed >50% of combined V1, V2 and V3 surface vertices responded significantly to both nasal and temporal hemiretina stimulation (A1 = 76%, A2 = 52%, A3 = 50%, A4 = 50%, A5 = 53%). In comparison, the same metric yielded an average value of 12.33% ($\pm 12\%$ SD) for control participants. In the following section, we examine the evidence for abnormal population receptive field properties in this overlap zone.

6.4.3 Variation in population receptive field size

A currently unanswered question is; what role does the abnormal temporal hemiretina projection play in visual perception in albinism? In order to understand the role of this representation, we examined the receptive field properties of early visual areas *in vivo* via pRF mapping. pRF sizes were derived by taking the Gaussian full-width half-maximum of the best-fitting model for each vertex, and binning the values in 6° bins across the stimulated zone up to 62° eccentricity. This procedure was performed independently for each hemisphere and hemifield stimulated, in regions of interest V1, V2 and V3.

Following stimulation to either nasal or temporal hemiretina, both controls and participants with albinism display a monotonic increasing relationship between pRF size and eccentricity in the hemisphere contralateral to stimulation, as expected from early visual areas (**Figure 6.7**). Control participants did not display significant contralateral responses to temporal retina stimulation. The normal contralateral response to nasal retina stimulation was similar between A1-A5 and controls, with similar slopes of receptive field size increase with eccentricity in V1. In area V2, A1 and A3 showed a trend for larger slopes of receptive field size increase, while A3, A4 and A5 showed similar trends in V3. In contrast, the typical ipsilateral response to temporal retina stimulation was comparable between A1-A5 and the control group across visual regions V1, V2 and V3. Finally, albino contralateral responses to temporal hemiretina in V1 showed similar receptive fields to the typical contralateral response, while V2 and V3 revealed a trend towards smaller receptive fields.

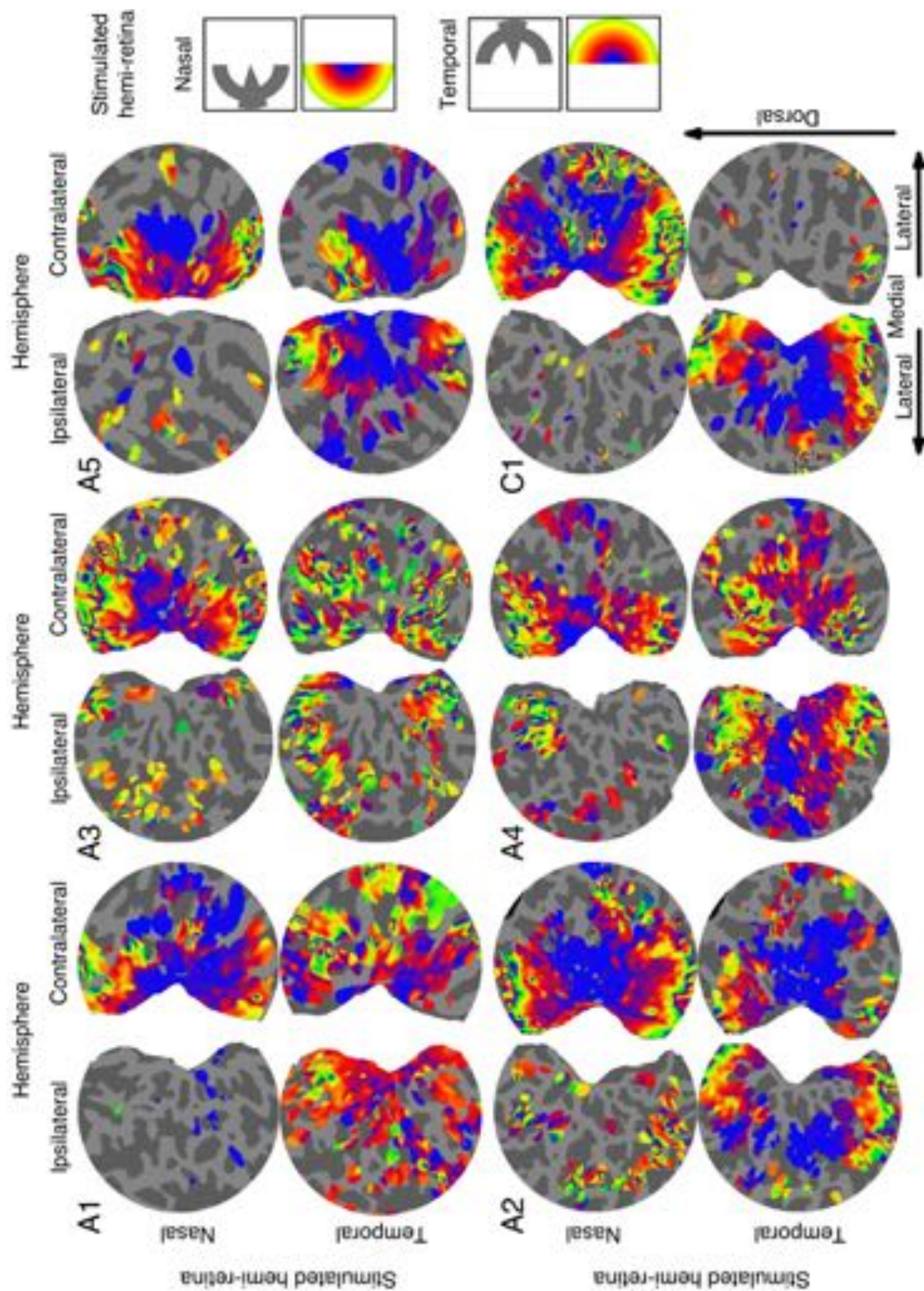
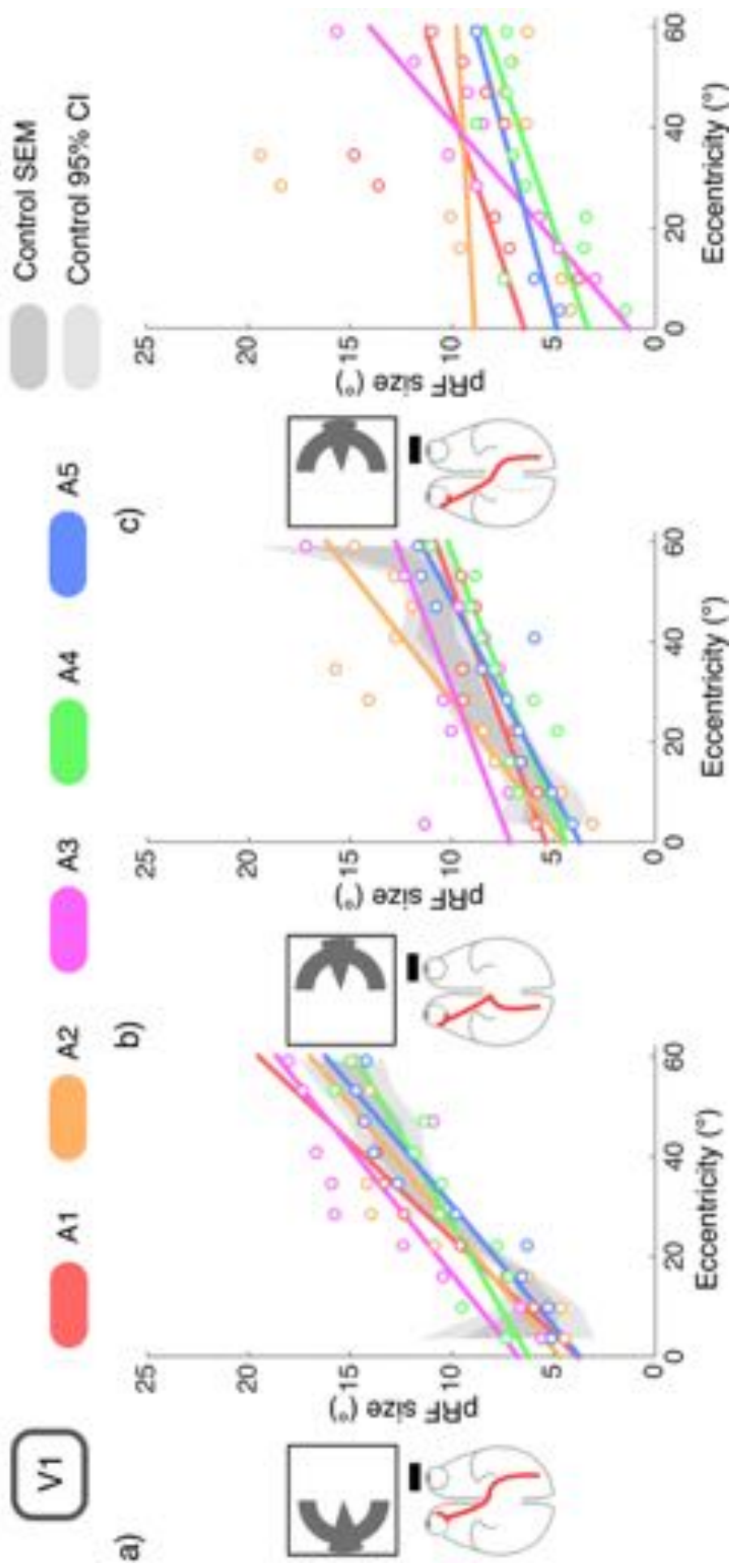
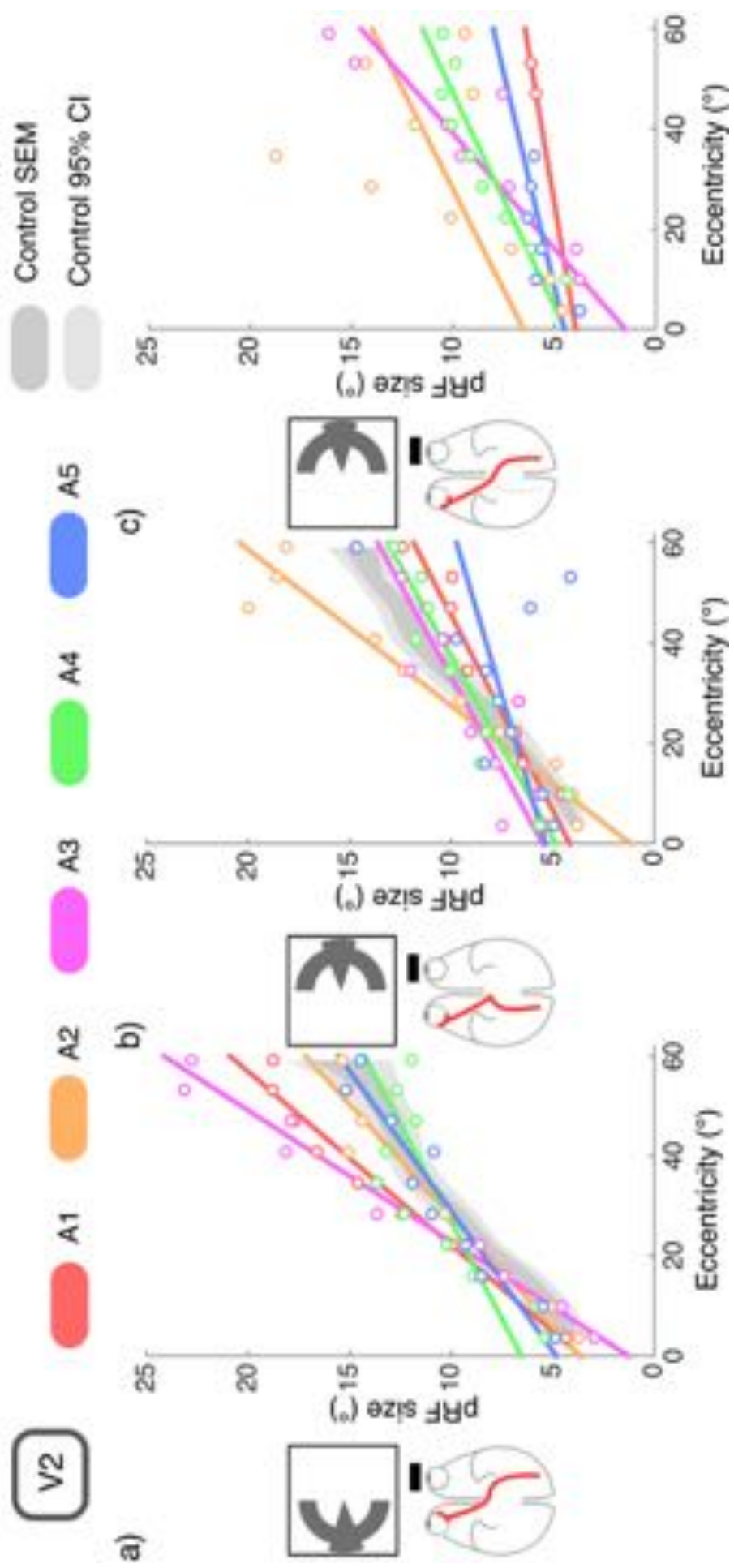


Figure 6.6 (previous page) Eccentricity responses to hemifield stimulation derived from population receptive field (pRF) mapping, displayed on flattened occipital cortex surface reconstruction. Stimulation was delivered monocularly to either the nasal or temporal hemiretina, and resulting eccentricity maps are displayed on hemispheres ipsilateral and contralateral to the stimulated eye in five participants with albinism (A1-A5) and one control (C1). In the control visual cortex, the nasal hemiretina is represented in the contralateral hemisphere, and the temporal hemiretina is represented in the ipsilateral hemisphere. However, the albino visual cortex shows contralateral responses to temporal hemiretina stimulation, seen in A1-A5. Note the overlap of nasal and temporal hemiretina representations in the contralateral hemisphere. Variability in the vertical line of decussation is apparent from the peripheral extent of the temporal hemiretina representation, and thus the degree of chiasmal misrouting may be inferred on an individual basis. Participants received stimulation monocularly to the eye with best visual acuity. Stimulus diagram displays stimulation the left eye for illustration. Vertices thresholded at $R^2 > 0.01$.





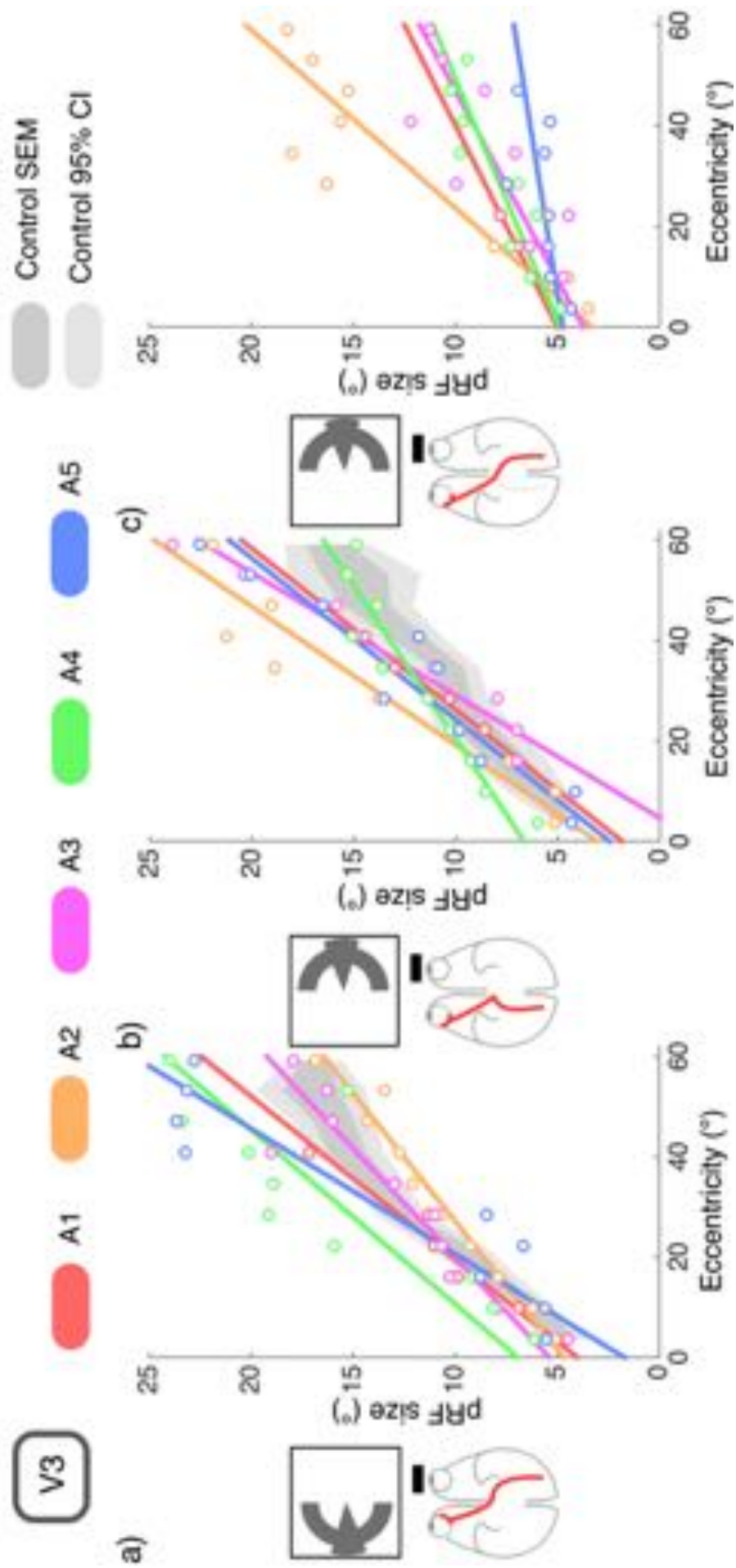


Figure 6.7 Population receptive field (pRF) size as a function of receptive field eccentricity in cortical visual areas V1, V2 and V3. Best linear fit for participants with albinism (A1-A5) represented Mean pRF size in successive 6° eccentricity bins and best linear fits displayed in colour for participants with albinism (A1-A5). Control group data ($N=10$) shown as standard error of the mean (dark grey) and 95% confidence intervals (light grey) of binned pRF sizes. (a) Contralateral responses to nasal retina stimulation. Significantly larger slopes of receptive field size increase with eccentricity detected for A1 and V3 in area V2, compared to normative control group ($p < .05$). (b) Ipsilateral responses to temporal stimulation, with similar receptive field profiles between A1-A5 and control group. (c) Contralateral responses to temporal retina stimulation. Significantly lower slopes of pRF size increase with eccentricity detected in area V3 for A1, A3, A4 and A5 ($p < .05$). Note that responses in panels (a) and (c) correspond to the same set of contralateral vertices under nasal and temporal hemiretina stimulation, respectively. No control data displayed in (c), as no significant contralateral responses to temporal retina stimulation were detected in the control group. Stimulus diagram displays stimulation to left eye for illustration, whereas each participant received stimulation to the eye with best visual acuity.

In order to assess these trends statistically, we employed a Bayesian hypothesis testing approach for contrasting single-case versus matched control samples (Crawford & Garthwaite, 2004; Crawford et al., 2010a; Crawford et al., 2011). These methods allow the comparison of outcome variables obtained from a single patient against a modestly sized normative control sample. Conservative in nature, the particular interval estimate test described in Crawford et al. (2011) and implemented here allows for estimation of point samples placing the patient within a given percentage of the control population that match or exceed the patient score in the outcome variable of interest. Individual linear fit slopes illustrated in **Figure 6.7** for participants A1-A5 were compared against the group mean slopes for the control group (N=10) using the single-case method. As correction for multiple comparisons is typically discouraged in Bayesian hypothesis testing (e.g. Gelman et al., 2012), we report uncorrected, two-tailed p-values for each test, as well as point estimate of percentage of control population falling below the patient's score.

6.4.3.1 *Contralateral responses to nasal hemiretina stimulation*

Following nasal hemiretina stimulation, responses in V1 contralateral to the stimulated eye were largely similar between the two groups, with no significant difference in slopes (A1 $p = .062$, A2 $p = .287$, A3 $p = .883$, A4 $p = .317$, A5 $p = .549$). However, contralateral V2 revealed significantly larger pRF size increase slopes for A1 (*slope difference* = 0.19, $p = .033$, *point estimate* = 96.63%) and A3 (*slope difference* = 0.17, $p = .045$, *point estimate* = 95.53%) with no-significant differences for A2 ($p = .134$), A4 ($p = .442$) or A5 ($p = .413$). Finally, no significant differences in slope were detected in V3 (A1 $p = .273$, A2 $p = .219$, A3 $p = .412$, A4 $p = .273$, A5 $p = .210$).

6.4.3.2 *Ipsilateral responses to temporal hemiretina stimulation*

The temporal hemiretina projection is split in individuals with albinism, with the central visual field projecting contralaterally, and the remaining eccentric portion projecting to the ipsilateral hemisphere. It is therefore not surprising that poor model fits were achieved in this latter representation for participants with albinism, particularly at low eccentricities (see **Figure 6.6b**). Here, responses in V1 ipsilateral to the stimulated eye were comparable between groups, with no significant differences in slopes in V1 (A1 $p = .539$, A2 $p = .308$, A3 $p = .592$, A4 $p = .267$, A5 $p = .909$), or V3 (A1 $p = .915$, A2 $p = .457$, A3 $p = .365$, A4 $p = .412$, A5 $p = .532$). In V2, however, significantly larger slopes of pRF size increase were detected for A2 (*slope difference* = .15, $p = .039$, *point estimate* = 98.04%), but not for A1 ($p = .728$), A3 ($p = .513$), A4 ($p = .786$) or A5 ($p = .058$).

6.4.3.3 *Contralateral responses to temporal hemiretina stimulation*

As we have previously seen, the temporal hemiretina projects part of the central visual field to the contralateral hemisphere, a feature not present in the healthy population. This response, with monotonic increase of pRF size with eccentricity, can be seen in early visual areas V1, V2 and V3 for participants with albinism studied here (**Figure 6.7c**). As expected, no contralateral response to nasal stimulation was detected in the control group, and we have therefore taken responses to ipsilateral stimulation as equivalent, in order to discern differences in pRF size increase between the control group and A1-A5.

Starting with V1, no significant differences in slope were observed (A1 $p = .909$, A2 $p = .464$, A3 $p = .470$, A4 $p = .871$, A5 $p = .901$). Similarly, no significant effects were observed in V2 (A1 $p = .641$, A2 $p = .340$, A3 $p = .524$, A4 $p = .745$, A5 $p = .772$). In contrast, responses in V3 were found to display significantly smaller slopes of pRF size increase for A1 (*slope difference* = 0.45, $p = .043$, *point estimate* = 2.13%), A3 (*slope difference* = 0.61, $p < .001$, *point estimate* = 1.11%), A4 (*slope difference* = 0.23, $p = .037$, *point estimate* = 3.70%) and A5 (*slope difference* = 0.18, $p = .047$, *point estimate* = 4.69%). No significant difference was detected for A2 ($p = .954$).

Note the effect in V3 is in the opposite direction to effects in the previous two conditions; contralateral responses to temporal hemiretina stimulation show a slower increase in pRF size with eccentricity when compared to responses in the control group responses for the same hemisphere, under nasal hemiretina stimulation.

In summary, variable pRF size variation with eccentricity was detected for participants with albinism when compared to a normative control group. Dissociated trends were observed, with greater increase in pRF size with eccentricity in the contralateral representation of nasal hemiretina, and the opposite effect for temporal hemiretina representations in the same cortical territory, with significant inter-subject variability. The relationship between variability and other outcome measures will be explored in the following sections.

6.4.4 **Line of decussation**

Chiasmatal overcrossing in albinism has the consequence of shifting the representation of the vertical meridian towards the temporal hemiretina, leaving a weak ipsilateral representation of visual space. This line of decussation can be approximated *in vivo* with electrophysiological (Dorey et al., 2003) and imaging methods (von dem Hagen et al., 2007). Here, the horizontal positions of pRFs derived from temporal hemiretina stimulation were used to estimate the line of decussation independently for each participant. The distribution of pRF horizontal positions in hemispheres ipsilateral and contralateral to the stimulated eye

are shown in **Figure 6.8**, where the difference in distributions formed an index of the rate of change, where a given horizontal position in the visual field stops being represented in the contralateral hemisphere and starts being represented in the ipsilateral hemisphere. This point of crossover was taken as the individual estimate of the line of decussation, revealing variability between participants with albinism. A1 showed an estimated line of decussation at 9.40° from midline, A2 at 4.40°, while A3 (0.91°), A4 (1.56°) and A5 (1.34°) all showed smaller deviations from midline. All participants with albinism showed lines of decussation biased towards the temporal hemiretina.

Variability in the line of decussation is linked to the retinal development trajectory, with more severe absence of retinal pigmentation associated with larger shifts in the line of decussation (von dem Hagen et al., 2007). The retinal developmental trajectory is evidenced in the retinal characteristics, such as foveal hypoplasia and retinal layer thickness. In order to assess the link between these, we analysed OCT retinal thickness estimates for inter-subject variability, focusing on two layers particularly affected in albinism: the ganglion cell layer (GCL), and the retinal pigment epithelium (RPE). A Bayesian statistical approach for contrasting single-case versus matched control samples was used, described in section 6.4.3. This approach allows comparisons between two cases given the outcome variable for each case and the variance in a modestly sized control sample (Crawford et al., 2010b; Crawford et al., 2011). Two-tailed p-values and effect size ranges reported.

GCL thickness. A1 ($M = 30.01$, $SD = 3.89 \mu\text{m}$) and A2 displayed the smallest GCL thickness, when compared to A3 ($M = 43.76$, $SD = 2.76 \mu\text{m}$), A4 ($M = 42.48$, $SD = 3.19 \mu\text{m}$) and A5 ($M = 40.65$, $SD = 3.53 \mu\text{m}$). Both A1 and A2 showed significantly thinner GCL when compared to their peers in pair-wise comparison tests (all tests $p < .05$, $df = 9$, *effect size range* = 1.94 – 6.01).

RPE thickness. Here three groups emerged, with A1 ($M = 16.61$, $SD = 1.32 \mu\text{m}$) displayed significantly thinner RPE layer thickness when compared with all other albino participants (all pair-wise tests $p < .01$, $df = 9$, *effect size range* = 4.47 – 9.77) followed by A2 ($M = 23.62$, $SD = 1.18 \mu\text{m}$), A3 ($M = 23.46$, $SD = 0.96 \mu\text{m}$) and A5 ($M = 26.43$, $SD = 1.00 \mu\text{m}$), with comparable values and finally A4 ($M = 31.95$, $SD = 1.00 \mu\text{m}$) with significantly thicker RPE (all pair-wise tests $p < .01$, $df = 9$, *effect size range* = 3.52 – 9.77).

In summary, A1 displayed both the largest shift in line of decussation and thinnest GCL and RPE retinal layer thickness, while A2 displayed a medium shift in line of decussation and significantly thinner GCL when compared to A3, A4 and A5. GCL thickness matched the imaging estimates most closely, with A1 and A2 displaying large shifts in line decussation and thinner bilateral GCLs, while A3, A4 and A5 displayed small shifts in line of decussation and thicker bilateral GCLs.

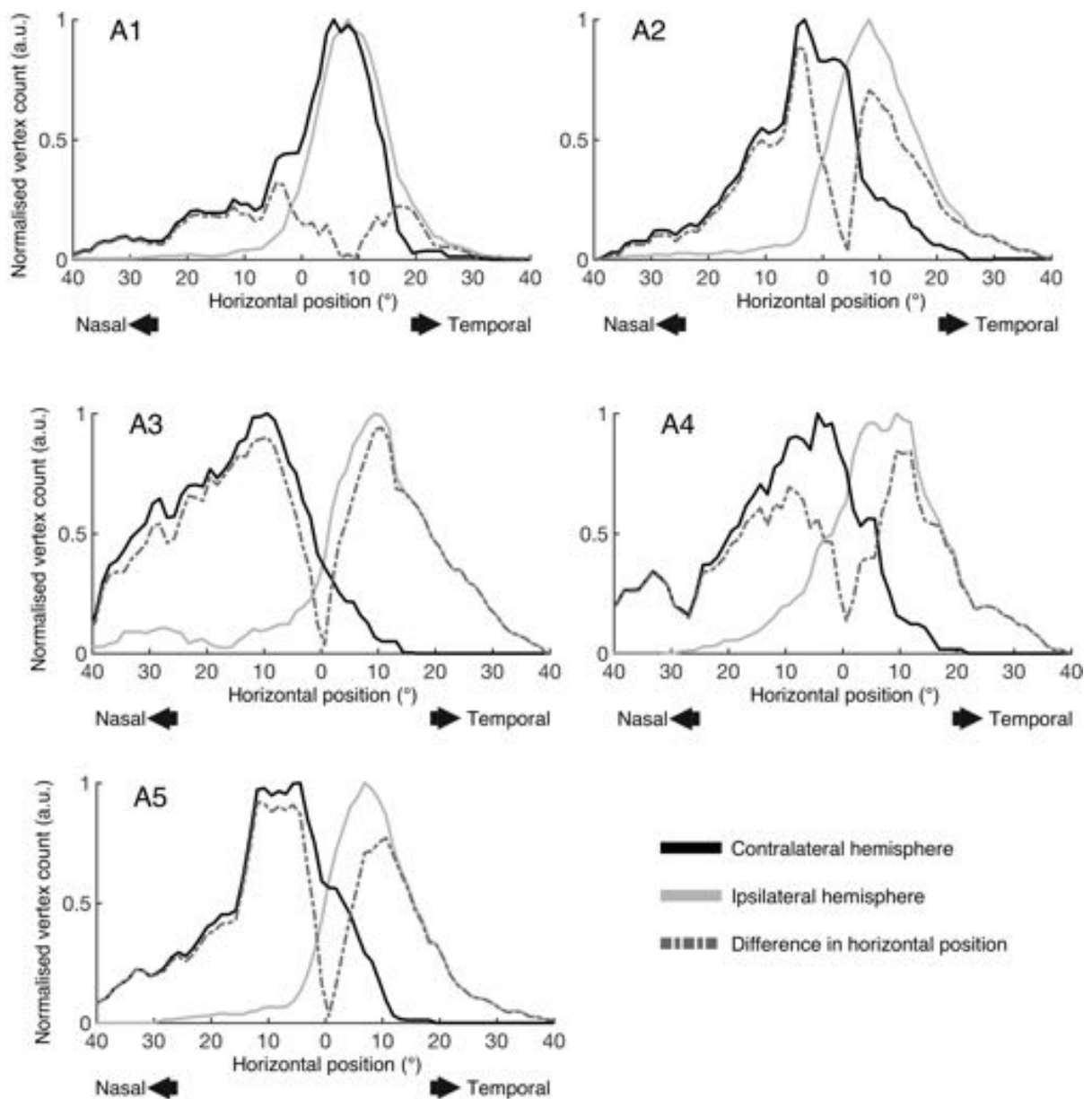


Figure 8.8 Horizontal population receptive field (pRF) position estimated under monocular stimulation of the temporal hemiretina, in the contralateral and ipsilateral hemispheres of participants with albinism (A1-A5). The distribution of differences in horizontal positions reveal the point of crossover between a given horizontal position in the visual field being represented in the contralateral and ipsilateral hemisphere, the line of decussation. Note the temporal bias in line of decussation for A1 and A2, and to a lesser extent in A3, A4 and A5. Y-axis corresponds to normalised vertex counts across visual areas V1, V2 and V3 for a single participant.

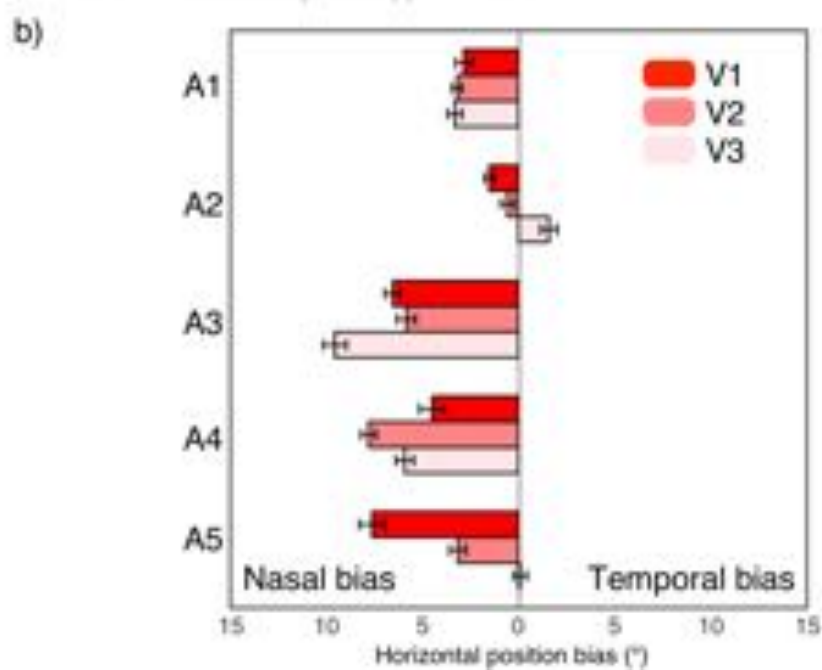
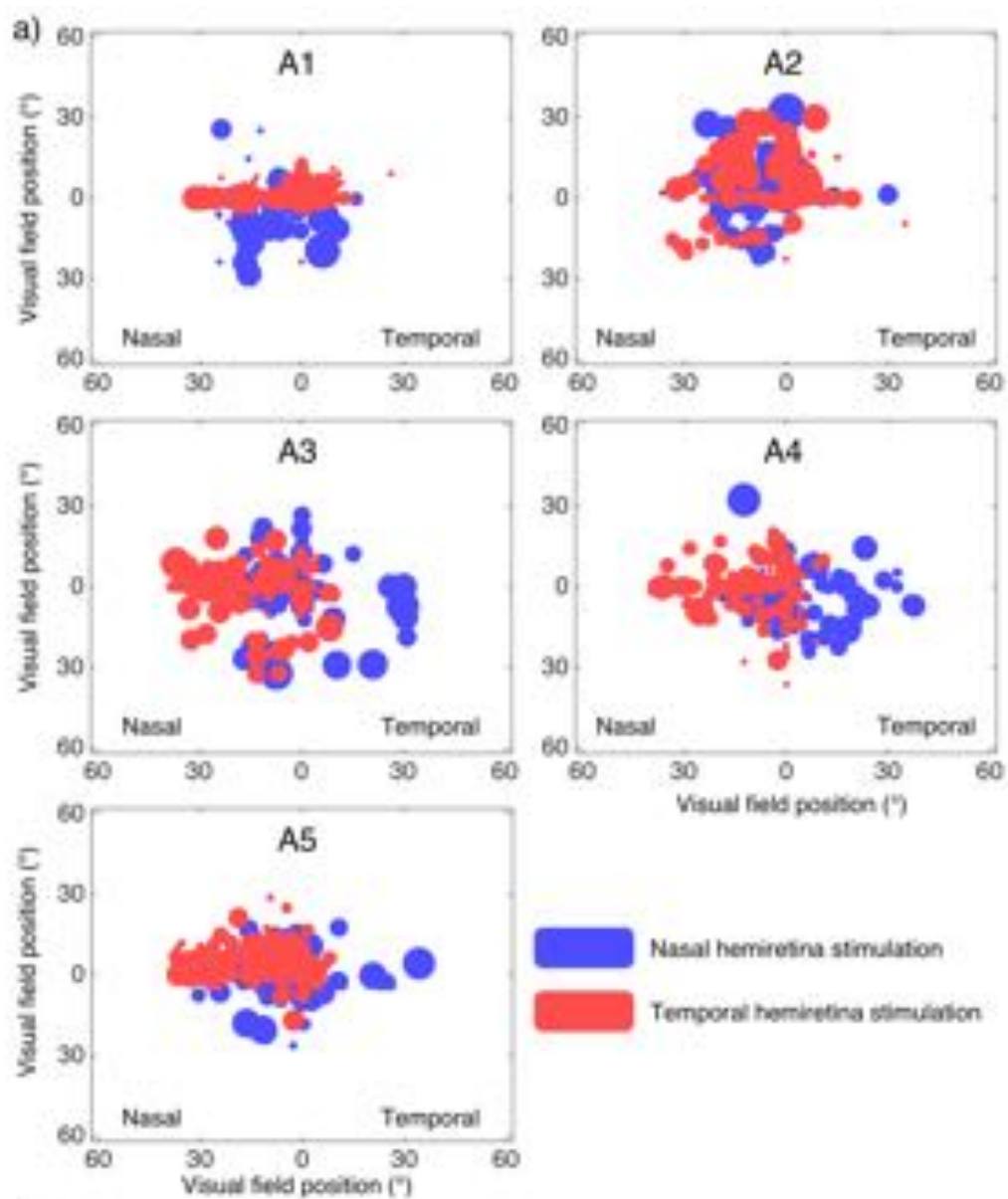


Figure 6.9 (Previous page) (a) back-projection of population receptive fields (pRF) in contralateral visual areas V1, V2 and V3 for participants with albinism A1-A5. A bias in the location of receptive fields estimated under nasal (blue) and temporal (red) hemiretina stimulation, indicates a bias towards nasal pRFs in the abnormal temporal hemiretina representation. Only vertices significant ($R^2 > 0.01$) in both conditions are included. pRFs with receptive fields $>15^\circ$ excluded from visualisation for clarity. (b) Horizontal bias in pRF location, as estimated by the mean horizontal position difference between pRF estimates under nasal and temporal hemiretina stimulation, in matching cortical locations. Bars extending to the left indicate a bias towards nasal pRFs, and bars extending to the right indicate a bias towards temporal pRFs under temporal hemiretina stimulation, relative to nasal hemiretina stimulation. A1 and A2 show little discrepancy in pRF positions between conditions, while A3, A4 and A5 show a 5-10° bias towards a nasal shift in the abnormal temporal hemiretina representation in the hemisphere contralateral to stimulation. Error bars indicate SEM.

6.4.5 Receptive field position shift

In addition to variation in pRF size, overlapping representations of the nasal and temporal retina in albino contralateral cortex may contain systematic variation in receptive field position. While it is clear from **Figure 6.6** that the two contralateral representations follow the same broad retinotopic plan, preferred retinal locations may vary systematically, for example biased towards the shifted line of decussation. In order to assess this, we examined the estimated pRF location for the same cortical location under nasal and temporal hemiretina stimulation, and calculated the mean difference in horizontal pRF position between conditions, across regions of interest V1, V2 and V3 for each participant (see **Figure 6.9**). This approach revealed a bias for nasal pRFs in the contralateral representation of the temporal hemiretina, particularly for A3 (*mean bias* = 7.32°, *SEM* = 0.50°), A4 (*mean bias* = 6.08°, *SEM* = 0.50°) and A5 (*mean bias* = 3.57°, *SEM* = 0.48°), and to a lesser extent in A1 (*mean bias* = 3.12°, *SEM* = 0.36°) and A2 (*mean bias* = 0.17°, *SEM* = 0.35°). Little evidence emerged for bias towards temporal pRFs in the temporal hemiretina representation.

These results are in agreement with estimates of the vertical line of decussation, where participants who display large shifts (A1, A2), also show the smallest discrepancy between nasal and temporal hemiretina representations in contralateral visual areas, while those with small decussation shifts (A3, A4, A5) display a large nasal bias for pRFs in the temporal hemiretina representation.

6.4.6 Dual receptive field (DRF) modelling

In order to further explore the underlying organisation of visual receptive fields in albino visual cortex, an additional level of analysis was performed where responses to nasal and temporal hemiretina stimulation were jointly modelled using both a classic 2D Gaussian pRF model, as implemented in the previous section, and a dual pRF model, with two receptive fields, mirror-symmetric across the vertical median, as a neuronal population-level approximation of the DRF model (Klemen et al., 2012). In order to assess differences in fits between the two models, we compared goodness of fit (R^2) estimates for each participant with a repeated measures t-test model.

In order to ensure a parametric test was appropriate, data were subjected to the Anderson-Darling test to assess whether the data departed significantly from a normal distribution. Vertex-wise R^2 values for each region of interest, in each participant were tested independently and no sample was found to violate the assumption of normality (*mean* $A = 644.04$, *SD* = 345.19, all tests $p < .001$). Bonferroni correction for multiple comparisons was applied across regions of interest.

For all participants, we observed larger R^2 estimates in the single pRF model across visual areas (**Figure 6.10**). Significantly better fits for the single pRF model in V1 were detected for all participants; A1 ($t = 3.22$, $df = 1512$, $p < .001$), A2 ($t = 4.65$, $df = 1406$, $p < .001$), A3 ($t = 4.71$, $df = 2184$, $p < .001$), A4 ($t = 11.55$, $df = 3121$, $p < .001$) and A5 ($t = 11.60$, $df = 1134$, $p < .001$). Similarly, in V2 significant differences were detected for A2 ($t = 5.57$, $df = 669$, $p < .001$), A3 ($t = 5.61$, $df = 2686$, $p < .001$), A4 ($t = 5.10$, $df = 1903$, $p < .001$), and A5 ($t = 4.80$, $df = 777$, $p < .001$), with a non-significant trend for A1 ($t = 3.03$, $df = 1504$, $p = .110$). Finally, significantly better fits for the single pRF model in V3 were once more detected for A2 ($t = 7.55$, $df = 2415$, $p < .001$), A3 ($t = 7.69$, $df = 1180$, $p < .001$), A4 ($t = 4.13$, $df = 1541$, $p < .001$), and A5 ($t = 5.40$, $df = 659$, $p < .001$), and a non-significant trend for A1 ($t = 0.11$, $df = 520$, $p = .409$). Overall, individual results show the dual receptive field model is either statistically indistinguishable, or a significantly poorer fit than the single receptive field throughout the cortical areas tested.

While the overall pattern of responses across A1-A5 favoured the classic single receptive field model, a further line of enquiry was pursued to assess whether the dual receptive field was a better fit in spatially localised subsets of vertices within the regions of interest sampled. The proportion of vertices where the dual receptive field model provided a significantly better fit (R^2 difference > 0.01) was consistently below 6% across all participants in bilateral V1, V2 and V3 vertices (A1 = 4.62%, A2 = 5.52%, A3 = 4.86%, A4 = 4.88%, A5 = 5.66%). In the small proportion of vertices where the dual pRF model outperformed the single pRF model, the mean difference in goodness of fit was at or below 0.03 (*mean R^2 difference*; A1 = 0.02, A2 = 0.03, A3 = 0.02, A4 = 0.02, A5 = 0.01). In addition, the spatial distribution of this subset of vertices revealed no coherent structure in visual cortical areas (see Figure 6.11). Together, these results indicate that the dual receptive field is a poor model of the overlapping cortical representation in contralateral visual cortex in participants with albinism.

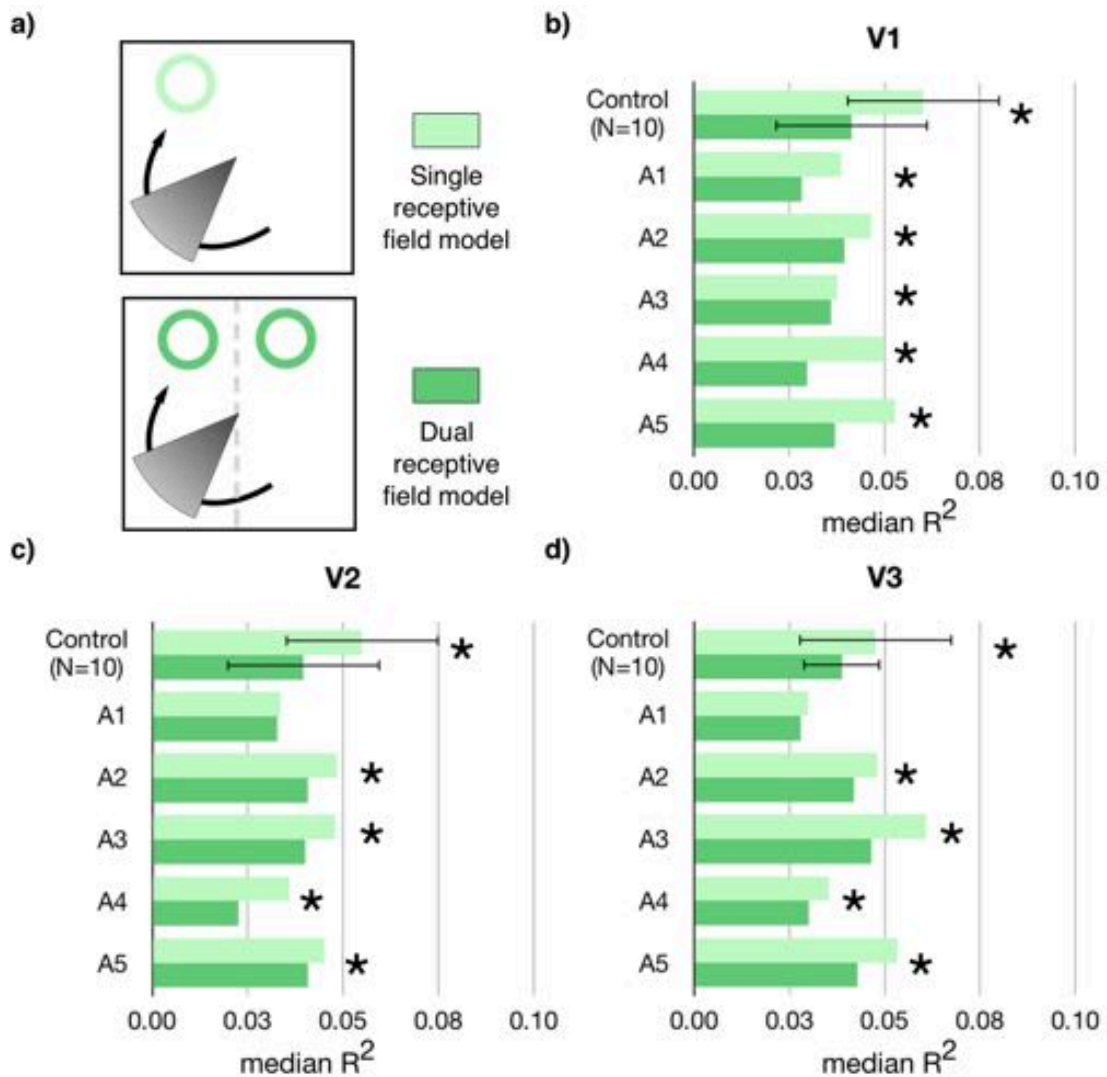


Figure 6.10 (a) BOLD responses to bilateral visual field stimulation were fitted with either a single or dual population receptive field (pRF) model. Dual receptive fields were mirrored across the vertical meridian, and of equal spread (σ). (b-d) Median goodness of fit (R^2) estimates for each model are displayed in areas V1, V2 and V3 for five participants with albinism (A1-A5) and 10 healthy controls. The single pRF model either outperformed the dual pRF model or was statistically equivalent for all participants in V1, V2 and V3. No individual comparison yielded significantly better fits for the dual pRF model over the single pRF model. Error bars represent SEM, asterisks denote significant pairwise t-test $p < 0.01$.

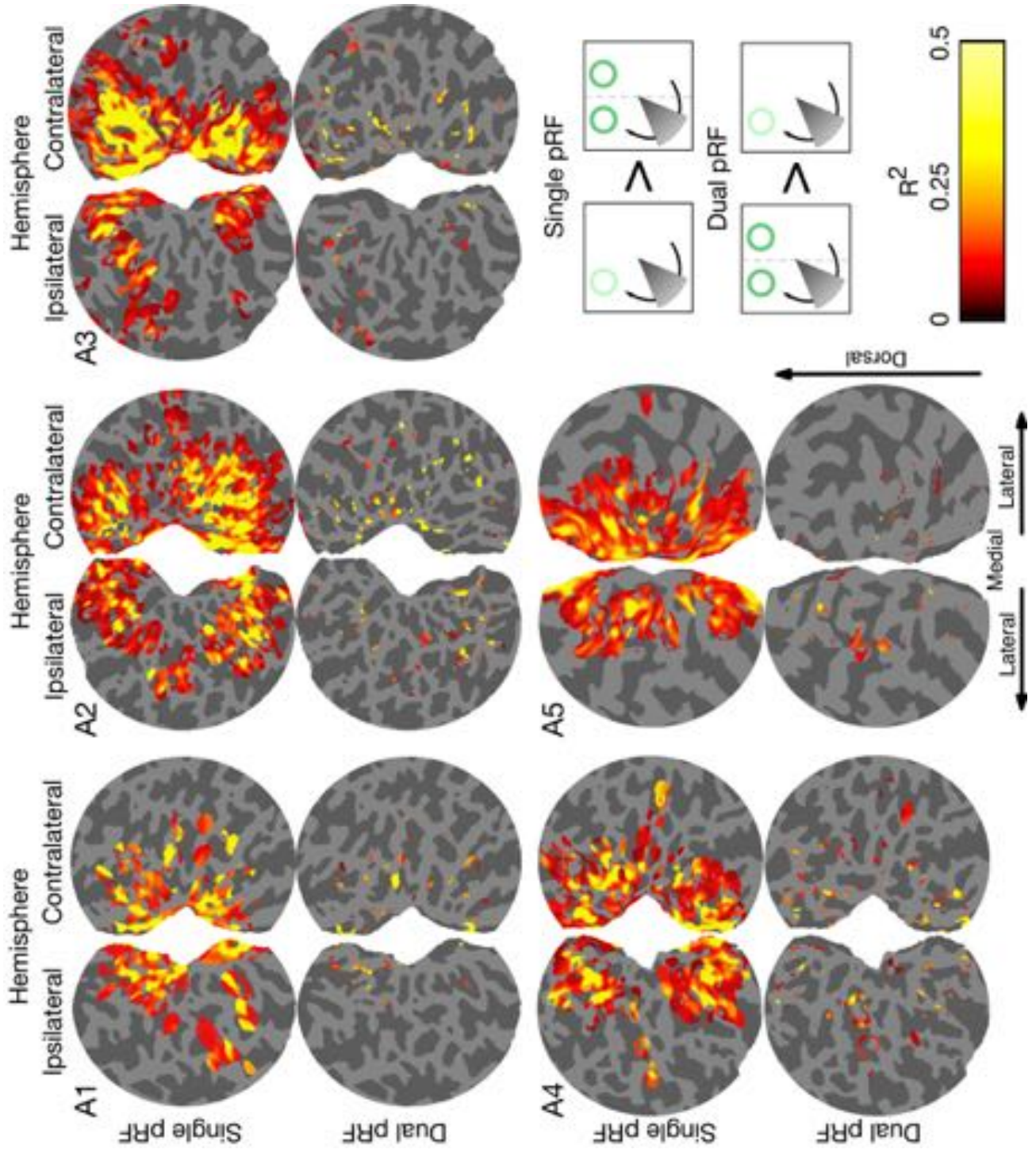


Figure 6.11 (previous page) Spatial distribution of vertices where a single population receptive field (pRF) model outperformed a mirrored dual pRF model (top row) or a dual pRF model outperformed a single pRF model (bottom row). Model goodness of fit (R^2) displayed on flattened occipital cortex for five participants with albinism (A1-A5), on hemispheres ipsilateral (left column) and contralateral (right column) to monocular eye stimulation. Both single and dual pRF models were fitted to concatenated conditions of nasal and temporal hemiretina stimulation, and single pRF model fits here are comparable to model fits seen for independent single pRF models of nasal and temporal hemiretina stimulation, displayed in Figure 6.6. Vertices where the dual pRF model outperforms the single pRF model do not form spatially coherent clusters and represent <6% of significant vertices across visual regions V1, V2 and V3. Vertices thresholded at $R^2 > 0.01$.

6.5 Discussion

In the present study, we have identified and characterised the abnormal visual field representation in five rare participants with albinism and minimal nystagmus. Following monocular stimulation of the temporal hemiretina, significant BOLD responses were observed in both ipsilateral and contralateral occipital cortices, reproducing the widely reported asymmetric lateralisation of responses in albinism (Creel et al., 1974; Carroll et al., 1980; Apkarian et al., 1983; Hedera et al., 1994; von dem Hagen et al., 2008). The abnormal response was found to be retinotopically organised, with the temporal hemiretina representation largely overlapping the nasal representation in the contralateral hemisphere, in agreement with previous electrophysiological (Guillery et al., 1984) and fMRI findings (Morland et al., 2002; Hoffmann et al., 2003; von dem Hagen et al., 2005; Kaule et al., 2014). Indeed, in the five participants with albinism reported in this study, over 50% of significantly activated vertices in regions V1, V2 and V3 responded to both nasal and temporal hemiretina stimulation in the hemisphere contralateral to stimulation. This abnormal temporal representation was further characterised by a shifted line of decussation, with foveal portions represented contralaterally, and eccentric portions represented in the ipsilateral hemisphere. This is again consistent with previous human fMRI literature (Hoffmann et al., 2003; von dem Hagen et al., 2007; Kaule et al., 2014).

One advantage of performing visual mapping with participants with unimpaired fixation is the potential for careful mapping of receptive field properties. In this study, we implemented a hemifield-restricted stimulus where in each run, a pair of de-phased, contrast-reversing apertures were presented to a single hemifield while participants fixated, therefore exclusively stimulating either the nasal or temporal hemiretina. In our sample of participants with albinism with minimal nystagmus, we were able to model the pRF responses to hemiretina mapping, revealing inter-subject variability in receptive field size, receptive field position for overlapping nasal and temporal representations, and estimates of line of decussation. Given that heterogeneity in clinical diagnosis and phenotype presentation in albinism is tightly linked with the degree of alteration in cortical representation following abnormal neurodevelopment (von dem Hagen et al., 2007; Hoffmann et al., 2015), we present an analysis of imaging based measures in relation to phenotype descriptors on a case-by-case basis, linking clinical presentation with altered cortical representations for visual space.

6.5.1 Phenotype analysis

In previous sections we have seen how fMRI-derived estimates of receptive field properties vary between participants with albinism and the control group, but also the heterogeneity in these metrics between participants with albinism. Here we present an analysis of imaging markers in relation to phenotype descriptors on a case-by-case basis.

6.5.1.1 A1

Participant A1 (F, 21 years old, OCA1A) presents a typical clinical case of developmental albinism – white blond hair, foveal hypoplasia, bilateral iris transillumination and a blonde fundus. Behaviourally, A1 did not display stereopsis, although good monocular acuity and fixation was observed. Under these circumstances, it may be expected that A1 displayed significant overcrossing temporal retina axons at the chiasm, manifesting into a large shift in the line of decussation. This is indeed what was observed, with an estimated shift of 9.40° based on lateralisation of BOLD responses to temporal hemiretina stimulation. When assessing the nature of the overlapping nasal and temporal hemiretina representations in contralateral cortex, a small nasal bias in pRF positions was detected, when comparing pRFs derived from temporal and nasal stimulation in matching cortical locations. This may be accounted for by the large shift in the line of decussation, where contralateral representations of the temporal hemiretina span both foveal and more peripheral representations, allowing greater overlap with the typical nasal representation. In contrast, for individuals where the temporal representation is predominantly foveal, these representations will tend to display nasal biases.

Finally, A1 displayed significantly increased pRF sizes in contralateral V2 under nasal stimulation, with a similar, but non-significant trend in V3. These trends may reflect an alteration in the role of extrastriate areas under abnormal overlapping representations, although the trend does not generalise to all participants.

6.5.1.2 A2

Participant A2 (M, 25 years old, OA1) presents a milder case of albinism, with a diagnosis of ocular albinism, dark blonde hair, no iris transillumination and a typically pigmented fundus. However, A2 displayed no stereopsis and foveal hypoplasia. The line of decussation shift estimated from BOLD responses was 4.40° , with significant temporal hemiretina responses in the contralateral hemisphere. This moderately sized shift in the line of decussation was accompanied with small discrepancy in horizontal position of overlapping pRFs in contralateral cortex, as seen in A1. Imaging markers indeed indicate that A2 is most similar to A1 in terms of cortical representations, despite the different clinical presentation. This

discrepancy may be resolved by the similarity in retinal development trajectory, as evidenced by retinal imaging (**Figure 6.3**). A2 displayed the smallest ganglion cell and photoreceptor layer thickness, most similar to A1, and significantly different from A3, A4 and A5.

Regarding pRF size estimates, A2 displayed a broadly similar pattern to A1, with non-significant trends toward larger pRFs in the contralateral hemisphere, and significantly larger pRF slope in the ipsilateral hemisphere. However, note that A2 also demonstrated a nasal reduction in visual field perimetry (**Figure 6.1**), potentially impairing the ability to sample the most eccentric representations of the nasal visual field. Nevertheless, results for A2 are consistent with a large shift in the line of decussation, broadly typical V1 pRFs with sizes within the control sample range, and a trend towards larger pRFs in extrastriate areas.

6.5.1.3 A3

Participant A3 (F, 50 years old, OA1) had a similar clinical presentation to A2: a diagnosis of ocular albinism, dark blonde hair, no iris transillumination, typically pigmented fundus, no stereopsis and foveal hypoplasia. In addition, a nystagmus-like horizontal eye movement pattern was detected, albeit at sub-clinical amplitudes (0.5°). A3 displayed broadly typical retinotopy, with a limited representation of the temporal fovea in the hemisphere contralateral to stimulation. Indeed, here participant A3 diverges from the previous participants, with a smaller temporal shift in the line of decussation (0.91°) and a large horizontal discrepancy in pRF locations for matching nasal and temporal retina representations in contralateral cortex ($M = 7.32^\circ$, $SD = 0.50^\circ$). pRF sizes are broadly in line with the control group data, except for a flattening of the increase in pRF size with eccentricity in contralateral V3 under temporal retina stimulation. This is most likely driven by the limited representation of the visual periphery in contralateral cortex, making a mostly foveal representation drive responses in this region.

6.5.1.4 A4

Participant A4 (M, 9 years old, OCA1B) presented blonde hair, bilateral iris transillumination, a blonde fundus, no stereopsis and foveal hypoplasia. In addition, visual field perimetry revealed a reduction in the dorsal visual field. OCA1B is typically considered a more severe form of albinism than ocular albinism, and A4 displays a larger shift in the line of decussation (1.59°), but still smaller when compared with A1 and A2. Large horizontal discrepancy in pRF locations for matching nasal and temporal retina representations were also detected in contralateral cortex ($M = 6.08^\circ$, $SD = 0.50^\circ$), and pRF sizes again fall broadly in line with control data, except for the reduction in pRF size increase with eccentricity in contralateral V3, as reported for A3.

6.5.1.5 A5

Participant A5 (M, 14 years old, OCA1B) presented blonde hair, bilateral iris transillumination, a blonde fundus, no stereopsis and foveal hypoplasia. A5 presents a very similar pattern to A4, with a small shift in the line of decussation (1.34°) and discrepancy in pRF locations in contralateral cortex ($M = 3.57^\circ$, $SD = 0.48^\circ$). Once more, pRF sizes fall broadly in line with the normative control data, with the exception of the flattened pRF size increase slope in contralateral V3, in a similar fashion to A3 and A4.

6.5.1.6 Summary

Three findings of interest emerge from the analysis presented here. First, evidence for enlarged pRF sizes in participants with significant shifts in the line of decussation (A1, A2) point towards a potentially altered role for regions representing the abnormally overlapping nasal and temporal hemiretina representations. Note however that this effect was not observed for area V1, but exclusively in extrastriate regions V2 and V3. This latter point is surprising given previous reports of reduced calcarine fissure length (Neveu et al., 2007) and increased grey matter volume and cortical thickness in albino V1 (von dem Hagen et al., 2005; Bridge et al., 2014). While one may expect such structural abnormalities to be linked with concomitant functional differences such as receptive field spatial sensitivity, as approximated in pRF metrics, it is worth highlighting that albinism is a heterogeneous disorder (Carroll et al., 1980; Neveu et al., 2003). It is therefore possible that individuals with no nystagmus in the primary position, such as those reported on here, may represent a unique population with reduced chiasmal abnormalities and therefore reduced anatomical or functional consequences at the level of cortical representations.

Second, the dissociation of participants with large (A1, A2) and small (A3, A4, A5) shifts in the line of decussation is well characterised by retinal layer thickness, specifically by the layer containing retinal ganglion cells (RGC). The degree of abnormal chiasmal crossing in albinism is well characterised as an issue of RGC differentiation and guidance (Petros et al., 2008). While the total number of RGCs is not thought to differ between healthy and albino individuals, altered retinal architecture is a hallmark of albinism (Charles et al., 1993; Summers, 1996). This result provides additional confirmation that retinal macrostructure can be directly linked to up-stream abnormalities in visual field representation at the level of cortex.

Finally, in participants with small shifts in the line of decussation (A3, A4, A5), consistent evidence for a flattening of pRF size increase in contralateral V3 under temporal stimulation is likely driven by predominantly foveal representations of the temporal retina, which tend to display small receptive fields.

6.5.2 Nature of the contralateral representation

The findings described of altered receptive field properties in albinism raise the question of functional significance for overlapping visual field representations in contralateral cortex. While it was originally postulated that the abnormal temporal representation might be suppressed (Guillery et al., 1974; Kaas, 2005), electrophysiological and functional imaging evidence in humans suggests this abnormal representation is indeed encoding valuable retinotopic information (Kaule et al, 2014). Here we show that both overlapping responses in contralateral V1 display similar pRF size increases with eccentricity, indicating a similar functional role in encoding of retinotopic information at the earliest stage of cortical processing. Altered receptive fields in extrastriate regions may indicate a shift in the role for nasal and temporal representations in these regions, with the potential for diverging roles in the processing of visual information, but significant levels of activation, retinotopic organisation and coherent receptive field increases with eccentricity all indicate this region plays an active role in the representation of the temporal hemiretina. It is also worth noting that inspection of responses to temporal hemiretina stimulation reveals a split representation across the cortical hemispheres, rather than a duplicate representation. This highlights the importance of the abnormal temporal representation in maintaining continuity of the spatial representation of the visual field, which may not be afforded by a suppressed representation.

6.5.3 Modelling responses to single and dual receptive fields

A currently outstanding issue in our understanding of albinism is how is visual information encoded when overlapping retinotopic representations are present. One possibility is that cortical cells with conservative organisation represent all the retinal inputs it receives, giving rise to DRF cells. Such cells would be responsive to mirrored nasal and temporal retinal locations and non-discriminatory of originating hemifield. Imaging evidence has suggested such cells may be present in achiasma, a related condition of optic nerve misrouting (Hoffmann et al., 2012). Alternatively, hemifield discrimination can take place at the early cortical level, with SRF cells responding to a single retinal location in order to integrate ocular dominance column information. Here, we modelled BOLD responses to bilateral visual field stimulation in participants with albinism with two models; a SRF model with a single population receptive field zone and a DRF model with two mirror-symmetrical population receptive fields divided by the vertical meridian. When assessed for model evidence, that is, how well each model fitted the data, the SRF model outperformed the DRF model in all participants, both healthy control and participants with albinism. Vertices where the DRF model provided a better fit were fewer than 6% of those sampled, and displayed no spatial clustering in cortex. Overall, evidence in this study suggests a rejection

of the DRF encoding model for human albinism, in agreement with previous psychophysical evidence (Klemen et al., 2012).

These results suggest hemifield information is therefore segregated at an early cortical level, and given the normal or sub-normal stereovision reported in albinos (Summers 1996), successful integration of ocular dominance column information without major sensory conflict. In order to achieve this, a degree of cortical plasticity must come into play, as contralateral cortical territories represent retinotopically-equivalent position in left and right visual fields that must be functionally segregated. If the 'true albino' pattern (Guillery et al., 1984) is an accurate model of visual field representation in the human, and the present study as well as recent fMRI findings suggest that may be the case (Hoffmann et al., 2003; von dem Hagen et al., 2007; Wolynski et al., 2010; Kaule et al., 2014) hemifield segregation may be achieved through the presence of hemifield columns. Nevertheless, the correct selection of sensory information across hemifield columns and between ocular dominance columns for stereopsis is not easily achieved with a conservative retinotopic organisation. Instead, these findings suggest a degree of developmental plasticity involved in providing a disambiguated sensory input to early visual processing, leading to normal or near-normal stereo vision in human albinism.

6.6 Conclusion

In summary, we have characterised the visual field responses and pRF properties of early visual cortex in five participants with albinism and minimal nystagmus. Overlapping retinotopic representations of the temporal hemiretina in the contralateral hemisphere were confirmed, corroborating previous reports, and novel pRF data revealed altered receptive field sizes in extrastriate visual cortex of human albinos. In addition, we modelled responses to bilateral stimulation in order to assess evidence for single- and dual receptive field models of overlapping retinotopic representations in contralateral cortex. We found no *in vivo* evidence for dual receptive fields, suggesting a degree of cortical plasticity allowing the segregation of hemifield information at the level of integration neurons in early visual cortex in human albinism.

Chapter 7

Interhemispheric connectivity in human albinism

7.1 Abstract

Albinism is a congenital disorder associated with abnormal projection of retinal information to the visual system. Despite aberrant post-chiasmal visual system organisation, most individuals with albinism have relatively normal visual spatial perception. This preserved ability is likely supported by an abnormally organised cortical representation of visual space, explored in the previous chapter, and evidencing the capacity of the developing visual system for plasticity. In particular, the nature of the overlapping nasal and temporal hemiretina representations in the contralateral hemisphere presents a challenge to understanding sensory integration in albinism. The high-detail foveal representation, typically segregated between hemispheres in early visual areas, is represented in overlapping territories in the contralateral hemisphere in albinism, potentially leading to alterations in the role of inter-hemispheric connectivity for sensory integration. In this chapter, functional and structural interhemispheric connectivity in human albino visual system is explored to elucidate possible mechanisms of sensory integration.

7.2 Introduction

Albinism is a congenital developmental disorder associated with abnormal development of the visual system, specifically the misrouting of the optic nerves, where temporal retina fibres over-project to the contralateral hemisphere, leaving a weak ipsilateral projection from each eye (Guillery et al., 1975; Neveu & Jeffery, 2007). While albinism is typically comorbid with other ophthalmological complaints, including reduced visual acuity, high refractive errors, and abnormal eye movements (Kinnear et al., 1985), individuals with albinism display relatively normal visual spatial perception and visually guided behaviour, despite aberrant optic nerve inputs to the visual system (Summers, 1996). How the abnormal sensory input is organised, in order to give rise to a coherent representation of visual space, is a currently outstanding question, both specifically in understanding cortical organisation in albinism, and more generally, the plastic capacity for development in the visual system.

The unusual arrangement of visual space representation in early visual cortex explored in the previous chapter raises the question of how efficient integration of visual information is achieved, in order to form a coherent representation of the visual field. In the normally developed visual system visual field information is lateralised, with interhemispheric transfer necessary in order to form a full representation of the visual field. In albinism, however, both left and right visual field information can be represented in the same hemisphere, at least

for the central portion of the visual field containing the foveal representation. In order to optimise information processing, the developing albino brain may incorporate one of the following three strategies; First, if the visual hemifield is successfully integrated at the intra-hemispheric level, diminishing the role of interhemispheric transfer for the formation of visual spatial representations in albino early visual cortex. Second, if visual hemifield integration is not achieved within a single hemisphere, an alternative mechanism may drive increased interhemispheric connectivity to allow integration of the now sundered temporal retina representation, split between the two hemispheres. Third and finally, if the developmental pattern for the formation of the visual system is strongly conservative, the albino brain may experience no alteration in interhemispheric connectivity, despite aberrant sensory input and altered visual field representations within cortical visual areas. The following experiment assesses evidence for and against these three strategies.

We examined structural and functional connectivity *in vivo* in five participants with albinism and ten healthy controls, with particular focus on inter-hemispheric connectivity between early visual areas. Specifically, we asked three questions; a) is there evidence for macro- or micro-structural differences in interhemispheric white matter fibre organisation between participants with albinism and controls, b) are those differences, if any, attributable to functionally-relevant segments of the splenium of the corpus callosum projecting to early visual areas V1, V2 and V3, and c) is there evidence for altered interhemispheric functional connectivity between early visual areas at rest in human albinism.

7.3 Materials and Methods

7.3.1 Participants

Five participants with albinism (A1-A5) and 10 healthy adult controls previously described in Chapter 6 took part in the study. This study was approved by the London - City and East Research Ethics Committee of the UK Health Research Authority.

7.3.2 Retinotopic mapping

Data acquired during population receptive field (pRF) mapping were used to localise visual areas (see Chapter 6 for further details). Polar angle estimates derived from pRF model fits were projected on the subject-specific reconstructed cortical surface and used to delineate areas V1, V2 and V3 in each occipital hemisphere independently. Resulting region definitions were subsequently used to sample resting-state fMRI signals and as seed and target regions for white matter tractography.

7.3.3 MRI acquisition

MR images were acquired on a 1.5T Avanto MRI system using a 32-channel head coil (Siemens Healthcare, Erlangen, Germany). Participants were instructed to lie still with their eyes open throughout acquisition. No visual stimulation was delivered. Resting-state fMRI was acquired for 300 volumes with a gradient echo EPI sequence (TR = 1 s, TE = 55 ms, 36 interleaved slices, resolution = 2.3 x 2.3 x 2.3 mm) using parallel multi-slice acquisition (multiband factor = 4) (Breuer et al., 2005). In addition, diffusion-weighted EPI volumes were acquired with 60 non-collinear gradient directions at $b = 1000$ s/mm² and 1 $b = 0$ s/mm² reference volume (TR = 7.50 s, TE = 104 ms, maximum gradient amplitude = 40 mT/m⁻¹, 46 interleaved axial slices, resolution = 2.3 x 2.3 x 2.3 mm). All EPI acquisitions included 10 dummy volumes at the beginning of each run that were automatically discarded to allow for stabilisation of the longitudinal magnetisation. Finally, a high resolution T1-weighted MPRAGE volume was also acquired (TR = 2.73 s, TE = 3.57 s, resolution = 1 x 1 x 1 mm) to aid registration.

7.3.4 Tractography analysis

Diffusion-weighted volumes were pre-processed using the FSL-FDT toolbox (Behrens et al. 2003). Each volume was registered to the first, non-diffusion-weighted volume in order to correct for motion and eddy current artefacts. Next, data were analysed with MRtrix (Tournier et al., 2012), where a standard diffusion tensor model was fitted and fractional anisotropy (FA) and mean diffusivity (MD) scalar maps were derived. FA is thought to reflect the degree of myelination, axon diameter, axonal density and the coherence of the underlying microstructure in the tissue sampled (Catani & Dell'Acqua, 2011; Jones et al., 2012). While not specific to any of these components, in healthy white matter tissue, as expected from healthy individuals with or without albinism, it reflects the general state of axonal bundles and their orientation, with higher values indicating thicker, more tightly packed axons with more coherent orientation. MD, on the other hand, reflects direction-independent water dispersion within the sampled tissue (Le Bihan et al., 2001; Ciccarelli et al., 2008). As a microstructural marker, it can be seen as having an inverse relationship to FA; larger, numerous and tightly packed axons create more restrictions to diffusing water, and therefore drive MD values down. Together, FA and MD are considered general markers of white matter integrity. In order to produce a model of white matter fibre orientation that accounts for voxels containing more than one fibre trajectory, a constrained spherical deconvolution (CSD) model was fitted (Tournier et al., 2007). Data were iteratively sampled to identify voxels containing a single coherently-oriented fibre bundle and this signal was taken as the base response function for every voxel during a deconvolution procedure which results in an n -fibre model at each voxel, where $1 \leq n \leq 8$.

Two white matter pathways were reconstructed using a probabilistic white matter tractography algorithm (step size = 0.2 mm, angular threshold = 1 mm, FA threshold = 0.1, number of streamlines = 10,000). First, the splenium of the corpus callosum was delineated manually on a single coronal slice centred on the midline and used as a seed region. Streamlines originating from the splenium and terminating in either left or right functional definitions of regions V1, V2 or V3 were retained. Subject-specific definitions of functional visual regions were derived from pRF retinotopic mapping. Second, the corticospinal tract was selected as a control structure, due to its lack of involvement in visual processing and anatomical distance from the other sampled structures. Streamlines were traced between manual definitions of the internal capsule and primary motor cortex in each hemisphere (Catani & Thiebaut de Schotten, 2008). All tracking was performed in subject native space.

As a further level of analysis, streamlines in the splenium were segmented based on projections between different levels of the visual system hierarchy. For each participant, streamlines were classified as belonging to the V1 \leftrightarrow V1 segment of the splenium if the streamline intersected functionally defined area V1 on both left and right hemispheres, and did not intersect areas V2 or V3 in either hemisphere. The equivalent approach was taken to derive V2 \leftrightarrow V2 and V3 \leftrightarrow V3 segments. Streamlines that intersected more than one visual area were excluded. Resulting white matter reconstructions were thresholded voxel-wise (>10% streamlines per voxel) and used as masks to extract total voxel count as a proxy for tract volume and mean microstructural markers (FA, MD) in each tract, in order to compare macro- and microstructural features between participants with albinism and the control group.

7.3.5 Functional connectivity analysis

Resting-state fMRI volumes were pre-processed in SPM8 (Wellcome Trust Centre for Neuroimaging, <http://www.fil.ion.ucl.ac.uk/spm>). All images were bias-corrected, realigned to the first image of each run, unwrapped to correct for static magnetic field inhomogeneities and slice timing-corrected to reduce variation in the time series introduced by the timing of slice acquisition. High-resolution anatomical images were processed with FreeSurfer (Dale et al., 1999; Fischl et al., 1999), creating a cortical surface render for each participant, and functional data were projected to the cortical surface. A linear regression was applied to remove signal contributions associated with participant motion within the run, as estimated from rigid-body registration. In addition, data were subject to a high-pass temporal filter (cut-off = 100 s) and surface-based spatial smoothing (FWHM = 3 mm).

Pre-processed time series were extracted from each region of interest, namely regions V1, V2 and V3 in both hemispheres, by applying principal component analysis (PCA) using a single value decomposition algorithm across voxels contained in each region, and selecting

the first principal component. This approach was favoured in order to reduce the dimensionality of the data and summarise temporally coherent features of the resting state signal within each region of interest. PCA is a common dimensionality reduction tool in neuroimaging, and appropriate where a consistent representation of the signal within each region is desired and where spatial independence is determined *a priori*, as in the case of ROI-based analysis (Beckmann & Smith, 2004; Cole et al., 2010). Resulting time series were then compared across regions within subjects using Pearson's product-moment correlation (r) and converted to r -prime (r') values via Fisher's z-transformation to regularise variance across samples and allow parametric statistical comparison.

7.4 Results

7.4.1 Structural connectivity

The splenium of the corpus callosum and corticospinal tracts were successfully reconstructed in all participants, with no macroscopic differences in bundle anatomy observed between participants with albinism and controls (see **Figure 7.1**).

7.4.1.1 Tract volume

In order to assess tract volume differences between groups, streamline visitation maps for each participant were thresholded, only retaining voxels visited by $\geq 10\%$ of streamlines generated. The number of surviving voxels for each tract were then normalised by dividing the total tract volume by the total intracranial volume (TIV) of each participant (Ciccarelli et al., 2003). Estimates of TIV were obtained by automatic segmentation and template normalisation of T_1 -weighted images in FreeSurfer (Buckner et al., 2004). While this approach does not provide precise quantification of the anatomical volume of white matter fascicles comparable to *ex vivo* dissection (e.g. Dauguet et al., 2007), it does permit relative quantification of normalised volumetric differences between populations (Chard et al., 2002; Wakana et al., 2007; Fernandez-Miranda et al., 2012).

Raw estimates of splenium volume were comparable between participants with albinism ($A1 = 13.66$, $A2 = 16.39$, $A3 = 15.39$, $A4 = 12.75$, $A5 = 15.80$ cm^3) and the normative control group (16.08 $\text{cm}^3 \pm 0.44$ SEM). Similarly, upon normalisation by total intracranial volume, estimates remained comparable (see **Figure 7.2**). In order to assess statistical differences between individual participants with albinism and the control group, we implemented the Bayesian hypothesis testing approach for contrasting single cases versus matched control samples (Crawford et al., 2011) previously described in section 6.4.3. All individual

comparisons are against $N = 10$ controls, two-tailed p -values reported below. Effect sizes and point estimate of percentage of control population falling below the patient's score are also reported for significant results. Normalised splenium and corticospinal tract volumes were assessed, with no significant difference detected between the control group and A1-A5 in either tract (all comparisons $p \geq 0.05$) see **Table 7.1** for individual results).

7.4.1.2 *Microstructural differences*

Microstructural differences between groups were probed by sampling two imaging markers: fractional anisotropy (FA) and mean diffusivity (MD) from each participant (see **Figure 7.3**). Regions of interest were defined as voxels containing >10% streamlines for each structure of interest (splenium of the corpus callosum, corticospinal tract), and voxel-wise microstructural values for each structure, in each individual were taken as samples for statistical analysis. As before, the Bayesian single cases versus control group test was used here to assess differences in tract microstructure.

No significant difference in FA was detected between the control group and participants with albinism for the splenium or the control corticospinal tract (all comparisons $p \geq 0.05$). Similarly, no significant differences in MD were detected for the splenium, or corticospinal tract (all comparisons $p \geq 0.05$, see **Table 7.1** for individual results).

In summary, no significant differences in gross anatomy, tract volume or tissue microstructure were detected in participants with albinism when compared with the normative control group. This broad similarity was not restricted to the region of interest involved in interhemispheric connectivity for the occipital lobes, the splenium of the corpus callosum, but the pattern of similarity was also seen in the control region, the corticospinal tract, indicating the similarity in macro- and microstructure is not circumscribed to the occipital area.

Figure 7.1 (previous page) Course of probabilistic tractography reconstruction of the splenium of corpus callosum (red) and control corticospinal tract (green) overlaid on native T1-weighted structural MRI. Tracts displayed five participants with albinism (A1-A5) and one representative participant (C1). The broad neuroanatomy of tracts of interest was in agreement with normative control data, and no significant tract volume or microstructural differences were detected.

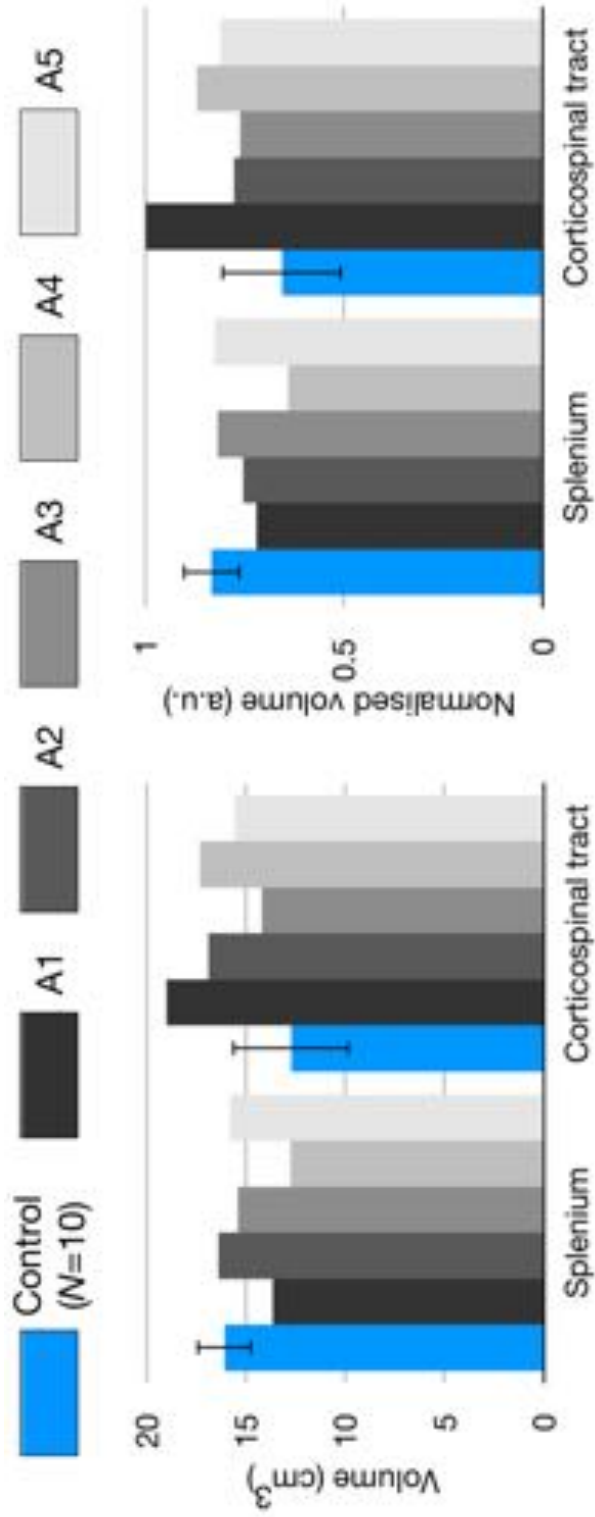


Figure 7.2 Estimates of white matter tract volume (cm³) and tract volume normalised by total intracranial volume (a.u.) in normative control group (N=10) and five participants with albinism (A1-A5). Volumes are displayed for splenium of the corpus callosum and bilateral corticospinal tracts, as derived from probabilistic tractography reconstructions. Only voxels visited by $\geq 10\%$ of streamlines were included in volume estimation. No significant difference in normalised tract volume was found between control group and A1-A5. Error bars indicate standard deviation for control group.

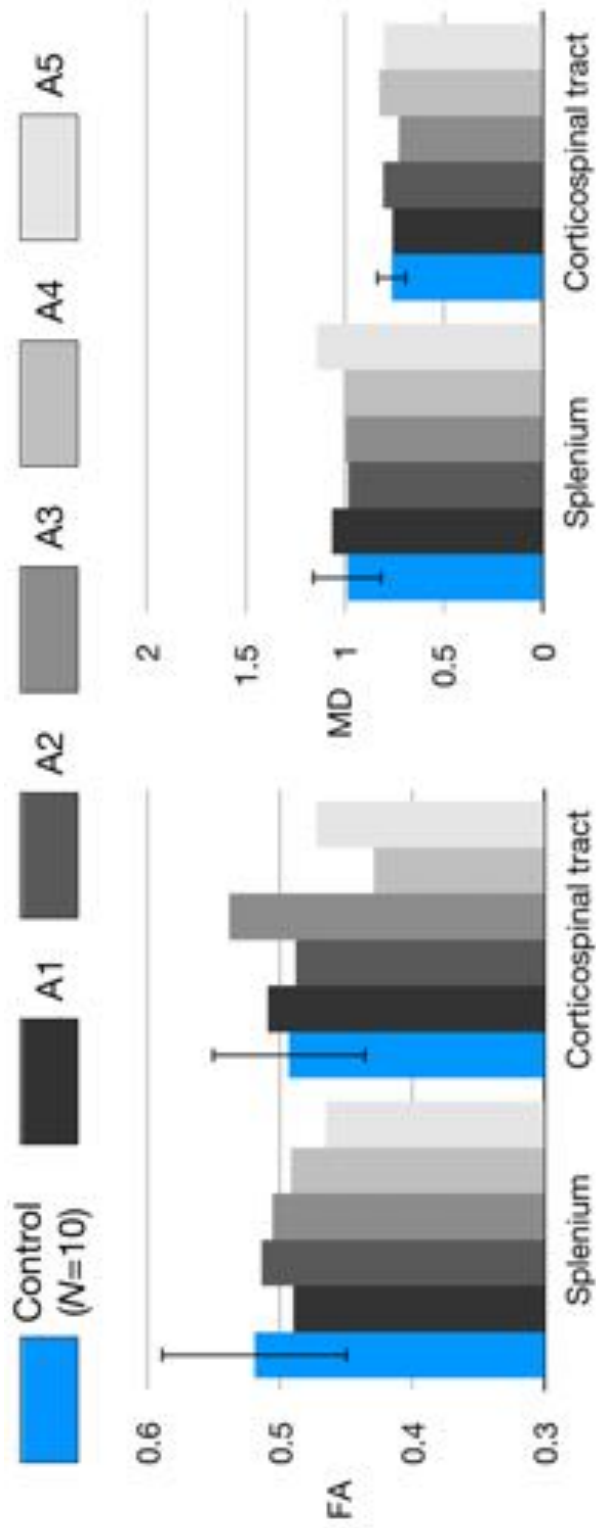


Figure 7.3 Mean fractional anisotropy (FA) and mean diffusivity (MD) in normative control group (N=10) and five participants with albinism (A1-A5). Microstructural values displayed for splenium of the corpus callosum and bilateral corticospinal tracts, as derived from probabilistic tractography reconstructions. Only voxels visited by $\geq 10\%$ of streamlines were included. No significant differences in microstructure were detected between the control group and A1-A5. Error bars indicate standard deviation for control group.

7.4.2 Hierarchical segmentation of the splenium

The splenium of the corpus callosum is integral to interhemispheric transfer of information between occipital visual regions and follows a stereotyped organisation of fibres, with individual segments mapping transcallosal connections between pairs of V1, V2 and V3 region (Saenz & Fine, 2010; Genç et al., 2011a). While no volumetric or microstructural differences were detected between A1-A5 and control group, it is possible that region-specific sub-fascicular differences are masked by the large anatomical extent of the splenium as a whole. In order to assess this, we divided reconstructions of the splenium into hierarchy-based segments corresponding to V1 \leftrightarrow V1, V2 \leftrightarrow V2 and V3 \leftrightarrow V3 projections.

7.4.2.1 Hierarchical segment macrostructure

The distribution of streamlines for each segment was confined to the antero-ventral splenium in all participants (**Figure 7.4**) in agreement with previous studies (Genç et al., 2011b). In order to ensure consistent sampling across participants, the number of streamlines retained in each segment of the splenium were assessed with the Bayesian single cases versus control group test (**Figure 7.5**). No significant effect of segment streamline count was found for V1 \leftrightarrow V1 (A1 $p = .989$, A2 $p = .631$, A3 $p = .688$, A4 $p = .142$, A5 $p = .476$), V2 \leftrightarrow V2 (A1 $p = .504$, A2 $p = .779$, A3 $p = .343$, A4 $p = .153$, A5 $p = .651$), or V3 \leftrightarrow V3 (A1 $p = .184$, A2 $p = .702$, A3 $p = .458$, A4 $p = .521$, A5 $p = .831$).

Volumetric differences were assessed by obtaining streamline visitation maps, thresholding each V1, V2 or V3 segment to include only retaining voxels visited by $\geq 10\%$ of streamlines retained, and normalising volume estimates by the combined volume of the bilateral corresponding visual area (see **Figure 7.5** for volume estimates of cortical definitions of V1, V2 and V3). This procedure ensures segment volume is not biased by differences in overall visual cortical area size (**Figure 7.6**). No significant difference in segment volume was found between A1-A5 and the control group for the V1, V2 or V3 segments of the splenium (all comparisons $p \geq 0.05$, see **Table 7.1** for individual results).

7.4.2.2 Hierarchical segment microstructure

Microstructural markers from V1, V2 and V3 segments of the splenium of the corpus callosum were sampled in a similar fashion, with each segment thresholded to include only retaining voxels visited by $\geq 10\%$ of streamlines retained, and voxel-wise microstructural values for each segment taken as samples for statistical analysis (**Figure 7.7**).

No significant difference in FA was detected between the control group and participants with albinism for the V1, V2 or V3 segment of the splenium (all comparisons $p \geq 0.05$). Similarly, no significant effect in MD was detected for V1, V2 or V3 segments (all comparisons $p \geq 0.05$, see **Table 7.1** for individual results).

In summary, upon inspection of functionally-defined segments of the splenium of the corpus callosum, no significant differences in streamline count, segment volume or tissue microstructure were detected when comparing participants with albinism and the normative control group. Together with results for the full extent of the splenium and corticospinal tract, these results argue for stability in structural inter-hemispheric connectivity for participants with albinism studied here.

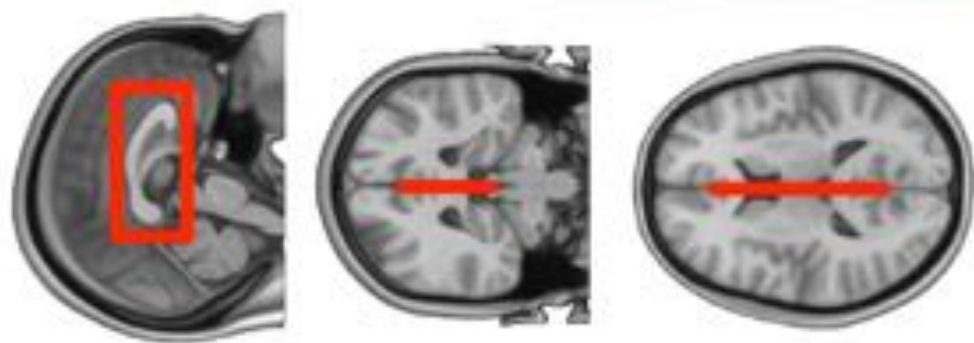
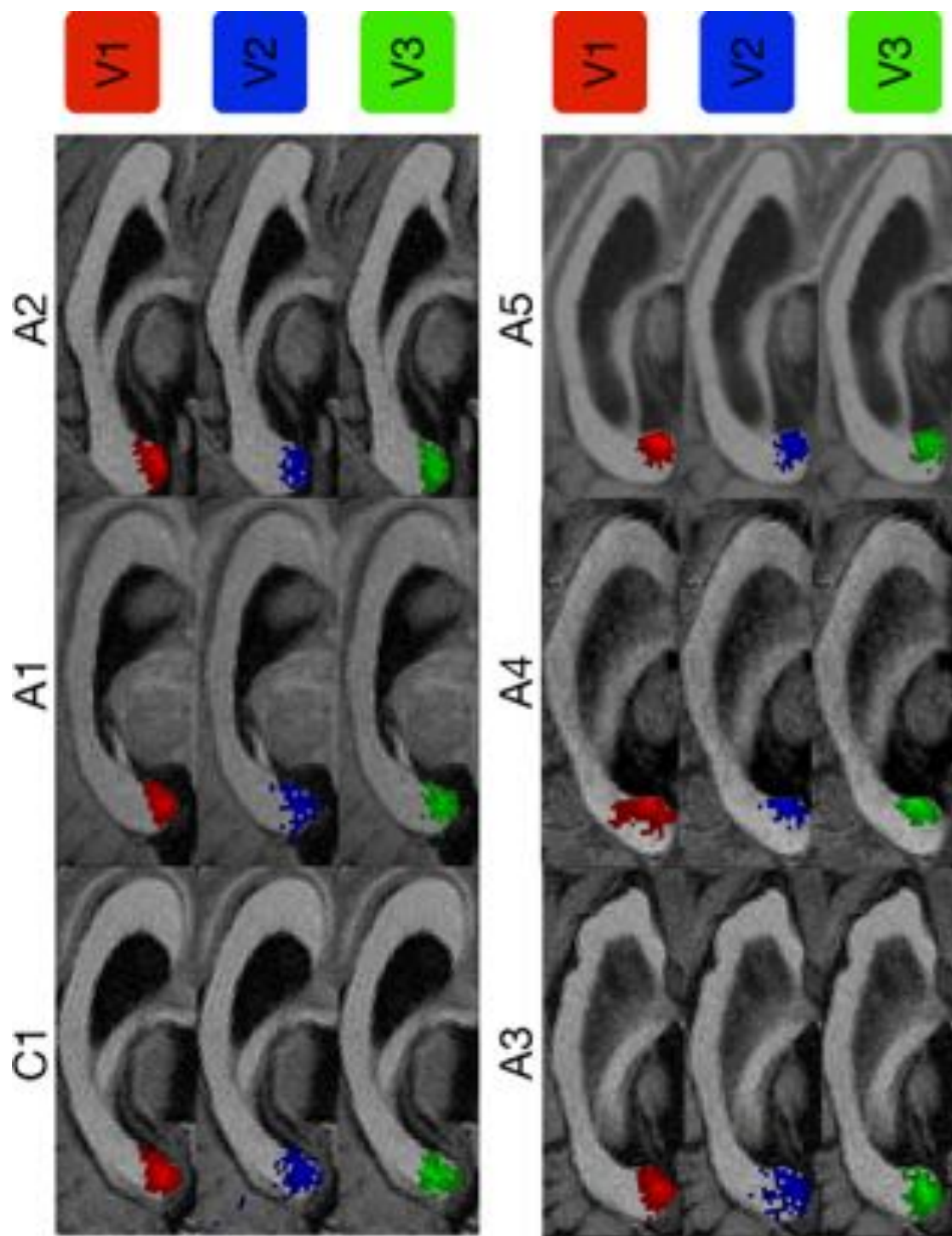


Figure 7.4 (previous page) Hierarchical segmentation of the splenium of the corpus callosum in one representative control (C1) and five participants with albinism (A1-A5). Functionally-defined segments of the splenium of the corpus callosum were generated by generating probabilistic tractography streamlines for the course of the splenium, and later classified as belong to either the V1 \leftrightarrow V1, V2 \leftrightarrow V2 or V3 \leftrightarrow V3 segments, depending on their cortical termination sites. Functionally-classified streamlines were largely confined to the antero-ventral portion of the splenium, in agreement with previous studies. No significant differences in splenium segment streamline count, volume or microstructure were detected when comparing A1-A5 with the control group using single case versus group analysis. Voxels thresholded at $\geq 10\%$ of retained streamlines.

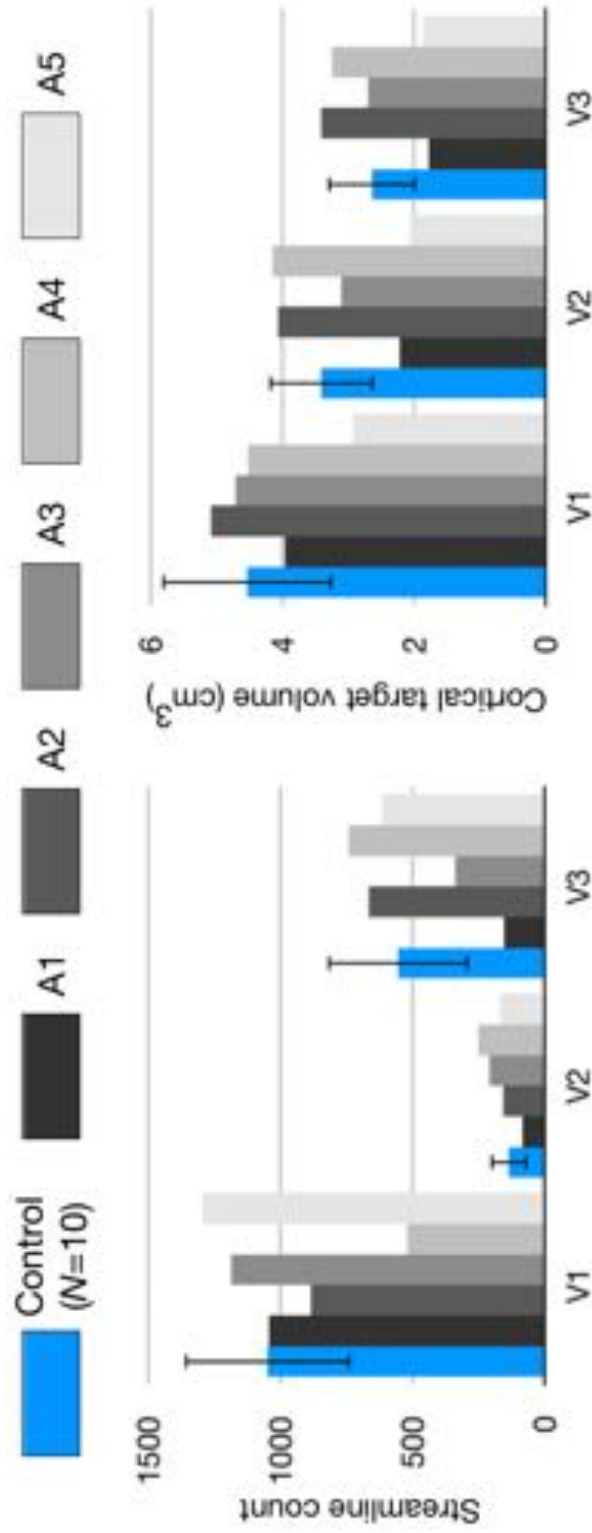


Figure 7.5 Probabilistic tractography streamlines in the splenium of the corpus callosum were classified as belonging to either the V1, V2 or V3 segments. Streamline counts for segmented bundles (absolute values), and volume of cortical targets (cm³) used to generate tract segmentation are shown for normative control group (N=10) and five participants with albinism (A1-A5). Volumetric measurements of target regions were estimated by projection from the cortical surface to 1mm isotropic volumetric space. No significant difference in streamline count was found between control group and A1-A5. Error bars indicate standard deviation for control group.

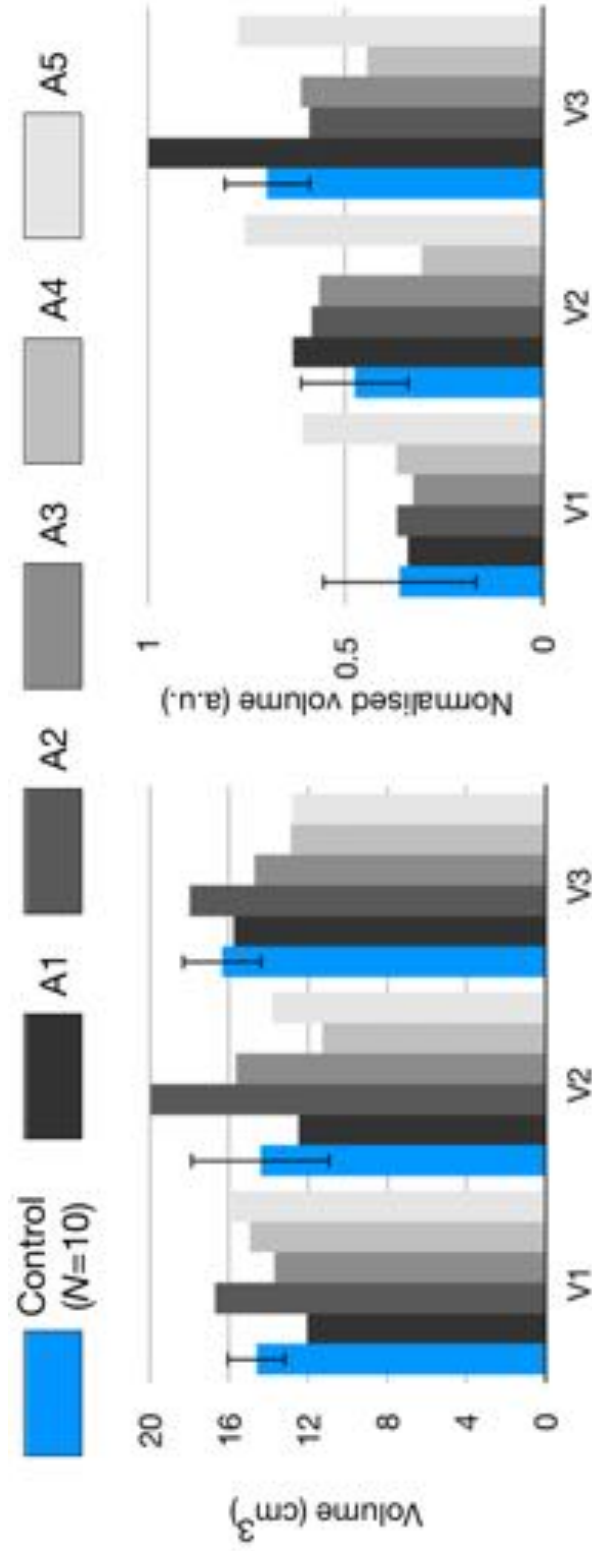


Figure 7.6 Estimates of white matter tract volume (cm^3) and tract volume normalised by volume of cortical target area (a.u.) in normative control group ($N=10$) and five participants with albinism (A1-A5). Volumes are displayed for functionally-defined V1, V2 and V3 segments of the splenium of the corpus callosum, as derived from probabilistic tractography reconstructions. Only voxels visited by $\geq 10\%$ of streamlines retained following streamline classification into segments were included in volume estimation. No significant difference in normalised tract volume was found between control group and A1-A5. Error bars indicate standard deviation for control group.

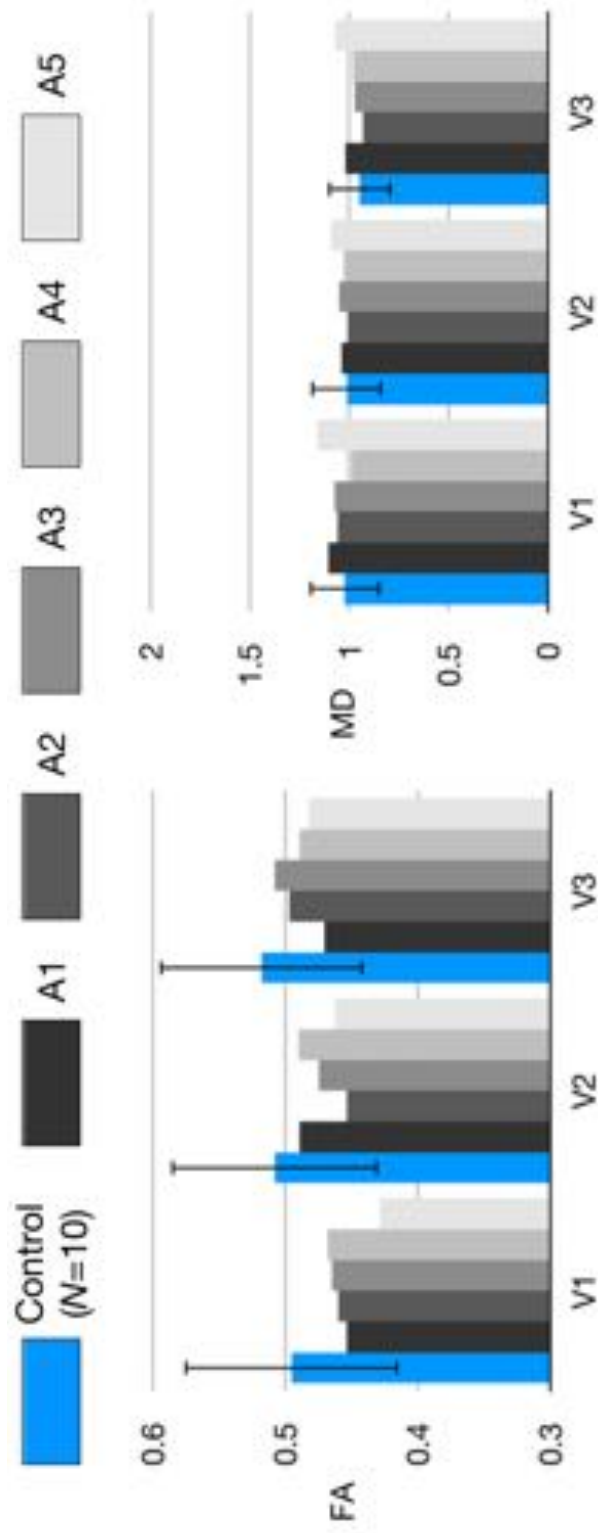


Figure 7.7 Mean fractional anisotropy (FA) and mean diffusivity (MD) in normative control group (N=10) and five participants with albinism (A1-A5). Microstructural values displayed for functionally-defined V1, V2 and V3 segments of the splenium of the corpus callosum, as derived from probabilistic tractography reconstructions. Only voxels visited by $\geq 10\%$ of streamlines were included. No significant differences in microstructure were detected between the control group and A1-A5. Error bars indicate standard deviation for control group.

Table 7.1 Hypothesis testing for structural connectivity analysis. Bayesian single cases versus matched control samples test (Crawford et al., 2011) used to assess differences between participants with albinism (A1-A5) and control sample ($N = 10$) in the following outcome variables; (a) white matter tract volume, (b) fractional anisotropy (FA) and (c) mean diffusivity (MD) along the course of the reconstructed white matter tract or segment. Two-tailed p -values reported below, no comparison was found to be significant at $p < .05$.

a) White matter tract volume single case versus control sample test p-value

	Splenium	Splenium segmentation			CST
		V1-V1	V2-V2	V3-V3	
A1	.172	.059	.806	.413	.076
A2	.316	.471	.891	.574	.329
A3	.836	.532	.759	.657	.404
A4	.052	.207	.902	.319	.064
A5	.917	.365	.412	.151	.768

b) White matter FA single case versus control sample test p-value

	Splenium	Splenium segmentation			CST
		V1-V1	V2-V2	V3-V3	
A1	.900	.633	.822	.567	.931
A2	.981	.690	.519	.792	.981
A3	.953	.724	.696	.904	.818
A4	.909	.758	.831	.728	.748
A5	.820	.425	.588	.667	.915

c) White matter MD single case versus control sample test p-value-1

	Splenium	Splenium segmentation			CST
		V1-V1	V2-V2	V3-V3	
A1	.900	.894	.973	.907	.992
A2	.991	.960	.987	.960	.869
A3	.992	.934	.947	.965	.891
A4	.992	.947	.987	.954	.809
A5	.799	.830	.894	.819	.881

7.4.3 Functional connectivity

The previous sections dealt primarily with structural measures, namely diffusion tractography and microstructural markers. While these metrics typically provide an account of the anatomical substrate of interhemispheric connectivity, they provide little information on the nature of information processing (Hagmann et al., 2006; Ciccarelli et al., 2008). In order to explore the functional connectivity of visual areas in albinism, resting-state fluctuations in BOLD signal were inspected in striate and extrastriate visual areas. Patterns of inter-hemispheric connectivity were estimated using a correlational approach, where time series observed at each region were directly compared to time series in all regions in the opposite hemisphere. These patterns are summarised in **Figure 7.8**.

In order to assess differences in patterns of functional connectivity between A1-A5 and the control group, correlation coefficients for subject-specific region pairs were regularised via Fisher's z-transform to r-prime (r') and compared via Bayesian single cases versus control sample tests (Crawford et al., 2011). Two-tailed p -values, effect sizes and point estimate of percentage of control population falling below the patient's score are reported. As the present analysis is not concerned with the directionality of connections, we considered symmetrical relationships, for example left V1 \Leftrightarrow right V2 and left V2 \Leftrightarrow right V1, equivalent for the purposes of statistical analysis.

7.4.3.1 Homologous connections

First, we compared the inter-hemispheric connectivity of homologous regions, that is, the functional connectivity between left and right hemisphere locations of V1, V2 and V3 (see **Figure 7.9**).

For area V1, we see a pattern of significantly lower inter-hemispheric connectivity, detected for A1 ($p < .001$, *effect size* = 4.47, *point estimate* = 0.11%), A2 ($p < 0.001$, *effect size* = 4.77, *point estimate* = 0.07%), and A5 ($p = 0.031$, *effect size* = 2.67, *point estimate* = 1.56%), with no significant difference for A3 ($p = .593$) or A4 ($p = .246$).

Connections between pairs of region V2 showed a more complex pattern of inter-subject variability, with significantly decreased connectivity for A2 ($p = 0.01$, *effect size* = 3.59, *point estimate* = 0.38%), and significantly increased connectivity for A4 ($p = .040$, *effect size* = 2.59, *point estimate* = 98.22%). No differences were detected for A1 ($p = .420$), A3 ($p = .330$) or A5 ($p = .090$).

Finally, area V3 shows a reversal of the pattern observed in V1, with significantly increased inter-hemispheric connectivity for A2 ($p = .040$, *effect size* = 2.57, *point estimate* = 98.16%), A3 ($p = .045$, *effect size* = 2.39, *point estimate* = 97.51%), A4 ($p < .001$, *effect size* = 4.13,

point estimate = 99.83%), A5 ($p = .040$, *effect size* = 2.48, *point estimate* = 97.87%) and a non-significant trend in A1 ($p = .670$).

7.4.3.2 *Cross-hierarchical connections*

Interhemispheric homologous cortical regions, such as left and right V1, are known to display synchronous activity at rest (Damoiseaux et al., 2006; Raemaekers et al., 2014), but this pattern is not limited to homologous regions and does indeed extend to pairs of regions that are computationally dependent, such as those spanning the visual cortical hierarchy (Buckner & Yeo, 2013). In order to assess these relationships, we also examined cross-hierarchical connectivity between pairs of regions in V1, V2 and V3, comparing connectivity indices for A1-A5 with the control group (**Figure 7.9**).

Bilateral connectivity between areas V1 and V2 showed no significant differences between participants with albinism and the control group (A1 $p = .567$, A2 $p = .858$, A3 $p = .999$, A4 $p = .464$, A5 $p = .493$). Similarly, bilateral connectivity between areas V1 and V3 displayed no significant differences (A1 $p = .853$, A2 $p = .549$, A3 $p = .411$, A4 $p = .236$, A5 $p = .107$). Finally, bilateral connectivity between areas V2 and V3 showed no significant differences (A1 $p = .770$, A2 $p = .370$, A3 $p = .492$, A4 $p = .350$, A5 $p = .320$).

In summary, for homologous pairs of regions V1, V2 and V3, we observed a gradient pattern of interhemispheric functional connectivity for A1-A5 when compared with a normative control group. The pattern is described by a decrease in inter-hemispheric connectivity in V1, transitioning into a pattern of increased connectivity in higher extrastriate areas, with significant inter-subject variability. In contrast to homologous pairs of regions, cross-hierarchical connections in the early visual system displayed no significant differences in functional connectivity for A1-A5.

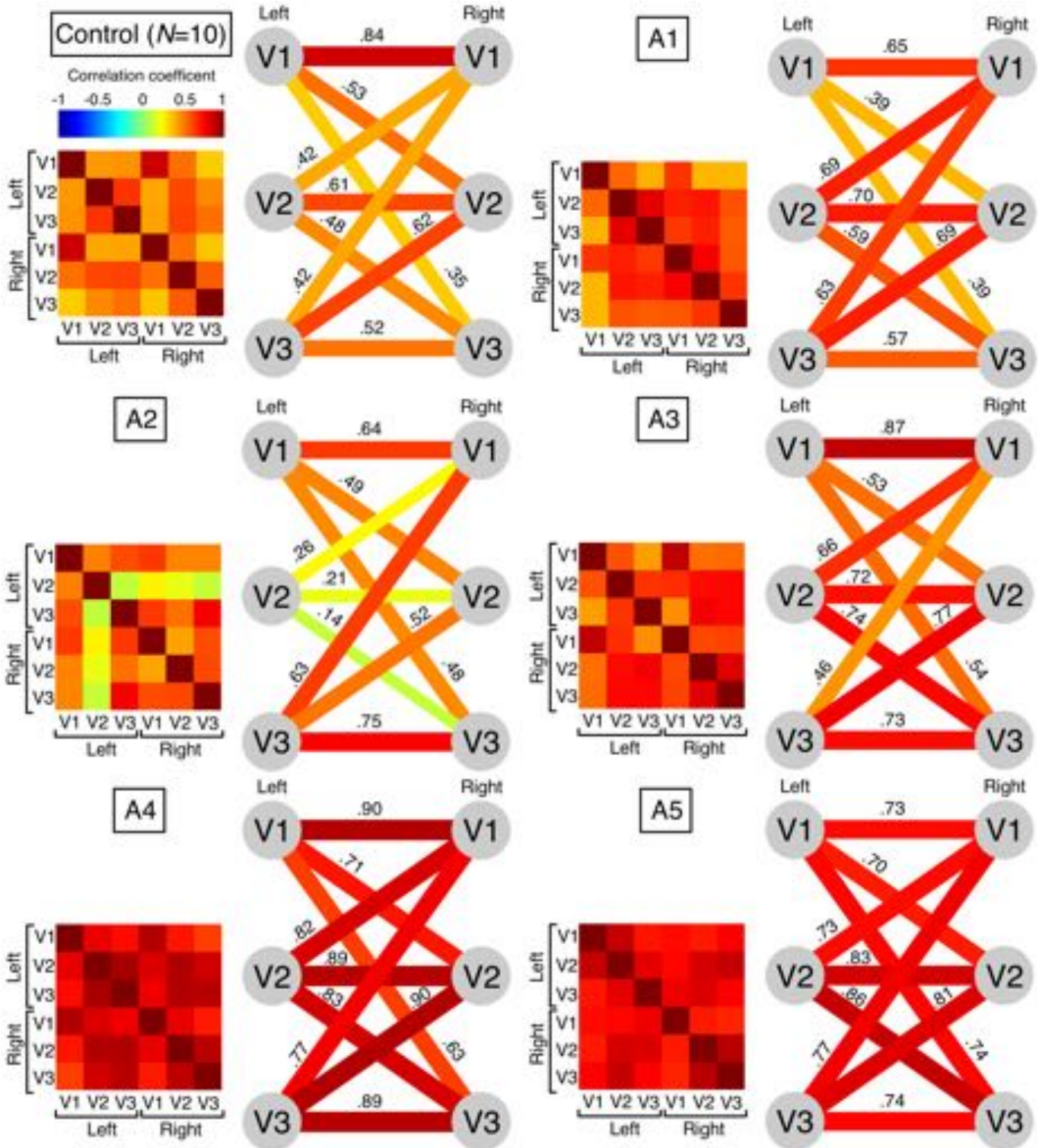


Figure 7.8 (previous page) Correlational interhemispheric functional connectivity for visual areas V1, V2 and V3 in participants with albinism (A1-A5) and average control group ($N=10$). Cells in correlation matrix and edges in diagram represent Pearson's correlation coefficient (r) between observed BOLD signals in pairs of regions. Colour illustrates relative correlation strength. For homologous pairs of regions, a variable gradient of interhemispheric functional connectivity was found for A1-A5. $V1 \Leftrightarrow V1$ showed lower interhemispheric connectivity for A1, A2 and A5, a mixture of increase and decrease in $V2 \Leftrightarrow V2$ and broadly an increase in $V3 \Leftrightarrow V3$ connectivity for A2, A3, A4 and A5 (all tests $p < .05$). No significant differences in cross-hierarchical connectivity were detected for A1-A5 when compared with the normative control group.

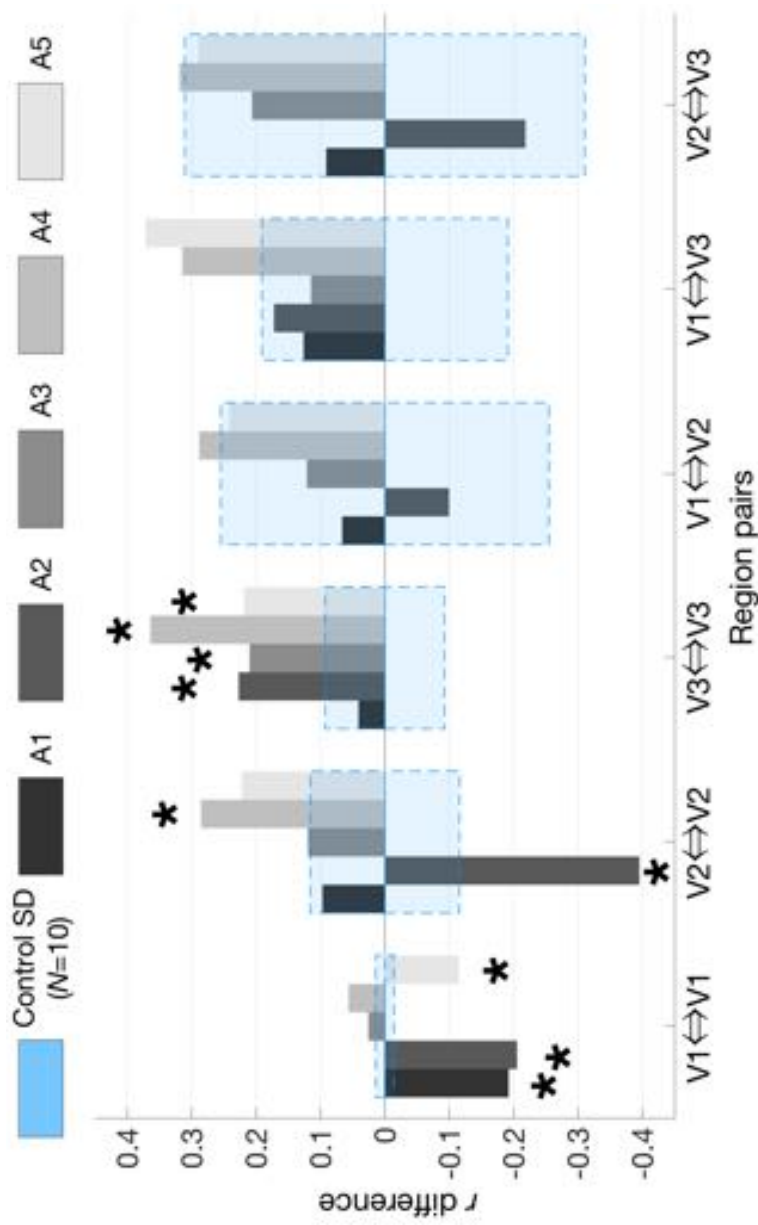


Figure 7.9 Differences in interhemispheric functional connectivity between participants with albinism (A1-A5) and average control group (N=10, blue). For each pair of regions, the difference between individual correlation coefficient and mean correlation coefficient for the control group are show. Significant differences in functional connectivity were detected in homologous region pairs V1 ↔ V1, V2 ↔ V2 and V3 ↔ V3, while no significant difference was detected in cross-hierarchical connections. Blue zone represents standard deviation in control group, and stars denote significant differences $p < .05$.

7.4.4 Lateralised functional connectivity

The analysis of functional connectivity so far has assumed symmetric relationships between hemispheres, drawing equivalence between, for example, left V1 \Leftrightarrow right V2 and left V2 \Leftrightarrow right V1. However, upon closer examination lateralised patterns of connectivity can be seen in **Figure 7.8**, most strikingly in patterns of low functional connectivity with region left V2 for participant A2. As a further level of analysis, selected patterns of inter-hemispheric asymmetry were assessed, with only connections displaying a difference in correlation coefficients (r_{diff}) greater than the standard deviation of the control group ($SD = 0.20$) were included in the analysis. A Bayesian standardised differences test for single cases, given the mean and variance in a modestly-sized control group (Crawford et al., 2010b; Crawford et al., 2011) was used to assess differences in connectivity lateralisation.

A1 displayed a moderate discrepancy in functional connectivity between left V1 \Leftrightarrow right V2 and left V2 \Leftrightarrow right V1 ($r_{diff} = 0.30$). However, this difference was not found to be statistically significant ($t = 1.11$, $df = 9$, $p = .295$).

A2 showed two moderate but non-significant discrepancies; between left V1 \Leftrightarrow right V2 and left V2 \Leftrightarrow right V1 ($r_{diff} = 0.22$, $t = 0.20$, $df = 9$, $p = .848$) and between left V1 \Leftrightarrow right V3 and left V3 \Leftrightarrow right V1 ($r_{diff} = 0.24$, $t = 0.39$, $df = 9$, $p = .703$). Of particular interest in A2, is the left V2 node, which shares low functional connectivity with all other cross-hemispheric target regions. Such localised discrepancies are unlikely to be caused by global subject motion issues, or generalised cardiac or respiratory artefacts (Birn, 2012) as adjacent cortical regions were successfully sampled, and show similar connectivity profiles to equivalent regions in other participants. As such, we may assume the observed connectivity pattern in left V2 for A2 was caused by contamination of the BOLD signal either as a result of localised venous drainage (Winawer et al., 2010), or contamination from non-grey matter tissue in the area sampled.

Finally, A3 displayed discrepancies between left V1 \Leftrightarrow right V3 and left V3 \Leftrightarrow right V1, and these were again non-significant ($r_{diff} = 0.38$, $t = 0.81$, $df = 9$, $p = .805$). A4 and A5 did not display lateralisation in cross-hierarchical interhemispheric connections where the difference in correlation coefficients matched the standard deviation of the control sample.

7.5 Discussion

Albinism is a rare developmental disorder where the cortical integration of visual information is poorly understood. In this work, we have presented a series of measures of anatomical and functional inter-hemispheric connectivity between early visual areas, revealing conservative structural organisation for interhemispheric transfer of visual information, but altered interhemispheric functional connectivity at rest. We discuss the implications of the findings in turn.

7.5.1 Stable interhemispheric structural connectivity

Through diffusion MRI tractography we reconstructed the splenium of the corpus callosum as the primary white matter structure subtending the inter-hemispheric transfer of visual information, and the corticospinal tracts as control regions for analysis of volumetric and microstructural metrics. Upon inspection, the anatomical course of these structures was found to be similar between participants with albinism (A1-A5) and the normative control group. Volumetric differences were assessed both by estimating the volume of each tract as the volume occupied by voxels traversed by $\geq 10\%$ of streamlines generated, and by normalizing said metric by the total intracranial volume for each participant. Similar volumes were measured for both albino and control groups in the splenium of the corpus callosum, and equivalent reconstructions were obtained for the control tract upon normalisation. No overt differences in broad tract anatomy or space occupancy were seen for the albino group. Similarly, assessment of microstructural markers revealed no significant differences in interhemispheric white matter integrity between participants with albinism and controls.

At first glance, these findings appear surprising in consideration of previous anatomical studies in albinism, where shorter calcarine sulci and increased cortical thickness and grey matter volume in the posterior calcarine region have been reported (Neveu et al., 2007; Bridge et al., 2014). These results have been interpreted as a lack of pruning around the calcarine sulcus due to the reduced foveal input in albinism (Mcketton et al., 2014), particularly as increased cortical thickness in striate cortex was negatively correlated with visual acuity in albinos (Bridge et al., 2014). Two lines of reasoning reconcile the results presented here with previous evidence of abnormal cortical anatomy in albinism. First, these studies have focused on the cortical consequences in albinism, but have largely ignored post-chiasmal white matter macro- and microstructure. To the best of our knowledge, only one other study has explicitly analysed inter-hemispheric white matter connectivity in albinism, and reported no significant difference in streamline density, FA or MD (Welton et al., 2016), in agreement with the present findings. Second, this result is consistent with albinism being primarily a disorder retinal (and by consequence, chiasmal)

development, impacting the cortical architecture of occipital visual areas due to altered sensory inputs, but not altering the conservative anatomical template of development for post-chiasmal structures. We can therefore interpret results presented here as evidence in favour of stability in post-chiasmal visual system organisation in albinism.

7.5.2 Altered functional connectivity

In addition to the structural integrity of interhemispheric white matter pathways, we also considered the functional connectivity between early visual areas in albinism. Specifically, participants underwent resting-state (also known as task-free) fMRI, where the BOLD time series observed in retinotopically-delineated regions V1, V2 and V3 were extracted and correlated with time series in regions in the opposite hemisphere. This approach allows the study of inherent cortical fluctuations, which are reflective of the degree of computational interdependence between two regions (Damoiseaux et al., 2006).

From these comparisons, we identified two main findings; first, no significant differences between A1-A5 and controls in cross-hierarchical patterns of functional connectivity, that is, synchronous fluctuations between pairs of regions at different levels of the cortical hierarchy and across hemispheres (e.g. left V1 \Leftrightarrow right V2). Second, a pattern of striate-extrastriate dissociation in interhemispheric functional connectivity for pairs of homologous regions, that is left V1 \Leftrightarrow right V1, left V2 \Leftrightarrow right V2 and left V3 \Leftrightarrow right V3, for participants with albinism when compared to the control group. The pattern was characterised by decreased inter-hemispheric connectivity in V1, a transition zone in V2 and increased inter-hemispheric connectivity in V3. However, significant inter-subject variability was observed in patterns of functional connectivity, and the following section aims to reconcile this variability with imaging and phenotype descriptions on a case-by-case basis.

7.5.2.1 A1

Participant A1 (F, 21 years old, OCA1A) followed the described pattern, with significantly decreased interhemispheric connectivity in V1 \Leftrightarrow V1, and a non-significant trend towards increased connectivity in V2 \Leftrightarrow V2 and V3 \Leftrightarrow V3. This places A1 in contrast with A2, A3, A4 and A5, for whom no difference in V1 connectivity was detected. This effect can be interpreted in light of estimates for line of decussation, retinal ganglion cell layer thickness and horizontal bias in contralateral representation explored in Chapter 6. A1 displayed the largest shift in line of decussation (9.40°) and therefore the largest extent of overlapping nasal and temporal hemiretina representations in contralateral visual cortex. As receptive fields for the centre of vision can be found within the same contralateral cortical territory, the need for integration at the earliest level of cortical visual processing is potentially

reduced, and here manifested in decreased interhemispheric connectivity in V1 at rest. In the case of A1, this speaks to the first proposed strategy of developmental organisation, where the requirement for interhemispheric integration of the monocular visual field is reduced when extensive overlapping representations exist in the same cortical territory.

7.5.2.2 A2

Participant A2 (M, 25 years old, OA1) displayed a similar pattern, with significantly reduced connectivity in $V1 \leftrightarrow V1$ and significantly increased connectivity in $V3 \leftrightarrow V3$. Note however that the $V2 \leftrightarrow V2$ comparison yielded significantly lower connectivity compared to the control group, in disagreement with the pattern in A1 and other participants with albinism. Upon closer inspection, A2 displayed abnormally low connectivity between left V2 and all other target regions, a feature not shared by the right hemisphere homologue. Consideration of the remaining homologue connectivity patterns, that is $V1 \leftrightarrow V1$ and $V3 \leftrightarrow V3$, and a significant shift in the line of decussation (4.40°), places A2 in agreement with the general trend seen in A1.

7.5.2.3 A3

Participant A3 (F, 50 years old, OA1) revealed a different pattern to A1 and A2, with no-significant but trending positive patterns of connectivity in $V1 \leftrightarrow V1$ and $V2 \leftrightarrow V2$, and a significant increase in connectivity in $V3 \leftrightarrow V3$ compared to controls. The similarity in $V1 \leftrightarrow V1$ connectivity to the control group can be accounted in opposition to results seen in A2 and A2; A3 displayed a small shift in the line of decussation (0.91°) and recruits interhemispheric integration in V1 at levels comparable to healthy individuals. Increases in extrastriate connectivity are more puzzling, and may be accounted for by an altered role for V2 and V3 in albinism. Extrastriate regions exhibit larger receptive fields than V1, and the increased overlap in visual field representations in extrastriate regions may drive enhanced connectivity, in relation to the small receptive fields in V1. Alternatively, this shift towards increased extrastriate interhemispheric connectivity may be reflective of broader changes in cortical functional connectivity in albinism, extending beyond early visual cortex.

7.5.2.4 A4

Participant A4 (M, 9 years old, OCA1B) showed a similar pattern to A3; no significant difference in connectivity in $V1 \leftrightarrow V1$ and significantly increased interhemispheric connectivity in $V2 \leftrightarrow V2$ and $V3 \leftrightarrow V3$.

7.5.2.5 A5

Participant A5 (M, 14 years old, OCA1B) displayed an intermediate pattern, with significantly decreased connectivity in $V1 \Leftrightarrow V1$ and significantly increased connectivity in $V2 \Leftrightarrow V2$ and $V3 \Leftrightarrow V3$. Despite a modest shift in the line of decussation (1.34°), A5 displayed reduced $V1 \Leftrightarrow V1$ connectivity albeit to a smaller extent when compared with A1 and A2.

7.5.3 Role of interhemispheric transfer in albinism

Overall, the patterns of structural and functional connectivity observed in this study can be reconciled under a model of shifted spatial integration. In neurotypical striate cortex, the central visual field is split and represented between the two hemispheres, with signals from matching retinal locations in each eye arriving to confluent cortical territories. Therefore, in order to integrate information across representations of the whole visual field, interhemispheric transfer is necessary. However, in albinism the monocular foveal representation may be entirely contained within a single hemisphere, by virtue of the overlapping nasal and temporal hemiretinal representations in the contralateral hemisphere. In this scenario, there is a reduced requirement for interhemispheric transfer in order to integrate visual information across the central visual field. How binocular integration occurs in such a scenario remains unclear, but it should be noted that none of the participants with albinism displayed binocular stereopsis. Therefore, the role of interhemispheric integration may be shifted in albinism towards extrastriate visual areas with larger receptive fields, evidenced here by increased interhemispheric connectivity in $V3 \Leftrightarrow V3$.

The increased interhemispheric extrastriate connectivity observed in albinism can be interpreted as a consequence of altered receptive field properties discussed in Chapter 6. In comparison to healthy controls, the larger receptive fields in albino V2 and V3 create more bilateral overlap in the midline zone of the visual field, meaning a larger extent of cortical territory in both hemispheres is driven by the same retinal input. This increase in input similarity would to some degree drive increased correlation in signals from bilateral extrastriate regions at rest. However, the bilateral overlap zone of the vertical meridian is relatively small, typically the central 2° (Lavidor & Walsh, 2004), and may be insufficient to fully account for changes in extrastriate connectivity, nor does it explain the decreased interhemispheric connectivity observed in albino V1.

An alternative explanation is to consider that striate cortex abnormalities in albinism are typically interpreted as indicative of poor foveal representation in albinism. One of the key ophthalmological features of albinism is underdevelopment or complete absence of the foveal pit, foveal hypoplasia (Kinneer et al., 1985; Charles et al., 1993). As a consequence,

the foveal region of the retina is under-represented in the LGN (Mcketton et al., 2014) and potentially in striate cortex (Neveu et al., 2007; von dem Hagen et al., 2007; Bridge et al., 2014). While poor foveal representations would account for the reduction in V1 \leftrightarrow V1 connectivity, they do not explain the shift towards increased connectivity in extrastriate areas. In addition, the group of participants with albinism studied here is unusual, due to their relatively normal acuity despite foveal hypoplasia, and may represent a separate sub-population within albinism. Indeed, one previous study examining functional connectivity in albinos detected increased interhemispheric connectivity in V1 (Welton et al., 2016). Two sources of variability may explain the discrepancy with the present findings. First, Welton et al. studied participants with moderate visual acuity, which as discussed may form a separate population from those participants studied here. Second, the study in question used an atlas-based definition of V1 to inspect functional connectivity. The extent of area V1 is highly variable between individuals (Schwarzkopf et al., 2010) and it is likely a template-based definition of V1 includes extrastriate cortical territories. It is therefore possible that the results in Welton et al. capture the increased interhemispheric connectivity we report for areas V2 and V3.

It is clear the foveal representation of visual space is of particular importance in albinism; it is significantly under-represented in sub-cortical and possibly cortical structures, and may be related to the abnormal gyrification and cortical thickness and volume in occipital areas (Neveu et al., 2007; von dem Hagen et al., 2007; Bridge et al., 2014). However, given the selection of participants with relatively spared vision in this study, variability in interhemispheric functional connectivity is better explained by a shift in the locus of spatial integration.

7.6 Conclusion

To summarise, in this experiment we have described the structural and functional inter-hemispheric connectivity of the early visual system in five rare participants with albinism. Anatomical courses, volumetric and microstructural measures of the splenium of the corpus callosum were found to be within the boundaries of the normative control group, indicating stable interhemispheric structural connectivity in albino occipital cortex. When assessing functional connectivity through resting-state fMRI correlational analysis, a dissociation in striate-extrastriate patterns of activity was observed, with decreases in V1 \leftrightarrow V1 connectivity, a mixed pattern in V2 \leftrightarrow V2 and increased connectivity in V3 \leftrightarrow V3, with significant inter-subject variability. A shift in the locus of spatial integration in albinism is proposed to account for variability in interhemispheric functional connectivity, with local

integration occurring in V1 and later interhemispheric transfer at the level of V2 and V3, illustrating the patterns of developmental plasticity in human albinism.

Chapter 8

General discussion

8.1 Introduction

Albinism in humans, and other mammalian species with front-facing eyes, is uniquely characterised by the misrouting of the optic nerves leading to abnormal retinal inputs to the visual system. Despite this fundamentally altered sensory input, most individuals with albinism experience relatively normal visual spatial perception and visuomotor behaviour. This specific abnormality makes albinism a valuable case for the study of the development of the visual system, and the balance between plasticity and stability in cortical organisation in the face of altered sensory inputs.

8.2 Summary of findings

In this thesis, four pieces of work are presented, two concerning the development of methods to study the functional and structural organisation of the visual system, and two investigations into the role of early visual cortical areas in the representation of visual space in human albinism.

8.2.1 Optimisation of population receptive field mapping in fMRI

Population receptive field (pRF) mapping is a non-invasive technique for examining the receptive field properties of neural populations *in vivo* (Dumoulin & Wandell, 2008). While the retinotopic organisation of brain structures was previously available for study in human fMRI (Engel et al., 1994; Sereno et al., 1995; DeYoe et al., 1996), only recent developments have allowed the capture of detailed receptive field information, previously only available from invasive electrophysiological methods. In this work, we compared multiple stimuli configurations for efficient estimation of pRF properties in human cortical areas, revealing significant effects of stimulus design on pRF parameter estimates. A novel simultaneous wedge and ring stimulus designed and proposed here, afforded accurate pRF estimation in a significantly reduced time, thus permitting the study of pRF properties in special populations, such as albinism, where poor fixation stability or low tolerance to prolonged MRI sessions create practical limitations on acquisition time. The stimulus described was implemented in the studies described in subsequent chapters for retinotopic localisation and pRF mapping.

8.2.2 Extrastriate projections in human optic radiation

A currently outstanding question in our neuroanatomical understanding of the visual system is; what white matter pathways subserve the transfer of retinal information to extrastriate cortical areas? The optic radiation is typically considered a projection from lateral geniculate nucleus in the thalamus to primary visual or striate cortex (Ebeling & Reulen, 1988; Wahler-Lück et al., 1991; Bürgel et al., 1999). Despite this, evidence from tracer studies in non-human animals have suggested a role for the optic radiation projecting to extrastriate areas (Garey & Powell, 1971; Maciewicz, 1975; Yuki & Iwai, 1981; Benevento & Yoshida, 1981; Fries, 1981; Bullier & Kennedy, 1983; Kennedy & Bullier, 1985). Whether this extrastriate projection also exists in the human, was previously unknown. This study, to the best of our knowledge, provides the first evidence for optic radiation projections to areas V2 and V3 in humans. We performed functionally-informed diffusion MRI tractography of the human optic radiations in healthy participants and identified direct extrastriate projections of the optic radiation in all hemispheres tested, characterising the microstructural properties of sub-fascicular segments to areas V2 and V3. In addition, this work permitted the development of a framework for functional-structural investigations of the visual system, integrating fMRI and diffusion MRI tractography to segment functionally-relevant bundles of white matter pathways. This methodological approach was then applied in Chapter 7.

8.2.3 Visual population receptive fields in human albinism

Recent fMRI studies have characterised the retinotopic organisation of visual areas in human albinism (e.g. Hoffmann et al., 2003; Kaule et al., 2014), but to date, no information on the precise visual field properties was available in humans. In order to assess these, we studied a small sample of rare participants with albinism and minimal nystagmus in the primary position, allowing mapping of pRF characteristics in early visual areas V1, V2 and V3. We identified abnormal temporal hemiretina representations in the hemisphere contralateral to monocular stimulation, in agreement with previous findings (Morland et al., 2002; Hoffmann et al., 2003; von dem Hagen et al., 2005; Kaule et al., 2014). pRF mapping revealed variability in receptive field sizes, linked to the degree of decussation in the optic chiasm, as inferred from clinical markers and the extent of the temporal hemiretina representation in contralateral visual cortex. Finally, we modelled bilateral cortical responses as a single or dual receptive field, finding no evidence for dual receptive field responses as previously reported in achiasma (Hoffmann et al., 2012), and in agreement with psychophysical evidence (Klemen et al., 2012). Overall, results reported here are consistent with a 'true albino' model of cortical organisation for human albinism, with altered columnar organisation representing separate visual hemifields, highlighting the role of developmental plasticity in albinism.

8.2.4 Interhemispheric connectivity in human albinism

While the previous chapter characterised cortical receptive fields in human albinism, this work does not provide a complete picture of the integrative role of early visual cortex. To this end, imaging data collected for participants in the previous study were re-visited to further explore inter-hemispheric connectivity in early visual cortex. Structural connectivity was assessed with fMRI-informed diffusion tractography, revealing interhemispheric connections with comparable anatomy and microstructure to the healthy control group. Functional connectivity was also assessed through comparisons of resting-state BOLD responses in areas V1, V2 and V3, revealing a striate-extrastriate dissociation in patterns of connectivity, with participants with albinism displaying reduced interhemispheric connectivity in $V1 \leftrightarrow V1$, a mixed pattern in $V2 \leftrightarrow V2$ and increased interhemispheric connectivity in $V3 \leftrightarrow V3$. A shift in the locus of spatial integration in albinism is proposed to account for variability in interhemispheric functional connectivity, with local integration occurring in V1 and later interhemispheric transfer at the level of V2 and V3, illustrating the pattern of developmental plasticity in human albinism.

8.3 Discussion of findings

Albinism, and its structural and functional consequences in the visual system, may be understood from a variety of perspectives. Here, we aim at providing a comprehensive account based on the opposing forces of plasticity and stability in visual system development.

Plasticity may be broadly understood as any alteration in the organisation of a system, in this case, the visual system. In the context of developmental plasticity, change is driven by underlying structural constraints (Guzzetta et al., 2010). Abnormal retinal input can therefore be understood as an underlying constrain on the development of the visual system in albinism, a developmental process that is driven by the formation of organised topographic representations of visual space in segregated cortical territories (Nahaus & Nielsen, 2014). This ‘topographic imperative’ can be seen as the other side of the coin, the programmed stability of cortical development towards a set of retinotopically organised visual maps. In the case of altered retinal input, these forces are in competition – stability driving the formation of topographically-organised representations and plasticity driving the development of a functional system, capable of representing visual space in a useful and meaningful way, enabling visual perception and visually-guided action.

Albinism, as a developmental condition, is an example of the drives for both plasticity and stability, producing varying solutions in cortical architecture, including the 'Boston' and 'Midwestern' patterns in Siamese cats (Cooper & Blasdel, 1980; Kaas, 2005) and the 'true albino' pattern in primates (Guillery et al., 1984; Hoffmann et al., 2003). The comparison drawn between albinism and achiasma is a useful one; achiasma, or complete lack of decussation of the optic fibres, is an extreme example of the need for plasticity. Under a conservative retinotopic model, approximately 50% of the visual field would be miss-represented in each cortical hemisphere, leading to major sensory conflict and presumably a poorly-functioning visual system. Despite these input constraints, the achiasmic cortex deviates from the standard retinotopy programme and instead presents two fully overlapping representations of opposite visual fields over the same cortical territory (Hoffmann et al., 2012; Davis-Thompson et al., 2013; Bao et al., 2015). While achiasma is a radical departure from the conservative organisation of visual cortex, it illustrates the capacity for developmental plasticity in the face of altered input. This accommodation to the nature of retinal inputs may indeed be a suitable account of the abnormal representation zone as reported in fMRI studies of albinism (Hedera et al., 1994; Morland et al., 2002; Hoffmann et al., 2003; Wolynski et al., 2010; Kaule et al., 2014) and in the present work. When the temporal and nasal hemiretina are represented in the same contralateral cortical territory in albinism, an overlapping representation similar to that in achiasma is indeed found. While this may be considered as further proof of the plastic capacity of the system, it is important to note both overlapping representations follow a conservative retinotopic pattern, thus hinting at the underlying constraints of organisation.

A significant departure between achiasma and albinism is evidence for and against a dual receptive field encoding of visual information. In a recent study of two achiasmic patients, Hoffmann et al. (2012) report BOLD modelling evidence for dual receptive field cells in early visual cortex; that is, cells representing mirror locations in left and right visual fields. Given the similarities in cortical representations in the abnormal zone with albinism, it is therefore of interest to ask whether this dual receptive field may also exist in the latter condition; work presented in Chapter 6 aims to answer this question, and revealed no evidence for such a model in the participants with albinism studied here, in agreement with the psychophysical literature (Klemen et al., 2012). In the balance between plasticity and stability, it appears albinism may be an example of the latter, in that cortical cells appear to be representing single visual field locations, as they typically do in healthy individuals. Nevertheless, this still presents an outstanding problem in visual field integration. If single cells represent either distant nasal or temporal hemiretinal locations within the same cortical territory, how are these signals integrated to form a coherent representation of the visual field? A proposed mechanistic explanation is that hemifield-selective cells are not arranged haphazardly, but instead follow a pattern akin to ocular dominance columns, at a finer scale than that

detectable by the present studies. Indeed, based on electrophysiological evidence from an albino primate, it has been suggested such cells organise themselves in hemifield columns of approximately the same size as ocular dominance columns (Guillery et al., 1984). Such organisation would be a prime example of developmental plasticity, as cortical cells arrange based on lateralisation of retinal input, but within the constraints of retinotopy. Whether these hypothetical hemifield columns exist in the human albino remains unclear, but recent developments in ultra-high field MRI have indicated it is possible to resolve ocular dominance columns (Yacoub et al., 2007; Yacoub et al., 2008; Cheng et al., 2012) and such methods may one day establish the neuroanatomical organisation of hemifield information in human albinism.

A further consideration in visual system development is the connectivity between visual regions. The healthy visual system relies on interhemispheric connections to join information from the lateralised visual field representations (Saenz & Fine, 2010; Genç et al., 2011b). In albinism, however, retinal representations are less lateralised, with representations of central left and right visual fields within the same hemisphere. This poses additional constraints on the integration of visual information, and as inputs from each eye are over-crossed in albinism, this limits the capacity of the system to match their inputs in early visual cortex. The present work suggests post-chiasmal anatomical connectivity in albinism is conservative, with no significant changes in interhemispheric white matter connections between occipital lobes, but instead evidence for altered functional connectivity has emerged (Welton et al., 2016; present work). A shift in the locus of spatial integration in albinism is proposed to account for changes in functional connectivity, with the lateralised representation of the central visual field driving intra-cortical integration in striate cortex and shifting interhemispheric transfer to extrastriate visual regions. While attractive, this model does not fully account for the role extrastriate areas play in representing visual space in albinism, and how they may interact with putative columnar organisation for visual fields. More careful examinations of sensory integration are necessary to address these issues.

An additional issue highlighted by the present work is the heterogeneity in clinical presentation and cortical organisation in albinism. Among the participants with albinism studied here, significant variability was found for line of decussation, receptive field properties, bias in horizontal receptive field position of overlapping nasal and temporal hemiretina representations and interhemispheric functional connectivity. These metrics reflect different aspects and consequences of the abnormal chiasmal crossing in albinism, but crucially all were highly related across experiments, with close correlation to the retinal ganglion cell layer contents, highlighting the retinal origin of abnormalities in albinism. While it is unclear from the current work how variation in abnormal retinal development drives heterogeneity in cortical representations, the consistency of retinotopic organisation despite

variable clinical presentation speaks to the conservative nature of visual system development, specifically in maintaining a stereotyped functional representation topography despite abnormal input.

Finally, it should be considered whether the population studied here, of participants with albinism, with spared acuity and minimal nystagmus, form a special sub-population from the larger group of albino individuals. It is true this group forms a distinctive sub-population insofar as their clinical presentation is atypical – reduced visual acuity is common (Kinnear, 1985; Summers, 1996) and approximately 88% of ocular albinism cases present nystagmus (Charles et al., 1993). However, the sub-population studied here presents many of the classical features of albinism; foveal hypoplasia, iris transillumination, no binocular stereopsis, and critically, bilateral representations of the temporal visual field under monocular stimulation. It is certainly possible that this sub-population more mildly affected by albinism experiences diminished effects of the cortical consequences of overcrossing at the chiasm. However, considering the conservative nature of cortical development, as evidenced in retinotopic organisation in this sub-population and the presence of overlapping representations of nasal and temporal hemiretina, as reported in previous studies of albinism (Hedera et al., 1994; Morland et al., 2002; Hoffmann et al., 2003; Wolynski et al., 2010; Kaule et al., 2014), we consider the possibility of a different developmental trajectory for cortical organisation in this sub-population unlikely. Findings highlighted here are therefore of general interest for their implications to the nature of plasticity in the neurodevelopment of the visual system under abnormal inputs.

In summary, the work presented in this thesis represents a novel exploration of the structural and functional organisation of the visual system in human albinism using *in vivo* non-invasive imaging techniques, and contributes to the current understanding of both albinism, and the affordances of plastic development in the human visual system more generally.

8.4 Future directions

While this work has provided an initial characterisation of the visual system organisation in albinism, it is not an exhaustive account of the complete circuit of visual space representation in human albinism, and such an effort would be beyond the scope of this doctoral thesis. In this section we propose four main avenues for future investigations.

First and foremost, the underlying single-cell neuronal representation of visual hemifield information remains unknown in human albinism. While a non-human primate model of

hemifield columnar representations exists (Guillery et al., 1984) and imaging evidence presented in this thesis agrees with this model, it is not sufficient to provide a complete account of the neuroanatomical representation of visual space in human albinism. In order to provide a complete account of the developmental consequences of albinism, a description of the neuronal representation of visual space will be necessary. Indeed, such evidence may be provided in the future, either through invasive electrophysiological recordings in the human, or more likely, through the development of neuroimaging techniques able to resolve cortical columnar organisation, such as those pioneered for the study of ocular dominance columns (Yacoub et al., 2008; Cheng et al., 2012).

Second, how visual space is represented at the macroscopic level in higher visual areas of human albinos, particularly in the dorsal stream, remains unclear. Recent fMRI evidence has characterised the retinotopic organisation in striate (Hoffmann et al., 2003) and extrastriate visual areas (Kaule et al., 2014; present work) in albinism. In combination with pRF mapping techniques, this approach is likely to provide a fuller account of the dorsal representations in the future. This is particularly relevant to the understanding of the visual system more broadly, as an integrated circuit providing computations on altered sensory input.

Third, the precise role played by extrastriate areas in the integration of visual information in albinism remains unclear. While it is apparent from the present work that early visual areas are retinotopically organised, and retain the abnormal representation of the temporal hemiretina seen in V1, their role in sensory integration, and how it differs from the normally-developed visual system, is not currently understood. Studies of such properties are likely to be amenable to electrophysiological investigations in non-human animals, where specific areas may be disrupted physically or chemically to investigate its contribution to the wider visual system.

Fourth and finally, the extent and importance of the foveal representation in albinism is currently poorly understood. Anatomical studies have suggested the foveal region of the retina is under-represented in its sub-cortical representation, and potentially in cortex as well. Whether this under-representation is present in striate or extrastriate visual areas, and what functional consequences they may have for the perception of fine visual detail and visually-guided behaviour, remains to be established, and is likely a valuable avenue for future *in vivo* investigations of albinism with functional neuroimaging techniques.

8.5 Clinical relevance

8.5.1 Diagnosis and prognosis

Misrouting of the optic nerves in albinism is typically confirmed via visual evoked potentials in electroencephalography, or EEG (Apkarian et al., 1983; Pott et al., 2003; Hoffmann et al., 2006), providing a quantitative estimate of the shift in the vertical line of decussation (Hoffmann et al., 2005). While fMRI may be similarly used to confirm optic nerve misrouting (von dem Hagen et al., 2008), the much greater spatial resolution of the method, when compared with EEG, provides additional topological information, including the retinotopic representation of the visual fields in albinism. Similarly, connectivity approaches such as diffusion MRI tractography and connectivity analysis in fMRI provide valuable insights into the anatomical and functional connectivity of the visual system in albinism, at a spatial resolution not available with other *in vivo* approaches. While not currently of direct clinical value, these measures may in future provide prognostic value, if relationships between patterns of cortical organisation and clinical treatment efficacy were to be established. This may be particularly relevant given the rising interest in neural connectivity approaches as biomarkers in the development of clinical interventions (e.g. Dong et al., 2003; Fox & Greicius, 2010).

8.5.2 Development of future treatments

Albinism is a non-progressive developmental disorder, and as such, much of the clinical care for patients with albinism is restricted to addressing the peripheral features of the condition, including refractive errors, nystagmus, strabismus and light sensitivity. No current clinical treatment is available that addresses the underlying feature of albinism, i.e. impaired biosynthesis of the pigment melanin. To date, one complete clinical trial has been conducted, aimed at improving vision in albinism through administration of a dopamine precursor, with negative results (Summers et al., 2014). While promising, this avenue of investigation relies on linking enhanced neural function and improving a perceptual or behavioural outcome, such as visual acuity. Therefore, in order to accurately assess the potential of future treatments, a clear understanding of the visual system organisation in albinism is needed. Such understanding will provide not only valuable outcome measures in terms of neuroanatomy and functional organisation, but also potential biomarkers of clinical relevance.

References

- Abadi, R. V., & Bjerre, A. (2002). Motor and sensory characteristics of infantile nystagmus. *British Journal of Ophthalmology*, *86*(10), 1152–1160.
- Amano, K., Wandell, B. A., & Dumoulin, S. O. (2009). Visual field maps, population receptive field sizes, and visual field coverage in the human MT+ complex. *Journal of Neuroscience*, *29*(10), 2704–2718.
- Andersson, J. L. R., Hutton, C., Ashburner, J., Turner, R., & Friston, K. (2001). Modeling geometric deformations in EPI time series. *NeuroImage*, *13*(5), 903–919.
- Ando, H., Kondoh, H., Ichihashi, M., & Hearing, V. J. (2007). Approaches to identify inhibitors of melanin biosynthesis via the quality control of tyrosinase. *Journal of Investigative Dermatology*, *127*(4), 751–761.
- Apkarian, P., Reits, D., Spekreijse, H., & Van Dorp, D. (1983). A decisive electrophysiological test for human albinism. *Electroencephalography and Clinical Neurophysiology*, *55*(5), 513–531.
- Arcaro, M. J., Pinsk, M. A., & Kastner, S. (2015). The anatomical and functional organization of the human visual pulvinar. *Journal of Neuroscience*, *35*(27), 9848–9871.
- Ashburner, J., & Friston, K. J. (1997). Spatial transformation of images. In *Human Brain Function* (pp. 44–58).
- Ashburner, J., & Friston, K. J. (2005). Unified segmentation. *NeuroImage*, *26*(3), 839–851.
- Bao, P., Purington, C. J., & Tjan, B. S. (2015). Using an achiasmatic human visual system to quantify the relationship between the fMRI BOLD signal and neural response. *eLife*, *4*, 1191.
- Barton, J. J. S., Hefter, R., Chang, B., Schomer, D., & Drislane, F. (2005). The field defects of anterior temporal lobectomy: a quantitative reassessment of Meyer's loop. *Brain*, *128*(9), 2123–2133.
- Baseler, H. A., Gouws, A., Haak, K. V., Racey, C., Crossland, M. D., Tufail, A., et al. (2011). Large-scale remapping of visual cortex is absent in adult humans with macular degeneration. *Nature Neuroscience*, *14*(5), 649–655.
- Basser, P. J., Pajevic, S., Pierpaoli, C., Duda, J., & Aldroubi, A. (2000). In vivo fiber tractography using DT-MRI data. *Magnetic Resonance in Medicine*, *44*(4), 625–632.
- Bassett, E. A., & Wallace, V. A. (2012). Cell fate determination in the vertebrate retina. *Trends in Neurosciences*, *35*(9), 565–573.
- Beaulieu, C. C. (2002). The basis of anisotropic water diffusion in the nervous system - a technical review. *NMR in Biomedicine*, *15*(7-8), 435–455.
- Behrens, T. E. J. T., Johansen-Berg, H. H., Woolrich, M. W. M., Smith, S. M. S., Wheeler-Kingshott, C. A. M., Boulby, P. A. P., et al. (2003a). Non-invasive mapping of

- connections between human thalamus and cortex using diffusion imaging. *Nature Neuroscience*, 6(7), 750–757.
- Behrens, T. E. J., Berg, H. J., Jbabdi, S., Rushworth, M. F. S., & Woolrich, M. W. (2007). Probabilistic diffusion tractography with multiple fibre orientations: what can we gain? *NeuroImage*, 34(1), 144–155.
- Behrens, T. E. J., Woolrich, M. W., Jenkinson, M., Johansen-Berg, H., Nunes, R. G., Clare, S., et al. (2003b). Characterization and propagation of uncertainty in diffusion-weighted MR imaging. *Magnetic Resonance in Medicine*, 50(5), 1077–1088.
- Benevento, L. A., & Standage, G. P. (1982). Demonstration of lack of dorsal lateral geniculate nucleus input to extrastriate areas MT and visual 2 in the macaque monkey. *Brain Research*, 252(1), 161–166.
- Benevento, L. A., & Yoshida, K. (1981). The afferent and efferent organization of the lateral geniculo-prestriate pathways in the macaque monkey. *Journal of Comparative Neurology*, 203(3), 455–474.
- Bhansali, P., Rayport, I., Rebsam, A., & Mason, C. (2014). Delayed neurogenesis leads to altered specification of ventrotemporal retinal ganglion cells in albino mice. *Neural Development*, 9(1), 11–15.
- Binda, P., Thomas, J. M., Boynton, G. M., & Fine, I. (2013). Minimizing biases in estimating the reorganization of human visual areas with BOLD retinotopic mapping. *Journal of Vision*, 13(7), 13–13.
- Birn, R. M. (2012). The role of physiological noise in resting-state functional connectivity. *NeuroImage*, 62(2), 864–870.
- Boot, F. H., Pel, J. J. M., van der Steen, J., & Evenhuis, H. M. (2010). Cerebral visual impairment: Which perceptive visual dysfunctions can be expected in children with brain damage? A systematic review. *Research in Developmental Disabilities*, 31(6), 1149–1159.
- Brainard, D. H. (1997). The psychophysics toolbox. *Spatial Vision*, 10(4), 433–436.
- Bressler, D. W., & Silver, M. A. (2010). Spatial attention improves reliability of fMRI retinotopic mapping signals in occipital and parietal cortex. *NeuroImage*, 53(2), 526–533.
- Breuer, F. A., Blaimer, M., Heidemann, R. M., Mueller, M. F., Griswold, M. A., & Jakob, P. M. (2005). Controlled aliasing in parallel imaging results in higher acceleration (CAIPIRINHA) for multi-slice imaging. *Magnetic Resonance in Medicine*, 53(3), 684–691.
- Brewer, A. A., & Barton, B. (2014). Visual cortex in aging and Alzheimer's disease: changes in visual field maps and population receptive fields. *Frontiers in Psychology*, 5, 74–74.
- Bridge, H. (2011). Mapping the visual brain: how and why. *Eye*, 25(3), 291–296.
- Bridge, H., Cowey, A., Ragge, N., & Watkins, K. (2009). Imaging studies in congenital anophthalmia reveal preservation of brain architecture in “visual” cortex. *Brain*, 132(12), 3467–3480.

- Bridge, H., Hagen, von dem, E. A. H., Davies, G., Chambers, C., Gouws, A., Hoffmann, M., & Morland, A. B. (2014). Changes in brain morphology in albinism reflect reduced visual acuity. *Cortex*, *56*, 64–72.
- Buckner, R. L., & Yeo, B. T. T. (2013). Border, map clusters, and supra-areal organization in visual cortex. *NeuroImage*, *93*(2), 292–297.
- Bullier, J., & Kennedy, H. (1983). Projection of the lateral geniculate nucleus onto cortical area V2 in the macaque monkey. *Experimental Brain Research*, *53*(1), 168–172.
- Buracas, G. T., & Boynton, G. M. (2007). The effect of spatial attention on contrast response functions in human visual cortex. *Journal of Neuroscience*, *27*(1), 93–97.
- Bürgel, U., Schormann, T., Schleicher, A., & Zilles, K. (1999). Mapping of histologically identified long fiber tracts in human cerebral hemispheres to the MRI volume of a reference brain: Position and spatial variability of the optic radiation. *NeuroImage*, *10*(5), 11–11.
- Cang, J., & Feldheim, D. A. (2013). Developmental mechanisms of topographic map formation and alignment. *Annual Review of Neuroscience*, *36*(1), 51–77.
- Carroll, W. M., Jay, B. S., McDonald, W. I., & Halliday, A. M. (1980). Two distinct patterns of visual evoked response asymmetry in human albinism. *Nature*, *286*(5773), 604–606.
- Catani, M., & Dell'Acqua, F. (2011). Mapping white matter pathways with diffusion imaging tractography: focus on neurosurgical applications. In H. Duffau (Ed.), *Brain Mapping: From Neural Basis of Cognition to Surgical Applications* (1st ed., pp. 61–75). New York: Springer.
- Catani, M., & Thiebaut de Schotten, M. (2008). A diffusion tensor imaging tractography atlas for virtual in vivo dissections. *Cortex*, *44*(8), 1105–1132.
- Catani, M., Howard, R. J., Pajevic, S., & Jones, D. K. (2002). Virtual in vivo interactive dissection of white matter fasciculi in the human brain. *NeuroImage*, *17*(1), 77–94.
- Catani, M., Jones, D. K., Donato, R., & Ffytche, D. H. (2003). Occipito-temporal connections in the human brain. *Brain*, *126*(Pt 9), 2093–2107.
- Centanin, L., & Wittbrodt, J. (2013). Retinal neurogenesis. *Development*, *141*(2), 241–244.
- Chard, D. T., Parker, G. J. M., Griffin, C. M. B., Thompson, A. J., & Miller, D. H. (2002). The reproducibility and sensitivity of brain tissue volume measurements derived from an SPM-based segmentation methodology. *Journal of Magnetic Resonance Imaging*, *15*(3), 259–267.
- Charles, S. J., Green, J. S., Grant, J. W., Yates, J., & Moore, A. T. (1993). Clinical features of affected males with X-linked ocular albinism. *British Journal of Ophthalmology*, *77*(4), 222–227.
- Chen, W., Zhu, X. H., Thulborn, K. R., & Ugurbil, K. (1999). Retinotopic mapping of lateral geniculate nucleus in humans using functional magnetic resonance imaging. *Proceedings of the National Academy of Sciences*, *96*(5), 2430–2434.

- Cheng, K., Waggoner, R. A., & Tanaka, K. (2001). Human ocular dominance columns as revealed by high-field functional magnetic resonance imaging. *Neuron*, *32*(2), 359–374.
- Ciccarelli, O., Catani, M., Johansen-Berg, H., Clark, C., & Thompson, A. (2008). Diffusion-based tractography in neurological disorders: concepts, applications, and future developments. *Lancet Neurology*, *7*(8), 715–727.
- Ciccarelli, O., Parker, G. J. M., Toosy, A. T., Wheeler-Kingshott, C. A. M., Barker, G. J., Boulby, P. A., et al. (2003). From diffusion tractography to quantitative white matter tract measures: a reproducibility study. *NeuroImage*, *18*(2), 348–359.
- Clatworthy, P. L., Williams, G. B., Acosta-Cabronero, J., Jones, S. P., Harding, S. G., Johansen-Berg, H., & Baron, J. C. (2010). Probabilistic tractography of the optic radiations—An automated method and anatomical validation. *NeuroImage*, *49*(3), 2001–2012.
- Cooper, M. L., & Blasdel, G. G. (1980). Regional variation in the representation of the visual field in the visual cortex of the Siamese cat. *Journal of Comparative Neurology*, *193*(1), 237–253.
- Cooper, M. L., & Pettigrew, J. D. (1979). The retinthalamic pathways in Siamese cats. *Journal of Comparative Neurology*, *187*(2), 313–348.
- Cowey, A., & Rolls, E. T. (1974). Human cortical magnification factor and its relation to visual acuity. *Experimental Brain Research*, *21*(5), 447–454.
- Crawford, J. R., & Garthwaite, P. H. (2004). Statistical methods for single-case studies in neuropsychology: Comparing the slope of a patient's regression line with those of a control sample. *Cortex*, *40*(3), 533–548.
- Crawford, J. R., Garthwaite, P. H., & Porter, S. (2010a). Point and interval estimates of effect sizes for the case-controls design in neuropsychology: Rationale, methods, implementations, and proposed reporting standards. *Cognitive Neuropsychology*, *27*(3), 245–260.
- Crawford, J. R., Garthwaite, P. H., & Ryan, K. (2011). Comparing a single case to a control sample: Testing for neuropsychological deficits and dissociations in the presence of covariates. *Cortex*, *47*(10), 1166–1178.
- Crawford, J. R., Garthwaite, P. H., & Wood, L. T. (2010b). Inferential methods for comparing two single cases. *Cognitive Neuropsychology*, *27*(5), 377–400.
- Creel, D. J. (1971). Visual system anomaly associated with albinism in the cat. *Nature*, *231*(5303), 465–466.
- Creel, D., Hendrickson, A. E., & Leventhal, A. G. (1982). Retinal projections in tyrosinase-negative albino cats. *Journal of Neuroscience*, *2*(7), 907–911.
- Creel, D., Witkop, C. J., & King, R. A. (1974). Asymmetric visually evoked potentials in human albinos: Evidence for visual system anomalies. *Investigative Ophthalmology*, *13*(6), 430–440.

- Crossland, M. D., Morland, A. B., Feely, M. P., Hagen, von dem, E. A. H., & Rubin, G. S. (2008). The effect of age and fixation instability on retinotopic mapping of primary visual cortex. *Investigative Ophthalmology & Visual Science*, *49*(8), 3734–3739.
- Cruz-Inigo, A. E., Ladizinski, B., & Sethi, A. (2011). Albinism in Africa: Stigma, slaughter and awareness campaigns. *Dermatologic Clinics*, *29*(1), 79–87.
- Curcio, C. A., & Allen, K. A. (1990). Topography of ganglion-cells in human retina. *Journal of Comparative Neurology*, *300*(1), 5–25.
- Daga, P. P., Winston, G. G., Modat, M. M., White, M. M., Mancini, L. L., Cardoso, M. J. M., et al. (2012). Accurate localization of optic radiation during neurosurgery in an interventional MRI suite. *Medical Imaging, IEEE Transactions on*, *31*(4), 882–891.
- Dale, A. M. A., Fischl, B. B., & Sereno, M. I. M. (1999). Cortical surface-based analysis - I. segmentation and surface reconstruction. *NeuroImage*, *9*(2), 179–194.
- Damoiseaux, J. S., Rombouts, S. A. R. B., Barkhof, F., Scheltens, P., Stam, C. J., Smith, S. M., & Beckmann, C. F. (2006). Consistent resting-state networks across healthy subjects. *Proceedings of the National Academy of Sciences of the United States of America*, *103*(37), 13848–13853.
- Dauguet, J., Peled, S., Berezovskii, V., Delzescaux, T., Warfield, S. K., Born, R., & Westin, C.-F. (2007). Comparison of fiber tracts derived from in-vivo DTI tractography with 3D histological neural tract tracer reconstruction on a macaque brain. *NeuroImage*, *37*(2), 530–538.
- Davies-Thompson, J., Scheel, M., Lanyon, L. J., & Barton, J. J. S. (2013). Functional organisation of visual pathways in a patient with no optic chiasm. *Neuropsychologia*, *51*(7), 1260–1272.
- de Haas, B., Schwarzkopf, D. S., Anderson, E. J., & Rees, G. (2014). Perceptual load affects spatial tuning of neuronal populations in human early visual cortex. *Current Biology*, *24*(2), R66–R67.
- Dell'Acqua, F., & Catani, M. (2012). Structural human brain networks. *Current Opinion in Neurology*, *25*(4), 375–383.
- DeYoe, E. A., Carman, G. J., Bandettini, P., Glickman, S., Wieser, J., Cox, R., et al. (1996). Mapping striate and extrastriate visual areas in human cerebral cortex. *Proceedings of the National Academy of Sciences*, *93*(6), 2382–2386.
- Dong, Q., Welsh, R. C., Chenevert, T. L., Carlos, R. C., Maly-Sundgren, P., Gomez-Hassan, D. M., & Mukherji, S. K. (2003). Clinical applications of diffusion tensor imaging. *Journal of Magnetic Resonance Imaging*, *19*(1), 6–18.
- Dorey, S. E., Neveu, M. M., Burton, L. C., Sloper, J. J., & holder, G. E. (2003). The clinical features of albinism and their correlation with visual evoked potentials. *British Journal of Ophthalmology*, *87*(6), 767–772.

- Dougherty, R. F., Ben-Shachar, M., Bammer, R., Brewer, A. A., & Wandell, B. A. (2005). Functional organization of human occipital-callosal fiber tracts. *Proceedings of the National Academy of Sciences*, *102*(20), 7350–7355.
- Drager, U. C. (1985). Birth dates of retinal ganglion cells giving rise to the crossed and uncrossed optic projections in the mouse. *Proceedings of the Royal Society of London Series B - Biological Sciences*, *224*(1234), 57–77.
- Dumoulin, S. O., & Wandell, B. A. (2008). Population receptive field estimates in human visual cortex. *NeuroImage*, *39*(2), 647–660.
- Dumoulin, S. O., Hess, R. F., May, K. A., Harvey, B. M., Rokers, B., & Barendregt, M. (2014). Contour extracting networks in early extrastriate cortex. *Journal of Vision*, *14*(5).
- Ebeling, U., & Reulen, H. J. (1988). Neurosurgical topography of the optic radiation in the temporal lobe. *Acta Neurochirurgica*, *92*(1-4), 29–36.
- Edmond, J. C., & Foroozan, R. (2006). Cortical visual impairment in children. *Current Opinion in Ophthalmology*, *17*(6), 509–512.
- El-Rafei, A., Engelhorn, T., Wärntges, S., Dörfler, A., Hornegger, J., & Michelson, G. (2011). A framework for voxel-based morphometric analysis of the optic radiation using diffusion tensor imaging in glaucoma. *Magnetic Resonance Imaging*, *29*(8), 1076–1087.
- Engel, S. A., Glover, G. H., & Wandell, B. A. (1997). Retinotopic organization in human visual cortex and the spatial precision of functional MRI. *Cerebral Cortex*, *7*(2), 181–192.
- Engel, S. A., Rumelhart, D. E., Wandell, B. A., Lee, A. T., Glover, G. H., Chichilnisky, E. J., & Shadlen, M. N. (1994). fMRI of human visual cortex. *Nature*, *369*(6481), 525.
- Erskine, L., & Herrera, E. (2014). Connecting the retina to the brain. *ASN Neuro*, *6*(6), 1–26.
- Erskine, L., Reijntjes, S., Pratt, T., Denti, L., Schwarz, Q., Vieira, J. M., et al. (2011). VEGF Signaling through Neuropilin 1 guides commissural axon crossing at the optic chiasm. *Neuron*, *70*(5), 951–965.
- Federow, H., Tribl, F., Halliday, G., Gerlach, M., Riederer, P., & Double, K. L. (2005). Neuromelanin in human dopamine neurons: Comparison with peripheral melanins and relevance to Parkinson's disease. *Progress in Neurobiology*, *75*(2), 109–124.
- Felleman, D. J., & Van Essen, D. C. (1991). Distributed hierarchical processing in the primate cerebral cortex. *Cerebral Cortex*, *1*(1), 1–47.
- Fernandez-Miranda, J. C., Pathak, S., Engh, J., Jarbo, K., Verstynen, T., Yeh, F.-C., et al. (2012). High-definition fiber tractography of the human brain. *Neurosurgery*, *71*(2), 430–453.
- Finlay, B. L. (2008). The developing and evolving retina: Using time to organize form. *Brain Research*, *1192*, 5–16.
- Fischl, B., Sereno, M. I., & Dale, A. M. (1999). Cortical surface-based analysis. II: Inflation, flattening, and a surface-based coordinate system. *NeuroImage*, *9*(2), 195–207.
- Fox, M. D., & Greicius, M. (2010). Clinical applications of resting state functional connectivity. *Frontiers in Systems Neuroscience*, *4*, 19–19.

- Fries, W. (1981). The projection from the lateral geniculate nucleus to the prestriate cortex of the macaque monkey. *Proceedings of the Royal Society of London Series B - Biological Sciences*, 213(1190), 73–80.
- Friston, K. J., Ashburner, J., Frith, C. D., Poline, J. B., Heather, J. D., & Frackowiak, R. S. (1995a). Spatial registration and normalization of images. In *Human Brain Function* (pp. 165–189). Academic Press USA.
- Friston, K. J., Frith, C. D., Turner, R., & Frackowiak, R. S. (1995b). Characterizing evoked hemodynamics with fMRI. *NeuroImage*, 2(2), 157–165.
- Fujita, N., Tanaka, H., Takanashi, M., Hirabuki, N., Abe, K., Yoshimura, H., & Nakamura, H. (2001). Lateral geniculate nucleus: anatomic and functional identification by use of MR imaging. *American Journal of Neuroradiology*, 22(9), 1719–1726.
- Garey, L. J., & Powell, T. P. (1971). An experimental study of the termination of the lateral geniculo-cortical pathway in the cat and monkey. *Proceedings of the Royal Society of London Series B - Biological Sciences*, 179(54), 41–63.
- Gelman, A., Hill, J., & Yajima, M. (2012). Why we (usually) don't have to worry about multiple comparisons. *Journal of Research on Educational Effectiveness*, 5, 189–211.
- Genç, E., Bergmann, J., Singer, W., & Kohler, A. (2011a). Interhemispheric connections shape subjective experience of bistable motion. *Current Biology*, 21(17), 1494–1499.
- Genç, E., Bergmann, J., Tong, F., Blake, R., Singer, W., & Kohler, A. (2011b). Callosal connections of primary visual cortex predict the spatial spreading of binocular rivalry across the visual hemifields. *Frontiers in Human Neuroscience*, 5, 161.
- Gray, H. (1918). *Anatomy of the human body*. Edinburgh: C Livingstone.
- Grieve, K. L., Acuña, C., & Cudeiro, J. (2000). The primate pulvinar nuclei: vision and action. *Trends in Neurosciences*, 23(1), 35–39.
- Grosso, M., Ricci, D., Bassi, L., Merchant, N., Doria, V., Arichi, T., et al. (2012). Development of the optic radiations and visual function after premature birth. *Cortex*, 1–8.
- Grønskov, K., Ek, J., & Brøndum-Nielsen, K. (2007). Oculocutaneous albinism. *Orphanet Journal of Rare Diseases*, 2(1), 43.
- Guillery, R. W. (1986). Neural Abnormalities of Albinos. *Trends in Neurosciences*, 9(8), 364–367.
- Guillery, R. W. R., Jeffery, G. G., & Saunders, N. N. (1999). Visual abnormalities in albino wallabies: A brief note. *Journal of Comparative Neurology*, 403(1), 33–38.
- Guillery, R. W., & Kaas, J. H. (1973). Genetic abnormality of the visual pathways in a “white” tiger. *Science*, 180(4092), 1287–1289.
- Guillery, R. W., Casagrande, V. A., & Oberdorfer, M. D. (1974). Congenitally abnormal vision in Siamese cats. *Nature*, 252(5480), 195–199.

- Guillery, R. W., Hickey, T. L., Kaas, J. H., Felleman, D. J., Debruyn, E. J., & Sparks, D. L. (1984). Abnormal central visual pathways in the brain of an albino green monkey (*cercopithecus aethiops*). *Journal of Comparative Neurology*, 226(2), 165–183.
- Guillery, R. W., Mason, C. A., & Taylor, J. S. (1995). Developmental determinants at the mammalian optic chiasm. *Journal of Neuroscience*, 15(7 Pt 1), 4727–4737.
- Guillery, R. W., Okoro, A. N., & Witkop, C. J. (1975). Abnormal visual pathways in the brain of a human albino. *Brain Research*, 96(2), 373–377.
- Guzzetta, A., D'Acunto, G., Rose, S., Tinelli, F., Boyd, R., & Cioni, G. (2010). Plasticity of the visual system after early brain damage. *Developmental Medicine and Child Neurology*, 52(10), 891–900.
- Haak, K. V., Cornelissen, F. W., & Morland, A. B. (2012). Population receptive field dynamics in human visual cortex. *PLoS ONE*, 7(5), e37686.
- Hagen, von dem, E. A. H., Hoffmann, M. B., & Morland, A. B. (2008). Identifying human albinism: A comparison of VEP and fMRI. *Investigative Ophthalmology & Visual Science*, 49(1), 238–249.
- Hagen, von dem, E. A. H., Houston, G. C. G., Hoffmann, M. B. M., Jeffery, G. G., & Morland, A. B. (2005). Retinal abnormalities in human albinism translate into a reduction of grey matter in the occipital cortex. *European Journal of Neuroscience*, 22(10), 2475–2480.
- Hagen, von dem, E. A. H., Houston, G. C., Hoffmann, M. B., & Morland, A. B. (2007). Pigmentation predicts the shift in the line of decussation in humans with albinism. *European Journal of Neuroscience*, 25(2), 503–511.
- Hagmann, P., Jonasson, L., Maeder, P., Thiran, J. P., Wedeen, V. J., & Meuli, R. (2006). Understanding diffusion MR imaging techniques: From scalar diffusion-weighted imaging to diffusion tensor imaging and beyond. *RadioGraphics*, 26(Supplement 1), S205–S223.
- Hansen, K. A., David, S. V., & Gallant, J. L. (2004). Parametric reverse correlation reveals spatial linearity of retinotopic human V1 BOLD response. *NeuroImage*, 23(1), 233–241.
- Harvey, B. M., & Dumoulin, S. O. (2011). The relationship between cortical magnification factor and population receptive field size in human visual cortex: Constancies in cortical architecture. *Journal of Neuroscience*, 31(38), 13604–13612.
- Hedera, P., Lai, S., Haacke, E. M., Lerner, A. J., Hopkins, A. L., Lewin, J. S., & Friedland, R. P. (1994). Abnormal connectivity of the visual pathways in human albinos demonstrated by susceptibility-sensitized MRI. *Neurology*, 44(10), 1921–1926.
- Henriksson, L., Karvonen, J., Salminen-Vaparanta, N., Railo, H., & Vanni, S. (2012). Retinotopic maps, spatial tuning, and locations of human visual areas in surface coordinates characterized with multifocal and blocked fMRI designs. *PLoS ONE*, 7(5), e36859.
- Hofer, S., Karaus, A., & Frahm, J. (2010). Reconstruction and dissection of the entire human visual pathway using diffusion tensor MRI. *Frontiers in Neuroanatomy*, 4, 15.

- Hoffmann, M. B., & Dumoulin, S. O. (2015). Congenital visual pathway abnormalities: a window onto cortical stability and plasticity. *Trends in Neurosciences*, 38(1), 55–65.
- Hoffmann, M. B., Kaule, F. R., Levin, N., Masuda, Y., Kumar, A., Gottlob, I., et al. (2012). Plasticity and stability of the visual system in human achiasma. *Neuron*, 75(3), 393–401.
- Hoffmann, M. B., Lorenz, B., Morland, A. B., & Schmidtborn, L. C. (2005). Misrouting of the optic nerves in albinism: Estimation of the extent with visual evoked potentials. *Investigative Ophthalmology & Visual Science*, 46(10), 3892–3898.
- Hoffmann, M. B., Seufert, P. S., & Schmidtborn, L. C. (2007). Perceptual relevance of abnormal visual field representations: Static visual field perimetry in human albinism. *British Journal of Ophthalmology*, 91(4), 509–513.
- Hoffmann, M. B., Tolhurst, D. J., Moore, A. T., & Morland, A. B. (2003). Organization of the visual cortex in human albinism. *Journal of Neuroscience*, 23(26), 8921–8930.
- Hoffmann, M., Lorenz, B., Preising, M., & Seufert, P. S. (2006). Assessment of cortical visual field representations with multifocal VEPs in control subjects, patients with albinism, and female carriers of ocular albinism. *Investigative Ophthalmology & Visual Science*, 47(7), 3195–3201.
- Hu, F., Hanifin, J. M., Prescott, G. H., & Tongue, A. C. (1980). Yellow mutant albinism: Cytochemical, ultrastructural, and genetic characterization suggesting multiple allelism. *American Journal of Human Genetics*, 32(3), 387–395.
- Huang, R.-S., & Sereno, M. I. (2013). Bottom-up retinotopic organization supports top-down mental imagery. *Open Neuroimaging Journal*, 7, 58–67.
- Hubel, D. H. D., & Wiesel, T. N. T. (1962). Receptive fields, binocular interaction and functional architecture in the cat's visual cortex. *Journal of Physiology*, 160, 106–154.
- Hubel, D. H., & Wiesel, T. N. (1969). Anatomical demonstration of columns in the monkey striate cortex. *Nature*, 221(5182), 747–750.
- Hubel, D. H., & Wiesel, T. N. (1971). Aberrant visual projections in the Siamese cat. *Journal of Physiology*, 218(1), 33–62.
- Hubel, D. H., & Wiesel, T. N. (1977). Ferrier lecture: Functional architecture of macaque monkey visual cortex. *Proceedings of the Royal Society of London Series B - Biological Sciences*, 198(1130), 1–59.
- Hummer, A., Ritter, M., Tik, M., Ledolter, A., Woletz, M., holder, G. E., et al. (2016). Eyetracker-based gaze correction for robust mapping of population receptive fields. *NeuroImage*, 1–38.
- Hutton, C., Bork, A., Josephs, O., Deichmann, R., Ashburner, J., & Turner, R. (2002). Image distortion correction in fMRI: A quantitative evaluation. *NeuroImage*, 16(1), 217–240.
- Ilija, M., & Jeffery, G. G. (1996). Delayed neurogenesis in the albino retina: evidence of a role for melanin in regulating the pace of cell generation. *Brain Research. Developmental Brain Research*, 95(2), 176–183.

- Jalkanen, R., Bech-Hansen, N. T., Tobias, R., Sankila, E. M., Mantyjarvi, M., Forsius, H., et al. (2007). A novel CACNA1F gene mutation causes Aland Island eye disease. *Investigative Ophthalmology & Visual Science*, 48(6), 2498–2502.
- Jeffery, G. G., & Erskine, L. (2005). Variations in the architecture and development of the vertebrate optic chiasm. *Progress in Retinal and Eye Research*, 24(6), 721–753.
- Jones, D. K., Knösche, T. R., & Turner, R. (2012). White matter integrity, fiber count, and other fallacies: The do“s and don”ts of diffusion MRI. *NeuroImage*, 73, 1–16.
- Kaas, J. H. (2005). Serendipity and the Siamese cat: The discovery that genes for coat and eye pigment affect the brain. *ILAR Journal*, 46(4), 357–363.
- Kaas, J. H., & Guillery, R. W. (1973). The transfer of abnormal visual field representations from the dorsal lateral geniculate nucleus to the visual cortex in siamese cats. *Brain Research*, 59, 61–95.
- Kaiser, P. K., & Boynton, G. M. (1996). Human color vision. Washington, DC: Optical Society of America.
- Kaule, F. R., Wolynski, B., Gottlob, I., Stadler, J., Speck, O., Kanowski, M., et al. (2014). Impact of chiasma opticum malformations on the organization of the human ventral visual cortex. *Human Brain Mapping*, 35(10), 5093–5105.
- Kay, K. N., Weiner, K. S., & Grill-Spector, K. (2015). Attention reduces spatial uncertainty in human ventral temporal cortex. *Current Biology*, 25(5), 595–600.
- Kay, K. N., Winawer, J., Rokem, A., Mezer, A., & Wandell, B. A. (2013). A two-stage cascade model of BOLD responses in human visual cortex. *PLoS Computational Biology*, 9(5), e1003079.
- Kennedy, H., & Bullier, J. (1985). A double-labeling investigation of the afferent connectivity to cortical areas V1 and V2 of the macaque monkey. *Journal of Neuroscience*, 5(10), 2815–2830.
- Kim, M., Ducros, M., Carlson, T., Ronen, I., He, S., Ugurbil, K., & Kim, D.-S. (2006). Anatomical correlates of the functional organization in the human occipitotemporal cortex. *Magnetic Resonance Imaging*, 24(5), 583–590.
- Kinnear, P. E. P., Jay, B. B., & Witkop, C. J. C. (1985). Albinism. *Survey of Ophthalmology*, 30(2), 75–101.
- Kiprono, S. K., Chaula, B. M., & Beltraminelli, H. (2014). Histological review of skin cancers in African albinos: A 10-year retrospective review. *BMC Cancer*, 14(1), 1–4.
- Klemen, J., Hoffmann, M. B., & Chambers, C. D. (2012). Cortical plasticity in the face of congenitally altered input into V1. *Cortex*, 48(10), 1362–1365.
- Kok, P., & de Lange, F. P. (2014). Shape perception simultaneously up- and downregulates neural activity in the primary visual cortex. *Current Biology*, 24(13), 1531–1535.
- Kolbe, S., Bajraszewski, C., Chapman, C., Nguyen, T., Mitchell, P., Paine, M., et al. (2011). Diffusion tensor imaging of the optic radiations after optic neuritis. *Human Brain Mapping*, 33(9), 2047–2061.

- Kommerell, G., Schmitt, C., Kromeier, M., & Bach, M. (2003). Ocular prevalence versus ocular dominance. *Vision Research*, 43(12), 1397–1403.
- Lagarias, J. C., Reeds, J. A., Wright, M. H., & Wright, P. E. (1998). Convergence properties of the Nelder-Mead simplex method in low dimensions. *SIAM Journal on Optimization*, 9(1), 112–147.
- Larsson, J., & Heeger, D. J. (2006). Two retinotopic visual areas in lateral occipital cortex. *Journal of Neuroscience*, 26(51), 13128–13142.
- Lavidor, M. & Walsh, V. (2004). The nature of the foveal representation. *Nature Reviews*, 5(9), 729–735.
- Le Bihan, D. (2003). Looking into the functional architecture of the brain with diffusion MRI. *Nature Reviews: Neuroscience*, 4(6), 469–480.
- Le Bihan, D., Mangin, J. F., Poupon, C., Clark, C. A., Pappata, S., Molko, N., & Chabriat, H. (2001). Diffusion tensor imaging: Concepts and applications. *Journal of Magnetic Resonance Imaging*, 13(4), 534–546.
- Leh, S. E., Chakravarty, M. M., & Ptito, A. (2008). The connectivity of the human pulvinar: A diffusion tensor imaging tractography study. *International Journal of Biomedical Imaging*, 2008(2), 1–5.
- Levin, N., Dumoulin, S. O., Winawer, J., Dougherty, R. F., & Wandell, B. A. (2010). Cortical maps and white matter tracts following long period of visual deprivation and retinal image restoration. *Neuron*, 65(1), 21–31.
- Logothetis, N. K. (2002). The neural basis of the blood-oxygen-level-dependent functional magnetic resonance imaging signal. *Philosophical Transactions of the Royal Society of London Series B, Biological Sciences*, 357(1424), 1003–1037.
- Lund, R. D. (1965). Uncrossed visual pathways of hooded and albino rats. *Science*, 149(3691), 1506–1507.
- Ma, Y., Ward, B. D., Ropella, K. M., & DeYoe, E. A. (2013). Comparison of randomized multifocal mapping and temporal phase mapping of visual cortex for clinical use. *NeuroImage. Clinical*, 3, 143–154.
- Maciewicz, R. J. (1975). Thalamic afferents to areas 17, 18 and 19 of cat cortex traced with horseradish peroxidase. *Brain Research*, 84(2), 308–312.
- Manger, P. R., & Rosa, M. G. P. (2005). Visual thalamocortical projections in the flying fox: Parallel pathways to striate and extrastriate areas. *Neuroscience*, 130(2), 497–511.
- Marcus, R. C., Wang, L. C., & Mason, C. A. (1996). Retinal axon divergence in the optic chiasm: midline cells are unaffected by the albino mutation. *Development*, 122(3), 859–868.
- Maunsell, J. H., & Newsome, W. T. (1987). Visual processing in monkey extrastriate cortex. *Annual Review of Neuroscience*, 10, 363–401.
- Mártinez-García, M., & Montoliu, L. (2013). Albinism in Europe. *The Journal of Dermatology*, 40(5), 319–324.

- Mcketton, L., Kelly, K. R., & Schneider, K. A. (2014). Abnormal lateral geniculate nucleus and optic chiasm in human albinism. *Journal of Comparative Neurology*, *522*(11), 2680–2687.
- Mohammad, S., Gottlob, I., Kumar, A., Thomas, M., Degg, C., Sheth, V., & Proudlock, F. A. (2011). The functional significance of foveal abnormalities in albinism measured using spectral-domain optical coherence tomography. *Ophthalmology*, *118*(8), 1645–1652.
- Montoliu, L., Grønskov, K., Wei, A.-H., Martínez-García, M., Fernández, A., Arveiler, B., et al. (2013). Increasing the complexity: New genes and new types of albinism. *Pigment Cell & Melanoma Research*, *27*(1), 11–18.
- Morland, A. B., Hoffmann, M., Neveu, M. M., & Holder, G. E. (2002). Abnormal visual projection in a human albino studied with functional magnetic resonance imaging and visual evoked potentials. *Journal of Neurology, Neurosurgery & Psychiatry*, *72*(4), 523–526.
- Nair, D. G. (2005). About being BOLD. *Brain Research Reviews*, *50*(2), 229–243.
- Nakagawa, S., Brennan, C., Johnson, K. G., Shewan, D., Harris, W. A., & Holt, C. E. (2000). Ephrin-B regulates the ipsilateral routing of retinal axons at the optic chiasm. *Neuron*, *25*(3), 599–610.
- Nauhaus, I., & Nielsen, K. J. (2014). Building maps from maps in primary visual cortex. *Current Opinion in Neurobiology*, *24*, 1–6.
- Neveu, M. M., & Jeffery, G. G. (2007). Chiasm formation in man is fundamentally different from that in the mouse, *21*(10), 1264–1270.
- Neveu, M. M., Hagen, von dem, E. A. H., Morland, A. B., & Jeffery, G. G. (2007). The fovea regulates symmetrical development of the visual cortex. *Journal of Comparative Neurology*, *506*(5), 791–800.
- Neveu, M. M., Jeffery, G. G., Burton, L. C., Sloper, J. J., & Holder, G. E. (2003). Age-related changes in the dynamics of human albino visual pathways. *European Journal of Neuroscience*, *18*(7), 1939–1949.
- Nurminen, L., Peromaa, T., & Laurinen, P. (2010). Surround suppression and facilitation in the fovea: Very long-range spatial interactions in contrast perception. *Journal of Vision*, *10*(13), 1–13.
- Oetting, W. S., & King, R. A. (1999). Molecular basis of albinism: Mutations and polymorphisms of pigmentation genes associated with albinism. *Human Mutation*, *13*(2), 99–115.
- Ogawa, S., Lee, T. M., Kay, A. R., & Tank, D. W. (1990). Brain magnetic resonance imaging with contrast dependent on blood oxygenation. *Proceedings of the National Academy of Sciences*, *87*(24), 9868–9872.
- Oldfield, R. C. (1971). The assessment and analysis of handedness: The Edinburgh inventory. *Neuropsychologia*, *9*(1), 97–113.

- Orban, G. A., Van Essen, D., & Vanduffel, W. (2004). Comparative mapping of higher visual areas in monkeys and humans. *Trends in Cognitive Sciences*, 8(7), 315–324.
- Papanikolaou, A., Keliris, G. A., Papageorgiou, T. D., Shao, Y., Krapp, E., Papageorgiou, E., et al. (2014). Population receptive field analysis of the primary visual cortex complements perimetry in patients with homonymous visual field defects. *Proceedings of the National Academy of Sciences*, 111(16), E1656–E1665.
- Parker, G. J. M., Haroon, H. A., & Wheeler-Kingshott, C. A. M. (2003). A framework for a streamline-based probabilistic index of connectivity (PICO) using a structural interpretation of MRI diffusion measurements. *Journal of Magnetic Resonance Imaging*, 18(2), 242–254.
- Párraga, R. G., Ribas, G. C., Welling, L. C., Alves, R. V., & de Oliveira, E. (2012). Microsurgical anatomy of the optic radiation and related fibers in 3-dimensional images. *Neurosurgery*, 71, 160–172.
- Pelli, D. G. D. (1997). The VideoToolbox software for visual psychophysics: Transforming numbers into movies. *Spatial Vision*, 10(4), 437–442.
- Peltier, J., Travers, N., Destrieux, C., & Velut, S. (2006). Optic radiations: A microsurgical anatomical study. *Journal of Neurosurgery*, 105(2), 294–300.
- Pessoa, L., & Adolphs, R. (2010). Emotion processing and the amygdala: from a 'low road' to "many roads" of evaluating biological significance. *Nature Reviews: Neuroscience*, 11(11), 1–10.
- Petros, T. J., Rebsam, A., & Mason, C. A. (2008). Retinal axon growth at the optic chiasm: To cross or not to cross. *Annual Review of Neuroscience*, 31(1), 295–315.
- Peuskens, D., van Loon, J., Van Calenbergh, F., van den Bergh, R., Goffin, J., & Plets, C. (2004). Anatomy of the anterior temporal lobe and the frontotemporal region demonstrated by fiber dissection. *Neurosurgery*, 55(5), 1174–1184.
- Pott, J., Jansonius, N. M., & Kooijman, A. C. (2003). Chiasmal coefficient of flash and pattern visual evoked potentials for detection of chiasmal misrouting in albinism. *Documenta Ophthalmologica*, 106(2), 137–143.
- Powell, H. W. R., Parker, G. J. M., Alexander, D. C., Symms, M. R., Boulby, P. A., Wheeler-Kingshott, C. A. M., et al. (2005). MR tractography predicts visual field defects following temporal lobe resection. *Neurology*, 65(4), 596–599.
- Puckett, A. M., & DeYoe, E. A. (2015). The attentional field revealed by single-voxel modeling of fMRI time courses. *Journal of Neuroscience*, 35(12), 5030–5042.
- Pujari, V. B., Jimbo, H., Dange, N., Shah, A., Singh, S., & Goel, A. (2008). Fiber dissection of the visual pathways: Analysis of the relationship of optic radiations to lateral ventricle: A cadaveric study. *Neurology India*, 56(2), 133–137.
- Purushothaman, G., Marion, R., Li, K., & Casagrande, V. A. (2012). Gating and control of primary visual cortex by pulvinar. *Nature Neuroscience*, 15(6), 905–912.

- Rachel, R. A., Dolen, G., Hayes, N. L., Lu, A., Erskine, L., Nowakowski, R. S., & Mason, C. A. (2002). Spatiotemporal features of early neuronogenesis differ in wild-type and albino mouse retina. *Journal of Neuroscience*, *22*(11), 4249–4263.
- Raemaekers, M., Schellekens, W., van Wezel, R. J. A., Petridou, N., Kristo, G., & Ramsey, N. F. (2014). Patterns of resting state connectivity in human primary visual cortical areas: A 7T fMRI study. *NeuroImage*, *84*(C), 911–921.
- Rashid, T., Upton, A. L., Blentic, A., Ciossek, T., Knöll, B., Thompson, I. D., & Drescher, U. (2005). Opposing gradients of Ephrin-As and EphA7 in the superior colliculus are essential for topographic mapping in the mammalian visual system. *Neuron*, *47*(1), 57–69.
- Rebsam, A., Bhansali, P., & Mason, C. A. (2012). Eye-specific projections of retinogeniculate axons are altered in albino mice. *Journal of Neuroscience*, *32*(14), 4821–4826.
- Reese, B. E. (2011). Development of the retina and optic pathway. *Vision Research*, *51*(7), 613–632.
- Reid, R. C., & Alonso, J. M. (1995). Specificity of monosynaptic connections from thalamus to visual cortex. *Nature*, *378*(6554), 281–284.
- Rice, D. S., Goldowitz, D., Williams, R. W., Hamre, K., Johnson, P. T., Tan, S. S., & Reese, B. E. (1999). Extrinsic modulation of retinal ganglion cell projections: analysis of the albino mutation in pigmentation mosaic mice. *Developmental Biology*, *216*(1), 41–56.
- Rice, M. L., Leske, D. A., Smestad, C. E., & Holmes, J. M. (2008). Results of ocular dominance testing depend on assessment method. *Journal of American Association for Pediatric Ophthalmology and Strabismus*, *12*(4), 365–369.
- Riley, P. A. (1997). Melanin. *International Journal of Biochemistry & Cell Biology*, *29*(11), 1235–1239.
- Rosenberg, T., & Schwartz, M. (1998). X-linked ocular albinism: prevalence and mutations - a national study. *European Journal of Human Genetics*, *6*(6), 570–577.
- Rosenberg, T., Schwartz, E. L., & Simonsen, S. E. (1990). Aland eye disease (Forsius-Eriksson-Miyake syndrome) with probability established in a Danish family. *Acta Ophthalmologica*, *68*(3), 281–291.
- Rovamo, J. J., & Virsu, V. V. (1979). An estimation and application of the human cortical magnification factor. *Experimental Brain Research*, *37*(3), 495–510.
- Rubino, P. A., Rhoton, A. L., Jr, Tong, X., & de Oliveira, E. (2005). Three-dimensional relationships of the optic radiation. *Neurosurgery*, *57*(Supplement 4), 219–227.
- Saenz, M., & Fine, I. (2010). Topographic organization of V1 projections through the corpus callosum in humans. *NeuroImage*, *52*(4), 1224–1229.
- Sanderson, K. J., Guillery, R. W., & Shackelford, R. M. (1974). Congenitally abnormal visual pathways in mink (*Mustela vison*) with reduced retinal pigment. *Journal of Comparative Neurology*, *154*(3), 225–248.

- Saygin, A. P., & Sereno, M. I. (2008). Retinotopy and attention in human occipital, temporal, parietal, and frontal cortex. *Cerebral Cortex*, *18*(9), 2158–2168.
- Schmitz, B., Schaefer, T., Krick, C. M., Reith, W., Backens, M., & Käsmann-Kellner, B. (2003). Configuration of the optic chiasm in humans with albinism as revealed by magnetic resonance imaging. *Investigative Ophthalmology & Visual Science*, *44*(1), 16–21.
- Schneider, K. A., & Kastner, S. (2005). Visual responses of the human superior colliculus: A high-resolution functional magnetic resonance imaging study, *94*(4), 2491–2503.
- Schneider, K. A., Richter, M. C., & Kastner, S. (2004). Retinotopic organization and functional subdivisions of the human lateral geniculate nucleus: A high-resolution functional magnetic resonance imaging study. *Journal of Neuroscience*, *24*(41), 8975–8985.
- Schwarzkopf, D. S., Anderson, E. J., de Haas, B., White, S. J., & Rees, G. (2014). Larger extrastriate population receptive fields in autism spectrum disorders. *Journal of Neuroscience*, *34*(7), 2713–2724.
- Schwarzkopf, D. S., Song, C., & Rees, G. (2010). The surface area of human V1 predicts the subjective experience of object size. *Nature Neuroscience*, *14*(1), 28–30.
- Seijas, O., Gómez de Liaño, P., Gómez de Liaño, R., Roberts, C. J., Piedrahita, E., & Diaz, E. (2007). Ocular dominance diagnosis and its influence in monovision. *American Journal of Ophthalmology*, *144*(2), 209–216.
- Sereno, M. I., & Tootell, R. B. (2005). From monkeys to humans: what do we now know about brain homologies? *Current Opinion in Neurobiology*, *15*(2), 135–144.
- Sereno, M. I., Dale, A. M., Reppas, J. B., Kwong, K. K., Belliveau, J. W., Brady, T. J., et al. (1995). Borders of multiple visual areas in humans revealed by functional magnetic resonance imaging. *Science*, *268*(5212), 889–893.
- Sereno, M. I., Lutti, A., Weiskopf, N., & Dick, F. (2013). Mapping the human cortical surface by combining quantitative T1 with retinotopy. *Cerebral Cortex*, *23*(9), 2261–2268.
- Seunirane, K. K., & Alexander, D. C. (2009). Multiple fibres: Beyond the diffusion tensor. In H. Johansen-Berg & T. E. J. Behrens (Eds.), *Diffusion MRI: from quantitative measurement to in vivo neuroanatomy*. PA.
- Shatz, C. J., & LeVay, S. (1979). Siamese cat: altered connections of visual cortex. *Science*, *204*(4390), 328–330.
- Sherbondy, A. J., Dougherty, R. F., Napel, S., & Wandell, B. A. (2008). Identifying the human optic radiation using diffusion imaging and fiber tractography. *Journal of Vision*, *8*(10), 12.
- Shipp, S. (2003). The functional logic of cortico-pulvinar connections. *Philosophical Transactions of the Royal Society of London Series B, Biological Sciences*, *358*(1438), 1605–1624.

- Simeonov, D. R., Wang, X., Wang, C., Sergeev, Y., Dolinska, M., Bower, M., et al. (2013). DNA variations in oculocutaneous albinism: An updated mutation list and current outstanding issues in molecular diagnostics. *Human Mutation*, *34*(6), 827–835.
- Sincoff, E. H., Tan, Y. X., & Abdulrauf, S. I. (2004). White matter fiber dissection of the optic radiations of the temporal lobe and implications for surgical approaches to the temporal horn. *Journal of Neurosurgery*, *101*(5), 739–746.
- Slotnick, S. D., & Yantis, S. (2003). Efficient acquisition of human retinotopic maps. *Human Brain Mapping*, *18*(1), 22–29.
- Smith, A. T., Singh, K. D., Williams, A. L., & Greenlee, M. W. (2001). Estimating receptive field size from fMRI data in human striate and extrastriate visual cortex. *Cerebral Cortex*, *11*(12), 1182–1190.
- Sperry, R. W. (1963). Chemoaffinity in the orderly growth of nerve fiber patterns and connections. *Proceedings of the National Academy of Sciences of the United States of America*, *50*(4), 703–710.
- Stejskal, E. O., & Tanner, J. E. (1965). Spin diffusion measurements: Spin echoes in the presence of a time-dependent field gradient. *Journal of Chemical Physics*, *42*(1), 288–292.
- Stone, J., Campion, J. E., & Leicester, J. (1978). The nasotemporal division of retina in the Siamese cat. *Journal of Comparative Neurology*, *180*(4), 783–798.
- Summers, C. G. (1996). Vision in albinism. *Transactions of the American Ophthalmological Society*, *94*, 1095–1155.
- Summers, C. G. (2009). Albinism: Classification, clinical characteristics, and recent findings. *Optometry and Vision Science*, *86*(6), 659–662.
- Summers, C. G., Connett, J. E., Holleschau, A. M., Anderson, J. L., De Becker, I., McKay, B. S., & Brilliant, M. H. (2014). Does levodopa improve vision in albinism? Results of a randomized, controlled clinical trial. *Clinical & Experimental Ophthalmology*, *42*(8), 713–721.
- Tootell, R. B., Mendola, J. D., Hadjikhani, N. K., Ledden, P. J., Liu, A. K., Reppas, J. B., et al. (1997). Functional analysis of V3A and related areas in human visual cortex. *Journal of Neuroscience*, *17*(18), 7060–7078.
- Tootell, R. B., Mendola, J. D., Hadjikhani, N. K., Liu, A. K., & Dale, A. M. (1998). The representation of the ipsilateral visual field in human cerebral cortex. *Proceedings of the National Academy of Sciences*, *95*(3), 818–824.
- Tournier, J. D., Calamante, F., & Connelly, A. (2007). Robust determination of the fibre orientation distribution in diffusion MRI: Non-negativity constrained super-resolved spherical deconvolution. *NeuroImage*, *35*(4), 1459–1472.
- Tournier, J. D., Calamante, F., & Connelly, A. (2012). MRtrix: Diffusion tractography in crossing fiber regions. *International Journal of Imaging Systems and Technology*, *22*(1), 53–66.

- Tournier, J. D., Calamante, F., Gadian, D. G., & Connelly, A. (2004). Direct estimation of the fiber orientation density function from diffusion-weighted MRI data using spherical deconvolution. *NeuroImage*, 23(3), 1176–1185.
- Tovée, M. J. (1996). An introduction to the visual system. Cambridge University Press.
- Tuch, D. S. (2004). Q-ball imaging. *Magnetic Resonance in Medicine*, 52(6), 1358–1372.
- Van Essen, D. C., & Maunsell, J. H. R. (1983). Hierarchical organization and functional streams in the visual cortex. *Trends in Neurosciences*, 6, 370–375.
- Van Essen, D. C., Newsome, W. T., & Maunsell, J. H. (1984). The visual field representation in striate cortex of the macaque monkey: asymmetries, anisotropies, and individual variability. *Vision Research*, 24(5), 429–448.
- Vanni, S., Henriksson, L., & James, A. C. (2005). Multifocal fMRI mapping of visual cortical areas. *NeuroImage*, 27(1), 95–105.
- Verghese, A., Kolbe, S. C., Anderson, A. J., Egan, G. F., & Vidyasagar, T. R. (2014). Functional size of human visual area V1: A neural correlate of top-down attention. *NeuroImage*, 1–26.
- Victor, J. D. J., Purpura, K. K., Katz, E. E., & Mao, B. B. (1994). Population encoding of spatial frequency, orientation, and color in macaque V1. *NeuroImage*, 72(5), 2151–2166.
- Wahler-Lück, M., Schütz, T., & Kretschmann, H. J. (1991). A new anatomical representation of the human visual pathways. *Graefe's Archive for Clinical and Experimental Ophthalmology*, 229(3), 201–205.
- Wakana, S., Caprihan, A., Panzenboeck, M. M., Fallon, J. H., Perry, M., Gollub, R. L., et al. (2007). Reproducibility of quantitative tractography methods applied to cerebral white matter. *NeuroImage*, 36(3), 630–644.
- Wandell, B. A., & Smirnakis, S. M. (2009). Plasticity and stability of visual field maps in adult primary visual cortex. *NeuroImage*, 10(12), 873–884.
- Wandell, B. A., & Winawer, J. (2011). Imaging retinotopic maps in the human brain. *Vision Research*, 51(7), 718–737.
- Wandell, B. A., & Winawer, J. (2015). Computational neuroimaging and population receptive fields. *Trends in Cognitive Neuroscience*, 19(6), 349–357.
- Wandell, B. A., Brewer, A. A., & Dougherty, R. F. (2005). Visual field map clusters in human cortex. *Philosophical Transactions of the Royal Society of London Series B, Biological Sciences*, 360(1456), 693–707.
- Wandell, B. A., Dumoulin, S. O., & Brewer, A. A. (2007). Visual field maps in human cortex. *Neuron*, 56(2), 366–383.
- Weinberger, D. R. D., Luchins, D. J. D., Morihisa, J. J., & Wyatt, R. J. R. (1982). Asymmetrical volumes of the right and left frontal and occipital regions of the human brain. *Annals of Neurology*, 11(1), 97–100.
- Welton, T., Ather, S., Proudlock, F. A., Gottlob, I., & Dineen, R. A. (2016). Altered whole-brain connectivity in albinism. *Human Brain Mapping*.

- Williams, S. E., Grumet, M., Colman, D. R., Henkemeyer, M., Mason, C. A., & Sakurai, T. (2006). A role for Nr-CAM in the patterning of binocular visual pathways. *Neuron*, *50*(4), 535–547.
- Williams, S. E., Mann, F., Erskine, L., Sakurai, T., Wei, S., Rossi, D. J., et al. (2003). Ephrin-B2 and EphB1 mediate retinal axon divergence at the optic chiasm. *Neuron*, *39*(6), 919–935.
- Williams, S. E., Mason, C. A., & Herrera, E. (2004). The optic chiasm as a midline choice point. *Current Opinion in Neurobiology*, *14*(1), 51–60.
- Winawer, J., Horiguchi, H., Sayres, R. A., Amano, K., & Wandell, B. A. (2010). Mapping hV4 and ventral occipital cortex: The venous eclipse. *Journal of Vision*, *10*(5), 1.
- Winston, G. P., Daga, P., Stretton, J., Modat, M., Symms, M. R., McEvoy, A. W., et al. (2012). Optic radiation tractography and vision in anterior temporal lobe resection. *Annals of Neurology*, *71*(3), 334–341.
- Winston, G. P., Mancini, L., Stretton, J., Ashmore, J., Symms, M. R., Duncan, J. S., & Yousry, T. A. (2011). Diffusion tensor imaging tractography of the optic radiation for epilepsy surgical planning: A comparison of two methods. *Epilepsy Research*, *97*(1-2), 124–132.
- Wolynski, B., Kanowski, M., Meltendorf, S., Behrens-Baumann, W., & Hoffmann, M. B. (2010). Self-organisation in the human visual system-Visuo-motor processing with congenitally abnormal V1 input. *Neuropsychologia*, *48*(13), 3834–3845.
- Wu, J., Yan, T., Zhang, Z., Jin, F., & Guo, Q. (2012). Retinotopic mapping of the peripheral visual field to human visual cortex by functional magnetic resonance imaging. *Human Brain Mapping*, *33*(7), 1727–1740.
- Yacoub, E., Harel, N., & Ugurbil, K. (2008). High-field fMRI unveils orientation columns in humans. *Proceedings of the National Academy of Sciences*, *105*(30), 10607–10612.
- Yacoub, E., Shmuel, A., Logothetis, N., & Ugurbil, K. (2007). Robust detection of ocular dominance columns in humans using Hahn Spin Echo BOLD functional MRI at 7 Tesla. *NeuroImage*, *37*(4), 1161–1177.
- Yan, T., Jin, F., & Wu, J. (2009). Correlated size variations measured in human visual cortex V1/V2/V3 with functional MRI. *Proceedings of Brain Informatics*, 1–9.
- Yogarajah, M., Focke, N. K., Bonelli, S., Cercignani, M., Acheson, J., Parker, G. J. M., et al. (2009). Defining Meyer's loop-temporal lobe resections, visual field deficits and diffusion tensor tractography. *Brain*, *132*(6), 1656–1668.
- Yoshida, K., & Benevento, L. A. (1981). The projection from the dorsal lateral geniculate nucleus of the thalamus to extrastriate visual association cortex in the macaque monkey. *Neuroscience Letters*, *22*(2), 103–108.
- Yu, T. W., & Bargmann, C. I. (2001). Dynamic regulation of axon guidance. *Nature Neuroscience*, *4*(Supp), 1169–1176.

- Yukie, M. M., & Iwai, E. E. (1981). Direct projection from the dorsal lateral geniculate nucleus to the prestriate cortex in macaque monkeys. *Journal of Comparative Neurology*, 201(1), 81–97.
- Zeki, S. M. (1978). Uniformity and diversity of structure and function in rhesus monkey prestriate visual cortex. *Journal of Physiology*, 277, 273–290.
- Zhou, H., Schafer, R. J., & Desimone, R. (2016). Pulvinar-Cortex Interactions in Vision and Attention. *Neuron*, 89(1), 209–220.
- Zimmermann, J., Goebel, R., De Martino, F., Van de Moortele, P. F., Feinberg, D., Adriany, G., et al. (2011). Mapping the organization of axis of motion selective features in human area MT using high-field fMRI. *PLoS ONE*, 6(12), e28716.
- Zucca, F. A., Basso, E., Cupaioli, F. A., Ferrari, E., Sulzer, D., Casella, L., & Zecca, L. (2013). Neuromelanin of the human substantia nigra: An update. *Neurotoxicity Research*, 25(1), 13–23.
- Zuiderbaan, W., Harvey, B. M., & Dumoulin, S. O. (2012). Modeling center-surround configurations in population receptive fields using fMRI. *Journal of Vision*, 12(3), 10.